LOW FIELD MAGNETORESISTIVE BEHAVIOUR OF $La_{1-x}A_xMnO_3$ (A=Sr, Ca) AND Sr_2FeMoO_6 PEROVSKITES

A THESIS

Submitted in partial fulfilment of the requirements for the award of the degree of

DOCTOR OF PHILOSOPHY

in

PHYSICS

by

ANURAG GAUR

DEPARTMENT OF PHYSICS
INDIAN INSTITUTE OF TECHNOLOGY ROORKEE
ROORKEE-247 667 (INDIA)

AUGUST, 2007

INDIAN INSTITUTE OF TECHNOLOGY ROORKEE
ROORKEE

CANDIDATE'S DECLARATION

I hereby certify that the work which is being presented in the thesis entitled **LOW FIELD MAGNETORESISTIVE BEHAVIOUR OF $La_{1-x}A_xMnO_3$ (A=Sr, Ca) AND Sr_2FeMoO_6 PEROVSKITES** in partial fulfilment of the requirements for the award of the degree of Doctor of Philosophy and submitted in the Department of Physics of the Indian Institute of Technology Roorkee, Roorkee is an authentic record of my own work carried out during a period from January, 2003 to August, 2007 under the supervision of Dr. G. D. Varma, Assistant Professor, Department of Physics, Indian Institute of Technology Roorkee, Roorkee.

The matter presented in the thesis has not been submitted by me for the award of any other degree of this or any other Institute.

23.8.07
(ANURAG GAUR)

This is to certify that the above statement made by the candidate is correct to the best of my knowledge.

(G. D. Varma)
Supervisor

Date: 23-08-2007

The Ph.D. Viva-Voice Examination of Mr. **ANURAG GAUR**, Research Scholar, has been held on 12-11-07

12-11-07
Signature of Supervisor

Jitendra Kumar
Signature of External Examiner

ABSTRACT

The discovery of negative magnetoresistance (MR) properties in manganese perovskite has demonstrated for the second time after the break through about high Tc superconducting cuprates that oxides offer a very promising field for the investigation of new materials with specific properties susceptible to be involved in device applications. In 1994, S. Jin et al observed about thousand-fold change in resistance in the epitaxial thin film of perovskite $La_{2/3}Ca_{1/3}MnO_3$ at a high magnetic field of 6 tesla and this extremely large change in resistance was epitomized by the name "Colossal magnetoresistance (CMR)". After that, perovskite manganites with mixed valence of manganese, $R_{1-x}A_xMnO_3$ (R is a rare earth such as La, Nd, Y etc.; A is alkaline earth such as Ca, Ba, Sr etc.) have been the subject of great interest for the scientific community because of colossal magnetoresistance (CMR). These doped perovskite manganites show the simultaneous appearance of metal to insulator and ferromagnetic to paramagnetic transition. From a fundamental point of view the CMR effect seems to be closely related to the double exchange mechanism between Mn^{3+} and Mn^{4+} ions proposed by de Gennes and Goodenough. Nevertheless recent studies made by Millis suggest that Jahn-Teller type electron phonon interactions are greatly involved in the appearance of such properties. Clearly, the knowledge of the crystal structure and chemical bonding of these compounds is of prime importance to understand the CMR properties of these compounds. The interest in these systems exists not only due to their application in magnetic recording/memories, magnetic switches, bolometric detectors etc but due to various interesting properties e.g. charge, orbital, spin ordering and spin-dependent tunneling exhibited by them. The large magnetoresistance of the order of 10^3 percent is observed at large magnetic fields of several tesla and only in a narrow temperature range around the

ferromagnetic transition temperature which restricts their potential applications. So, to observe the large MR over a wide temperature range and relatively smaller external magnetic fields (~mT) is of great importance from the applications point of view.

In addition, the publication by Kobayashi et al in 1998 about the half-metallic character of Sr_2FeMoO_6 triggered a renewed interest in double perovskites materials in the context of their potential applications in the field of spin electronics. Kobayashi et al reported that Sr_2FeMoO_6, an oxide material of $A_2BB'O_6$ type double perovskite structure, has high Curie temperature (T_C ~410 K) and high degree of spin polarization. They observed that Sr_2FeMoO_6 shows large magnetoresistance at room temperature and this property is attractive from the standpoint of both Physics and engineering. The room temperature magnetoresistance is really a good aspect of this compound due to its high Curie temperature but the magnitude of MR at room temperature is small and generally observed at high magnetic field (in tesla range).

Thus, to obtain the large MR at relatively smaller external magnetic fields (~mT) and in a wide temperature range is still required in both perovskite manganites and double perovskites compounds for the applications point of view. Therefore, in the present thesis work, we aimed to improve the large magnetoresistance at low value of fields and in wide range of temperature. The approach to produce the low field magnetoresistance (LFMR) is to exploit the high degree of spin polarization of conduction electrons of these half metallic compounds, $La_{0.7}Sr_{0.3}MnO_3$ (LSMO) and $La_{0.67}Ca_{0.33}MnO_3$ (LCMO) manganites and Sr_2FeMoO_6 double perovskite, by modifying their grain boundaries and generating the tunneling barriers between the grains. In perovskite manganites (LSMO and LCMO), we modified the grain boundaries through varying the particle size by sintering them at different temperatures and by making the composites of these manganites (LSMO and LCMO) with

secondary phases like insulating oxides (NiO, TiO_2, Co_3O_4) and a polymer material (PPS). In double perovskite Sr_2FeMoO_6, we produced the spin disorder by generating the tunneling barriers of insulating $SrMoO_4$ phase between Sr_2FeMoO_6 grains during synthesis by optimizing the synthesis conditions. We have studied the magnetic (e.g. Curie temperature, magnetization) and magnetotransport characteristics (e.g. metal to insulator transition and magnetoresistance) of manganites and double perovskite and correlated them with their structural and microstructural characteristics.

The present thesis is divided into seven chapters. The **first chapter** contains an introductory aspects and surveys of the field and describes the basic structure, phase diagram and causes of magnetoresistance in both of the studied manganites and double perovskite systems.

The **second chapter** describes the prominent techniques for structural, electrical and magnetic characterization employed in the present investigations. These techniques include X-ray diffraction (XRD) for phase identification, scanning electron microscopy (SEM) using secondary electron imaging mode for investigating the surface morphology and energy dispersive X-ray (EDX) spectroscopy for elemental analysis. Different techniques that have been used to prepare bulk samples such as solid state reaction and sol-gel method have also been described in detail in this chapter. Besides this, the four probe technique for resistivity and magnetoresistance measurements and vibrating sample magnetometer for magnetic property measurements have also been outlined.

The **third chapter** describes the sintering temperature effect on magnetotransport and magnetic properties of $La_{0.7}Sr_{0.3}MnO_3$ (LSMO) and $La_{0.67}Ca_{0.33}MnO_3$ (LCMO) polycrystalline samples. The polycrystalline LSMO and LCMO samples were prepared by sol-gel method. The samples were sintered at different temperatures ranging from 600-

1000°C and found that particle size increases with increasing the sintering temperature. It is shown that magnetotransport properties of both compounds strongly depend on sintering temperature (Ts) as well as particle size. Substantial decrease in insulator-metal transition temperature (T_{IM}) and enhancement in resistivity is found on lowering the sintering temperature. T_{IM} decreases from 303 to 175 K for LSMO and 272 to 186 K for LCMO samples as sintering temperature decreases from 1000-600 °C. Furthermore, reduction in magnetization and slight decrease in paramagnetic-ferromagnetic (PM-FM) transition temperatures (Tc) has been observed as sintering temperature decreases. Tc decreases from 330 to 311 K for LSMO and 288 to 258 K for LCMO as sintering temperature decreases from 1000-600 °C. The magnetoresistance (MR) at T<Tc increases on decreasing the sintering temperature as well as increasing the applied magnetic field. It has been found that the maximum MR is shown by the samples of smallest particles sintered at lowest temperature (600 °C) in both of LSMO and LCMO systems. Furthermore in LCMO samples, at/around Tc the intrinsic contribution of MR occurs which is more in the larger size samples.

The **fourth chapter** embodies the synthesis, magnetic and magnetotransport characteristics of the composites $La_{0.7}Sr_{0.3}MnO_3$ (LSMO) with insulating oxides NiO and TiO_2. The $(LSMO)_{1-x}/(NiO)_x$ and $(LSMO)_{1-x}/(TiO_2)_x$ composites with x = 0.0, 0.05, 0.10, 0.15 and 0.20 were prepared via solid state reaction process. Detailed studies of magnetic and magnetotransport properties of both the composite systems have been performed. Both, X-ray diffraction and scanning electron microscopy observations reveal that there is no reaction between the parent CMR oxide (LSMO) and second phase material (NiO and TiO_2) and the second phase material segregates at the grain boundaries and on the surfaces of LSMO grains. It has been observed that the incorporation of second phase material into the CMR matrix lowers the T_{IM} and suppresses the ferromagnetic order of CMR compound. The value

of T_{IM} decreases from 315 to 156 K for $(LSMO)_{1-x}/(NiO)_x$ and 315 to 185 K for $(LSMO)_{1-x}/(TiO_2)_x$ when x varies from 0 to 0.20. Moreover, the value of Curie temperature (Tc) decreases from ~343 K to ~318 K with increasing NiO content (x) from 0.0 to 0.20 in case of $(LSMO)_{1-x}/(NiO)_x$ composite. However in case of $(LSMO)_{1-x}/(TiO_2)_x$, Tc is almost independent of TiO_2 content (x) and it is ~345 K for all the samples. The enhancement in LFMR is observed in low temperature range (below 130 K) up to x = 0.15 and x = 0.10 for the composites $(LSMO)_{1-x}/(NiO)_x$ and $(LSMO)_{1-x}/(TiO_2)_x$, respectively at low value of magnetic field H~3 kOe. Moreover, the enhancement in MR is observed even at high temperature (near room temperature) in $(LSMO)_{1-x}/(NiO)_x$ composite for all values of x taken in the present work.

The fifth chapter describes the low field magnetotransport behaviour along with magnetic properties of the composites $La_{0.67}Ca_{0.33}MnO_3$ (LCMO) with inorganic oxide Co_3O_4 and organic polymer, polyphenylene sulfide (PPS). The $(LCMO)_{1-x}/(Co_3O_4)_x$ with x = 0.0, 0.05, 0.10, 0.15 and 0.20 and $(LCMO)_{1-x}/(PPS)_x$ with x = 0.0, 0.10, 0.20 and 0.30

of both the composite systems have been performed. XRD and SEM results reveal that second phase material (Co_3O_4 and PPS) does not enter into the LCMO lattice and is found to remain at grain boundary regions and on the surfaces of LCMO grains. A clear insulator to metal transition is observed at 260 K in virgin LCMO sample while that vanishes in the $(LCMO)_{1-x}/(Co_3O_4)_x$ combined samples in the measured temperature range (80-300 K). In case of $(LCMO)_{1-x}/(PPS)_x$, T_{IM} decreases from 265 to 105 K when x increases from x = 0.0 to x = 0.30. Resistivity of the composite samples increases sharply as a consequence of Co_3O_4 and PPS addition, especially on the low temperatures. Moreover, the value of Tc decreases from ~289 K to ~270 K with increasing Co_3O_4 content (x) from 0.0 to 0.20 in case

of $(LCMO)_{1-x}/(Co_3O_4)_x$ composite. However, the value of Tc for $(LCMO)_{1-x}/(PPS)_x$ composites is almost independent of PPS content (x) and it is ~279 K for all the samples. An enhancement in LFMR is observed for the composites $(LCMO)_{1-x}/(Co_3O_4)_x$ up to x = 0.10 and $(LCMO)_{1-x}/(PPS)_x$ up to x = 0.20 at the temperatures below 125 K and 175 K, respectively at low value of magnetic field H ~3 kOe.

The **sixth chapter** describes the studies on magnetic and magnetotransport characteristics of Sr_2FeMoO_6 (with different phase purity) and Ni doped $Sr_2(Fe_{1-x}Ni_x)MoO_6$ ($0 \leq x \leq 0.15$) double perovskite. The **first section** of the chapter is devoted to study the magnetic and magnetotransport properties of Sr_2FeMoO_6 with different phase purities. We synthesized the single phase Sr_2FeMoO_6 (sample B) and Sr_2FeMoO_6 with ~10 % $SrMoO_4$ impurity phase (sample C) by sintering the material in different environments. The synthesis conditions were optimized in such a way so that 10 % $SrMoO_4$ impurity phase, present in sample C, could segregates at the boundaries of Sr_2FeMoO_6 grains and generates the thin tunneling barriers for the conduction of charge carriers. Both of the samples show semiconducting behaviour in the entire measured temperature range (80-300 K). The resistance of sample C is more as compared to sample B while the value of magnetization is less. An enhancement in LFMR is observed for the sample C (having 10 % insulating $SrMoO_4$ phase) as compared to single phase sample B at low value of magnetic field H ~3 kOe.

The effect of Ni doping in Sr_2FeMoO_6 on magnetic and magneto-electrical transport properties is reported in the **second section** of **chapter six**. The polycrystalline $Sr_2(Fe_{1-x}Ni_x)MoO_6$ ($0 \leq x \leq 0.15$) samples were prepared by solid-state reaction process. The X-ray diffraction results show gradual decrease in degree of cationic order with increasing Ni content and increase in the anti-site defects. The Curie temperature (Tc) of the $Sr_2(Fe_{1-}$

$_xNi_x)MoO_6$ is enhanced systematically from 408 to 424 K as x increases from 0 to 0.15. However, magnetization is observed to decrease with increasing Ni content. The resistivity of all the samples exhibits semiconducting behavior in measured temperature range (80-300 K). Furthermore, the low field magnetoresistance is observed to decrease with increasing the Ni concentration.

The **seventh chapter** contains the brief summary and conclusions on the work presented in the thesis through chapters three to six. The overall comments and recommendations have also been added in this chapter.

LIST OF PUBLICATIONS

A. Papers In Referred Journals

1. Magnetoresistance behaviour of $La_{0.7}Sr_{0.3}MnO_3$/NiO composites.
Anurag Gaur and G. D. Varma
Solid State Communication, **139**, 310 (2006)

2. Enhanced low field magnetoresistance in $La_{0.7}Sr_{0.3}MnO_3$ /TiO_2 composite.
Anurag Gaur, G. D. Varma and H.K. Singh
Journal of Physics D: Applied Physics, **39**, 3531 (2006)

3. Sintering temperature effect on electrical transport and magnetoresistance in nanophasic $La_{07}Sr_{03}MnO_3$ manganite.
Anurag Gaur and G. D. Varma
Journal of Physics: Condensed Matter, **18**, 8837 (2006)

4.* Effect of large compressive strain on low field electrical transport in $La_{0.88}Sr_{0.12}MnO_3$ thin films.
R. Prasad, **Anurag Gaur**, P.K. Siwach, G. D. Varma, A. Kaur and H.K. Singh
Journal of Physics D: Applied Physics, **40**, 2954 (2007)

5. Low field magnetoresistance in $La_{0.67}Ca_{0.33}MnO_3$ and Co_3O_4 combined system.
Anurag Gaur and G. D. Varma
Journal of Alloys & Compounds,doi:10.1016/j.jallcom.2006.11.132, (2006) (In press)

6. Enhancement in Curie temperature and reduction in magnetoresistance of $Sr_2(Fe_{1-x}Ni_x)MoO_6$ ($0 \leq x \leq 0.15$).
Anurag Gaur, G.D. Varma and H.K.Singh
Journal of Alloys & compounds,doi:10.1016 /j.jallcom.2007.06.024, (2007) (In press)

7. Improved magneto-transport in LCMO-Polymer (PPS) composite.
Anurag Gaur and G. D. Varma
Solid State Communication, doi: 10.1016/j.ssc.2007.08.004, (2007) (In press)

8. Enhanced magnetoresistance in double perovskite Sr_2FeMoO_6 through $SrMoO_4$ tunneling barriers.
Anurag Gaur and G. D. Varma
Material Science & Engineering B,doi:10.1016/j.mseb.2007.07.062, (2007) (In press)

9. Sintering temperature effect on magnetotransport properties of nanocrystalline $La_{2/3}Ca_{1/3}MnO_3$ manganite.
Anurag Gaur and G. D. Varma
Journal of Material Science, (2007) (Submitted)

---

* Work not included in the present thesis

B. Papers In Conferences

1. Electrical transport behaviour of $La_{0.7}Sr_{0.3}MnO_3/TiO_2$ composites
   Anurag Gaur and G.D. Varma
   In the proceedings of "National Conference on Condensed Matter and Material Physics (CMMP), M.S. University Baroda, India (2006)

2. Electrical and magnetic properties of $La_{0.7}Sr_{0.3}MnO_3/TiO_2$ composites
   Anurag Gaur and G.D. Varma
   In the proceedings of "17th Annual Meeting of Material Research Society of India (MRSI)", Lucknow University Lucknow, India (2006)

3. Large magnetoresistance in nanoparticles of $La_{0.7}Ca_{0.3}MnO_3$ synthesized at low temperatures
   Anurag Gaur and G.D. Varma
   In the proceedings of "International Conference on Material Chemistry (ISMC-06)", B.A.R.C, Mumbai, India (2006)

4. Enhanced magnetoresistance in LCMO/Co_3O_4 composites
   Anurag Gaur and G.D. Varma
   In the proceedings of "51th Solid State (DAE) Physics Symposium (SSPS), B. University, Bhopal, India, (2006)

5. Effect of gaseous environments during synthesis on magnetotransport characteristics of Sr_2FeMoO_6
   Anurag Gaur, G.D. Varma and H.K. Singh
   In the proceedings of "18th Annual Meeting of Material Research Society of India (MRSI)", N.P.L., New Delhi, India (2007)

6. Enhanced intergrain tunneling magnetoresistance in double perovskite Sr_2FeMoO_6
   Anurag Gaur and G.D. Varma
   In the proceedings of "International Conference on Materials for Advanced Technology (ICMAT-07)" **MRSS and NUS, Singapore** (2007)

ACKNOWLEDGEMENTS

My research work involved the contributions and cooperation from many people to whom I would always remain thankful.

First of all, I would like to express my sincere sense of gratitude to my respected supervisor, Dr. G. D. Varma for his guidance, inspiration and encouragement throughout this work. I was fortunate enough to have an opportunity to work under his supervision and gain from his knowledge and experience.

I also have the deep sense of gratitude to Prof. Jagdish Rai and Prof. I. S. Tyagi, Present and Former Head, Department of Physics, for providing me all the necessary facilities required for the accomplishment of this work. I am also grateful to my SRC members, Prof. B.D. Indu (Chairman DRC), Prof. Anil Kumar (External member, Chemistry) and Dr. Tashi Nautiyal (Internal member) for constructive criticisms and valuable suggestions at every stage of the work.

I am also grateful to all the faculty members of Physics Department, Prof S. Auluck, Prof. R. Nath, Prof. A.K. Jain, Prof. G.S. Singh, Prof. Vir Singh, Prof. Rajesh Srivastava, Prof. A.N. Tripathi, Late Dr. S.K. Barthwal, Dr. V.K. Tondan, Dr. K.L. Yadav, Dr. Aalok Mishra, Dr. Vipul Rastogi and Dr. B.K. Patra due to their continuous inspiration, timely encouragement and valuable suggestions.

I am deeply indebted to Prof. D. Pandey (B.H.U.), Dr. H. K. Singh (N.P.L., New Delhi), Dr. N.P. Lalla and Dr. P.K. Siwach (UGC-DAE consortium, Indore) for their valuable suggestions and discussions. Also they were a constant source of encouragement and moral support.

I express my special thanks to my lab mates Mr. Vijay Kumar Sharma, Nigamananda Ojha and Nagesh Kumar for their enormous help and cooperation and I always enjoyed working with these fellows. The help provided by Mr. Vijay Kumar Sharma during write up of the thesis is especially acknowledged. I also thanks to Mr. Neeraj Panwar and Mr. Ravikant Prasad (N.P.L. New Delhi) for their cooperation and help during stay at N.P.L.

I am highly obliged and wish to express my sincere thanks to the technical and official staff of the Department of Physics, I.I.T. Roorkee.

I would like to thanks the technical staff of the Institute Instrumentation Center (IIC), I.I.T. Roorkee, Mrs. Rekha Sharma, Mr. S.D. Sharma, Mr. Jagdish Saini, Mr. Shiv Kumar Saini, Mr. Virendra Singh, Mr. Anil Kr. Saini and Mr. Mahmood for their help at the various stages of the characterization of the samples.

I express my special thanks to my lovely friends, Ramesh Chand, Manoj Kumar, Sapan Mohan Saini, Nirpendra Singh, Suresh Kumar, Anu Bala, Ajeet Pandey, Bhupander, Ajay Prakesh, Sukhjeet, Lalita, Payal, Sudha, M. Ahmad, Chandrashakher, Poonam, Charu, Pramod, Kanishka, Ajay, Arvind, Vinod, Deepak Tyagi, Nitin Singh, Krishna, Parminder Saini, Vikas Pundeer, Vijay Tiwari, Neerpal and Kuldeep Rana, who always motivate and encourage me at every moment and keep me always cheerful and happy. I enjoyed a lot with their company especially during tea times, short trips at Haridwar and made my stay really memorable in I.I.T. Roorkee. Thanks also go to my seniors, Dr. Dinesh Kumar Sharma, Dr. Amrish Panwar and Dr. Raj Kumar Chauhan for their help and motivation.

Finally I express my heartfelt gratitude to my highly respectable and adorable father, Mr. Ram Kumar Sharma and mother, Mrs. Prebha Sharma for their unconditional love, encouragement and blessings. Words can never express my feelings for them. I also express gratitude to my Didi, Ms Seema Sharma, Jiju, Naresh Kumar Sharma and thanks to my younger sister, Lata Gaur, and brother, Umesh Gaur for their love, moral support and encouragement and a lot of love to my lovely nephew, Tushar.

I also want to express my sincere thanks to all those who directly or indirectly helped me at various stage of the work but I could not mention their name due to shortage of the space.

The financial support provided by University Grant Commission (U.G.C.), New Delhi, is gratefully acknowledged.

23/08/07

(Anurag Gaur)

I.I.T. Roorkee

August, 2007

LIST OF TABLES

LIST OF FIGURES

GLOSSARY OF SYMBOLS

AF	antiferromagnetic
AFM	antiferromagnetic metal
APB	anti-phase boundary
AS	anti-site
CI	charge ordered insulator
CMR	colossal magnetoresistance
CO	charge ordering
DE	double exchange
DFT	density function theory
EDAX	energy dispersive X-ray analysis
FM	ferromagnetic
GB's	grain boundaries
GMR	giant magnetoresistance
H	magnetic field
HFMR	high field magnetoresistance
HTMR	high temperature magnetoresistance
ITMR	intergrain tunneling magnetoresistance
LCMO	$La_{0.67}Ca_{0.33}MnO_3$
LFMR	low field magnetoresistance
LSMO	$La_{0.7}Sr_{0.3}MnO_3$
M_S	saturation magnetization
MR	magnetoresistance

PI	paramagnetic insulator
PM	paramagnetic
PPS	polyphenylene sulfide
RE	rare earth
ρ	resistivity
SDT	spin dependent tunneling
SEM	scanning electron microscopy
SFMO	Sr_2FeMoO_6
T_C	Curie temperature
T_{CO}	charge ordering temperature
T_{IM}	insulator to metal transition temperature
T_N	Neel temperature
TEM	transmission electron microscopy
TMR	tunneling magnetoresistance
VRH	variable range hopping
VSM	vibrating sample magnetometer
XRD	X-ray diffraction

CONTENTS

Chapter - 1

INTRODUCTION

1.1 REVIEW OF MAGNETORESISTANCE (MR) BASED TECHNOLOGY

Materials have been playing a pivotal role in the advancement of technology since the stone, bronze and iron ages. The present information age relies on the development of "smart" and "smaller" magnetic materials for memories, data storage and other devices. The magnetic materials can be divided into numerous categories, depending on their properties and applications. The prime examples are the transition metal oxides having perovskite structure which form an important class of materials from the point of view of technological applications as well as fundamental physics [1]. The perovskite metal oxides constitute an interesting class of materials with a wide range of properties. They exhibit a variety of phenomena such as ferroelectricity in titanates [2], high temperature superconductivity in cuprates [3] and colossal magnetoresistance in manganites (doped $LaMnO_3$) [4] and double perovskite (Sr_2FeMoO_6) [5].

The perovskite manganites and double perovskites have various applications such as magnetic disks and tapes for data storage, magnetic field sensors, read heads etc. The most exciting application of these materials is magnetic recording and data storage. The idea of storing information magnetically is based on the fact that a reading sensor (called a read head) can be used to read the magnetization of local magnetic moments (called magnetic bits) whose direction codes for 0 or 1 on the magnetic disk. In order to enhance the capacity of storage devices, several steps can be taken such as (1) reduction of the read head to

magnetic disk distance, (2) enhancement of the sensitivity of the magnetic sensor, and (3) reduction of magnetic bit size. Materials with large changes in resistance in response to low magnetic fields (typically in the range of 0-200 Gauss) are an important aspect in enhancing storage density. In 1990, IBM introduced a magnetoresistive (MR) based read head, which is based on the variation of electrical resistance of read element by the magnetic field of the storage medium instead of just reading the alternating magnetic field on a disk (see Fig. 1.1).

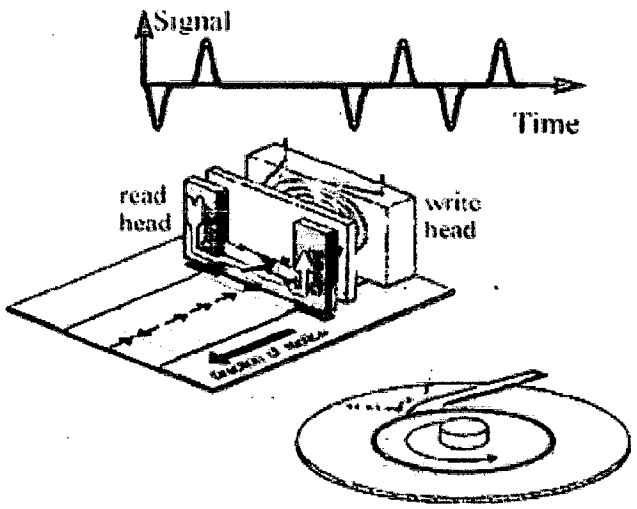

Figure 1.1: IBM introduced read/write head design. The signal of magnetoresistance used to read the states of magnetic bits are shown in the upper curve [6].

Figure 1.1 illustrates a design to read and write the state of magnetic bits in advanced magnetic disk drives [6]. The read head consist of a MR sensor between two magnetic shields. The inductive heads write bits of information by magnetizing very small regions along concentric tracks. In the process of reading, the existence of a magnetic transition or flux reversal between bits causes to change the magnetic orientation in the MR sensor and that will induce to change the resistance of the sensor. Large magnetoresistance materials are being developed to improve the sensitivity of read heads. The sensor's output voltage (or signal) is the product of the resistance change (ΔR) and read bias current. The output signal is

amplified by low-noise electronics and sent to the data detection electronics. Now a days, this technology dominates the market. In 1997, IBM developed an innovated technology by introducing giant magnetoresistive (GMR) heads. The giant magnetoresistive (GMR) heads, built as a sandwich of magnetic and nonmagnetic material layers, improve the read heads sensitivity. Curie Munce, director of storage systems and technology announced the possibility that hard disk drives can store data at an areal density more than 100 gigabits per square inch of platter space. The key factor for the growth of magnetism based technology is the increase in the areal density. The areal density of the state of the art production was 700 Mbit per inch^2 in 1995. In the quest to lower the cost and improve the performance, the areal density has increased more than 20 million-fold in modern disk drives and currently doubles every year (Fig.1.2).

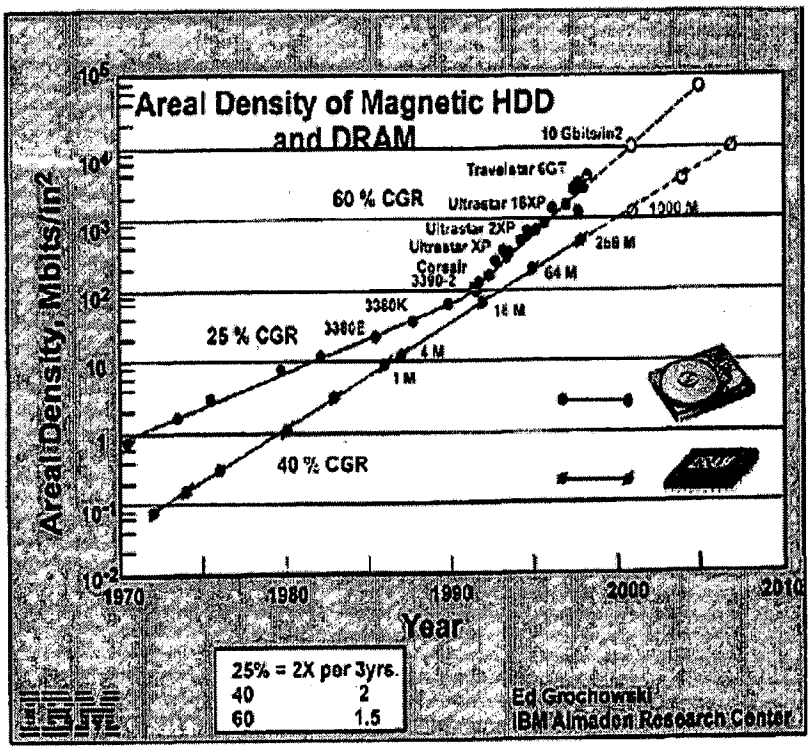

Figure 1.2: The areal density advancements in IBM's hard disks [7].

The pursuit of higher areal densities still continues, as is evident in recent laboratory experiments of recording densities beyond 100 Gbit per inch^2 [8]. In September 2006, Hitachi Global Storage Technologies demonstrated an areal density of 345 Gbit per inch^2 on perpendicular recording technology and the next big challenge now looming ahead is to achieve 1 Tbit per inch^2 recording density up to 2009 [9].

The main limitation on the size of the smallest bit depends on the design of read-write head and the intrinsic signal-to-noise ratio of the material. The next generation devices will be based on giant and colossal magnetoresistive materials. Very sensitive magnetoresistive materials called giant magnetoresistive (GMR) materials and extremely sensitive materials are called colossal magnetoresistive (CMR) materials. The discovery of CMR materials is the result of intense research to find the new materials in the past few years. These materials exhibit a resistance change when subjected to a magnetic field and may eventually be used into magnetoresistive (MR) heads to achieve the required areal densities. Commercialization of the GMR and CMR effects will require materials which have both high magnetization and large change in magnetoresistance on the application of small magnetic fields of the order of few tens of Gauss or smaller. Thus, the research on magnetic materials is going on to understand their magnetic and magnetotransport properties so that they can significantly contribute to the technology advancement [10].

1.2 THE PHENOMENON OF MAGNETORESISTANCE

Magnetoresistance (MR) is the relative change in the electrical resistance or resistivity of a material on the application of a magnetic field. MR is generally defined by the equation,

$$MR(\%) = \left[\frac{\Delta R}{R(0)}\right] \times 100$$

$$= \left[\frac{R(H) - R(0)}{R(0)}\right] \times 100 \qquad (1.1)$$

where R(0) and R(H) are the resistances or resistivities at a given temperature in the zero and applied magnetic fields, respectively. MR can be positive or negative depending on the increase or decrease in the resistivity, respectively. Most of the metals show MR but only a few percent. Nonmagnetic pure metals and alloy generally have a positive MR that depends on the square of magnetic field (H). However, magnetic materials show negative MR owing to the suppression of spin disorder by the magnetic field. Nonmagnetic metals such as Au, exhibit small MR but the ferromagnetic metals such as Fe and Co show the MR up to 15 %. The semi-metal Bi also shows the 18 % MR in a transverse field of 0.6 T, which rises to a 40 fold change at 24 T [11]. Cu is more typical for MR and very strong magnetic field (24 T) changes only ~2 % MR at room temperature.

TYPES OF MAGNETORESISTANCE

1.2.1 Anisotropic magnetoresistance (AMR)

In ferromagnetic metals and alloys, MR effects are obtained in low fields. AMR measures the changes in resistance observed when the direction of current flowing through a sample changes its direction from parallel to the internal magnetization to being perpendicular to it. The physical origin of AMR lies in spin orbit coupling. The typical size of AMR is ~1 % at 5-10 Oe for bulk permalloy ($Ni_{81}Fe_{19}$), whereas the same value (~1 %) will be obtained at higher field of 1 T for permalloy wires due to large aspect ratio [12]. AMR is present in all ferromagnets and is defined as the resistivity change as a function of angle between the

current (J) and magnetization (M). If ρ_{II} and $\rho_{\perp}$ denote the resistivity in the longitudinal ($JIIM$) and transverse ($J \perp M$) geometries, respectively, then AMR is defined as,

$$AMR = \frac{\rho_{II} - \rho_{\perp}}{(1/3)\rho_{II} + (2/3)\rho_{\perp}} \tag{1.2}$$

An extensive discussion regarding AMR in elemental ferromagnets was reviewed by Campbell and Fert [13]. The AMR is a low field effect and was found to be much smaller than the CMR [14-16].

1.2.2 Tunneling magnetoresistance (TMR)

TMR is observed in magnetic tunnel junctions and is drawing considerable attention due to the advent of sophisticated thin film junction preparation techniques [17]. Magnetic tunnel junction consists of two ferromagnetic metallic layers separated by a thin insulating barrier layer. The insulating layer is so thin (of the order of few nanometer) that electron can tunnel through the barrier if a bias voltage is applied between the two metal electrodes through the insulator. The most important property of a magnetic tunnel junction is that the tunneling current depends on the relative orientation of the magnetization of the two FM layers, which can be changed by an applied magnetic field. This phenomenon is called tunneling magnetoresistance (TMR). TMR is the consequence of spin dependent tunneling (SDT) due to an imbalance in the electric current carried by up and down spin electrons through a tunneling barrier. Spin dependent tunneling was discovered in pioneering experiments by Tedrow and Meservey [18]. The relationship between SDT and TMR was explained by Julliere [19] within a simple model that quantifies the magnitude of TMR in terms of the spin polarization of the ferromagnetic electrodes as measured in the experiments on superconductors [18]. As per Julliere's model the TMR is given as,

$$TMR = \frac{2\rho_1\rho_2}{1-\rho_1\rho_2} \tag{1.3}$$

Where $\rho_i = \frac{\rho_i^{\uparrow} - \rho_i^{\downarrow}}{\rho_i^{\uparrow} + \rho_i^{\downarrow}}$ (i = 1, 2) is the effective spin polarization of two electrodes. For the case of two identical ferromagnets, the TMR is always negative, it diverges for two half metallic electrodes. It can be both positive and negative. A few years ago, Miyazaki and Tezuka (1995) [20] demonstrated the possibility of large values of TMR in magnetic tunnel junctions with Al_2O_3 insulating layers. Moodera et al. [21] reported TMR values for a $Co/Al_2O_3/Ni_{80}Fe_{20}$ junction of 20.2 %, 27.1 % and 27.3 % at 295, 77 and 4.2 K, respectively. Various workers have reported TMR values in excess of 100 % at 4.2 K for ferromagnetic oxide tunneling junctions based on manganites electrodes [22-33]. Recently, extremely large TMR values up to 1800 % were obtained by Bowen et al. [34] in LSMO/STO/LSMO/Co/Au structure. The exteremly large TMR response (1800 %) at 4 K leads to a spin polarization of the LSMO at the interface with STO of at least 95 %. Moreover, the temperature dependence of the TMR in this optimally etched junction vanishes only at T = 280 K. Strains as well as mixed valence of Mn ions at the interface are the deciding factors to have large TMR response, as deduced from EELS measurements coupled with HREM observations by Pailloux et al. [35]. Moreover, the isotropic magnetoresistance has been observed in magnetic ion diluted semiconducting thin films [36]. The magnetoresistance associated with tunneling processes across grain boundaries will be named hereafter intergrain tunneling magnetoresistance (ITMR). ITMR is strongly dependent on the microstructure and it is an extrinsic phenomenon. ITMR follows that an ensemble of grains separated by insulating grain boundaries can be viewed as a network of electrodes embedded in an insulating matrix. According to the simplest TMR theory [37], this constitutes a higher resistance state

compared to the low resistance state achieved above the saturation field, when all the magnetizations of neighbouring grains are parallel. Hence, under the application of an external magnetic field, the sample undergoes a resistivity decrease as the magnetization approaches saturation. In order to give a theoretical approach to the functional dependence of the ITMR on the magnetic field, people use Inoue and Maekawa's [38] model for the ITMR of a set of monodisperse magnetic particles in an insulating matrix. This model is an extension of Slonczewski's model for the conductivity of a tunnel junction, where the electrodes are forming an arbitrary angle [39].

1.2.3 Giant magnetoresistance (GMR)

In 1986, the possibility of exchange interaction between ferromagnetic films across a nonmagnetic metallic interlayer was experimentally shown in Fe/Cr structures [40] and rare earth based yttrium multilayers [41]. In MR heads, the output is directly proportional to the MR ratio. Scientists and engineers have been searching for the materials that can show larger changes in resistivity than the classical material permalloy (see Fig. 1.3). Figure 1.3 shows that $\Delta R/R$ of the double layer GMR (4 %) is better than that of the anisotropic magnetoresistance (AMR) [42]. In 1988, GMR was first reported by Baibich et al. [43] in an antiferromagnetically coupled multilayer of Fe/Cr prepared by molecular beam epitaxy. In $Fe_{3nm}/Cr_{0.9nm}$ multilayers, a GMR ratio was found to be 85 % at 4.2 K [44]. The GMR multilayers normally need a large saturation field to overcome the antiferromagnetic coupling of magnetic layers to show the large magnetoresistance ratio. GMR occurs in materials that have alternating layers of ferromagnetic and nonmagnetic materials. The parallel spin acts as a shunting current, lowering the resistivity of the complete stack of layers considerably compared to antiparallel moments. The effect was subsequently found to occur in a number of multilayers magnetic film systems.

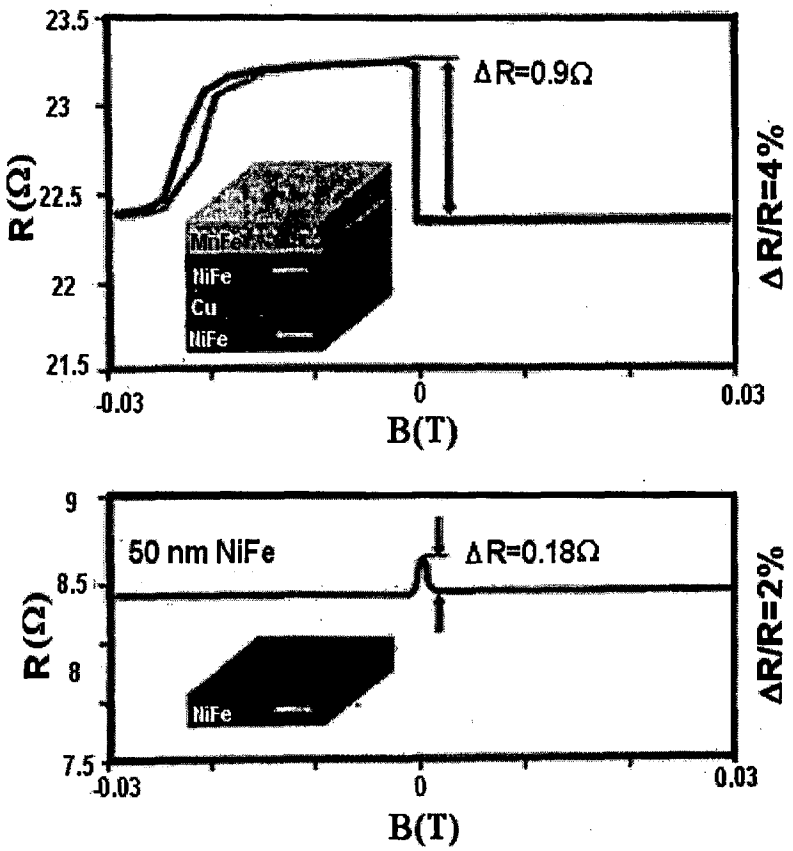

Figure 1.3: Comparison of magnetic field sensor outputs of GMR (top) and AMR (bottom) effects [42].

In Co/Ru, Co/Cr and Fe/Cr multilayers, Parkin et al. [45] reported the fact that the strength of the antiferromagnetic coupling is a periodic function of the nonmagnetic spacer. The origin of oscillatory antiferromagnetic coupling has been derived by the RKKY theory [46] and quantum well models [47].

In fact, the field sensitivity of GMR multilayers is inferior to the AMR ratio of NiFe because of the huge saturation field in the multilayers. For example, CoFe/Cu multilayers are not easy to implement in practical devices such as recording heads. Therefore an alternative GMR structure with NiFe/Cu/NiFe/FeMn is considered (Fig. 1.4).

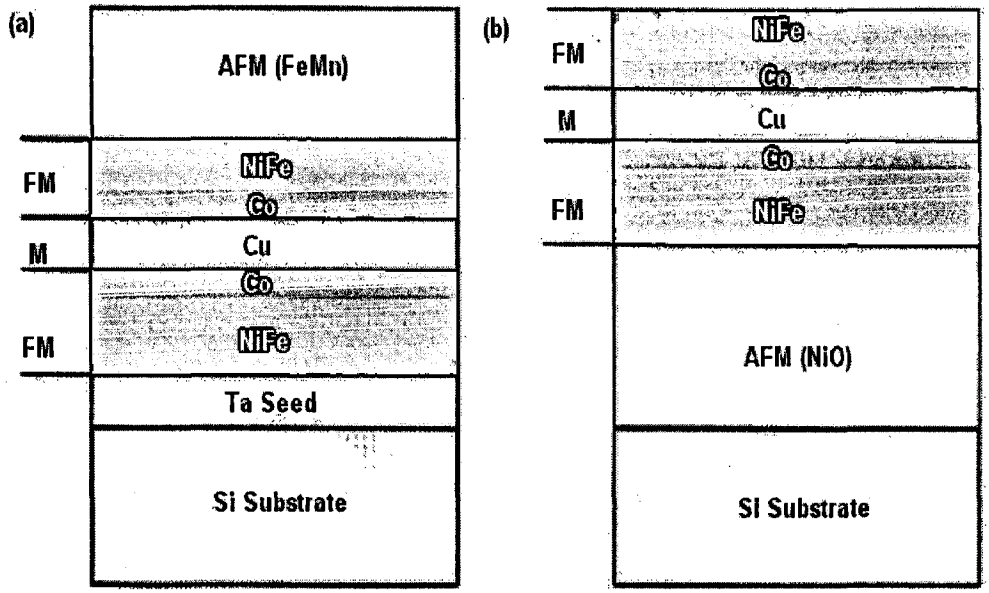

Figure 1.4: Typical examples of schematic cross sections of a **(a)** top spin valve and a **(b)** bottom spin valve. Note that FM, M and AFM refer to ferromagnet, noble metal and antiferromagnet, respectively [48].

In the Fig. 1.4 (a), the FeMn layer pins the magnetization of the top NiFe layer through exchange anisotropy [49]. The FM (or antiferromagnetic) interaction between the FM, NiFe layers is much weaker than the one in the GMR multilayer such that the bottom NiFe magnetization can switch under a small field ~6 Oe only. These GMR sandwiches are called "spin valves". The Si / Ta / NiFe(5 nm) / Co(2 nm) / Cu(2 nm) / Co(2 nm) / NiFe(3 nm) / FeMn(15 nm) spin valve shows a GMR ratio of ~9 %, where Co is for the purpose of enhancement of interfacial spin dependent scattering and Ta seed layer is for promoting desirable film texture and morphology. The Si / NiO(75 nm) / NiFe(3 nm) / Co(2 nm) / Cu(2 nm) / Co(2 nm) / NiFe(5 nm) spin valves shows a GMR ratio of ~12 % [48]. Thereafter, a bottom spin valve structure of Si / NiO(50 nm) / Co(2.5 nm) / Cu(1.9 nm) / Co(3 nm) and a symmetric spin valve structure of Si / NiO(50 nm) / Co(2.5 nm) / Cu(1.9 nm) / Co(4 nm) / Cu(1.9 nm) / Co(2.5 nm) / NiO(50 nm) achieve GMR ratios of 19 % and 25 %, respectively. Spin dependent scattering [50] (see Fig. 1.5) and intergrain tunneling [51] are known

mechanisms of GMR. Spin up electrons and spin down electrons travel randomly inside the layers (see Fig. 1.5).

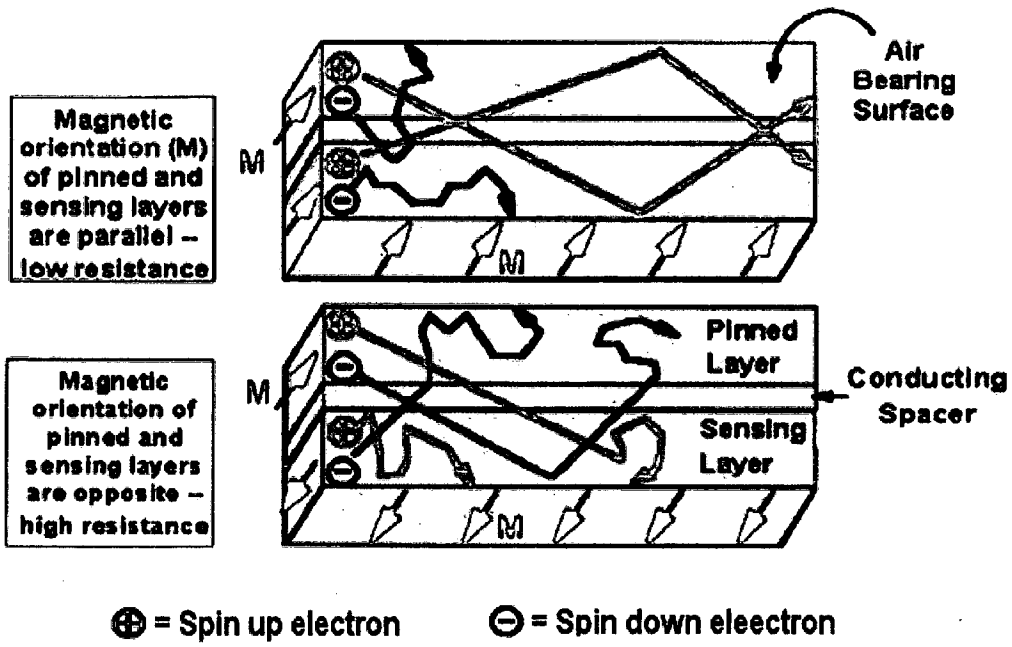

Figure 1.5: Spin-valve structure of a GMR read-head device. The schematic of spin-dependent scattering of the conduction carriers within the magnetic layers or at the boundaries of the magnetic layers is also shown [52].

In parallel magnetization arrangement (upper panel of Fig. 1.5), spin down electrons are scattered but spin up electrons travel freely inside the layers. On the other hand, in antiparallel magnetization arrangement (down panel of Fig. 1.5), electrons of both spin alignment are scattered. Therefore there is a significant difference in resistance measured between spin parallel and spin antiparallel arrangements. In case of strong and effective scattering process, the resistance becomes larger due to reduction in the mean free path of an electron between scattering process. A simplistic calculation by using a resistor network shows a significant difference in resistance (see Fig. 1.6).

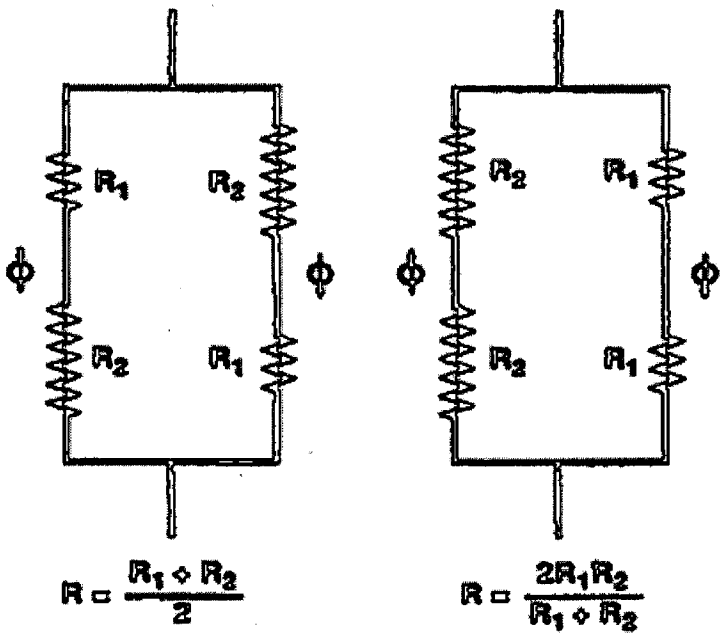

Figure 1.6: A simplified equivalent resistor array displaying the GMR effect showing the high (left panel) and low (right panel) resistance states [53].

1.2.4 Colossal magnetoresistance (CMR)

A large number of studies on manganites have been performed for the past decade since the giant magnetoresistance (GMR) effect and its technological applications were recognized [54, 55]. The perovskite based manganese oxide of the form $RE_{1-x}AE_xMnO_3$, where RE is a trivalent rare earth element, e.g. La, Pr, Nd etc., and AE is divalent alkaline earth element, e.g. Ca, Ba, Sr etc., has drawn the attention of scientific community due to extremely large (colossal) change in magnetoresistance. Chahara et al. (1993) [56], von Helmholtz et al. (1993) [55] and Jin et al. (1994) [54] observed a high magnetoresistance in these doped rare earth manganites (bulk as well as thin films) in a magnetic field of several tesla (~6 T) (Fig. 1.7). Comparatively, the MR value is +3 % for permalloy (80 % Ni-20 % Fe) but -5 % to -50 % for GMR [57, 58]. Jin et al. [54] found that in La-Ca-Mn-O thin films

(1000 ~ 2000 Å) grown on (100) $LaAlO_3$ substrates by pulse laser deposition, the MR was as large as 99.9 % at T = 77 K and H = 6 T.

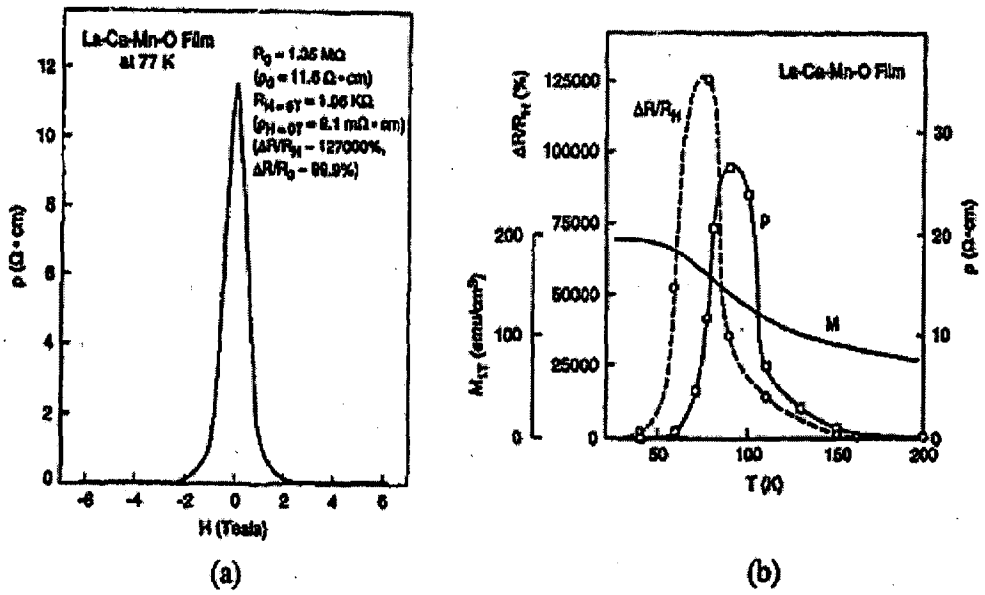

Figure 1.7: Colossal magnetoresistance (CMR) in epitaxial $La_{1-x}Ca_xMnO_3$ thin films for x = 0.33. **(a)** Resistivity vs. fields (H). **(b)** $\Delta R/R_H$ (%), ρ and M vs. temperature. Note that $[\rho(0)-\rho(H)]/\rho(H)$ = 127,000 % and $[\rho(H)-\rho(0)]/\rho(0)$ = 99.9 % [54].

For device applications, magnetic materials must be developed that can exhibit high sensitivity at room temperature and are sensitive to the fields of the order of ~100 Oe. The physical origin of the magnetoresistance in manganites is completely different from the giant magnetoresistance effect (GMR). Since the doped perovskite manganites are the theme of the present thesis work so the basics of these colossal magnetoresistance materials are described and discussed in detail in the next sections.

1.3 COLOSSAL MAGNETORESISTANCE IN MANGANITES

1.3.1 History of manganites

Since the late 1940's, various studies of the polycrystalline ceramic samples of mixed valance manganese perovskites were carried out by Jonker et al. [59, 60]. Jonker and van Santen initiated the sample preparation, study of the crystal structure of polycrystalline samples of $La_{1-x}Ca_xMnO_3$ series and reported ferromagnetism and anomalies in the conductivity at the Curie temperature with variation in lattice parameter as a function of hole doping. Other systems such as $La_{1-x}Ba_xMnO_3$ (only for $x<0.5$) and $La_{1-x}Sr_xMnO_3$ (only for $x<0.7$) were also reported. In 1954, Volger observed a notable decrease of resistivity for $La_{0.8}Ca_{0.2}MnO_3$ in FM state, in applied magnetic fields [61]. After that significant research effort have started on the studies of low temperature measurements of various physical properties of manganites such as specific heat, magnetization, dc and ac resistivity, magnetoresistance, magnetostriction, I-V curves, dielectric constant, Seebeck effect and Hall effect [61, 62]. After these pioneering experiments, Wollan and Koehler [63] carried out extensive neutron diffraction study to characterize and draw the first magnetic structures of $La_{1-x}Ca_xMnO_3$ in the entire composition range. Wollan and Koehler were among the first to use the technique of neutron scattering to study magnetism in materials. They found that in addition to FM phase many other interesting anti-ferromagnetic phases were also present in manganites. Among them the most exotic spin arrangement is the CE-type state, which is a mixture of the C-phase and the E-phase. This CE-state was the first evidence of charge-ordering and mixed phase (phase separation) tendencies in the manganites.

On the other hand, in 1969 and 1970, flux grown single crystals of $La_{1-x}Pb_xMnO_3$ ($0.2<x<0.44$) were studied by Searle and Wang [64]. They reported metallic conductivity below the Curie temperature (Tc) and a large negative magnetoresistance (~20 %) at 1 T near

Tc, which is similar to polycrystalline $La_{1-x}Sr_xMnO_3$. Jirak et al. [65] and Pollert et al. [66] studied the structure and magnetic properties of another very popular manganites $(Pr,Ca)MnO_3$ by X-ray and neutron diffraction technique. They observed charge-ordering phases which are totally different from the ferromagnetic phases of other manganites. A burst of research activity on manganites started during 1990 because of the observation of large magnetoresistance. Kusters et al. (1989) [67] observed the large MR effect on bulk $Nd_{0.5}Pb_{0.5}MnO_3$. Another work by von Helmholtz et al. [55] on thin films of $La_{2/3}Ba_{1/3}MnO_3$ also revealed a large MR effect at room temperature. Thereafter, similar conclusion was reached by Chahara et al. [56] using thin films of $La_{3/4}Ca_{1/4}MnO_3$ and Ju et al. [68] for films of $La_{1-x}Sr_xMnO_3$. They all observed MR values larger than those observed in artificially engineered multilayers (GMR) [69]. A defining moment for the field of manganites was the publication by Jin et al. [54] of results with truly colossal magnetoresistance (CMR). In 1994, Jin et al. reported MR ((R_H-R_0) x100/R_H) close to 1500 % at 200 K and over 100,000 % at 77 K and H=6 T for thin films of $La_{0.67}Ca_{0.33}MnO_3$ grown on (100) $LaAlO_3$ substrate by pulse laser deposition. This enormous (thousand-fold) change in resistivity is really colossal. One year later (1995), Xiong et al. [70] reported MR ratio of over 100,000 % using thin films of $Nd_{0.7}Sr_{0.3}MnO_3$ near 60 K and in the presence of magnetic field of 8 T. These studies clearly indicate that the colossal magnetoresistance (CMR) manganites are the potential alternative for giant magnetoresistance (GMR) systems.

1.3.2 Crystallographic structure

The structure of the $RE_{1-x}M_xMnO_3$ oxides is close to that of the cubic perovskite (Fig. 1.8). The large sized RE trivalent ions and M divalent ions occupy the A-site with 12-fold oxygen coordination. The smaller Mn ions in the mixed-valence state Mn^{3+}–Mn^{4+} are located

at the centre of an oxygen octahedron, the B-site with 6-fold coordination. For the stoichiometric oxide, the proportions of Mn ions in the valence states 3^+ and 4^+ are respectively, $(1 - x)$ and x. The structure of the manganites is governed by the tolerance factor $t = (r_A + r_O)/\sqrt{2}(r_B + r_O)$. The perovskite structure is stable for $0.89 < t < 1.02$, $t = 1$ corresponds to the perfect cubic closely packed structure. Generally, t differs appreciably from 1 and the manganites have, at least at low temperature, a lower rhombohedral symmetry or orthorhombic structure. This is illustrated by the orthorhombic structure of $LaMnO_3$ (Fig. 1.9).

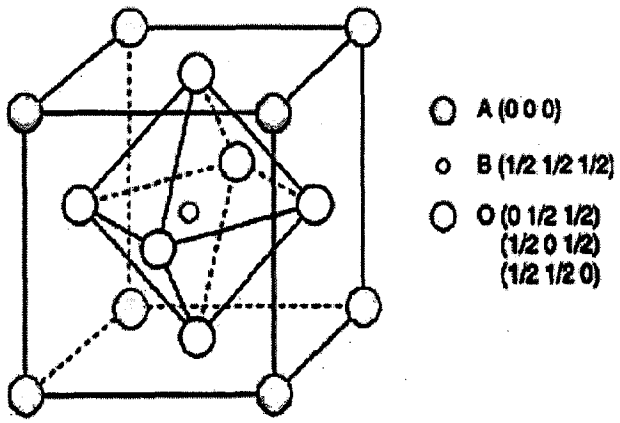

Figure 1.8: Schematic view of the cubic perovskite structure.

$LaMnO_3$ is the parent compound of the most investigated manganites by partial substitution of La by Ca and Sr. This doping with some divalent cation (Ca, Sr, etc.) causes the distortion in the structure due to differences in the size of the various atoms and leads to Jahn-Teller effect, which will be discussed in section 1.3.4 [71].

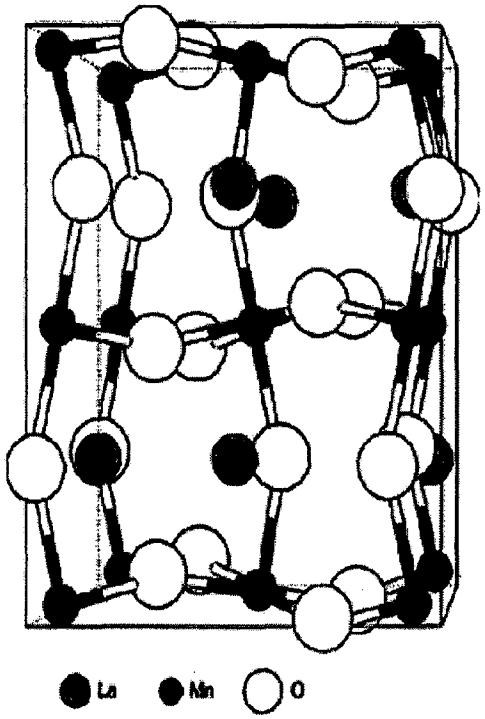

Figure 1.9: Crystallographic structure of $LaMnO_3$.

1.3.3 Phase diagram

Most of the recent work has focused on Ca and Sr substituted compounds and the CMR trends, encountered as a function of divalent ion concentration (x), are observed for both dopant types. However, there are some differences in the phase diagrams for the two cases, owing mainly to the size difference between Ca and Sr ions. For Sr substitution, Tokura and collaborators have established the phase behaviour as a function of x in melt grown crystals of $La_{1-x}Sr_xMnO_3$ [72–75]. Ceramic samples have also been studied by Mahendiran et al. [76]. As shown in Fig. 1.10 (a), there are three distinct ground states: the spin-canted insulator, the FM insulator, and the FM metal. At high temperatures there appear to be two distinct phases, paramagnetic insulator (PI) and paramagnetic metal (PM). The vertical lines demarcating these phases are determined by crossover in $\rho(T)$ between

semiconducting (insulating) and metallic behaviour, as shown in Fig. 1.10 (a). Accompanying the insulator–metal transition at low temperature is an orthorhombic ($x \leq 0.175$) to rhombohedral ($x > 0.175$) transition. An important aspect of Sr substitution is the inability to obtain single-phase material for $x > 0.6$. However, within the range of phase stability, there is a remarkably large variation in transport from good metal for $x > 0.3$ to insulator for $x \leq 0.15$. It should be noted that the crossover from metallic to insulating behaviour at $T = 0$ occurs in a very narrow concentration region. At the low end of the substitution series a remarkable field-induced structural transition is observed. As shown in Fig. 1.11, for $x = 0.17$, the orthorhombic–rhombohedral phase transition temperature can be modified by about 50 K with application of a 7 T field [74]. Substitution on the La site modifies the phase behaviour through size effects as for $(Nd_{1-y}Sm_y)_{0.5}Sr_{0.5}MnO_3$ [77, 78]. This compound exhibits an instability towards either the FM ground state ($y = 0.875$, T_c = 110 K) or a high-ρ, low-M ($y = 0$, $T_{ins} = 160$) state, most likely either charge ordered or antiferromagnetic (or both). Similar behaviour is also found in $Pr_{0.5}Sr_{0.5}MnO_3$ [79] and $Pr_{0.7}(Sr, Ca)_{0.3}MnO_{3-\delta}$ [80, 81].

The phase diagram and low-temperature behaviour of $La_{1-x}Ca_xMnO_3$ was explored in detail [82, 83] and is shown in Fig. 1.10 (b). It is similar to that of Sr doping, especially in the region for $x < 0.5$. For $0.2 < x < 0.5$, the transition is defined by anomalies in ρ(T), which move to higher temperature upon application of an applied magnetic field. Here one sees the origin of the CMR effect: the paramagnetic phase ρ(T) is semiconducting and therefore, the system undergoes an insulator–metal transition as H increases for fixed temperature . For $x > 0.5$, a well defined critical line with maximum around $T \sim 270$ K is seen in the $T_C - x$ plane (Fig. 1.10 (b)). This phase boundary defines the charge ordering (CO) transition which is directly seen by TEM.

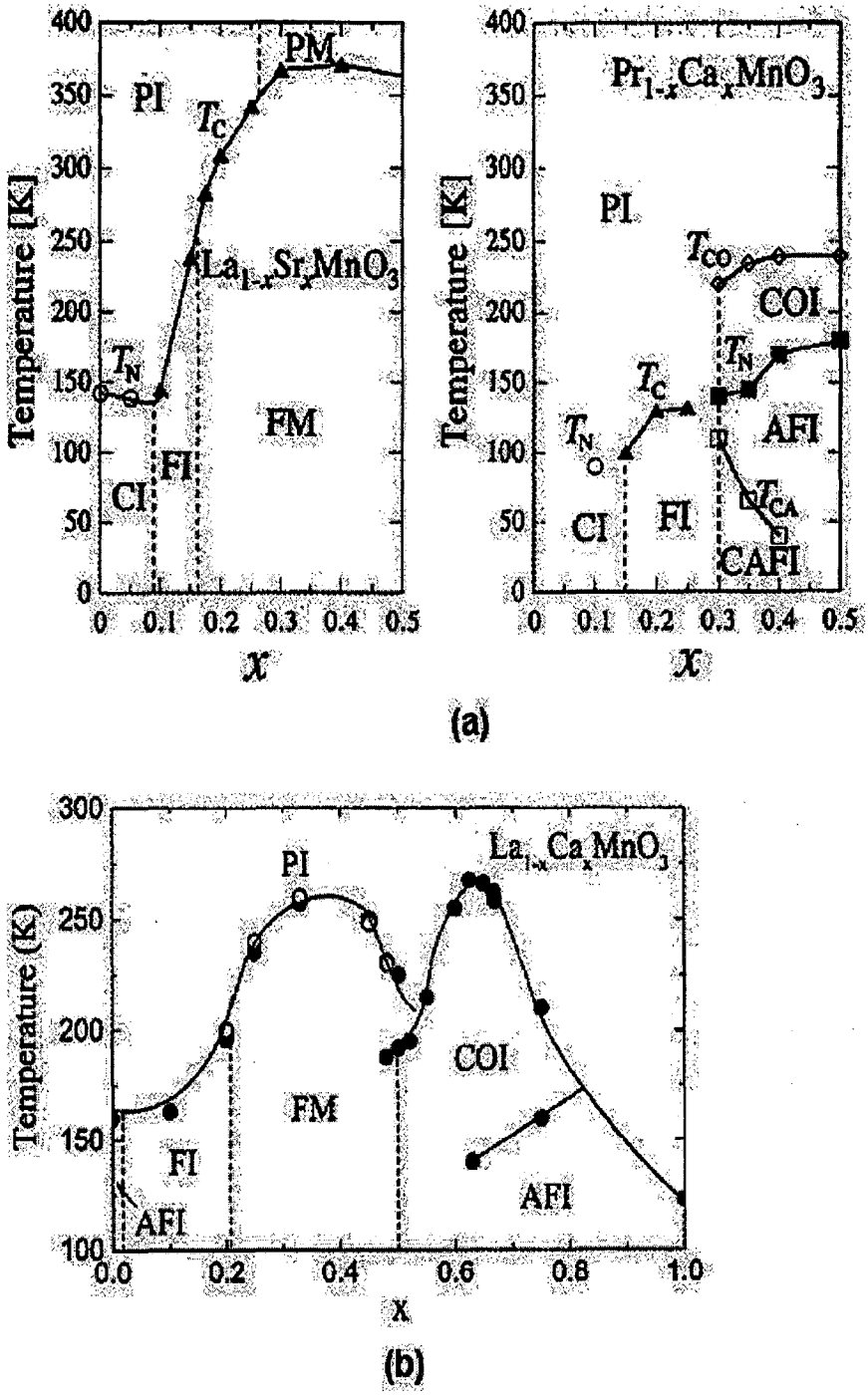

Figure 1.10: **(a)** Magnetic and electronic phase diagrams of $La_{1-x}Sr_xMnO_3$ and $Pr_{1-x}Ca_xMnO_3$. The various states are: paramagnetic insulating (PI), paramagnetic metal (PM), canted insulating (CI), ferromagnetic insulating (FI), ferromagnetic metal (FM), canted antiferromagnetic insulating (CAFI), and charge-ordered insulating (COI). T_C, T_N, and T_{CO}, are Curie, Neel, and charge-ordering temperatures, respectively. **(b)** Phases diagram for $La_{1-x}Ca_xMnO_3$. Reproduced from (a) [72, 89] and (b) [82].

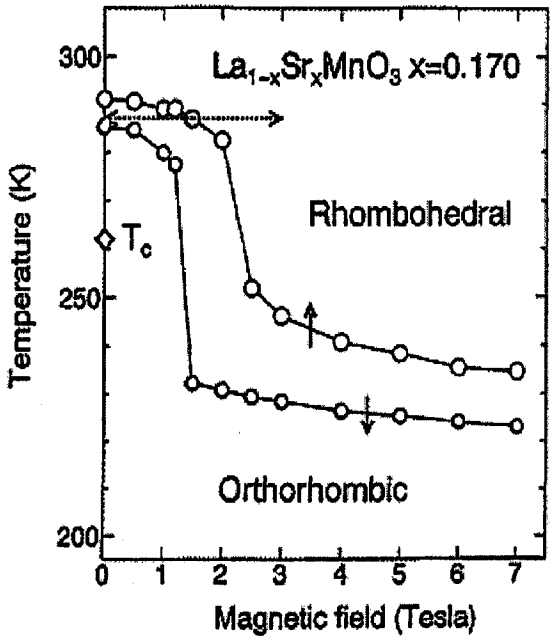

Figure 1.11: Structural phase diagram of $La_{1-x}Sr_xMnO_3$ (x = 0.17). The structural phase transition temperatures from the rhombohedral ($R\bar{3}c$) to orthorhombic (Pbnm) phase in the cooling run are shown by closed circles and open circles are obtained on warming [74].

The low-temperature state in this doping regime was shown by Wollan and Koehler to be AF [63], and Ramirez et al. [84] found evidence from bulk measurements, specific heat C(T), susceptibility χ(T), and sound velocity v(T) for an additional transition around T ~ 170 K which they ascribed to the AF transition. Later single-crystal work by Bao et al. [85] on $Bi_{0.18}Ca_{0.82}MnO_3$ confirmed this assignment by showing the appearance of AF neutron diffraction peaks, clearly separated from the charge order features. Charge order is also seen in $La_{1-x}Ca_xMnO_3$ for x = 0.51 [82, 86]. Cheong et al. studied the phase behaviour in $La_{1-x}Ca_xMnO_3$ and reported that below transition temperatures in the range 100–260 K, compounds with $0.2 < x < 0.5$ are ferromagnetic and metallic, whereas those with $0.5 < x < 0.9$ are antiferromagnetic and charge ordered [87]. As depicted in Fig. 1.10 (b), as the material is cooled from room temperature, a FM state first develops, and then followed by a CO/AF state which exhibits meta-magnetic like behaviour [88]. The phase diagram for

$Pr_{1-x}Ca_xMnO_3$ was mapped out by Tomioka et al. [89] for $x < 0.5$ (Fig. 1.10 (a)). Because the Pr^{3+} ion is slightly smaller than La^{3+}, the phase behaviour also differs. In single crystals, a succession of transitions from high-temperature charge ordering to low-temperature AF insulating and then canted AF states, were inferred from ρ(T) data. Much attention has been paid to the compound $Pr_{0.7}Ca_{0.3}MnO_3$ [90–92] which exhibits a first-order phase transition, in an applied magnetic field, at about 100 K between a low-temperature metallic and canted FM state and a higher temperature insulating, AF and CO state. The most unusual aspect of this material is that on first cooling from room temperature to 4.2 K, metallic behaviour is not obtained until a field is applied. Application of a field of 5 T from a zero-field-cooled state leads to a change in resistance of nearly ten orders of magnitude.

1.3.4 Electronic structure and Jahn Teller (JT) distortion

The physical properties of the doped perovskite manganites ($LaMnO_3$) involve a complex interplay between the spin, charge and orbital degree of freedoms, which strongly depends on the site of occupancy of the d-orbitals. For an isolated 3d ion, five degenerated orbital states are available to the 3d electrons with $l = 2$. In a crystal, the degeneracy is partly lifted by the crystal field. The five d-orbitals are split by a cubic crystal field into three t_{2g} orbitals and two e_g orbitals. For the MnO_6 octahedron, the splitting between the lowest t_{2g} level and the highest e_g level is Δ~1.5 eV (Fig. 1.12). For Mn^{3+} and Mn^{4+} ions, the intra-atomic correlations ensure parallel alignment of the electron spins (first Hund's rule) and the corresponding exchange energy of about 2.5 eV being larger than the crystal field splitting Δ. Mn^{3+} is $3d^4$, $t_{2g}^{3\uparrow}e_g^{1\uparrow}$with S = 2 whereas Mn^{4+} is $3d^3$, $t_{2g}^{3\uparrow}$ with S = 3/2. Their respective magnetic moments are $4\mu_B$ and $3\mu_B$, neglecting the small orbital contribution. In a crystal field of symmetry lower than cubic, the degeneracy of the e_g and t_{2g} levels is lifted, as shown

in the Fig. 1.12 for an axial elongation of the oxygen octahedron. Although the energy of Mn^{4+} remains unchanged by such a distortion but the energy of Mn^{3+} is lowered. Thus, Mn^{3+} has a marked tendency to distort its octahedral environment in contrast to Mn^{4+}. This Jahn–Teller distortion is rather effective in the lightly doped manganites, i.e. with a large concentration (1 – x), of Mn^{3+} ions. The Jahn–Teller distortions are not independent from one Mn^{3+} site to another (cooperative Jahn–Teller effect). This is illustrated by the structure of $LaMnO_3$ (Fig. 1.9) in which the MnO_6 octahedra are strongly elongated within the ab plane in a regular way leading to a doubling of the unit cell. On increasing the Mn^{4+} content, the Jahn–Teller distortions are reduced and the stabilization of the $3z^2–r^2$ e_g orbital becomes less effective. Nevertheless, in a large number of manganites, the e_g orbitals of two types, $3z^2–r^2$ and $x^2–y^2$, are not occupied by the e_g electrons of Mn^{3+} at random and an orbital order is achieved.

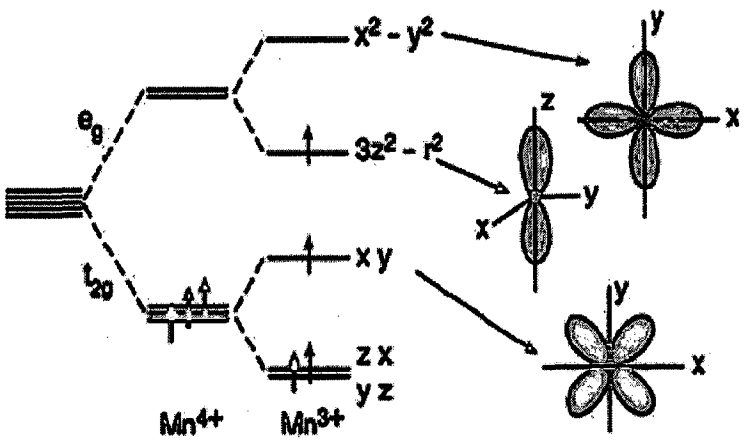

Figure 1.12: Energy levels and orbitals of Mn^{4+} and Mn^{3+} in a crystal field of octahedral symmetry and with axial elongation [4].

As far as manganites are concerned, there are 21 degree of freedom (modes of vibration) for the movement of oxygen and Mn ion [93]. Out of these only two types of distortion (modes

of vibrations) are relevant for the splitting of e_g doublet i.e. JT distortion: Q_2 and Q_3 [94]. The Q_3 is a tetragonal distortion which results in elongation or contraction of MnO_6 octahedra. However, in case of manganites the effective distortion is the basal plane distortion (called as Q_2 mode) in which one diagonally opposite O pair is displaced outwards and the other pair displaced inward. As Mn^{4+} does not have an electron in the e_g states, it will not act as JT ion. Lattice distortion of the octahedral can be static or dynamic. When the carriers have certain mobility, the distribution of Mn^{3+} and Mn^{4+} ions is random and changes with time. Therefore, electron-phonon coupling arises and, in fact, Millis et al. [95] and Roder et al. [96] have claimed that it is necessary to take account of the lattice vibrations to explain the change in curvature of the resistivity close to Tc. Moreover, due to large Hund's coupling, magnetic polarons can be formed [97]. The localization of the carrier in lattice and/or magnetic polarons can explain the activated behaviour of the resistivity for T>Tc [98]. For narrow bandwidth, the localization induced by lattice deformations is much relevant and leads to charge/orbital ordering and stripe formation [99, 100].

1.3.5 Theoretical models

1.3.5.1 Exchange interactions

The magnetic properties of the manganites are governed by exchange interactions between the Mn ion spins. These interactions are relatively large between two Mn spins separated by an oxygen atom and are controlled by the overlap between the Mn d-orbitals and the O p-orbitals. The corresponding superexchange interactions depend on the orbital configuration following the rules of Goodenough–Kanamori. Generally, for Mn^{4+}–O–Mn^{4+}, the interaction is AF, whereas for Mn^{3+}–O–Mn^{3+}, it may be F or AF [101], such as in $LaMnO_3$ where both F and AF interactions coexist. A peculiar and interesting case is that of

Mn^{3+}–O–Mn^{4+}, for which the Mn ions can exchange their valence by a simultaneous jump of the e_g electron of Mn^{3+} on the oxygen (O) p-orbital and from the O p-orbital to the empty e_g orbital of Mn^{4+}. This mechanism of double exchange (DE) originally proposed by Zener [102] ensures a strong ferromagnetic-type interaction. As shown by Anderson and Hasegawa [103], the probability of the e_g electron transfer from Mn^{3+} to neighbouring Mn^{4+} is $t_0 \cos(\theta/2)$, where t_0 is the transfer integral and θ is the angle between the Mn spins (Mn^{3+} and Mn^{4+}) in the case of strong Hund coupling (Fig. 1.13). The process of electron transfer lifts the degeneracy of the configurations Mn^{3+}–O– Mn^{4+} and Mn^{4+}–O–Mn^{3+} leading to two energy levels $E_{t=0} \pm t_0 \cos(\theta/2)$. The energy gain of the parallel spin configuration, $\theta = 0$, which maximizes t, with respect to the antiparallel one, $\theta = \pi$, reveals the ferromagnetic character of the DE interaction. However, the DE angular dependence of $\cos(\theta/2)$ is quite different from $\cos(\theta)$ of the usual exchange interaction. This different angular dependence in conjunction with the competition between DE ferromagnetism and superexchange antiferromagnetism is responsible for the origin of the complex magnetic phase diagram of manganites versus the doping level (x). In particular, canted AF phases at small x were predicted by de Gennes [104]. These result from the energy gain of first-order in the canting angle for DE, which overcomes the energy increase of second-order in the canting angle for the AF superexchange. Ferromagnetic metallic (FM) phases with high Curie temperature, Tc, are required for potential applications. In the first approximation, one can neglect the Mn^{3+}–Mn^{3+} interaction since it is either F or AF depending on the orbital configuration and both F and AF interactions currently coexist in the same compound such as in $LaMnO_3$. Then, supposing the Mn^{4+}–Mn^{4+} AF superexchange and Mn^{3+}–Mn^{4+} F DE interaction to be of same magnitude, the mean field approximation leads to $Tc \sim 2x(1 - x) - x^2$, which is maximum for

x = 1/3 . The fact that the FM phases are generally found around x = 1/3 in manganites is in agreement with this crude model.

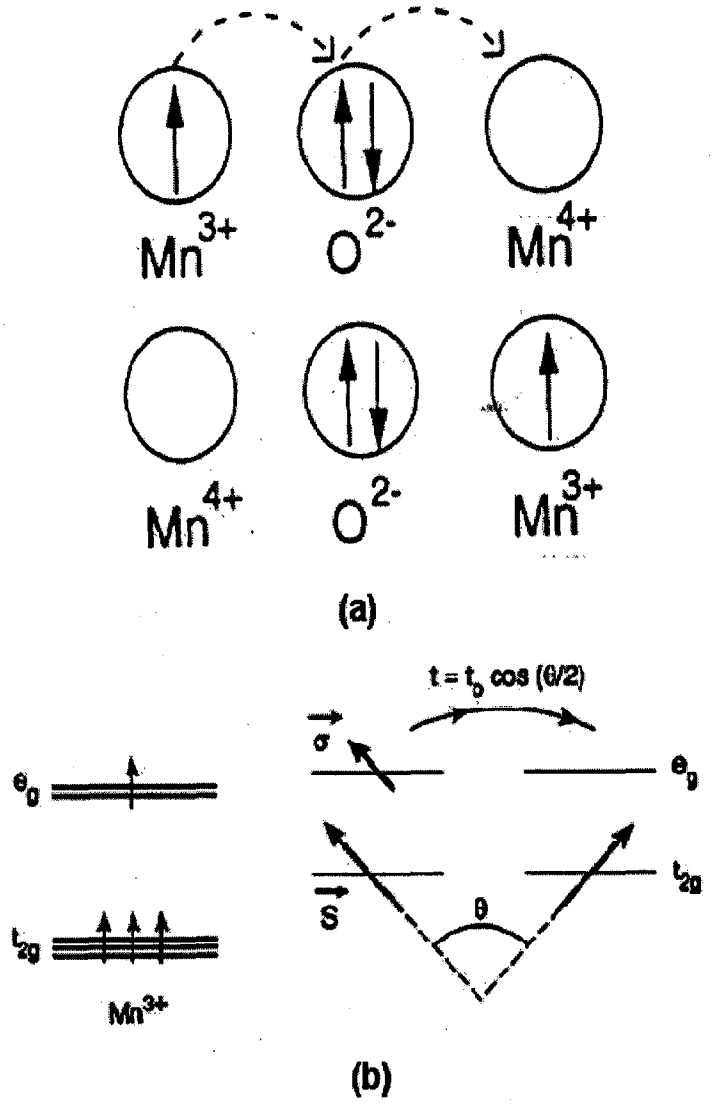

Figure 1.13: **(a)** Schematic view of the double exchange mechanism proposed by Zener **(b)** Sketch of the de Gennes spin canted states [104].

Zener made a rough estimation of electrical conductivity based on Einstein's relation and the diffusion constant of a hole located at a Mn^{4+} site which comes to be,

$$\sigma \approx \frac{xe^2}{ah}\left(\frac{T_C}{T}\right) \tag{1.4}$$

where σ = electrical conductivity, h = the Planck's constant, e = electronic charge, Tc = ferromagnetic transition temperature, x = concentration of Mn^{4+} ions and a =lattice parameter or Mn-Mn distance. Zener's model was based on the assumption that the manganites are uniform and homogeneous without any form of coexisting clusters of competitive phases. de Gennes [104] in a mean-field type description revisited the problem in 1995, treating the effect of double exchange in the presence of antiferromagnetic background. He formulated the DE problem for a lattice and derived a band model for the motion of holes. de Gennes considered a layered material with 'N' magnetic ions per unit volume, each spin 'S' coupled ferromagnetically to its 'Z' neighbour on the same layer with exchange energy 'J" and antiferromagnetically to 'Z' neighbours on adjacent layers with energy 'J'. de Gennes predicted that at low doping level, an antiferromagnetic superexchange interaction competes with the ferromagnetic DE interaction which leads to spin-canted state. However, recent studies have shown that a strong alternative to canted states is provided by the tendency of phase separation.

de Gennes further considered localization and self trapping of charge carriers which gives rise to local distortion of the spin lattice i.e. the concept of magnetic polaron [105]. Another pioneer theoretical study in manganites was carried out by Goodenough [101] regarding the charge, orbital and spin arrangements in the non-ferromagnetic regime of the phase diagram of LCMO [106]. The approach of Goodenough was based on the notions of 'semicovalent bond' and elastic energy considerations. Semicovalent bond or semicovalency arises when the overlap of spin polarized s and p orbitals of Mn ions with occupied orbitals of the oxygen allow only covalent bonds involving electrons of one spin direction [101]. Kubo and Ohata [107] considered a fully quantum mechanical approach employing mean-field theory for metallic double-exchange ferromagnets. They calculated a magnetic phase

diagram, resistivity and the magnetoresistance. Their results show a ferromagnetic to paramagnetic transition at Tc, accompanied by a change in the temperature dependence of resistivity, and diverging magnetoresistance at Tc.

1.3.5.2 Electron-phonon coupling and other theories

The double exchange theory is still not sufficient to handle the very complex phase diagram of manganites. For instance, there are compounds such as $La_{1-x}Sr_xMnO_3$ that actually do not have the CE-phase at x = 0.5, while others do. There are compounds that are never metallic, while others have a paramagnetic state with standard metallic characteristics. And even more important in the early studies of manganites, there was no proper rationalization for the large MR effect. It is only with the use of state of art many-body tools that result the large magnetotransport effects, which are to be understood. Thanks to theoretical developments in recent years that can address the competition among the different phases of manganites, their clustering and mixed-phase tendencies and dynamic Jahn-Teller polaron formation. The prevailing idea to explain the curious magnetotransport behaviour of manganites changed in the mid-90's from the simple double exchange scenario to a more elaborated picture where a large Jahn-Teller (JT) effect, which occurs in the Mn^{3+} ions, produces a strong electron-phonon coupling that persist even at densities where a ferromagnetic ground state is observed. In fact, in the undoped limit x = 0, and even at finite but small x, it is well known that a robust static structural distortion is present in the manganites. In this context, it is natural to imagine the existence of small lattice polarons in the paramagnetic phase above Tc, and it was believed that these polarons lead to the insulating behaviour of this regime. The fact that double exchange can not be enough to understand the physics of manganites is clear from several points of views. Millis, Shraiman

and Littlewood [95] arrived at this conclusion by presenting the estimations of the critical Curie temperature and of the resistivity using the DE framework. It is clear that one-orbital model is incomplete for quantitative studies since it can not describe the key orbital ordering of manganites and the proper charge order state at near x = 0.5, which are so important for CMR effect found in low-bandwidth manganites. Not even a fully disordered set of classical spins can scatter electrons as much as needed to reproduce the experiments again, unless large antiferromagnetic regions appear in a mixed phase regime.

Millis, Shraiman and Mueller [108] argued that the physics of manganites is dominated by the interplay between a strong electron-phonon coupling and the large Hund coupling effect that optimizes the electronic kinetic energy by the generation of a FM phase. The large value of the electron phonon coupling is clear in the regime of manganites below x = 0.20, where a static JT distortion plays a key role in the physics of the material. Millis, Shraiman and Mueller argued that a dynamical JT effect may persist at higher hole densities, without leading to long range order but producing important fluctuations that localize electrons by splitting the degenerate e_g levels at a given MnO_6 octahedron. The calculations were carried out using the infinite dimensional approximation that corresponds to a local mean-field technique where the polaron can have only one site extension and the classical limit for the phonons and spins was used. The coulomb interaction was neglected but further work, reviewed below, showed that JT and coulombic interactions lead to very similar results [109]. Millis, Shraiman and Mueller [108] argued that the ratio $\lambda_{eff} = E_{JT}/t_{eff}$ dominates the physics of the problem. Here E_{JT} is the static trapping energy at a given octahedron and t_{eff} is an effective hopping that is temperature dependent following the standard DE discussion. In this context it was conjectured that when the temperature is larger than Tc the effective coupling λ_{eff} could be above the critical value that leads to insulating behaviour due to

electron localization, while it becomes smaller than the critical value below Tc, leading to metallic behaviour. There are various other theories/models, e.g. Vibronic model of Goodenough [110], Bi-polaronic model of Alexandrov [111], Magnetoimpurity theory of Nagaev [112] and Falicov-Kimball like approach of TV Ramakrishnan [113] etc. that explains some aspect of doped perovskite manganites, but a satisfactory theory of manganites is still lacking.

1.3.6 Electrical conductivity and charge-ordering

The transfer of e_g electron from Mn^{3+} to Mn^{4+} by DE (Fig. 1.13) is the basic mechanism of electrical conduction in the manganites. In those with strong DE, the e_g electrons become delocalized in the ferromagnetic phase for a certain range of doping centered around $x \approx 1/3$ and a FM state is established at low temperature. In contrast to the 3d ferromagnetic metals such as Ni or Fe where the up and down-spin bands are both occupied and they are separated by 1 eV or more and the upper band is empty, leading to a half-metallic behaviour. The conduction band of such a half-metallic ferromagnet is thus fully spin-polarized and is of large potential interest for spin electronics [114]. The electronic structure of $La_{1-x}M_xMnO_3$ (M = Ca, Sr, Ba) has been theoretically investigated by the local spin-density approximation (LSDA) [115–118]. Whereas $LaMnO_3$ is found to be an AF insulator with a gap in the half-filled e_g band resulting from the Jahn–Teller distortion, a half-metallic ferromagnetic ground state is obtained for $x = 1/3$, with the electronic structure near the Fermi level mainly consisting of substantially hybridized bands derived from majority spin Mn e_g and O p states. The manganites with $x < 0.5$ have a conduction band more than half-filled whereas those with $x > 0.5$ have a conduction band less than half-filled and thus, the respective charge carriers are holes and electrons. They are currently labelled as hole-

doped and electron-doped manganites, respectively. When increasing x above 0.5, the number of ferromagnetic DE links decreases and that of AF coupled Mn^{4+} increases. This favours AF or canted AF phases in which the motion of charge carriers is hindered. At certain doping levels such as x = 0.5 corresponding to Mn^{3+}–Mn^{4+} species with a 1 : 1 ratio, a real-space ordering of charge carriers takes place when their long-range Coulomb interaction overcomes their kinetic energy [100, 119–121]. This charge ordered insulating (COI) state is favoured by the presence of small size cations at the site A, for instance in the case of $Pr_{1-x}Ca_xMnO_3$ [120]. The transition to the charge-ordered (CO) phase is a first order phase transition accompanied by an abrupt increase in resistivity and abrupt changes in the lattice parameters with lowering temperature. It is also closely related to the orbital ordering through the Jahn–Teller effect of Mn^{3+} [122, 123].

The general tendency of charge carrier localization and ordering in doped Mott insulators [124, 125] is particularly strong in doped manganites, due to the relatively enhanced (electron/hole) carrier-lattice coupling. In addition, there exists orbital degree of freedom of the e_g electrons in Mn^{3+} ions. This orbital ordering can lower the electronic energy through the Jahn-Teller mechanism. Therefore, there exists orbital ordering (OO), in addition to charge ordering in mixed valent manganites. The first direct evidence of charge ordering in $La_{0.5}Ca_{0.5}MnO_3$ (Tc $\approx$ 220 K) was provided by electron diffraction studies reported by Chen and Cheong (1996) as shown in Fig. 1.14 [126]. They observed quasi-commensurate satellite reflections close to the onset of antiferromagnetism with a modulation wave vector $2\pi/a$ ({1/2}-ε, 0, 0). They interpreted these reflections as result from the coherent ordering of $Mn^{3+}O_6$ and $Mn^{4+}O_6$ octahedra, as expected for a charge ordered phase. Radaelli et al. [127] reported a detailed synchrotron X-ray and neutron diffraction investigations of 50 % Ca doped $LaMnO_3$. They observed weak satellites reflection in X-ray

diffraction pattern which was consistent with that of Chen and Cheong [126]. In $La_{1/3}Ca_{2/3}MnO_3$, there are twice as many Mn^{4+} ($3d^3$) ions as the Mn^{3+}($3d^4$) ions, and the ordering of diagonal rows of Mn^{4+} and Mn^{3+} ions plus the orientational ordering of the d_z^2 orbital in Mn^{3+} gives rise to the striped pattern as shown in Fig. 1.15.

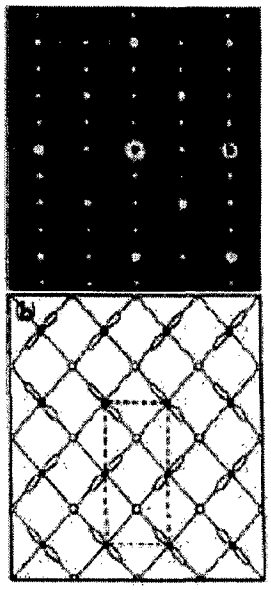

Figure 1.14: (a) [001] Zone-axis electron diffraction pattern obtained at 95 K. The fundamental Bragg peaks labeled a, b, and c can be indexed as (200), (020), and (110), respectively. The presence of superlattice spots with modulation wave vector (1/2, 0, 0) or (0, 1/2, 0) is evident. Kinematically forbidden (100) and (010) spots also appear as a result of multiple scattering. **(b)** Schematic charge-ordering picture of Mn^{4+} and Mn^{3+} ions. Open and closed circles represent $Mn^{4+}$and Mn^{3+}ions, respectively. The orientational order of dz^2 orbitals of Mn^{3+} ions which results in the cell doubling along the a axis is also indicated [126].

In the Fig. 1.15 (a), diagonal charge stripes are evident, and their periodicity is ~16.5 Å. These ~16.5 Å charge stripes form the pattern in the real space image [128] obtained from electron microscopy for x = 2/3. The similar charge/orbital ordering scheme for x = 0.5 is shown in Fig. 1.15 (b), where there are just as many Mn^{4+} ions as Mn^{3+} ions. In this case, the diagonal charge stripes adopt a wave vector $\delta = 0.5$ with a spacing of ~11 Å. Mori et al. [128] have reported a different pattern of charge localization in the charge-ordered phase of

$La_{1-x}Ca_xMnO_3$ ($x \geq 0.5$) employing transmission electron microscopy at 95 K. They observed extremely stable pairs of $Mn^{3+}O_6$ stripes, with associated large lattice contraction (due to the Jahn-Teller effect), separated periodically by stripes of non distorted $Mn^{4+}O_6$ octahedra.

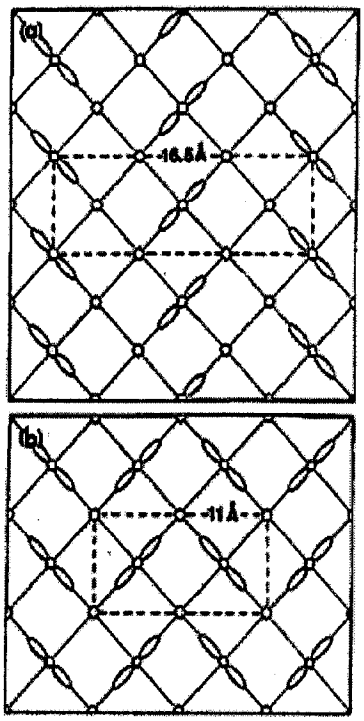

Figure 1.15: (a) Schematic real-space charge-ordering picture of Mn^{4+} (open circles) and Mn^{3+} (closed circles) ions for the 16.5 Å diagonal stripes appearing in the x = 0.67 sample. The orientational order of d_z^2 orbitals of Mn^{3+} ions is also indicated. For comparison, a similar schematic for the sample of x = 0.5 is shown in **(b)** which demonstrates 11 Å periodic stripes. Dashed lines in (a) and (b) indicate the unit cell of the superlattice [126].

These periodicities, which adopt integer values between 2 and 5 times the lattice parameter of the orthorhombic unit cell, corresponds to the commensurate carrier concentrations of x = 1/2, 2/3, 3/4 and 4/5. For other values of x, the pattern of charge ordering is a mixture of the two adjacent commensurate configurations. These paired Jahn-Teller stripes appear therefore to be the fundamental building blocks of the charge-ordered state in the manganites. The charge ordering in manganites has been accompanied by an increase in sound velocity, change in lattice parameters, anomalies in heat capacity, magnetization resistivity and the

activation energy for conduction. These orbital/charge order can readily be melted to ferromagnetic metallic state by application of various impulses such as magnetic field [129], pressure [130], exposure to X-ray photons [131], high voltage (250-700 V) [132], electric field [133] and visible-IR light laser pulse [134]. Charge ordering (CO) similar to that found in $La_{0.5}Ca_{0.5}MnO_3$ has been reported for $Nd_{0.5}Sr_{0.5}MnO_3$ [135] and $Pr_{0.5}Ca_{0.5}MnO_3$ [136]. Both these compounds exhibit the antiferromagnetic structure. However, not all $A_{0.5}A'_{0.5}MnO_3$ compounds exhibit charge ordering behaviour. For example, $Pr_{0.5}Sr_{0.5}MnO_3$ [137] has a type–A antiferromagnetic insulating ground state. It has also been demonstrated that the equal amounts of Mn^{3+} and Mn^{4+} is not a prerequisite to charge ordered behaviour. $Pr_{0.7}Ca_{0.3}MnO_3$ has also been reported to exhibit the CE-type antiferromagnetic structure, suggesting a similar charge ordering as in $La_{0.5}Ca_{0.5}MnO_3$ [101]. Kumar et al. [138] have carried out detailed investigations on the effect of average radius of the A-site cations $\langle r_A \rangle$ on CO properties and concluded that Tco increases with decrease in $\langle r_A \rangle$. The phenomenon of charge/orbital ordering in manganites is very interesting and relevant to explain various peculiar properties such as colossal magnetoresistance and phase separation [100, 139-141]. Recently, Loudon et al. [142] have observed CO-FM phase in $La_{0.5}Ca_{0.5}MnO_3$ employing Lorentz electron microscopy at 90 K. They observed an inhomogeneous mixture of ferromagnetic (3.4±0.2 μB per μN) and antiferromagnetic (zero-moment) regions which extend for several micrometers, and can span several crystallographic grains. Loudon et al. have suggested that CO occurs not only in regions with no net magnetization, but can also occur in ferromagnetic regions. This is consistent with the similar coexistence in $La_{0.25}Pr_{0.375}Ca_{0.375}MnO_3$ as observed by Mori et al. [143]. Tendeloo et al. have extensively reviewed the structure and microstructural aspects of colossal magnetoresistive materials with special reference to charge ordering [144]. Very recently Sagdeo et al. reported the

electron diffraction evidence of charge ordering at room temperature in $La_{1-x}Ca_xMnO_3$ ($0.55 \leq x \leq 0.67$) [145]. Gupta et al. also reported the direct evidence for charge ordering and electronic phase separation in $Bi_xSr_{1-x}MnO_3$ at room temperature [146].

1.3.7 Metal–insulator transition and CMR

The simple manganites with strong double exchange (DE), such as $La_{1-x}M_xMnO_3$ (M = Ca, Sr, Ba) with $x \approx 1/3$, exhibit a transition from a high temperature paramagnetic (P) semi-conducting or insulating (I) phase to a low temperature FM phase. An example is given in Fig. 1.16 for a $La_{0.825}Sr_{0.175}MnO_3$ single crystal. In the P phase, the electrical resistivity generally exhibits strong temperature dependence. Different $\rho(T)$ laws have been used in fitting the experimental data, the most popular ones being: (i) simple thermal activation law $\rho = \rho_\infty \exp(E_0/k_BT)$, with a typical gap value of about 0.1 eV; (ii) hopping of adiabatic polarons $\rho \sim T \exp(E_0/k_BT)$; (iii) Mott variable range- hopping (VRH), $\rho = \rho_\infty \exp[(T_0/T)^{1/4}]$. Each of these laws have some physical origins, which are respectively: (i) the existence of a pseudo gap at the Fermi level in the P phase [147]; (ii) the local lattice distortion accompanying the moving charge carrier (Jahn–Teller polaron); (iii) the localization of the charge carriers by the magnetic disorder [148]. In a restricted range of temperature, it is practically impossible to discriminate between these different $\rho(T)$ laws. At low T, the spontaneous alignment of the Mn spins below the Curie temperature (Tc), allows a delocalization of the e_g electrons, leading to a low resistivity FM phase with $\rho \approx \rho_o + aT^2$ for $T \ll Tc$. This alignment of the Mn spins can be induced for $T \gg Tc$, or reinforced for $T \ll Tc$, by applying an external magnetic field. The maximum effect is obtained close to T_C (Fig. 1.16) since the initial magnetic susceptibility diverges as $T \rightarrow Tc$. Thus, these manganites have a rather large negative magnetoresistance, the so-called CMR, which peaks at about Tc.

This phenomenon, initially reported in $Nd_{0.5}Pb_{0.5}MnO_3$ [149], has been later observed in a rather large number of manganites. In general, since the resistivity of the P phase strongly increases on decreasing T, whereas those of the FM phase decreases, the CMR is larger and larger as T_C is smaller and smaller, at least for a given doping level. For instance, a resistance ratio $R(0)/R(6T) > 10^3$ was observed in a thin film of $La_{0.67}Ca_{0.33}MnO_3$ with $T_C \approx 80$ K [54], whereas in a film of same composition with Tc = 260 K this ratio is only of about 4 [150]. Similarly, a strong CMR increase is observed in polycrystalline samples of $(La_{1-x}Y_x)_{0.7}Ca_{0.3}MnO_3$, in which Tc is decreased by increasing the yttrium concentration x [151].

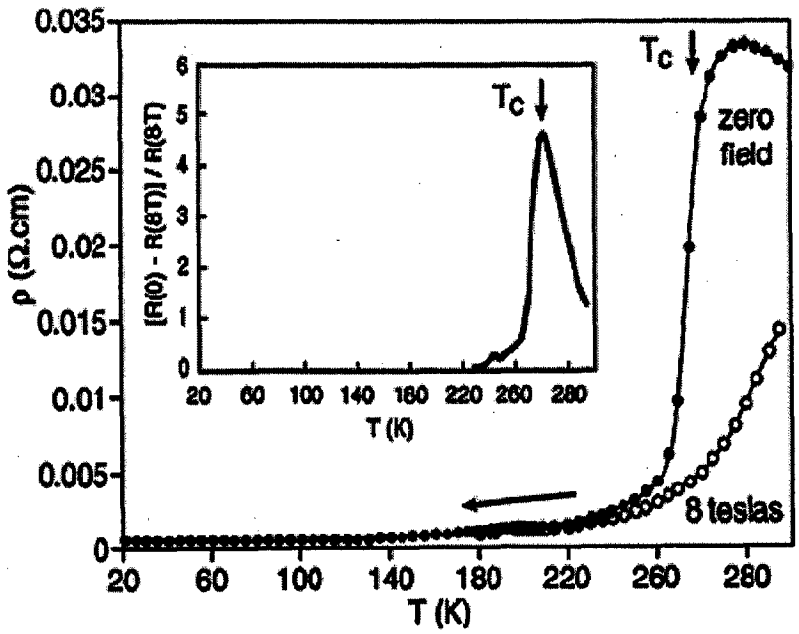

Figure 1.16: Resistivity in zero field and in a 8 T applied field versus temperature, of a single crystal of $La_{0.825}Sr_{0.175}MnO_3$. In inset, magnetoresistance ratio versus temperature. The arrow indicates the Curie temperature, Tc. [256].

A first interpretation of CMR was based on the DE model in which the Mn lattice bears localized S = 3/2 spins, resulting from the three t_{2g} electrons, and the mobile e_g electrons having a transfer integral (t) between two neighbouring Mn ions, $t = t_0 \cos(\theta/2)$,

where θ is the angle between the 3/2 spins of the Mn neighbours [103]. A detailed MR calculation taking into account DE and Hund's coupling has shown an explicit dependence of the resistivity (ρ), on the magnetization (M), by the simple expression, $\rho/\rho_o = 1-C(M/M_{sat})^2$, at small relative magnetization M/M_{sat} values. For a strong Hund's coupling, $J_H \gg t$, $C \approx 4$, whereas $C = 1$ in the weak coupling limit. This relation between resistivity and magnetization is in good agreement with the experimental data on $La_{0.825}Sr_{0.175}MnO_3$ [152]. The dependence of ρ with magnetization can also be interpreted in the VRH model that includes a decrease of the localization potential on increasing M/M_{sat}. The experimental data for a thin film of $La_{0.7}Ca_{0.3}MnO_3$ were satisfactorily fitted to the magnetization dependent variable range hopping (VRH) law $\ln(\rho/\rho_\infty) = [T_0(1-(M/M_{sat})^2)/T]^{1/4}$ [148]. However, these models do not take into account the electron–phonon interaction, which is proved to be important in Mn perovskites, for instance from the large isotopic effect observed on T_C and on transport properties by substitution of ^{18}O to ^{16}O [153, 154]. Moreover, theoretical models including electron–phonon coupling have also been proposed [95].

1.3.8 Electronic phase separation

It has been recently predicted from computational studies of realistic models that an electronic phase separation can occur in manganites in a certain range of doping [155]. In particular, at low doping level and at low temperature, a phase separation between hole-poor AF regions and hole-rich F regions is energetically more favourable than the homogenous canted AF phase. The energy of the charge carriers is minimal for F ordering. With a density insufficient for establishing the F ordering in the entire sample, the carriers concentrate into droplets or stripes which become ferromagnetic inside the insulating AF matrix. Such a phase separation was predicted earlier for degenerate magnetic semiconductors and conjectured for

manganites [156, 157]. On increasing the doping level, the ferromagnetic regions become connected to each other and a low electrical resistance is achieved above the percolation threshold. Interesting tunneling effects of the charge carriers between the ferromagnetic entities just below the percolation threshold and a high sensitivity of the tunneling current to magnetic field might be expected. Experimental observation of electronic phase separation in manganites is not as straightforward. Local probes such as neutron scattering and nuclear magnetic resonance (NMR) are needed and the data interpretation is rarely unambiguous. Among the experiments interpreted by a phase separation, one can mention the neutron scattering studies of lightly doped single crystals of $La_{1-x}Ca_xMnO_3$ revealing the existence of magnetic heterogeneities at nanometer scale [158]. In the same compound with $x \approx 0.2$, the coexistence of F and AF regions was also proposed from ^{139}La NMR spectra and nuclear relaxation [159]. Moreover, Battabyal et al. [160] analyzed the seebeck-coefficient in $La_{0.7}Sr_{0.3-x}Ag_xMnO_3$ samples in terms of phase separation model.

1.3.9 Low field magnetoresistance and spin-dependent tunneling

The CMR of mixed-valence manganites requires large applied magnetic fields, typically of a few tesla. In simple manganites exhibiting a paramagnetic–ferromagnetic transition, the MR is very large around Tc, whereas it becomes negligible at temperatures much lower than Tc, where the magnetization is close to saturation. However, polycrystalline samples of ferromagnetic $La_{1-x}M_xMnO_3$ (M = Ca, Sr, Ba, Pb) exhibit a low field negative magnetoresistance (LFMR), which increases with decreasing temperature and particle size [51, 161]. This LFMR is clearly related to the alignment of the ferromagnetic domains in the typical field range 0–0.1 T. The relative MR, $-\Delta\rho/\rho$, can reach 50 % at low temperature. This phenomenon, which differs from the intrinsic CMR, is reminiscent of the giant

magnetoresistance (GMR) of granular alloys of ferromagnetic and noble metals [162]. It is attributed to spin-dependent transmission of electrons across the grain boundaries, which was evidenced in nice experiments performed on the manganite films deposited on a $SrTiO_3$ bicrystal substrate [163, 164]. The spin-dependent tunnelling between two ferromagnetic manganite films across a thin insulating barrier was also investigated. These tunneling structures have shown MR values of 50-90 % at few tens of Oe at 4.2 K. Even higher values have been observed in some structures, but with poor reproducibility, presumably due to defects in the barrier layer or at the interfaces [165]. Compared to similar experiments of tunneling between metallic films, one benefits from the large spin polarization (P) of the manganite. The relative difference between the tunneling currents for antiparallel and parallel configurations is equal to the product of the polarizations of the two films, $(I_{\uparrow\downarrow} - I_{\uparrow\uparrow}) / (I_{\uparrow\downarrow} + I_{\uparrow\downarrow}) = P_1 \cdot P_2$. For two Ni films with $P_1 = P_2 = 0.11$, this difference is very small, of the order 1% instead of 1 for full polarization, $P_1 = P_2 = 1$. Indeed, a large field effect on the tunneling current between $La_{0.7}Sr_{0.3}MnO_3$ (LSMO) films across $SrTiO_3$ has been observed at low temperature but the effect decreased rapidly with increasing the temperature [166, 167]. A large low field magnetoresistance component has also been observed in polycrystalline manganites samples, where disruption in the crystalline order at grain boundaries induces a local spin disorder [43, 51, 168]. Using grain boundaries (GB's) to manipulate magnetic behaviour thus proves to be a simple method for enhancing the low field sensitivity of half metallic materials. Significant differences in the magnetoresistance (MR) properties of polycrystalline and single crystal samples have been reported since the initial discovery of CMR in the manganites. In particular, early work on bulk polycrystalline samples have shown a substantial MR at temperatures much below Curie temperature (Tc), while the MR magnitude is usually very small in single crystals or epitaxial films of same composition [82,

152, 169, 170]. A number of subsequent studies, both on bulk and thin film samples, have been undertaken to specifically clarify the role of GB's on the MR behaviour of manganites [43, 51, 163, 171, 172].

In a most cited study, Hwang et al. [51] found that intergrain tunneling is induced by the scattering across grain boundaries in polycrystalline samples. They found that in polycrystalline samples, the resistivity is ~10 times and ~18 times greater than a single crystal for the polycrystalline samples sintered at 1700 ^{0}C and 1300 ^{0}C, respectively (see Fig. 1.17 (a)). However magnetization curves of polycrystalline samples and a single crystal seem very similar, implying that the intergrain properties reflect bulk intrinsic properties [see Fig. 1.17 (c)]. The MR in the polycrystalline samples is dominated by transport across grain boundaries that are significantly sensitive to the application of magnetic field, while the intrinsic negative MR in single crystal is due to the suppression of spin fluctuations. They suggested that spin-polarised intergrain tunneling was involved in their results. The original work of the MR in granular nickel films were based on the tunneling of spin-polarised electrons between magnetic metallic particles [173, 174].

In the tunneling process with the conservation of the electron spin, an additional magnetic coupling energy was also considered, when the magnetic moments of the neighbouring grains were not parallel. By considering the magnetic field dependence of this intergrain coupling energy, the first term in the high temperature expansion of the MR [174] is given by

$$\frac{\Delta\rho}{\rho} = -\frac{JP}{4K_BT}\left[m^2(H,T) - m^2(0,T)\right] \qquad (1.5)$$

where J is intergrain exchange constant, P is the electron polarization and m is the magnetization normalized to the saturation value. In polycrystalline $La_{2/3}Sr_{1/3}MnO_3$, the

sharp drop in resistance is correlated with the abrupt increase in magnetization. The MR is negative when J is positive, pointing to an antiferromagnetic intergrain interaction. The ferromagnetic alignment of the grains by an applied field increases electron tunneling as in the case of spin valves.

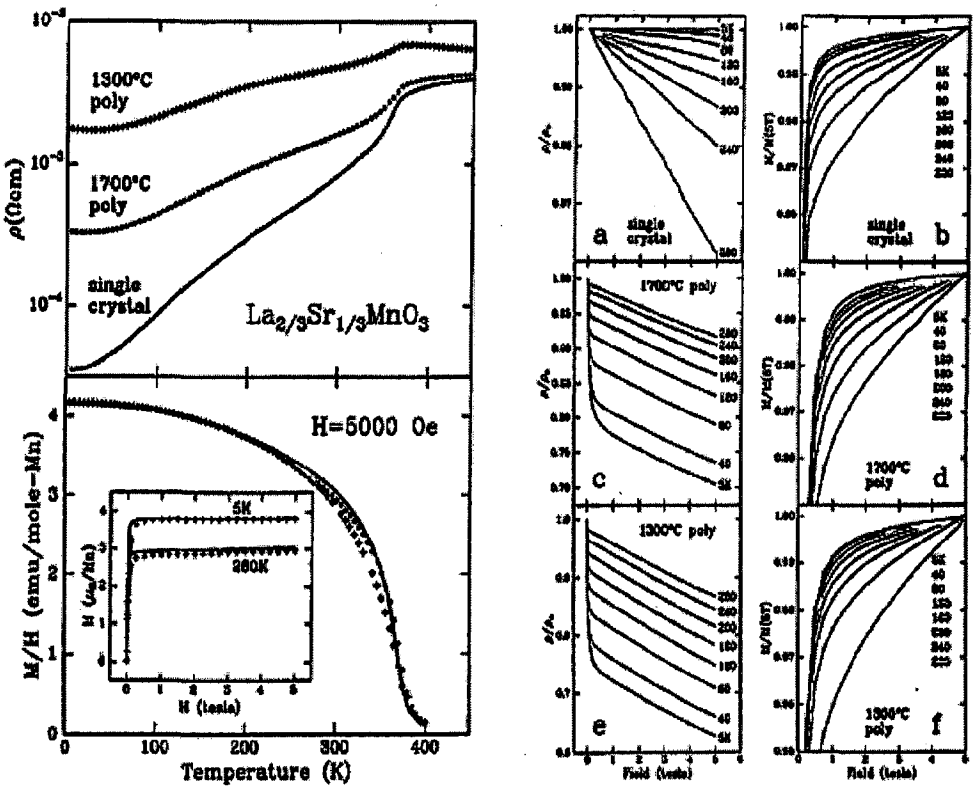

(a) (b) (c)

Figure 1.17: Comparisons of resistivity-magnetization measurements of two polycrystalline samples and a single crystal $La_{2/3}Sr_{1/3}MnO_3$. **(a)** The top shows the resistivity vs. temperature curve of two polycrystalline samples with final sintering temperatures of 1300 ^{0}C and 1700 ^{0}C and a single crystal. The bottom shows the magnetization vs. temperature at H=0.5 T with an inset of M (μ_B/Mn) vs. H (T) at 5 K and 280 K. **(b)** The normalized resistivity vs. H (T) and **(c)** the normalized magnetization vs. H(T) from 5 K to 280 K are shown [51].

One reason that spin polarised transport effects is significant in the perovskite manganites is the high degree of spin polarization in these materials. Figure 1.18 shows energy level diagram of a normal itinerant ferromagnet such as Ni with a very wide conduction band (~4.5 eV) which minority and majority carrier bands are shifted by a gap exchange energy (~0.6

eV) and a partial polarization of the electrons is about 11 % [175]. On the other hand, in manganites, a relatively narrow majority carrier conduction band (~1.5 eV) is fully split from the minority band by a large Hund's energy and exchange energy (~2.5 eV), resulting in a nearly complete polarization of the electrons [176]. Since the high degree of spin polarization in the perovskite manganites was shown [51, 177], spin polarised transport effects have attracted much attention because of their technological applications such as spin polarization dependent phenomena and low field magnetoresistance.

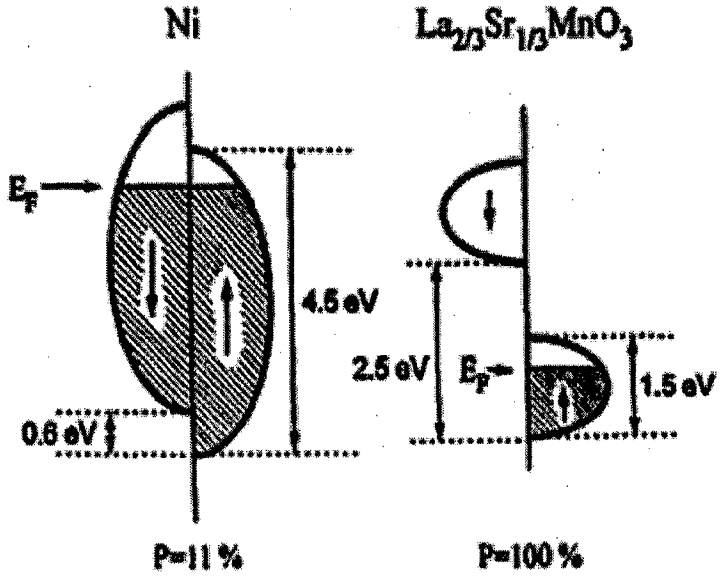

Figure 1.18: Comparison diagram of energy levels of the conduction band of Ni with $La_{2/3}Sr_{1/3}MnO_3$ [175, 176].

1.4 MAGNETORESISTANCE IN DOUBLE PEROVSKITES

1.4.1 Historical overview

Oxide perovskites with ferromagnetic behaviour around room temperature were first reported in 1950 in the pioneering studies on manganites ($AMnO_3$; A = divalent or trivalent cation) by Jonker and Van Santen [59]. In these compounds, the existence of mixed valence in Mn allowing for an electron transfer through oxygen orbitals was invoked in order to

explain the ferromagnetic behaviour via a double exchange mechanism proposed by Zener [102]. This discovery encouraged further studies on oxide materials that could show ferromagnetism at high temperatures via some electron transfer mechanism between mixed valence transition metals, in analogy to the observed behaviour in manganites. In 1961, ferrimagnetic behaviour above room temperature in double perovskite oxides ($A_2BB'O_6$; A = divalent or trivalent cation; B and B' = transition metals) was reported by Longo and Ward [178]. Subsequent experiments on Re-based double perovskites further explored their magnetic and electrical properties [179, 180]. This finding on Re-based double perovskites stimulated the research on new ferromagnetic compounds with double perovskite crystallographic structure, such as B' = Mo-based and W-based double perovskites, reported by Patterson and coworkers in 1963 [181]. That study showed that ferromagnetism above room temperature was also possible in some of these compounds. Strong steric effects associated with the cation size at the A site of A_2FeMoO_6 were already noticed in the study by Galasso et al. [182]. Since these initial times, it was noticed that ordinary superexchange rules could not account for the ferrimagnetic ordering of B and B' sites observed with microscopic techniques in these compounds [180, 183–185]. Unexpectedly, the A_2FeMoO_6 and A_2FeReO_6 compounds were also found to be highly conductive [180, 184]. All these features suggested that the involved physics was much richer than expected. Even though some small activity kept on going on this class of materials for the last three decades, the publication by Kobayashi et al. in 1998 of the half-metallic properties of Sr_2FeMoO_6 triggered a renewed interest in these materials in the context of their potential applications in the field of spin electronics [5]. In fact, that paper of Kobayashi et al. has been cited more than 610 times according to the ISI Web of Knowledge database.

Kobayashi et al. [5] reported that Sr_2FeMoO_6, an oxide material of $A_2BB'O_6$ type double perovskite structure, shows high T_C as well as high spin polarization. Fe-based double perovskite oxides A_2FeMoO_6 (A = Sr, Ba and Ca) have been examined for their remarkable tunneling-type magnetoresistance (TMR) effect observed at low applied magnetic fields and at room temperature [186–191]. Among the A_2FeMoO_6 materials, Ca_2FeMoO_6 shows the Tc (345–380 K) [192–194], Sr_2FeMoO_6 shows the highest T_C (400–430 K) [5, 195–198] and Ba_2FeMoO_6 shows the Tc (308–367 K) [193, 199, 200]. In these compounds, the B positions of the perovskite structure are occupied alternately by Fe and Mo atom, in such a way that each FeO_6 octahedron is corner-linked to six MoO_6 octahedra and vice versa. Each Fe cation that is misplaced in a Mo position is called an antisite (AS) defect. The magnetic structure of the material has been described as an ordered arrangement of parallel Fe^{3+} ($3d^5$, S=5/2) magnetic moments antiferromagnetically coupled with Mo^{5+} ($4d^1$, S=1/2) spins. The observed magnetoresistance (MR) has been associated with electron tunnelling through the insulator barriers formed at the grain boundaries (GB's). It is believed that the structure and microstructure of A_2FeMoO_6 are critical factors for the realization of large TMR values. The material properties are very sensitive to synthesis methods as well as processing conditions, such as temperature, time, and atmosphere for heat treatment. The technologically interesting low-field TMR (at $H \leq 1$ T) is strongly dependent on the concentration of antisite defects as well as on the grain size and nature of grain boundaries. Since the ionic sizes of Fe^{3+} and Mo^{5+} are similar, the concentration of AS defects in A_2FeMoO_6 is finite and Fe and Mo ions are positioned in a random fashion. The relation between the saturation magnetization (M_S) and the concentration of AS defects has been widely investigated [201–203]. The influence of AS defects on the Curie temperature of double perovskites has also been studied [196, 204]. Based on the results of ab initio calculations, Saha-Dasgupta and Sarma [205] showed

that the presence of AS defects would result in a reduction of M_S and electron spin polarization at the Fermi level. Sanchez et al. [206] and Navarro et al. [207] identified the existence of AS defects within the grains as a cause for MR and M_S reduction. It is known that the TMR value can be influenced by the nature of GB's. Niebieskikwiat et al. [208] reported that when a material is weak in GB insulating barriers, the disorder of AS defects would results in TMR response deterioration. In contrast, for high resistivity values, the effect of AS defects is entirely masked by the effect of GB barriers, and the TMR is mainly determined by the strength of the GB barriers. They took a parameter $s\Delta^{1/2}$, as a quantitative measure of the strength of the GB barriers, where Δ and s is the energy and width of the GB barriers, respectively. The microscopic physical properties of the GB's such as connectivity, defects structure, and local density of states are included in s and Δ, and the strength of GB barriers ($s\Delta^{1/2}$) can be directly measured by the value of resistivity [208]. It has also been observed that in polycrystalline samples of Sr_2FeMoO_6, the TMR can be readily improved through an oxygen-induced enhancement of GB barriers [209]. According to the intergrain tunnelling model of half-metallic particles,

$$MR = [\rho(H = 0) - \rho(H)]/\rho(H = 0)$$

$$= 1/[\, f(\theta_{ij})] - 1, \qquad (1.6)$$

where $f(\theta_{ij}) = \cos^2(\theta_{ij}/2) + 2S/(2S+1)^2 \sin^2(\theta_{ij}/2)$, and θ_{ij} denotes the relative orientation of the magnetization of neighbouring grains [210]. For Sr_2FeMoO_6 with core spin S = 5/2, 76 % MR is predicted [211]. Consequently, the MR of polycrystalline Sr_2FeMoO_6 may be improved further by modifying the nature of the GB's. These studies shows that these theoretically considered half-metallic double perovskites with such a high Curie temperature definitely deserve for further studies.

1.4.2 Crystallographic structure

Double ordered perovskites ($A_2BB'O_6$) possess a modified perovskite structure (ABO_3), where the BO_6 and $B'O_6$ octahedra are alternatively arranged in two interleaving fcc sublattices. The A sites are occupied by alkaline or rare earth ions, while the B sites correspond to transition metal ions, as shown in Fig. 1.19. This cubic structure can be well described within the Fm3m space group. However, this structure is very often distorted as a consequence of steric pressure and temperature variations. As in the case of the manganites, the octahedra can undergo cooperative tilting distortions towards the most energetically favourable structure in response to the size mismatch between the A and B–B' cations, which brings about a symmetry reduction of the cubic cell. By means of the $a^0a^0c^-$ tilting in Glazer's notation, the cubic structure transforms into a tetragonal one. The pristine cubic cell is then denominated the pseudocubic cell, and the Fm3m space group no longer applies because several symmetries, such as the C_4 around the a-axis and the σ_h with respect to the (001) plane, are lost. Instead, the higher set of symmetry operations compatible with the evolution of the structural parameters, I4/m tetragonal space group is more favourable. As shown in Fig. 1.19, when the tetragonal distortion takes place, a new unit cell can be found. The actual unit cell is smaller than the pseudocubic cell, having the a and b-axis along the pseudocubic [110] and [1$^-$10] lattice vectors. As explained in Fig. 1.19, the lattice parameters of the tetragonal (tetra) and the pseudocubic (ps) cells are related as follows [212],

$$c = c_{tetra} = c_{ps}$$

$$a = b = a_{tetra} = a_{ps}/\sqrt{2}. \qquad (1.7)$$

Thus, the lattice parameter of the pseudocubic cell, a_{ps}, which is equal to c prior to the distortion, can be used to quantify the tetragonal distortion as:

$$t = 1 - \frac{a_{ps}}{c} = 1 - \frac{a\sqrt{2}}{c} \tag{1.8}$$

The double perovskite structure can also show a lower degree of symmetry, especially when very small cations are placed at the A site. This is the monoclinic $P2_1/n$ space group, which is generated by the $a^0b^-c^-$ tilting of the cubic structure. In this case, $a \neq b \neq c$ and $\beta \neq 90^\circ$. The crystallographic structure of a double perovskite can be anticipated beforehand on the basis of the mismatch between the length occupied by the A cation and the space left inside the oxygen interstices (see Fig. 1.19).

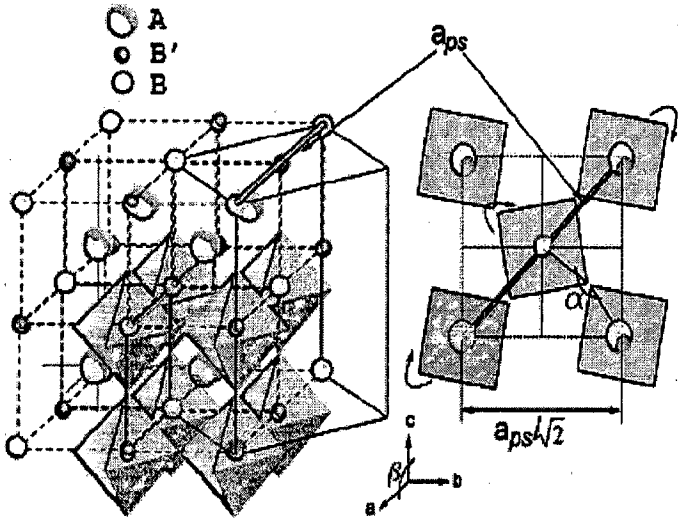

Figure 1.19: Left: structure of an ideal cubic double perovskite with chemical formula $A_2BB'O_6$. Oxygen atoms are located at the octahedra vertex and B and B' atoms are alternated. Solid lines depict the tetragonal unit cell. **Right:** top view of the tetragonal unit cell showing the $a^0a^0c^-$ tilting. The thick line is the lattice parameter of the cubic (left) and pseudo cubic (right) cell [212].

In order to measure such mismatch, we can define a tolerance factor analogously to the perovskites. The tolerance factor (f) in double perovskites, has to take into account the two possible distances B–O and B'–O, so

$$f = \frac{r_A + r_O}{\sqrt{2\left(\langle r_B \rangle + r_O\right)}} \tag{1.9}$$

$$f_{obs} = \frac{d_{A-O}}{\sqrt{2\langle d_{B-O} \rangle}} \tag{1.10}$$

where r_i is the effective ionic radius of the i atom (i = A, B, B', O) tabulated by Shannon, and d_{j-O} are the averaged atomic distances between the j atom (j = A, B, B') and the nearest oxygen neighbours that belong to the AO_{12}, BO_6 or $B'O_6$ polyhedra. It is noteworthy that in the A_2FeMoO_6 compounds, and following equation (1.9) and Shannon's tabulated values [213], the theoretical tolerance factors for the A = Ca ($P2_1/n$), Sr (I 4/m) and Ba (Fm3m) become respectively 0.9422, 0.9766, and 1.026, whereas the observed ones are 0.9522, 0.9984 and 1.000, respectively.

1.4.3 Interplay between electronic structure and magnetism

Ferromagnetism in high T_C double perovskites arises from the spins of the B and B' site ions. Given the unique aspects of Sr_2FeMoO_6 (SFMO) and its historical importance, we will discuss its electronic and magnetic properties. In SFMO, the $Fe^{3+}(3d^5)$ and $Mo^{5+}(4d^1)$ orbitals are at octahedral interstices formed by negative O^{2-} charges (see Fig. 1.19). Consequently, the ground state is a triplet, and the first excited state a doublet, namely the t_{2g} and e_g, respectively. They are separated by an energy gap Δ_{CEF} = 10 Dq ~ 1 eV [5], where Dq is the strength of the crystal electric field (CEF).

In the high spin configuration, the Fe^{3+} atom bears a S = 5/2 spin moment. This entails a strong exchange splitting Δ_{ex} ~ 3 eV between the spin up and spin down states, as has been shown in band structure calculations based on density functional theory (DFT) [5, 188]. The same result is obtained for Fe atoms having Re neighbours [214, 215], whereas in

the case of B = Cr (Cr^{3+}, S = 3/2) and B = Mn (Mn^{2+}, S = 5/2) compounds the Hund's intra-atomic exchange splitting amounts to about 2 eV [216, 217] and 4 eV [215], respectively. Therefore, in most of the cases $\Delta_{ex} \gg \Delta_{CEF}$ at the B site. On the contrary, the exchange coupling strength of the non-magnetic B' site is negligible, so that the splitting due to the CEF prevails. For instance, Δ_{ex} of the $Mo^{5+}(4d^1)$ manifold is nearly one order of magnitude smaller than in 3d atoms, as shown in Fig. 1.20.

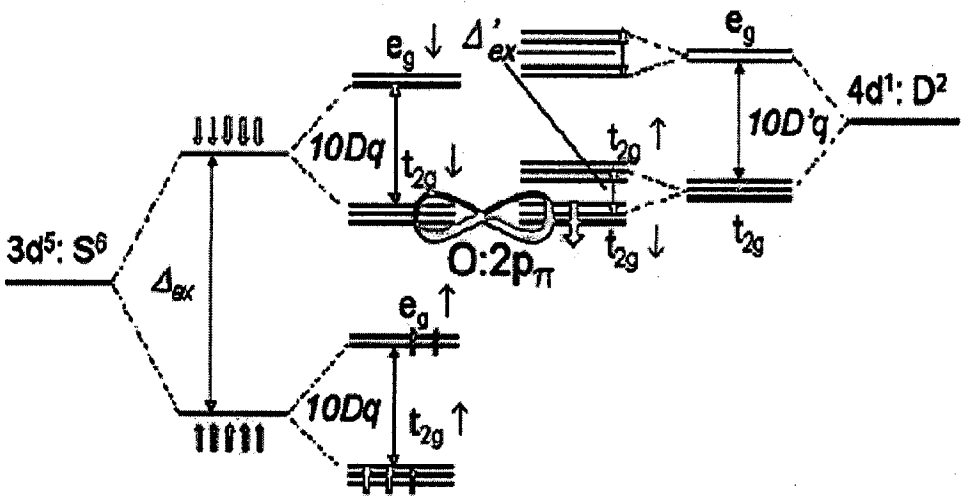

Figure 1.20: Energy levels schematic diagram of Sr_2FeMoO_6 as calculated by Kobayashi [5]. The Fermi level lies at the band formed exclusively by the Fe($t_{2g}\downarrow$)–O(2p)–Mo($t_{2g}\downarrow$) sub-band [5].

Within this ionic picture one might suppose that, in analogy with the manganites, the antiferromagnetic superexchange interaction between neighbouring B and B' sites having occupied and partially filled t_{2g} states [218], would bring about a ferrimagnetic arrangement of their 5 μ_B/f.u. and −1 μ_B/f.u. respective spin moments. However, this model does not support two of the main physical properties of SFMO. First, the highly spin polarized metallic state below Tc [5, 219] and the non-integer valence of Fe reported in Mossbauer and X-ray absorption experiments [220, 221–224]. Second, the high magnetic ordering temperature observed in SFMO is incompatible with a superexchange based magnetic

coupling within a localized picture of the d-type electrons. Although neutron powder diffraction, NMR and XMCD studies have shown experimental evidences of the ferrimagnetic arrangement [193, 225–227], the large Tc values would require a superexchange coupling between Mo and Fe at least comparable to that of Mn^{4+}–Mn^{4+} pairs in manganites (T_N = 120 K in $LaCaMnO_3$ [228]), which is not expected due to the non-magnetic nature of Mo. Furthermore, magnetic susceptibility measurements in the paramagnetic regime yielded a positive exchange Curie–Weiss constant, thus suggesting a magnetic interaction which is ferromagnetic in nature [229].

In the pioneer calculation of the density of states (DOS) by Kobayashi et al. using the DFT technique [5], the majority spin up channel exhibits a band gap of ~0.8 eV. The minority spin down Mo and Fe t_{2g} levels are partially filled, whereas the e_g levels are empty (see Fig. 1.21 (a)). The bands lying at the Fermi level exhibit a full negative spin polarization (P = −1), and are predominantly from Mo and Fe t_{2g}, with some small admixture of the O 2p states. The calculation yields the expected values for the Δ_{CEF}, and for the exchange splitting at the Fe atom, Δ_{ex}. However, the Mo $t_{2g}\downarrow$ is anomalously broadened and pushed down to the Fermi level. Considering a tight binding model containing d orbitals at the Fe and Mo sites and p orbitals at the oxygen sites, Sarma et al. [188] realized that this anomalous splitting could only be fitted with effective intra-atomic exchange strength (Δ'_{ex}), approximately 20 times larger than the expected one for a non-magnetic atom like Mo. The key ingredient for such an enhanced Δ'_{ex} is the presence of electron hopping interactions between Fe and Mo states with the same spin and orbital symmetry, which allow the Fe(t_{2g})–O(2p)–Mo(t_{2g}) hybridization and, as a consequence, the energy of Mo spin down states comes down and the spin up states goes further up. In agreement with the experimental observations [220–223, 230–236], the charge transfer due to the hopping mechanism produces a $Fe^{(3-\delta)+}$/$Mo^{(5+\delta)+}$ (or

$Fe^{(3-\delta)+}/Re^{(5+\delta)+}$) state with $0 < \delta < 1$, as originally proposed by Garcıa-Landa et al. [237]. In addition since the available Fe t_{2g} states are purely spin down polarized, the electron hopping can only occur when the localized Fe spin moments are ferromagnetically aligned. Thus, the hopping interaction reinforces the ferromagnetic arrangement of the nearest neighbouring Fe atoms, consequently increasing Tc. The antiferromagnetic coupling between Fe and Mo prior to the hopping interaction is crucial, otherwise the shift of the bare $t_{2g}\downarrow$ and $t_{2g}\uparrow$ Mo levels would have opposite direction, resulting in a reduced Tc [188].

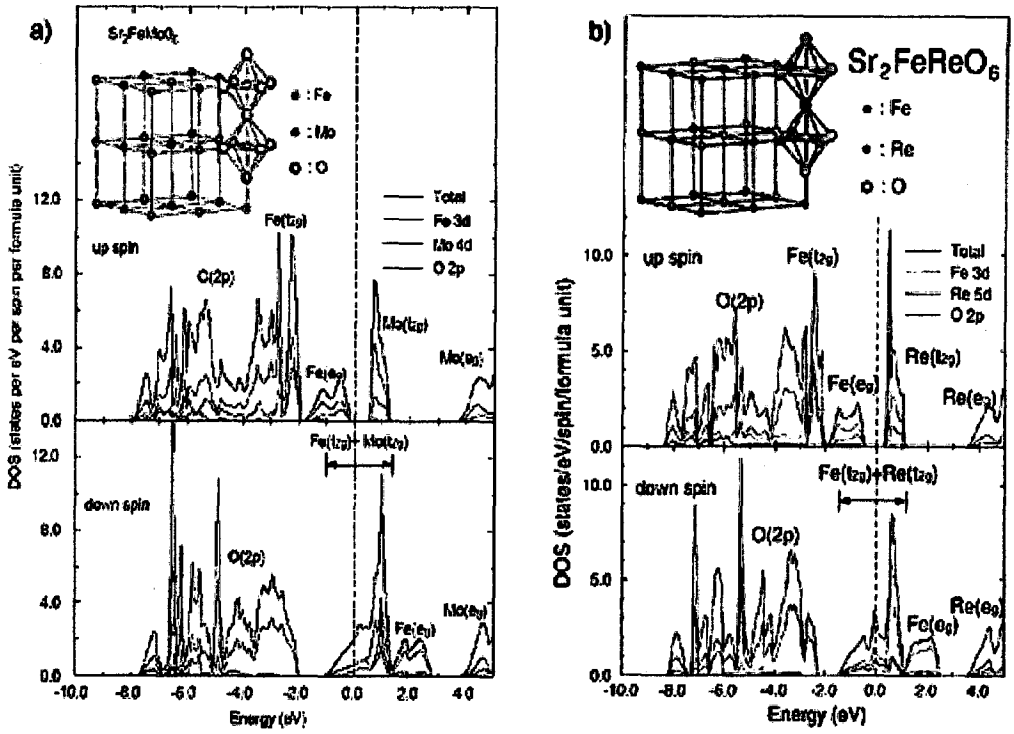

Figure 1.21: The density of states of Sr_2FeMoO_6 **(a)** and Sr_2FeReO_6 **(b)** as calculated by Kobayashi [5, 214]. The Fermi level lies at the band formed exclusively by the Fe($t_{2g}\downarrow$)–O(2p)–Mo/Re(t_{2g}) sub-band.

The compulsory requirement in Sarma's model is that the Fermi level must be located within the large energy gap in the electronic band structure of the B atom states. In the case of Sr_2FeMoO_6 [5] and Sr_2FeReO_6 [214], the gap is formed between the Fe $e_g\uparrow$ and $t_{2g}\downarrow$ bands, as shown in Fig. 1.21, whereas in the A_2CrWO_6 compound the gap is located between the Cr $t_{2g}\uparrow$ and $e_g\uparrow$ bands [216, 217]. The energy gain by exchange splitting due to the hopping

mechanism between non-magnetic atoms and high spin 3d metals was generalized by Kanamori et al. [238] for other transition metal compounds. On the other hand, the A_2FeWO_6 series (A = Ba, Sr) was found to be insulating and showed commensurate antiferromagnetic arrangements of the Fe moments [239], which might result from the strong Fe^{2+}/W^{6+} character of the valence state and the consequent absence of hopping electrons. As discussed by Fang et al. [240], the higher energy of the W 5d states as compared to the Mo 4d and Re 5d ones passivates the hopping mechanism. Then, the bare antiferromagnetic superexchange interaction stabilizes the low Neel temperature antiferromagnetism observed in Sr_2FeWO_6 compound. This has been recently illustrated using a simplified double exchange Hamiltonian in the $Sr_2FeMo_xW_{1-x}O_6$ series alloyed at the B' site [241], which shows an AFM insulator to FM metal transition when Mo content increases up to x ~ 0.3, in agreement with earlier experimental data [242]. Ferromagnetism was also found in A_2CrReO_6 [243, 244], A_2MnReO_6 [245, 246] and also in a variety of B-substituted compounds [247, 248].

1.4.4 Magnetoresistance studies

Due to the marked half-metallic character (P = −1) of the minority spin electrons lying at the $B(t_{2g}\downarrow)$–$O(2p)$–$B'(t_{2g}\downarrow)$ hybrid band, which are responsible for both the conduction mechanism and the ferromagnetic interaction, strong magnetoresistance effects are expected in the ferromagnetic phase of double perovskites. Hereafter we define the spin polarization, P, as:

$$P = \frac{N_\uparrow - N_\downarrow}{N_\uparrow + N_\downarrow} \tag{1.11}$$

where $N_{\uparrow(\downarrow)}$ is the density of occupied states per unit volume at the Fermi level in the majority (minority) spin sub-band. Thus, when one of the spin projected density of states is gapped at

the Fermi level, the value of spin polarization (P) is 1 (−1). In the case of many double perovskites such as $(Sr,Ca,Ba)_2FeMoO_6$, $(Sr,Ca,Ba)_2FeReO_6$, Sr_2CrReO_6 and $(Sr,Ca)_2CrWO_6$, the theoretically predicted spin polarization is P = −1, as shown in Fig. 1.21. Further characterization of the spin polarization by means of the tunnel magnetoresistance (TMR) response in tunnel junctions with electrodes based on double perovskites has been frustrated by the difficulty to grow flat double perovskite thin films with high quality. Bibes et al. [249] applied advanced lithography techniques to pattern nano-sized tunnel junctions over sub-micrometric continuous SFMO islands grown by pulse laser deposition. Their SFMO/$SrTiO_3$/Co tunnel junctions exhibited a TMR = 50 % at 4 K, which corresponds to P = −0.86 within Julliere's model [19]. High quality epitaxial SFMO with atomically smooth surfaces can be grown on $SrTiO_3$ (001) and (111) substrates, but the method calls for very high deposition temperatures (around 900 ^{0}C) and it is extremely sensitive to the deposition atmosphere (the oxygen partial pressure must be below 10^{-5} mbar) [250–252]. Therefore, most of the studies reported about the spin dependent transport in double perovskites were performed in polycrystalline ceramics. We will focus on the magnetoresistance properties of such specimens, which indeed raises the main interest of double perovskites for potential technological applications. The reason is that the magnetoresistive response concentrates at moderate magnetic fields (<1 kOe), which, together with the low manufacturing cost of double perovskites and their high Tc, makes these compounds very attractive for applications as magnetic field sensors and contactless potentiometers [253]. A number of irrefutable evidences point out that the MR in granular double perovskites arises from spin dependent scattering at the grain boundaries. The underlying conduction mechanism is electron tunnelling across insulating grain boundaries of the granular material. Double perovskites meet the two essential prerequisites for the TMR to occur in polycrystalline samples: $P \neq 0$ in

the bulk grain and insulating grain boundaries small enough to allow tunnelling between grains. The magnetoresistance associated with tunnelling processes across grain boundaries will be named hereafter intergrain tunnelling magnetoresistance (ITMR). According to the simplest TMR theory [19], this constitutes a higher resistance state compared to the low resistance state achieved above the saturation field, when all the magnetizations of neighbouring grains are parallel. Hence, under the application of an external magnetic field, the sample undergoes a resistivity decrease as the magnetization approaches saturation. In order to give a theoretical approach to the functional dependence of the ITMR on the magnetic field, people use Inoue and Maekawa's [38] model for the ITMR of a set of monodisperse magnetic particles in an insulating matrix. This model is an extension of Slonczewski's model for the conductivity of a tunnel junction, where the electrodes are forming an arbitrary angle [39]. Yin et al. [254] patterned a Wheatstone bridge straddling an artificial grain boundary in a SFMO epitaxial film grown on top of a $SrTiO_3$ bicrystal, which is shown in Fig. 1.22 (a). Only two branches of the bridge cross the grain boundary. The 1000 Å epitaxial film showed metallic conductivity similar to the one reported for the single crystal [219], as well as a low saturation magnetization and remanence that are attributable to a large concentration of antisite (AS) and anti phase boundary (APB). They showed a strong low field unbalance of the bridge when a magnetic field is applied, as displayed in Fig. 1.22 (b). In spite of the large defect concentration, the two remaining branches without grain boundary only exhibit a negligible linear magnetoresistance. This fact demonstrates that the bridge unbalance is due to the ITMR effect taking place at the intersections of the Wheatstone bridge with the grain boundary, and that the bulk AS and APB defects only plays a minor role in the magnetotransport properties. Another solid proof of the origin of the low field magnetoresistance (LFMR) is the appealing work by Niebieskikwiat et al. [208]. They

monitor in situ the oxidation state of the grain boundaries in several polycrystalline SFMO specimens, and change independently the AS level by means of different sintering temperatures.

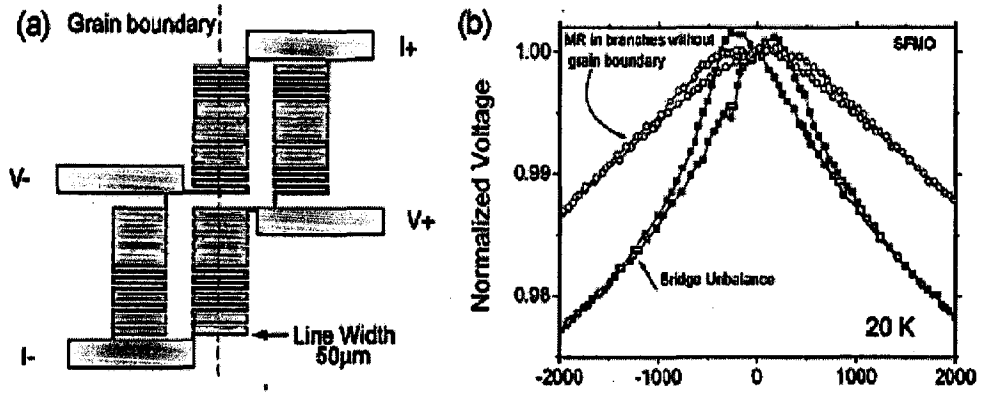

Figure 1.22: **(a)** Wheatstone bridge patterned in a 1000 Å SFMO epitaxial film [254]. The artificial grain boundary crosses only two branches of the bridge. **(b)** Comparison of the bridge unbalance (solid squares) and the magnetoresistance at the branches without grain boundary. The bridge unbalance is therefore due to the ITMR effect taking place at the grain boundary. Data is taken from [254].

They demonstrate how the LFMR is set by the grain boundary conductivity and nature rather than by the Fe/Mo disorder. Along this, Zhong et al. have reported very recently a method to tune the quality of the insulating grain boundaries based on a sonochemical reaction with water which alters the $SrMoO_4$ content at the grain surface [255].

Due to intensive research in the field of high T_C double perovskites since the publication by Kobayashi et al. of their half metallic nature in 1998 [5], several families of these compounds are ready to be explored as active elements in actual devices. Although we could not identify any double perovskite matching all the desirable industrial requirement (high room temperature MR, Tc well above room temperature, 100 % of spin polarization, low coercivity and thermal stability) but the extremely attractive possibilities of this theoretically considered half-metal (Sr_2FeMoO_6) with such a high Curie temperature

definitely deserve for further studies on room temperature MR and spin polarization in bulk and thin films.

1.5 APPLICATIONS OF MAGNETORESISTIVE MATERIALS

Half metallic CMR manganites and double perovskites are suitable for large potential applications based on their various physical and chemical properties [186, 256, 257]. The magnetic field sensitivity of the transport properties, the strong metal insulator transition at the Curie temperature, the half metallicity of the electronic bands, etc., are the properties of these systems that could be exploited in a variety of devices.

The magnetoresistance of these systems might be used in magnetic sensors, magnetoresistive read heads, magnetoresistive random access memory and magnetic switches. Magnetic sensors can be made from either thin films or single crystals and can be used to sense the magnitude of a magnetic field in one or several directions by choosing the right crystal form and demagnetizing factor. A good low field magnetoresistive response, however, can be obtained in manganite samples with a high density of grain boundaries and in tunnel spin valve structures. One of the first working devices of this kind was constructed by Sun et al. (1996) [166]. It consists of two layers of ferromagnetic $La_{0.67}Ca_{0.33}MnO_3$, separated by a $SrTiO_3$ spacer layer, and shows a resistance decrease by a factor of 2 in a field of less than 20 mT. The main disadvantage of devices based on grain-boundary magnetoresistance or on ferromagnetic tunneling junctions is that large magnetic field sensitivities are only achieved at temperatures below 200 K.

The large temperature coefficient of resistance (TCR, calculated as (1/R)(dR/dT)) just below the resistivity peak makes these CMR materials interesting for use in bolometric detectors [258, 259]. Bolometer is an instrument for detecting and measuring radiation.

Indeed, the TCR can reach 15 % per degree at 300 K [260], which is about one order of magnitude larger than that of VO_2, the material commonly used in bolometers.

Since the properties of the CMR materials are quite spectacular at reduced temperatures, i.e. below 100 K, so at these low temperatures, the combination of high-T_C superconducting cuprates thin films and CMR manganites could lead to Hybrid HTSC–CMR structures [261, 262]. These HTSC–CMR structures not only lead to potentially new spin-injection devices but also may serve as a useful medium for understanding some of the forefront theoretical ideas.

The magnetoresistive microphone is also an example of manganites applications. A small La-Ca-Mn-O type MR sensor, about 2mm × 4mm in size, is mounted on a plastic diaphragm. As a sound wave hits the diaphragm and makes it vibrate, the MR sensor moves in relation to the magnet that supplies a gradient field. The resulting change in the magnetic field intensity on the sensor causes a change in resistivity, increasing or decreasing the voltage by many millivolts even in the unamplified condition. The effect decreases with the distance from the sound source.

However, still there is no device based on double perovskites but the high Curie temperature and significant MR at room temperature of these compounds could offer advantageous performances with respect to existing solid state devices.

1.6 MOTIVATION OF THE PRESENT PROBLEM

A great deal of attention has been focused on the magnetoresistance (MR) properties of doped manganese perovskites with a formula $Ln_{1-x}A_xMnO_3$ (where Ln is a trivalent rare-earth element and A is a divalent alkaline earth element) [141] and double perovskites [5]. While the magnetoresistance in these materials can be of unprecedented magnitude, in most

of cases the large resistance changes are achieved only in a strong field in the Tesla range, thus severely limiting their practical utility. Reducing the field scale and increasing the operating temperature has been the goal of a number of research groups worldwide from the applications point of view. There has been progress in reducing the field scale by taking advantage of the high degree of spin polarization of the conduction electrons [5, 263]. Spin-polarised photoemission [263, 264] and scanning tunneling spectroscopy [265, 266] measurements both have provided direct evidence of half-metallic density of states in these materials.

One approach for reducing the field scale in these half metallic manganites and double perovskites has been to explore the extrinsic magnetoresistance properties of polycrystalline samples both in the form of bulk ceramics and thin films. Measurement on these samples have shown that the disruption in the crystalline order at the grain boundaries, by generating the artificial grain boundaries and tunneling barriers, is sufficient to induce a local spin disorder which results in a large low-field MR component, especially at low temperatures.

In the present thesis work, we also aimed to improve the large magnetoresistance at low value of fields and in wide range of temperature. The approach to produce the LFMR is to exploit the high degree of spin polarization of conduction electrons by modifying the grain boundaries through varying the particle size, by making the composite of the CMR manganites with a secondary phase like an insulating oxide and a polymer material and by generating the tunneling barriers of $SrMoO_4$ impurity phase in Sr_2FeMoO_6 double perovskite by modifying the synthesis conditions.

We modified the gain boundaries of $La_{0.7}Sr_{0.3}MnO_3$ (LSMO) and $La_{0.67}Ca_{0.33}MnO_3$ (LCMO) samples by varying the particle size. The samples were prepared by sol gel method

and sintered at different temperatures ranging from 600-1000 ^{0}C to produce the particles of different sizes. The enhancement in magnetoresistance (MR) at T<Tc is observed on decreasing the sintering temperature as well as particle size. The enhancement in magnetoresistance at low field (H~ 3 kOe) is observed by making the various composites of CMR manganites (LSMO, LCMO) with other insulating oxides such as NiO, TiO_2, Co_3O_4 and polymer (PPS). It has been found that the second phase material (NiO, TiO_2, etc.) sits on the grain boundaries or on the surfaces of CMR grains and produces the spin disorder by spin polarised tunneling through grain boundary barriers of second phase material and help in the increment of low field magnetoresistance.

We also generated the inbuilt tunneling barriers of $SrMoO_4$ phase in the matrix of Sr_2FeMoO_6 double perovskite by modifying the synthesis conditions and a significant enhancement in low field magnetoresistance is observed. Furthermore, the effect of Ni doping at Fe site on magnetotransport properties of Sr_2FeMoO_6 is also studied, which results the enhancement in Curie temperature.

REFERENCES

1. Rao C N R & Raveau B, "Transition metal oxides: Structure, properties and synthesis of ceramic oxides", John Willey and Sons Inc., (2 ed) (1998).
2. Cross L E, "Relaxor ferroelectrics", Ferroelectrics, **76,** 241 (1987).
3. Tinkham M, "Introduction to superconductivity", McGraw Hill Book Company, (1996).
4. Tokura Y, "Colossal magnetoresistive oxides", Gordon and Breach Publishers, London, (2000).
5. Kobayashi K I, Kimura T, Sawada H, Terakura K & Tokura Y, "Room temperature magnetoresistance in an oxide material with an ordered double perovskite structure", Nature (London), **395,** 677 (1998).
6. IBM websites: http://www.almaden.ibm.com/st/projects/magneto/giantmr/; http://www.research.ibm.com/research/demos/gmr/cyberdemo1.html
7. Speliotis D E, "Magnetic recording beyond the first 100 Years", J. Magn. Magn. Mater., **193,** 29 (1999).
8. Hong J, Kane J, Hashimoto J, Yamagishi M, Noma K & Kanai H, "Spin-valve head with specularly reflective oxide layers for over 100 Gb/in^{2}", Presented at 12th Annual Magnetic Recording Conf (TMRC 2001), University of Minnesota, Minneapolis, August 20–22, (2001).
9. http://www.hitachigst.com/hdd/research/recording_head/pr/index.html; Wood R, "The feasibility of magnetic recording at 1 terabit per square inch", IEEE Trans. Mag., **36,** 36 (2000).

10. Moser A, Takano K, Margulies D T, Albrecht M, Sonobe Y, Ikeda Y, Sun S & Fullerton E E, "Magnetic recording: advancing into the future", J Phys D: Appl Phys, **35** R157 (2002).

11. Pippard A B, "Magnetoresistance", Cambridge University Press Cambridge U.K. (1984); Pippard A B, "Magnetoresistance in metals", Cambridge University Press Cambridge U. K. (1989).

12. Fert A & Piraux, "Magnetic nanowires", J. Magn. Mag. Mater., **200**, 338 (1999).

13. Campbell I A & Fert A, "Ferromagnetic materials", Vol. 3, ed. by Wohlfarth E P, (Amesterdam: North-Holland) p. 751 (1982).

14. Li X W, Gupta A, Xiao G & Gong G Q, "Low-field magnetoresistive properties of polycrystalline and epitaxial perovskite manganite films", Appl. Phys. Lett., **71**, 1124 (1997).

15. Ziese M & Sena S P, "Anisotropic magnetoresistance of thin $La_{0.7}Ca_{0.3}MnO_3$ films", J. Phys.: Condens Matter., **10**, 2727 (1998).

16. O'Donnell J, Eckstein J N & Rzchowski M S, "Temperature and magnetic field dependent transport anisotropies in $La_{0.7}Ca_{0.3}MnO_3$ films", Appl. Phys. Lett., **76**, 218 (2000).

17. Tsymbal Y, Mryasov O N & Leclair P R, "Spin-dependent tunnelling in magnetic tunnel junctions", J. Phys.: Condens Matter, **15**, R109 (2003).

18. Meservay R & Tedrow P M, "Spin-polarized electron tunneling", Phys. Rep., **238**, 173 (1994).

19. Julliere M, "Tunneling between ferromagnetic films", Phys. Lett. A, **54**, 225 (1975).

20. Miyazaki T & Tezuka N J, "Giant magnetic tunneling effect in $Fe/Al_2O_3/Fe$ junction", J. Magn. Magn. Mater., **139**, L231 (1995).

21. Moodera J S, Nowak J & van de Veerdonk R J M, "Interface magnetism and spin wave scattering in ferromagnet-insulator-ferromagnet tunnel junctions", Phys. Rev. Lett., **80**, 2941 (1998).

22. Sun J Z, Gallagher W J, Duncombe P R, Krusin-Elbaum L, Altoman R A, Gupta A, Lu Y, Gong G Q & Xiao G, "Observation of large low-field magnetoresistance in trilayer perpendicular transport devices made using doped manganate perovskites", Appl. Phys. Lett., **69**, 3266 (1999).

23. Lu Y, Li W, Gong G Q, Xiao G, Gupta A, Lecoeur P, Sun J Z, Wang Y Y & Dravid V P, "Large magneto-tunneling effect at low magnetic fields in micrometer-scale epitaxial $La_{0.67}Sr_{0.33}MnO_3$ tunnel junctions", Phys. Rev. B, **54**, R8357 (1996).

24. Li X W, Lu Y, Gong G Q, Xiao G, Gupta A, Leocoeur P, Sun J Z, Wang Y Y & Dravid V P, "Epitaxial $La_{0.67}Sr_{0.33}MnO_3$ magnetic tunnel junctions ", J. Appl. Phys., **81**, 5509 (1997).

25. Sun J Z, Krusin-Elbaum, Duncombe P R, Gupta A & Laibowitz R B, "Temperature dependent, non-ohmic magnetoresistance in doped perovskite manganate trilayer junctions", Appl. Phys. Lett., **70**, 1769 (1997).

26. Sun J Z, "Thin-film trilayer manganate junctions", Phil Trans. R. Soc. A, **356**, 1663 (1998).

27. Sun J Z, Abraham, Roche K & Parkin S S P, "Temperature and bias dependence of magnetoresistance in doped manganite thin film trilayer junctions", Appl. Phys. Lett., **73**, 1008 (1998).

28. Viret M, Drouet M, Nassar J, Contour J P, Fermon C & Fert A, "Low-field colossal magnetoresistance in manganite tunnel spin valves", Europhys. Lett., **39**, 545 (1997).

29. Moon-Ho J, Mathur N D, Todd N K & Blamire M G, "Very large magnetoresistance and coherent switching in half-metallic manganite tunnel junctions", Phys. Rev. B, **61**, R14905 (2000).

30. Moon-Ho J, Mathur N D, Evetts J E & Blamire M G, "Coherent magnetic reversal in half-metallic manganite tunnel junctions", Appl. Phys. Lett., **77**, 3803 (2000).

31. Obata T, Manako T, Shimakawa Y & Kubo Y, "Tunneling magnetoresistance at up to 270 K in $La_{0.8}Sr_{0.2}MnO_3/SrTiO_3/La_{0.8}Sr_{0.2}MnO_3$ junctions with 1.6-nm-thick barriers", Appl. Phys. Lett., **74**, 290 (1999).

32. Yin H Q, Zhou J S & Goodenough J B, "Near-room-temperature tunneling magnetoresistance in a trilayer $La_{0.67}Sr_{0.33}MnO_3/La_{0.85}Sr_{0.15}MnO_3/La_{0.67}Sr_{0.33}MnO_3$ device", Appl. Phys. Lett., **77**, 714 (2000).

33. Noh J S, Nath T K, Eom C B, Sun J Z, Tian W & Pan, "Magnetotransport in manganite trilayer junctions grown by 90° off-axis sputtering", Appl. Phys. Lett., **79**, 233 (2001).

34. Bowen M, Bibes M, Barthelwmy A, Contour J P, Anane A, Lemaitre Y & Fert A, "Nearly total spin polarization in $La_{2/3}Sr_{1/3}MnO_3$ from tunneling experiments", Appl. Phys. Lett., **82**, 233 (2003).

35. Paillous F, Imhoff D, Sikora T, Barthelemy A, Maurice J L, Contour J P, Colleix C & Fert A, "Nanoscale analysis of a $SrTiO_3/La_{2/3}Sr_{1/3}MnO_3$ interface", Phys. Rev. B, **66**, 014417 (2002).

36. Budhani R C, Pant P, Rakshit R K, Senapati K, Mandal S, Pandey N K & Kumar J, "Magnetotransport in epitaxial films of degenerate semiconductor $Zn_{1-x}Co_xO$", J. Phys.: Conden. Matter, **17**, 75 (2005).

37. Julliere M, "Tunneling between ferromagnetic films", Phys. Lett. A, **54**, 225 (1975).

38. Inoue J & Maekawa S, "Theory of tunneling magnetoresistance in granular magnetic films", Phys. Rev. B, **53**, R11927 (1996).

39. Slonczewski J C, "Conductance and exchange coupling of two ferromagnets separated by a tunneling barrier", Phys. Rev. B, **39**, 6995 (1989).

40. Grunberg P, Schreiber R, Pang Y, Brodsky M B & Sowers H, "Layered magnetic structures: Evidence for antiferromagnetic coupling of Fe Layers across Cr interlayers", Phys. Rev. Lett., **57**, 2442 (1986).

41. Salamon M B, Sinha S, Rhyne J J, Cunningham J E, Erwin R W, Borchers J & Flynn C P, "Long-range incommensurate magnetic order in a Dy-Y multilayer", Phys. Rev. Lett., **56**, 259 (1986); Maykrzak C F, Cable J W, Kwo J, Hong M, Mc Whan D B, Yafet Y, Waszczak J V & Vettier C, "Observation of a magnetic antiphase domain structure with long-range order in a synthetic Gd-Y superlattice", Phys. Rev. Lett., **56**, 2700 (1986).

42. Hartmann U, "Magnetic multilayer and giant magnetoresistance: Fundamentals and industrial applications" (Springer, Berlin), p. 62 (2000).

43. Baibich M N, Broto J M, Fert A, Nguyen Van Dau F & Petroff F, "Giant magnetoresistance of (001)Fe/(001)Cr magnetic superlattices", Phys. Rev. Lett., **61**, 2472 (1988).

44. H. Yamamto & T. Shinjo, "Magnetoresistance of multilayes", IEEE Trans. J. Magn. Jap., **7**, 674 (1992).

45. Parkin S S P, More N & Roche K P, "Oscillations in exchange coupling and magnetoresistance in metallic superlattice structures: Co/Ru, Co/Cr, and Fe/Cr", Phys. Rev. Lett., **64**, 2304 (1990).

46. Bruno P & Chappert C, "Oscillatory coupling between ferromagnetic layers separated by a nonmagnetic metal spacer", Phys. Rev. Lett., **67**, 1602 (1991).

47. Edwards D M, Erickson R P, Mathon J, Muniz R B & Villeret M, "Spin current and exchange coupling in magnetic multilayers", Matrials Science & Eng. B, **31**, 25 (1995).

48. Wang S X & Taratorin A M, "Magnetic Information Storage Technology", (Academic press, New York), p.166 (1999).

49. Dieny B, Speriosu V S, Parkin S S P, Gurney D A, Wilhoit D R & Mauri D, "Giant magnetoresistive in soft ferromagnetic multilayers", Phys. Rev. B, **43**, 1297 (1991).

50. Barthelemy A, Fert V, Baibich M N, Hadjoudj S & Petroff F, "Magnetic and transport properties of Fe/Cr superlattices", J. Appl. Phys., **67**, 5908 (1990); Haas C, "Spin-disorder scattering and magnetoresistance of magnetic semiconductors", Phys. Rev., **168**, 531 (1968); Binasch G, Grunberg P et al, "Enhanced magnetoresistance in layered magnetic structures with antiferromagnetic interlayer exchange", Phys. Rev. B, **39**, 4828 (1989).

51. Hwang H Y, Cheong S W, Ong N P & Batlogg B, "Spin-polarized intergrain tunneling in $La_{2/3}Sr_{1/3}MnO_3$", Phys. Rev. Lett., **77**, 2041 (1996).

52. Belleson J & Grochowski, "The era of giant magnetoresistive heads"; http://www.storage.ibm.com/hdd/technolo/gmr/fig8.gif.

53. White R L, "Giant magnetoresistance: a primer", IEEE Trans. Mag., **28**, 2482 (1992).

54. Jin S, Teifel T H, McCormack M, Fastnacht R A, Ramesh R & Chen L H, "Thousand fold change in resistivity in magnetoresistive La-Ca-Mn-O films", Science, **264**, 413 (1994).

55. Von Helmolt R, Wecker J, Holzapfel B, Schultz L & Samwer K, "Giant negative magnetoresistance in perovskitelike $La_{2/3}Ba_{1/3}MnO_x$ ferromagnetic films", Phys. Rev. Lett., **71,** 2331 (1993).

56. Chahara K, Ohno T, Kasai M & Kozond Y, "Magnetoresistance in magnetic manganese oxide with intrinsic antiferromagnetic spin structure", Appl. Phys. Lett., **63,** 1990 (1993).

57. Chien C L, Xiao J O, Jiang J S, "Giant negative magnetoresistance in granular ferromagnetic systems", J. Appl. Phys., **73,** 5309, (1993); Parkin S S P, Badhra R, Roche K P, "Oscillatory magnetic exchange coupling through thin copper layers", Phys. Rev. Lett., **66,** 2152 (1991).

58. Fullerton E E, Conover M J, Mattson J E, Sowers C H & Bader S D, "150% magnetoresistance in sputtered Fe/Cr(100) superlattices", Appl. Phys. Lett., **63,** 1699 (1993).

59. Jonker G H & Van Santen J H, "Ferromagnetic compounds of manganese with perovskite structure", Physica, **16,** 337 (1950).

60. Jonker G H, "Magnetic compounds with perovskite structure IV: Conducting and non-conducting compounds", Physica, **22,** 707 (1956).

61. Volger J, "Further experimental investigations on some ferromagnetic oxidic compounds of manganese with perovskite structure", Physica, **20,** 49 (1954).

62. Jonker G H, "Semiconducting properties of mixed crystals with perovskite structure", Physica, **20,** 1118 (1954).

63. Wollan E O & Koehler W C, "Neutron diffraction study of the magnetic properties of the series of perovskite-type compounds $[(1-x)La, xCa]MnO_3$", Phys. Rev., **100,** 545 (1955).

64. Searle C W & Wang S T, "Studies of the ionic ferromagnet (LaPb)MnO_3: III Ferromagnetic resonance studies", Can. J. Phys., **47**, 2703 (1969).

65. Jirak Z, Vratislav S & Zajicek J, "The Magnetic Structure of $Pr_{0.9}Ca_{0.1}MnO_3$", Phys. Stat. Sol., **52**, K39 (1979).

66. Pollert E, Krupicka S & Kuzmicova E, "Structural study of $Pr_{1-x}Ca_xMnO_3$ and $Y_{1-x}Ca_xMnO_3$ perovskites", J. Phys. Chem. Solids, **43**, 1137 (1982).

67. Kusters R M, Singleton D A, Keen D A, McGreevy R & Hayes W, "Magnetoresistance measurements on the magnetic semiconductor $Nd_{0.5}Pb_{0.5}MnO_3$", Physica B, **155**, 362 (1989).

68. Ju H L, Kwon C, Li Q, Green R L & Venkatesan T, "Giant magnetoresistance in $La_{1-x}Sr_xMnO_z$ films near room temperature", Appl. Phys. Lett., **65**, 2108 (1994).

69. Parkin S S P, "Giant magnetoresistance in magnetic nanostructures", Annu. Rev. Mater. Sci., **25**, 357 (1995).

70. Xiong G C, Li Q, Ju H L, Bhagat S M, Lofland S E, Green R L & Venkatesan T, "Giant magnetoresistive memory effect in $Nd_{0.7}Sr_{0.3}MnO_z$ films", Appl. Phys. Lett., **67**, 3031 (1995).

71. Jahn H A & Teller E, "Stability of polyatomic molecules in degenerate electronic states", Proc. Roy. Soc. A, **161**, 220 (1937).

72. Urushibara A, Moritomo Y, Arima T, Asamitsu A, Kido G & Tokura Y, "Insulator-metal transition and giant magnetoresistance in $La_{1-x}Sr_xMnO_3$", Phys. Rev. B, **51**, 14103 (1995).

73. Tokura Y, Urushibara A, Moritomo Y, Arima T, Asamitsu A, Kido G & Furukawa N, "Giant Magnetotransport Phenomena in Filling-Controlled Kondo Lattice System: $La_{1-x}Sr_xMnO_3$", J. Phys. Soc. Japan, **63**, 3931 (1994).

74. Asamitsu A, Moritomo Y, Tomioka Y, Arima T & Tokura Y, "A structural phase transition induced by an external magnetic field", Nature, **373,** 407 (1995).

75. Kuwahara H, Tomioka Y, Asamitsu A, Moritomo Y & Tokura Y, "A first-order phase transition induced by a magnetic field", Science, **270,** 961 (1995).

76. Mahendiran R, Raychaudhuri A K, Chainani A, Sarma D D & Roy S B, "Large magnetoresistance in $La_{1-x}Sr_xMnO_3$ and its dependence on magnetization", Appl. Phys. Lett., **66,** 233 (1995).

77. Tokura Y, Kuwahara H, Moritomo Y, Tomioka Y & Asamitsu A, "Competing instabilities and metastable states in $(Nd,Sm)_{1/2}Sr_{1/2}MnO_3$", Phys. Rev. Lett., **76,** 3184 (1996).

78. Caignaert V, Maignan A & Raveau B, "Up to 50000 per cent resistance variation in magnetoresistive polycrystalline perovskites $Ln_{2/3}Sr_{1/3}MnO_3$ (Ln=Nd; Sm)", Solid State Commun., **95,** 357 (1995).

79. Tomioka Y, Asamitsu A, Moritomo Y, Kuwahara H & Tokura Y, "Collapse of a charge-ordered state under a magnetic field in $Pr_{1/2}Sr_{1/2}MnO_3$", Phys. Rev. Lett., **74,** 5108 (1955).

80. Raveau B, Maignan A & Caignaert V, "Spectacular giant magnetoresistance effects in the polycrystalline perovskite $Pr_{0.7}Sr_{0.05}Ca_{0.25}MnO_{3-\delta}$", J. Solid State Chem., **117,** 424 (1995).

81. Maignan A, Simon C, Caignaert V & Raveau B, "Magnetic field dependence of the resistance and magnetization of the giant magnetoresistive $Pr_{0.7}Ca_{0.25}Sr_{0.05}MnO_3$ polycrystalline sample", J. Magn. Magn. Mater., **152,** L5 (1996).

82. Schiffer P, Ramirez A P, Bao W & Cheong S W, "Low temperature magnetoresistance and the magnetic phase diagram of $La_{1-x}Ca_xMnO_3$", Phys. Rev. Lett., **75,** 3336 (1995).

83. Gong G Q, Canedy C, Xiao G, Sun J Z, Gupta A & Gallagher W J, "Colossal magnetoresistance of 1000000-fold magnitude achieved in the antiferromagnetic phase of $La_{1-x}Ca_xMnO_3$", Appl. Phys. Lett., **67,** 1783 (1995); Gong G Q, Gupta A, Xiao G, Lecoeur P & McGuire T R, "Perovskite oxide superlattices: Magnetotransport and magnetic properties", Phys. Rev. B, **54,** R3742 (1996).

84. Ramirez A P, Schiffer P, Cheong S W, Bao W, Palstra T T M, Gammel P L, Bishop D J & Zegarski B, "Thermodynamic and electron diffraction signatures of charge and spin ordering in $La_{1-x}Ca_xMnO_3$", Phys. Rev. Lett., **76,** 3188 (1996).

85. Bao W, Axe J D, Chen C H & Cheong S W, "Impact of charge ordering on magnetic correlations in perovskite $(Bi,Ca)MnO_3$", Phys. Rev. Lett., **78,** 543 (1997).

86. Chen C H & Cheong S W, "Commensurate to incommensurate charge ordering and its real-space images in $La_{0.5}Ca_{0.5}MnO_3$", Phys. Rev. Lett., **76,** 4042 (1996).

87. Cheong S W & Hwang H Y, "Colossal magnetoresistive oxides monographs in condensed matter science", Ch. 7 (ed. by Tokura Y) (Gordon & Breach, Reading, UK) (2000).

88. Xiao G, McNiff E J Jr, Gong G Q, Gupta A, Canedy C L & Sun J Z, "Magnetic-field-induced multiple electronic states in $La_{0.5}Ca_{0.5}MnO_{3+\delta}$", Phys. Rev. B, **54,** 6073 (1996).

89. Tomioka Y, Asamitsu A, Kuwahara H, Moritomo Y & Tokura Y, "Magnetic-field-induced metal-insulator phenomena in $Pr_{1-x}Ca_xMnO_3$ with controlled charge-ordering", Phys. Rev. B, **53,** R1689 (1996).

90. Barratt J, Lees M R, Balakrishnan G & Paul D M, "Insulator–metal transitions in $Pr_{0.7}Ca_{0.3}MnO_3$ induced by a magnetic field", Appl. Phys. Lett., **68,** 424 (1996).

91. Yoshizawa H, Kawano H, Tomioka Y & Tokura Y, "Neutron-diffraction study of the magnetic-field-induced metal-insulator transition in $Pr_{0.7}Ca_{0.3}MnO_3$", Phys. Rev. B, **52,** R13145 (1995).

92. Yoshizawa H, Kawano H, Tomioka Y & Tokura Y, "Magnetic-field-induced metal-insulator transition in $Pr_{0.7}Ca_{0.3}MnO_3$", J. Phys. Soc. Japan, **65,** 1043 (1996).

93. Orbach R & Stapleton H J, "Electron spin-lattice relaxation", Chapter 2 of "Electron paramagnetic resonance" S Geschwind (ed) Plenum Press New York (1972).

94. Kanamori J, "Crystal distortion in magnetic compounds", J. Appl. Phys. Suppl., **31,** 14S (1960).

95. Millis A J, Littlewood P B & Shraiman B I, "Double exchange alone does not explain the resistivity of $La_{1-x}Sr_xMnO_3$", Phys. Rev. Lett., **74,** 5144 (1995).

96. Roder H, Zang J & Bishop A R, "Lattice effects in the colossal magnetoresistance manganites", Phys. Rev. Lett.,**76,** 1536 (1996).

97. Millis A J, "Lattice effects in magnetoresistive manganese perovskites", Nature, **392,** 147 (1998).

98. Cahn R W, "Materials science: Rapid alloy assessment", Nature, **410,** 643 (2001).

99. van den Brink J, Khaliullin G & Khomskii D I, cond-matt/0206053 "Colossal Magnetoresistance" T Chatterji (ed) Kulwer Academic Publishers Dordrecht Netherlands (2004).

100. Rao C N R, Arulraj A, Cheetham A K & Raveau B, "Charge ordering in the rare earth manganates: the experimental situation", J. Phys.: Condens. Matter, **12,** R83 (2000).

101. Goodenough J B, "Theory of the role of covalence in the perovskite-type manganites [La, M(II)]MnO_3", Phys. Rev., **100,** 564 (1955).

102. Zener C, "Interaction between the d shells in the transition metals", Phys. Rev., **81,** 440 (1951).

103. Anderson P W & Hasegawa H, "Considerations on double exchange", Phys. Rev., **100,** 675 (1955).

104. de Gennes P G, "Effects of double exchange in magnetic crystals", Phys. Rev., **118,** 141 (1960).

105. Alexandro A S & Bratkovsky A M, "Carrier density collapse and colossal magnetoresistance in doped manganites", Phys. Rev. Lett., **82,** 141 (1999).

106. Wollan E O & Koehler W C, "Neutron diffraction study of the magnetic properties of the series of perovskite-type compounds [(1-x)La, xCa]MnO_3", Phys. Rev., **100,** 545 (1955).

107. Kubo K & Ohata N, "A Quantum Theory of Double Exchange", J. Phys. Soc. Jap., **33,** 21 (1972).

108. Millis A J, Shraiman B I & Mueller R, "Dynamic Jahn-Teller effect and colossal magnetoresistance in $La_{1-x}Sr_xMnO_3$", Phys. Rev. Lett., **77,** 175 (1996).

109. Hotta T, Malvezzi A & Dagotto E, "Charge-orbital ordering and phase separation in the two-orbital model for manganites: Roles of Jahn-Teller phononic and Coulombic interactions", Phys. Rev. B, **62,** 9432 (2000).

110. Goodenough J B, "Electronic structure of CMR manganites", J. Appl. Phys., **81,** 5330 (1997).

111. Alexandrov A S & Bratkowsky A M, "Carrier density collapse and colossal magnetoresistance in doped manganites", Phys. Rev. Lett., **82,**141 (1999).

112. Nagaev E L, "Lanthanum manganites and other giant-magnetoresistance magnetic conductors", Usp. Fiz. Nauk., **166,** 833 (1996).

113. Ramakrishnan T V, Krishnamurthy H R, Hassan S R & Pai G V, "Theory of insulator metal transition and colossal magnetoresistance in doped manganites", Phys. Rev. Lett., **92,** 157203 (2004).

114. Gregg J F, Petej I, Jouguelet E & Dennis C, "Spin electronics: a review", J. Phys. D: Appl. Phys., **35,** R121 (2002).

115. Sathpathy A, Popovic Z S & Vukajlovic F R, "Electronic structure of the perovskite oxides: $La_{1-x}Ca_xMnO_3$", Phys. Rev. Lett., **76,** 960 (1996).

116. Pickett W E & Singh D J, "Electronic structure and half-metallic transport in the $La_{1-x}Ca_xMnO_3$ system", Phys. Rev. B, **53,** 1146 (1996).

117. Zhuang M, Zhang W & Ming N, "Spin-disorder-scattering-induced spectral-weight transfer and pseudogap in doped perovskite $LaMnO_3$", Phys. Rev. B, **56,** 14547 (1997).

118. Singh D J & Pickett W E, "Pseudogaps, Jahn-Teller distortions, and magnetic order in manganite perovskites", Phys. Rev. B, **57,** 88 (1998).

119. Kuwahara H, Tomioka Y, Asamitsu A M & Tokura Y, "A first-order phase transition induced by a magnetic field", Science, **270,** 961 (1995).

120. Tokura Y, Tomioka Y, Kuwahara H, Asamitsu A, Morimoto Y & Kasai M, "Origins of colossal magnetoresistance in perovskite-type manganese oxides", J. Appl. Phys., **79,** 5288 (1996).

121. Schiffer P, Ramirez A P, Bao A W P & Cheong S W, "Low temperature magnetoresistance and the magnetic phase diagram of $La_{1-x}Ca_xMnO_3$", Phys. Rev. Lett., **75,** 3336 (1995).

122. Radaelli P G, Marezio M, Hwang H Y, Cheong S W & Batlogg B, "Charge localization by static and dynamic distortions of the MnO_6 octahedra in perovskite manganites", Phys. Rev. B, **54,** 8992 (1996).

123. Ahn K H & Millis A J, "Interplay of charge and orbital ordering in manganese perovskites", Phys. Rev. B, **58,** 3697 (1998).

124. Cheong S W & Hwang H Y, "Ferromagnetism vs charge/orbital ordering in mixed-valent manganites, in "Colossal Magnetoresitance Oxides", Y Tokura (ed.) Gordon and Breach London (2000).

125. Cheong S W, Hwang H Y, Chen C H, Batlogg B, Rupp Jr L W & Carter S A, "Charge-ordered states in $(La,Sr)_2NiO_4$ for hole concentrations n_h=1/3 and 1/2", Phys. Rev. B, **49**, 7088 (1994).

126. Chen C H & Cheong S W, "Commensurate to incommensurate charge ordering and its real-space images in $La_{0.5}Ca_{0.5}MnO_3$", Phys. Rev. Lett., **76**, 4042 (1996).

127. Radaelli P G, Cox D E, Marezio M & Cheong S W, "Charge, orbital, and magnetic ordering in $La_{0.5}Ca_{0.5}MnO_3$", Phys. Rev. B, **55**, 3015 (1997).

128. Mori S, Chen C H & Cheong S W, "Pairing of charge-ordered stripes in $(La,Ca)MnO_3$", Nature, **392**, 473 (1998).

129. Kuwahara H, Tomioka Y, Asamitsu A M & Tokura Y, "A first-order phase transition induced by a magnetic field", Science, **270**, 961 (1995).

130. Moritomo Y, Kiwahara H, Tomioka Y & Tokura Y, "Pressure effects on charge-ordering transitions in Perovskite manganites", Phys. Rev. B, **55**, 7549 (1997).

131. Kiryukhin V, Casa D, Hill J P, Keimer B, Vigliante A, Tomioka Y & Tokura Y, "An X-ray-induced insulator-metal transition in a magnetoresistive manganites", Nature, **386**, 813 (1997).

132. Asamitsu A, Tomioka Y, Kuwahara H & Tokura Y, "Current switching of resistive states in magnetoresistive manganites", Nature, **388**, 50 (1997).

133. Ponnambalam V, Parashar S, Raju A R & Rao C N R, "Electric-field-induced insulator–metal transitions in thin films of charge-ordered rare-earth manganates", Appl. Phys. Lett., **74**, 206 (1999); Parashar S, Ebenso E E, Raju A R and Rao C N R, "Insulator–metal transitions induced by electric and magnetic fields in thin films of charge-ordered $Pr_{1-x}Ca_xMnO_3$", Solid State Commun., **114**, 295 (2000).

134. Miyano K, Tanaka T, Tomioka Y & Tokura Y, "Photo-induced insulator-to-metal transition in a perovskite manganite", Phys. Rev. Lett., **78**, 4257 (1997).

135. Kawano H, Kajimoto R, Yoshizawa H, Tomioka Y, Kuwahara H & Tokura Y, "Magnetic ordering and relation to the metal-insulator transition in $Pr_{1-x}Sr_xMnO_3$ and $Nd_{1-x}Sr_xMnO_3$ with x = 1/2", Phys. Rev. Lett., **78**, 4253 (1997).

136. Goff R J & Attfield J P, "Charge ordering in half-doped manganites", Phys. Rev. B, **70**, 140404(R) (2004).

137. Knizek K, Jirak Z, Pollert E & Zounova F, "Structure and magnetic properties of $Pr_{1-x}Sr_xMnO_3$ perovskites", J. Solid State Chem., **100**, 292 (1992).

138. Kumar N & Rao C N R, "The nature of charge ordering in rare earth manganates and its strong dependence on the size of the a-site cations", J. Solid State Chem., **129**, 363 (1997).

139. Raveau B, Hervieu M, Maignan A & Martin C, "The route to CMR manganites: what about charge ordering and phase separation", J. Mater. Chem., **11**, 29 (2001).

140. Tomioka Y, Okuda T, Okunoto Y, Asamitsu A, Kuwahara H & Tokura Y, "Charge/orbital ordering in perovskite manganites", J. Alloys Compd., **326**, 27 (2001).

141. Rao C N R & Raveau B (eds), "Colossal magnetoresistance charge ordering and related properties of manganese oxides", World Scientific Singapore (1998).

142. Loudon J C, Mathur N D & Midgley P A, "Charge-ordered ferromagnetic phase in $La_{0.5}Ca_{0.5}MnO_3$", Nature, **420**, 797 (2002).

143. Mori S, Asaka T and Matsui Y, "Observation of magnetic domain structure in phase-separated manganites by Lorentz electron microscopy", J. Electron Microsc., **51**, 225 (2002).

144. Van Tendeloo G, Lebedev O I, Hervieu M & Raveau B, "Structure and microstructure of colossal magnetoresistant materials", Rep. Prog. Phys., **67**, 1315 (2004).

145. Sagdeo P R, Anwar S & Lalla N P, "Electron diffraction evidence of charge-ordering at room-temperature in $La_{1-x}Ca_xMnO_3$ ($0.55 \leq x \leq 0.67$)", Solid State Commun., **137**, 158 (2006).

146. Gupta A, Samanta S B, Awana V P S, Kishan H, Awasthi A M, Bhardwaj S, Narlikar A V, Frontera C & Garcia-Munoz J L, "Direct evidence for charge ordering and electronic phase separation in $Bi_xSr_{1-x}MnO_3$ at room temperature", Physica B, **370**, 172 (2005).

147. Zhuang M, Zhang W & Ming N, "Spin-disorder-scattering-induced spectral-weight transfer and pseudogap in doped perovskite $LaMnO_3$", Phys. Rev. B, **56**, 14547 (1997).

148. Viret M, Ranno L & Coey J M D, "Magnetic localization in mixed-valence manganites", Phys. Rev. B, **55**, 8067 (1997).

149. Kusters R M, Singleton J, Keen D A, McGreevy R & Hayes W, "Magnetoresistance measurements on the magnetic semiconductor $Nd_{0.5}Pb_{0.5}MnO_3$", Physica B, **155**, 362 (1989).

150. Snyder G F, Hiskes R, DiCarolis S, Beasley M R & Geballe T H, "Intrinsic electrical transport and magnetic properties of $La_{0.67}Ca_{0.33}MnO_3$ and $La_{0.67}Sr_{0.33}MnO_3$ MOCVD thin films and bulk material", Phys. Rev. B, **53**, 14434 (1996).

151. Fontcuberta J, Martinez B, Seffar A, Pinol S, Garcia-Munoz J L & Obradors X, "Colossal magnetoresistance of ferromagnetic manganites: Structural tuning and mechanisms", Phys. Rev. Lett., **76**, 1122 (1996).

152. Tokura Y, Urushibara A, Moritomo Y, Arima T, Asamitsu A, Kido G & Furukawa N, "Giant magnetotransport phenomena in filling-controlled kondo lattice system: $La_{1-x}Sr_xMnO_3$" , J. Phys. Soc. Japan, **63**, 3931 (1994).

153. Zhao G, Conder K, Keller H & Muller K A, "Giant oxygen isotope shift in the magnetoresistive perovskite $La_{1-x}Ca_xMnO_{3+y}$", Nature, **381,** 676 (1996).

154. Babushkina N A, Belova L M, Gorbenko O Yu, Kault A R, Bosak A A, Ozhogin V I & Kugel K I, "Metal-insulator transition induced by oxygen isotope exchange in the magnetoresistive perovskite manganites", Nature, **391**, 159 (1998).

155. Yunoki S, Hu J, Malvezzi A L, Moreo A, Furukawa N & Dagotto E, "Phase separation in electronic models for manganites", Phys. Rev. Lett., **80**, 845 (1998).

156. Nagaev E L, "Lanthanum manganites and other giant-magnetoresistance magnetic conductors", Phys. Uspekhi, **39**, 781 (1996).

157. Khomskii D I & Sawatzky G A, "Interplay between spin, charge and orbital degrees of freedom in magnetic oxides", Solid State Commun., **102**, 87 (1997).

158. Hennion M, Moussa F, Rodriguez-Carvajal J, Pinsard L & Revcolevschi A, "Coherent waves of magnetic polarons propagating in $La_{1-x}Ca_xMnO_3$: An inelastic-neutron-scattering study ", Phys. Rev. B, **56**, R497 (1997).

159. Allodi G, De Renzi R & Guidi G, "^{139}La NMR in lanthanum manganites: Indication of the presence of magnetic polarons from spectra and nuclear relaxations", Phys. Rev. B, **57**, 1024 (1998).

160. Battabyal M & Dey T K, "Seebeck coefficient in polycrystalline $La_{0.7}Sr_{0.3-x}Ag_xMnO_3$ pellets: Analysis in terms of a phase separation model", J. Phys.: Conden. Matter, **18**, 493 (2006).

161. Mahesh R, Mahendiran R, Raychaudhuri A K & Rao C N R, "Effect of particle size on the giant magnetoresistance of $La_{0.7}Ca_{0.3}MnO_3$", Appl. Phys. Lett., **68**, 2291 (1996).

162. Berkowitz A E, Mitchell J R, Carey M J, Young A P, Zhang S, Spada F E, Parker F T, Hutten A & Thomas G, "Giant magnetoresistance in heterogeneous Cu-Co alloys", Phys. Rev. Lett., **68**, 3745 (1992); Xiao J Q, Jiang J S & Chien C L, "Giant magnetoresistance in nonmultilayer magnetic systems", Phys. Rev. Lett., **68**, 3749 (1992).

163. Mathur N D, Burnell G, Isaac S P, Jackson T J, Teo B J, Mac Manus-Driscoll J L, Cohen L F, Evetts J E & Blamire M G, "Large low-field magnetoresistance in $La_{0.7}Ca_{0.3}MnO_3$ induced by artificial grain boundaries", Nature, **387**, 266 (1997).

164. Steenbeck K, Eick T, Kirsch K, O'Donnell K & Steinbeiss E, " Influence of a 36.8° grain boundary on the magnetoresistance of $La_{0.8}Sr_{0.2}MnO_{3-\delta}$ single crystal films", Appl. Phys. Lett., **71**, 968 (1997).

165. Sun J Z, Krusin-Elabaum L, Duncombe P R, Gupta A & Laibowitz R B, "Temperature dependent, non-ohmic magnetoresistance in doped perovskite manganate trilayer junctions", Appl. Phys. Lett., **70**, 1769 (1997).

166. Sun J Z, Gallagher W J, Duncombe P R, Krusin-Elbaum L, Altman R A, Gupta A, Lu Y, Gong G Q & Xiao G, "Observation of large low-field magnetoresistance in trilayer perpendicular transport devices made using doped manganate perovskites", Appl. Phys. Lett., **69**, 3266 (1996).

167. Viret M, Drouet M, Nassar J, Contour J-P, Fermon C & Fert A, "Low-field colossal magnetoresistance in manganite tunnel spin valves", Europhys. Lett., **39**, 545 (1997).

168. Shames A I, Rozenberg E, Gorodetsky G, Arsenov A A, Shulyatev D A, Mukovskii Y M, Gedanken A & Pang G, "Electron magnetic resonance studies of magnetic inhomogeneities in crystalline and nanosized powders of $La_{1-x}Sr_xMnO_3$", J. Appl. Phys., **91**, 7929 (2002).

169. Mahendiran R, Ramesh R, Raychaudhuri A K & Rao C N R, "Composition dependence of giant magnetoresistance in $La_{1-x}Ca_xMnO_3$ ($0.1 \leq x \leq 0.9$)", Solid State. Commun., **94**, 515 (1995).

170. Gupta A, McGuire T R, Duncombe P R, Rupp M, Sun J Z, Gallagher W J & Xiao G, "Growth and giant magnetoresistance properties of La-deficient $La_xMnO_{3-\delta}$($0.67 \leq x \leq 1$) films", Appl. Phys. Lett., **67**, 3494 (1995).

171. Fu Y, "Grain-boundary effects on the electrical resistivity and the ferromagnetic transition temperature of $La_{0.8}Ca_{0.2}MnO_3$", Appl. Phys. Lett., **77**, 118 (2000).

172. Das S & Dey T K, "Role of spin polarized tunneling in magnetoresistance and low temperature minimum of polycrystalline $La_{1-x}K_xMnO_3$ (x = 0.05, 0.1, 0.15) prepared by pyrophoric method", Bull. Mater. Science, **29**, 633 (2006).

173. Gittleman J I, Goldstein Y & Bozowski S, "Magnetic properties of granular nickel films", Phys. Rev. B, **5**, 3609 (1972).

174. Helman J S & Abeles B, "Tunneling of spin-polarized electrons and magnetoresistance in granular Ni films", Phys. Rev. Lett., **37**, 1429 (1976).

175. Tedrow P M & Meservey R, "Spin polarization of electrons tunneling from films of Fe, Co, Ni, and Gd", Phys. Rev. B, **7**, 318 (1973).

176. Okimoto Y, Katsufuji T, Ishikawa T, Urushibara, Arima T & Tokura Y, "Anomalous variation of optical spectra with spin polarization in double-exchange ferromagnet: $La_{1-x}Sr_xMnO_3$", Phys. Rev. Lett., **75**, 109 (1995).

177. Milner A, Gerber A, Groisman B, Karpovsky & Gladkikh A, "Spin-dependent electronic transport in granular ferromagnets", Phys. Rev. Lett., **76**, 475 (1996).

178. Longo J & Ward R, "Magnetic compounds of hexavalent rhenium with the perovskite-type structure", J. Am. Chem. Soc., **83**, 2816 (1961).

179. Sleight A W, Longo J & Ward R, "Compounds of Osmium and Rhenium with the ordered perovskite structure", Inorg. Chem., **1**, 245 (1962).

180. Sleight A W & Weiher J F, "Magnetic and electrical properties of Ba_2MReO_6 ordered perovskites", J. Phys. Chem. Solids, **33**, 679 (1972).

181. Patterson F K, Moeller C W & Ward R, "Magnetic oxides of Molybdenum(V) and Tungsten(V) with the ordered perovskite structure", Inorg. Chem., **2**, 196 (1963).

182. Galasso F S, Douglas F C & Kasper R J, "Relationship between magnetic curie points and cell sizes of solid solutions with the ordered perovskite structure", J. Chem. Phys., **44**, 1672 (1966).

183. Nakayama S, Nakagawa T & Nomura S, "Neutron diffraction study of $Sr_2(FeMo)O_6$", J. Phys. Soc. Japan, **24**, 219 (1968).

184. Nakagawa T, "Magnetic and electrical properties of ordered perovskite $Sr_2(FeMo)O_6$ and its related compounds", J. Phys. Soc. Japan, **24**, 806 (1968).

185. Yokoyama H & Nakagawa T, "Nuclear magnetic resonances of Mo^{95}, Mo^{97} and Fe^{57} in $Ba_2(FeMo)O_6$, $Sr_2(FeMo)O_6$ and $Ca_2(FeMo)O_6$", J. Phys. Soc. Japan, **28**, 1197 (1970).

186. Tomioka Y, Okuda T, Okimoto Y, Kumai R, Kobayashi K-I & Tokura Y, "Magnetic and electronic properties of a single crystal of ordered double perovskite Sr_2FeMoO_6", Phys. Rev. B, **61**, 422 (2000).

187. Sharma A, Berenov A, Rager J, Branford W, Bugoslavsky Y, Cohen L F & MacManus-Driscoll J L, "Enhanced intergrain magnetoresistance in bulk Sr_2FeMoO_6 through controlled processing", Appl. Phys. Lett., **83**, 2384 (2003).

188. Sarma D D, Mahadevan P, Saha-Dasgupta T, Ray S & Kumar A, "Electronic structure of Sr_2FeMoO_6", Phys. Rev. Lett., **85**, 2549 (2000).

189. Yanagihara H, CheongW, Salamon M B, Xu S & Moritomo Y, "Critical behavior of single-crystal double perovskite Sr_2FeMoO_6", Phys. Rev. B, **65**, 092411 (2002).

190. Popov G, Greenblatt M & Croft M, "Large effects of A-site average cation size on the properties of the double perovskites $Ba_{2-x}Sr_xMnReO_6$: A d^5-d^1 system", Phys. Rev. B, **67**, 024406 (2003).

191. Phillips K, Chattopadhyay A & Millis A J, "Dynamical mean-field theory of double perovskite ferrimagnets", Phys. Rev. B, **67**, 125119 (2003).

192. Rubi D, Frontera C, Fontcuberta J, Wojcik M, Jedryka E & Ritter C, "Ferromagnetic coupling in $Nd_xCa_{2-x}FeMoO_6$ double perovskites: Dominant band-filling effects", Phys. Rev. B, **70**, 094405 (2004).

193. Ritter C, Ibarra M R, Morellon L, Blasco J, Garcia J & De Teresa J M, "Structural and magnetic properties of double perovskites $AA'FeMoO_6$ ($AA' = Ba_2$, BaSr, Sr_2 and Ca_2)", J. Phys.: Condens. Matter, **12**, 8295 (2000).

194. Alonso J A, Casais M T, Martinez-Lope M J, Martinez J L, Velasco P, Munoz A & Fernandez-Diaz M T, "Preparation, crystal structure, and magnetic and

magnetotransport properties of the double perovskite Ca_2FeMoO_6", Chem. Mater., **12**, 161 (2000).

195. Navarro J, Frontera C, Balcells L I, Martınez B & Fontcuberta J, "Raising the Curie temperature in Sr_2FeMoO_6 double perovskites by electron doping", Phys. Rev. B, **64**, 092411 (2001).

196. Navarro J, Nogues J, Munoz J S & Fontcuberta J, "Antisites and electron-doping effects on the magnetic transition of Sr_2FeMoO_6 double perovskite", Phys. Rev. B, **67**, 174416 (2003).

197. Frontera C, Rubi D, Navarro J, Garcıa-Munoz J L, Fontcuberta J & Ritter C, "Effect of band filling and structural distortions on the Curie temperature of Fe-Mo double perovskites", Phys. Rev. B, **68**, 012412 (2003).

198. Huang Y H, Linden J, Yamauchi H & Karppinen M, "Simple and efficient route to prepare homogeneous samples of Sr_2FeMoO_6 with a high degree of Fe/Mo Order", Chem. Mater., **16,** 4337 (2004).

199. Sriti F, Maignan A, Martin C & Raveau B, "Influence of Fe-Site substitutions upon intragrain and intergrain magnetoresistance in the double-perovskite Ba_2FeMoO_6", Chem. Mater., **13**, 1746 (2001).

200. Zhong W, Wu X L, Tang N J, Liu W, Chen W, Au C T & Du Y W, "Magnetocaloric effect in ordered double-perovskite Ba_2FeMoO_6 synthesized using wet chemistry", Eur. Phys. J. B, **41**, 213 (2004).

201. Ogale A S, Ogale S B, Ramesh R & Venkatesan T, "Octahedral cation site disorder effects on magnetization in double-perovskite Sr_2FeMoO_6: Monte Carlo simulation study", Appl. Phys. Lett., **75**, 537 (1999).

202. Balcells L I, Navarro J, Bibes M, Roig A, Martınez B & Fontcuberta J, "Cationic ordering control of magnetization in Sr_2FeMoO_6 double perovskite", Appl. Phys. Lett., **78**, 781 (2001).

203. Sakuma H, Taniyama T, Kitamoto Y & Yamazaki Y, "Cation order and magnetic properties of double perovskite Sr_2FeMoO_6", J. Appl. Phys., **93**, 2816 (2003).

204. Alonso J L, Fernandez L A, Guinea F, Lesmes F & Martın-Mayor V, "Phase diagram and influence of defects in the double perovskites", Phys. Rev. B, **67**, 214423 (2003).

205. Saha-Dasgupta T & Sarma D D, "Ab initio study of disorder effects on the electronic and magnetic structure of Sr_2FeMoO_6", Phys. Rev. B, **64,** 064408 (2001).

206. Sanchez D, Alonso J A, Garcıa-Hernandez M, Martınez-Lope M J, Martınez J L & Mellergard A, "Origin of neutron magnetic scattering in antisite-disordered Sr_2FeMoO_6 double perovskites", Phys. Rev. B, **65**, 104426 (2002).

207. Navarro J, Balcells L I, Sandiumenge F, Bibes M, Roig A, Mart'ınez B & Fontcuberta J, "Antisite defects and magnetoresistance in Sr_2FeMoO_6 double perovskite", J. Phys.: Condens. Matter, **13**, 8481 (2001).

208. Niebieskikwiat D, Prado F, Caneiro A & Sanchez R D, "Antisite defects versus grain boundary competition in the tunneling magnetoresistance of the Sr_2FeMoO_6 double perovskite", Phys. Rev. B, **70**, 132412 (2004).

209. Niebieskikwiat D, Caneiro A, Sanchez R D & Fontcuberta J, "Oxygen-induced grain boundary effects on magnetotransport properties of $Sr_2FeMoO_{6+\delta}$", Phys. Rev. B, **64,** 180406(R) (2001).

210. Coey J M D, Berkowitz A E, Balcells L I, Putris F F & Barry A, "Magnetoresistance of Chromium dioxide powder compacts", Phys. Rev. Lett., **80,** 3815 (1998).

211. Yuan C L, Wang S G, Song W H, Yu T, Dai J M, Ye S L & Sun Y P, "Enhanced intergrain tunneling magnetoresistance in double perovskite Sr_2FeMoO_6 polycrystals with nanometer-scale particles", Appl. Phys. Lett., **75**, 3853 (1999).

212. Serrate D, Teresa J M D & Ibarra M R, "Double perovskites with ferromagnetism above room temperature", J. Phys.: Condens. Matter, **19**, 023201 (2007).

213. Shannon R D, "Revised effective ionic radii and systematic studies of interatomic distances in halides and chalcogenides", Acta Crystallogr., **A32**, 751 (1976).

214. Kobayashi K I, Kimura T, Tomioka Y, Sawada H & Terakura K, "Intergrain tunneling magnetoresistance in polycrystals of the ordered double perovskite Sr_2FeReO_6", Phys. Rev. B, **59**, 11159 (1999).

215. Wu H, "Electronic structure study of double perovskites A_2FeReO_6 (A=Ba,Sr,Ca) and Sr_2MMoO_6 (M=Cr,Mn,Fe,Co) by LSDA and LSDA+U", Phys. Rev. B, **64**, 125126 (2001).

216. Philipp J B, Majewski P, Alff L, Erb A & Gross R, "Structural and doping effects in the half-metallic double perovskite A_2CrWO_6 (A=Sr, Ba, and Ca)", Phys. Rev. B, **68**, 144431 (2003).

217. Vaitheeswaran G, Kanchana V & Delin A, "Pseudo-half-metallicity in the double perovskite Sr_2CrReO_6 from density-functional calculations", Appl. Phys. Lett., **86**, 032513 (2005).

218. Wollan E O, "Magnetic coupling in crystalline compounds: A phenomenological theory of magnetism in 3d metals", Phys. Rev., **117**, 387 (1960).

219. Tomioka Y, Okuda T, Okimoto Y, Kumai R, Kobayashi K I & Tokura Y, "Magnetic and electronic properties of a single crystal of ordered double perovskite Sr_2FeMoO_6", Phys. Rev. B, **61**, 422 (2000).

220. Gopalakrishnan J, Chattopadhyay A, Ogale S B, Venkatesan T & Greene R L, "A case of metallic and nonmetallic double perovskites: study of A_2FeReO_6 (A=Ba, Sr, Ca)", Phys. Rev. B, **62**, 9538 (2000).

221. Linden J, Yamamoto T, Karppinen M & Yamauchi H, "Evidence for valence fluctuation of Fe in Sr_2FeMoO_{6-w} double perovskite", Appl. Phys. Lett., **76**, 2925 (2000).

222. Balcells L I, Navarro J, Bibes M, Roig A, Martınez B & Fontcuberta J, "Cationic ordering control of magnetization in Sr_2FeMoO_6 double perovskite", Appl. Phys. Lett., **78**, 781 (2001).

223. Greneche J M, Venkatesan M, Suryanarayanan R & Coey J M D, "Mössbauer spectrometry of A_2FeMoO_6 (A Search for antiphase =Ca,Sr,Ba): domains", Phys. Rev. B, **63**, 174403 (2001).

224. Colis S, Stoeffler D, M'eny C, Fix T, Leuvrey C, Pourroy G, Dinia A & Panissod P, "Structural defects in Sr_2FeMoO_6 double perovskite: Experimental versus theoretical approach", J. Appl. Phys., **98**, 033905 (2005).

225. Kapusta C, Riedi P C, Zajac D, Sikora M, De Teresa J M, Morellon L & Ibarra M R, "NMR study of double perovskite Sr_2FeMoO_6", J. Magn. Magn. Mater., **242**, 701 (2002).

226. Sanchez D, Alonso J A, Garcıa-Hernandez M, Martınez-Lope M J, Martınez J L & Mellegard A, "Origin of neutron magnetic scattering in antisite-disordered Sr_2FeMoO_6 double perovskites", Phys. Rev. B, **65**, 104426 (2002).

227. Besse M et al, "Experimental evidence of the ferrimagnetic ground state of Sr_2FeMoO_6 probed by X-ray magnetic circular", Europhys. Lett., **60**, 608 (2002).

228. Schiffer P, Ramirez A P, Bao W & Cheong S W, "Low temperature magnetoresistance and the magnetic phase diagram of $La_{1-x}Ca_xMnO_3$", Phys. Rev. Lett., **75,** 3336 (1995).

229. Martınez B, Navarro J, Balcells L I & Fontcuberta J, "Electronic transfer in Sr_2FeMoO_6 perovskites", J. Phys.: Condens. Matter, **12,** 10515 (2000).

230. Kapusta C, Zajac D, Riedi P C, Sikora M, Oates C J, Blasco J & Ibarra M R, "NMR study of A_2FeMO_6 (A=Ca, Sr, Ba, M=Mo, Re) double perovskites", J. Magn. Magn. Mater., **272–276,** e1619 (2004).

231. Kang J S et al, "Bulk-sensitive photoemission spectroscopy of A_2FeMoO_6 double perovskites (A=Sr, Ba)", Phys. Rev. B, **66,** 113105 (2002).

232. Herrero-Martın J, Garcıa J, Subıas G, Blasco J & Sanchez M C, "An x-ray spectroscopic study of A_2FeMoO_6 and $Sr_2Fe_{1-x}Cr_xMoO_6$ double perovskites", J. Phys.: Condens. Matter, **16,** 6877 (2004).

233. Herrero-Martın J, Garcıa J, Subıas G, Blasco J & Sanchez M C, "X-ray absorption spectroscopic study on A_2FeReO_6 double perovskites", J. Phys.: Condens. Matter, **17,** 4963 (2005).

234. Moreno M S, Gayone J E, Abbate M, Caneiro A, Niebieskikwiat D, Sanchez R D, de Siervo A, Landers R & Zampieri G, "Fe and Mo valences in Sr_2FeMoO_6", Solid State Commun., **120,** 161 (2001).

235. Nakamura S, Tanaka M, Kato H & Tokura Y, "Mössbauer study on the ordered double perovskite A_2FeReO_6 (A = Ca, Sr)", J. Phys. Soc. Japan, **72,** 424 (2003).

236. Moreno M S, Gayone J E, Abbate M, Caneiro A, Niebieskikwiat D, S´anchez R D, De Siervo A, Landers A & Zampieri G, "Fe and Mo valences in Sr_2FeMoO_6", Solid State Commun., **120,** 161 (2001).

237. Garcıa-Landa B, Ritter C, Ibarra M R, Blasco J, Algarabel P A, Mahendiran R & Garcıa J, "Magnetic and magnetotransport properties of the ordered perovskite Sr_2FeMoO_6", Solid State Commun., **110**, 435 (1999).

238. Kanamori J & Terakura K, "A general mechanism underlying ferromagnetism in transition metal compounds", J. Phys. Soc. Japan, **70**, 1433 (2001).

239. Azad A K, Eriksson S G, Mellegard A, Ivanov S A, Eriksen J & Rundlof H, "A study on the nuclear and magnetic structure of the double perovskites A_2FeWO_6 (A = Sr, Ba) by neutron powder diffraction and reverse Monte Carlo modeling", Mater. Res. Bull., **37**, 1797 (2002).

240. Fang Z, Terakura K & Kanamori J, "Strong ferromagnetism and weak antiferromagnetism in double perovskites: Sr_2FeMO_6 (M=Mo, W, and Re)", Phys. Rev. B, **63**, 180407(R) (2001).

241. Carvajal E, Navarro O, Allub R, Avignon M & Alascio B, "Ferromagnetic transition in ordered double perovskites and related alloys", Eur. Phys. J. B, **48**, 179 (2005).

242. Kobayashi K I, Okuda T, Tomioka Y, Kimura T & Tokura Y, "Possible percolation and magnetoresistance in ordered double perovskite alloys $Sr_2Fe(W_{1-x}Mo_x)O_6$", J. Magn. Magn. Mater., **218**, 17 (2000).

243. De Teresa J M, Serrate D, Ritter C, Blasco J, Ibarra M R, Morellon L & Tokarz W, "Investigation of the high Curie temperature in Sr_2CrReO_6", Phys. Rev. B, **71**, 092408 (2005).

244. Kato H, Okuda T, Okimoto Y, Tomioka Y, Oikawa K, Kamiyama T & Tokura Y, "Structural and electronic properties of the ordered double perovskites A_2MReO_6 (A=Sr,Ca; M=Mg,Sc,Cr,Mn,Fe,Co,Ni,Zn)", Phys. Rev. B, **69**, 184412 (2004).

245. Popov G, Greenblatt M & Croft M, "Large effects of A-site average cation size on the properties of the double perovskites $Ba_{2-x}Sr_xMnReO_6$: A d^5-d^1 system", Phys. Rev. B, **67,** 024406 (2003).

246. Popov G, Lobanov V, Tsiper E V, Greenblatt M, Caspi E N, Borissov A, Kiryukhin V & Lynn J W, "Crystallographic and magnetic structure of the Sr_2MnReO_6 double perovskite", J. Phys.: Condens. Matter, **16**, 135 (2004).

247. Blasco J, Ritter C, Morellon L, Algarabel P A, De Teresa J M, Serrate D, Garcıa J & Ibarra M R, "Structural, magnetic and transport properties of $Sr_2Fe_{1-x}Cr_xMoO_{6-y}$", Solid State Sci., **4**, 651 (2002).

248. Ritter C, Blasco J, De Teresa J M, Serrate D, Morellon L, Garcıa J & Ibarra M R, "Structural and magnetic details of 3d-element doped $Sr_2Fe_{0.75}T_{0.25}MoO_6$", Solid State Sci., **6**, 419 (2004).

249. Bibes M et al, "Tunnel magnetoresistance in nanojunctions based on Sr_2FeMoO_6", Appl. Phys. Lett., **83**, 2629–31 (2003).

250. Westerburg W, Reisinger D & Jacob G, "Epitaxy and magnetotransport of Sr_2FeMoO_6 thin films", Phys. Rev. B, **62**, R767 (2000).

251. Asano H, Kohara Y & Matsui M, "Coherent epitaxy and magnetic properties of Sr_2FeMoO_6 thin films on $Ba_{0.4}Sr_{0.6}TiO_3$-buffered $SrTiO_3$ substrates", Japan. J. Appl. Phys., **41**, L1081 (2002).

252. Sanchez D, Garcıa-Hernandez M, Auth N & Jacob G, "Structural, magnetic, and transport properties of high-quality epitaxial Sr_2FeMoO_6 thin films prepared by pulsed laser deposition", J. Appl. Phys., **96**, 2736 (2004).

253. Fontcuberta J et al, "Magnetoresistive oxides: new developments and applications", J. Magn. Magn. Mater., **242**, 98 (2002).

254. Yin H Q, Zhou J S, Zhou J P, Dass R, McDevitt J T & Goodenough J B, "Intra- versus intergranular low-field magnetoresistance of Sr_2FeMoO_6 thin films", Appl. Phys. Lett., **75**, 2812 (1999).

255. Zhong W, Liu W, Au C T & Du Y W, "Tunnelling magnetoresistance of double perovskite Sr_2FeMoO_6 enhanced by grain boundary adjustment", Nanotechnology, **17**, 250 (2006).

256. Haghiri-Gosnet A M & Renard J P, "CMR manganites: physics, thin films and devices", J. Phys. D: Appl. Phys., **36**, R127 (2003).

257. Zeise M, "Colossal magnetoresistance, half metallicity and spin electronics", Philos. Trans. Roy. Soc. A, **358,** 137 (2000).

258. Choudhary R J, Ogale A S, Shinde S R, Hullavarad S, Ogale S B, Bathe R N, Patil S I and Kumar R, "Evaluation of manganite films on silicon for uncooled bolometric applications", Appl. Phys. Lett., **84**, 3846 (2004).

259. Rajeswari M, Chen C, Goyal A, Kwon C, Robson M C, Ramesh R, Venkatesan T & Lakeou S, "Low-frequency optical response in epitaxial thin films of $La_{0.67}Ca_{0.33}MnO_3$ exhibiting colossal magnetoresistance", Appl. Phys. Lett., **68,** 3555 (1996).

260. Goyal A, Rajeswari M, Shreekala R, Lofland S E, Bhagat S M, Boettcher T, Kwon C, Ramesh R & Venkatesan T, "Material characteristics of perovskite manganese oxide thin films for bolometric applications", Appl. Phys. Lett., **71**, 2535 (1997).

261. Fu C C, Huang Z & Yeh N C, "Spin-polarized quasiparticle transport in cuprate superconductors", Phys. Rev. B, **65**, 224516 (2002).

262. Chen Z Y, Biswas A, Zutic I, Wu T, Ogale S B, Green R L & Venkatesan T, "Spin-polarized transport across a $La_{0.7}Sr_{0.3}MnO_3/YBa_2Cu_3O_{7-x}$ interface: Role of Andreev bound states", Phys. Rev. B, **63,** 212508 (2001).

263. Park J H, Vescovo E, Kim H J, Kwon C, Ramesh R & Venkatesan T, "Direct evidence for a half-metallic ferromagnet", Nature, **392**, 794 (1998).

264. Park J H, Vescovo E, Kim H J, Kwon C, Ramesh R & Venkatesan T, "Magnetic properties at surface boundary of a half-metallic ferromagnet $La_{0.7}Sr_{0.3}MnO_3$", Phys. Rev. Lett., **81**, 1953 (1998).

265. Wei J Y T, Yeh N C & Vasquez R P, "Tunneling evidence of half-metallic ferromagnetism in $La_{0.7}Ca_{0.3}MnO_3$", Phys. Rev. Lett., **79**, 5150 (1997).

266. Wei J Y T, Yeh N C, Vasquez R P & Gupta A, "Tunneling evidence of half-metallicity in epitaxial films of ferromagnetic perovskite manganites and ferrimagnetic magnetite", J. Appl. Phys., **83**, 7366 (1998).

Chapter - 2

EXPERIMENTAL TECHNIQUES

2.1 INTRODUCTION

The main objectives of the present investigations are to synthesize the manganites and double perovskite materials and study their structural, magnetic and magnetotransport properties. In this chapter, we describe and discuss the various experimental techniques employed in the present investigations for (a) synthesis of bulk polycrystalline samples (b) characterization of structural-microstructural features and (c) evaluation of magnetotransport properties, e.g. insulator-metal transition temperature (T_{IM}), paramagnetic-ferromagnetic transition temperature (Tc) and magnetoresistance (MR) characteristics of the studied samples. In the present work, the polycrystalline bulk samples are prepared by standard solid-state reaction and sol-gel processes. X-ray diffraction (XRD) measurements have been used to determine the crystal structure of the materials. Scanning electron microscopy (SEM) coupled with energy dispersive X-ray analyser (EDAX) has been employed to examine the morphology and chemical composition of the studied samples. The fundamental phenomenon is revealed by the measurements of resistivity and magnetoresistance (MR) as a function of both temperature and magnetic field. Magnetization measurements have contributed to understand the magnetic nature of these materials. The overall experimental procedures are shown in Fig. 2.1.

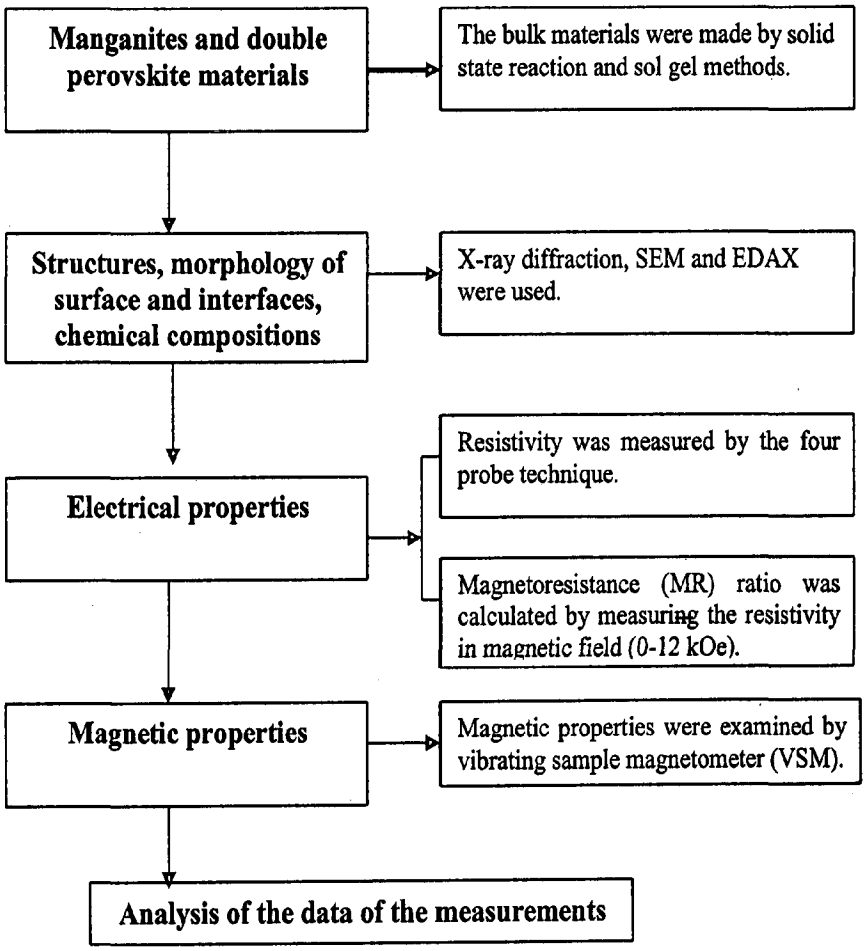

Figure 2.1: The overall experimental procedures.

2.2 SAMPLE PREPARATION

The bulk polycrystalline samples of the perovskite manganites and double perovskites were prepared by solid state reaction and sol gel processes. The details of these processes are described in the next subsections.

2.2.1 Solid state reaction method

Solid state reaction is the most common method for the production of perovskite oxides from the oxides, nitrates, carbonates, sulphates, acetates and other metal salts. In this

method, the solid reactants are heat treated to produce a new solid. In the synthesis of manganites and double perovskites, there are six steps: weighing of the chemicals, powder mixing, grinding, calcination, pelletizing and sintering. The details steps for the formation of the studied materials by solid state reaction method are shown in the Fig. 2.2.

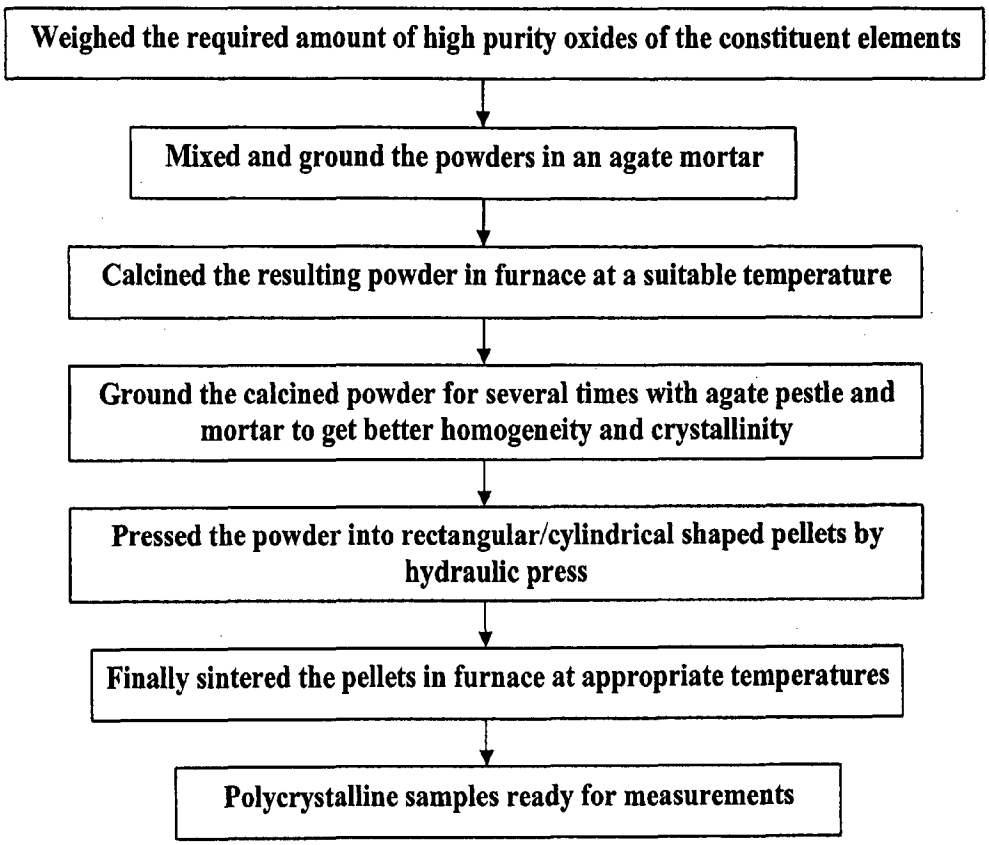

Figure 2.2: The detail steps for the formation of the studied materials by solid state reaction method.

The first step is to weigh out the material by using the electronic balance. The amount of the material is estimated from its reaction formula. The second step is mixing of these weighed precursors powders. Apart from breaking up agglomerates and forming an intimate mixture of the constituents, a mixing process introduces defects into crystal, which may enhance diffusion and accelerates calcination. Calcination causes the constituents to interact by

inter diffusion of ions and so reduces the extent of the diffusion that must occur during the sintering in order to obtain a homogenous body. The calcination conditions are important factor for controlling shrinkage during the sintering. The calcined powder was pressed in the form of pellets by hydraulic press machine. Dry pressing is carried out in a Die with movable top and bottom punches. A cavity is formed with the bottom punch in a low position and this is filled with free flowing granulated powder. Loose powder is compressed and densified into a shape called pellet. The hydraulic pressure is used for this purpose. Compacting pressures generally lie between 10-20 tones per square inch. The heating of a solid to a high temperature, below its melting point, to make complete reaction between precursor materials is known as sintering. Sintering converts the material into a denser structure of crystallites joined to one another by grain boundaries. After sintering the pellet at desired temperatures, the sample is ready for further characterizations.

Powder preparation by solid state reactions generally has an advantage in terms of production cost. However, the powder quality is also an important consideration for advanced perovskites. The powders are normally agglomerated and a grinding step is required to produce powders with better characteristics [1]. Grinding with ball mills leads to contamination of the powder with impurities. Incomplete reactions, especially in poorly mixed powders, may produce undesirable phases. The need to calcine the starting material at a higher temperature raises the cost. Despite the several disadvantages, this conventional process has still been widely used in industry.

2.2.2 Sol-gel method

In sol–gel method, the materials are obtained from solution via gelation. It can be used as an optional, often more controllable, way of making ceramics or glasses that can also

be prepared with other techniques. But the high homogeneity of the constituent elements and the mild processing conditions of the sol–gel synthesis, such as moderate preparation temperatures, makes it possible to obtain unique materials, not accessible with other techniques. Sol–gel methods have been used commercially since 1930's, but the real take off was not until 1970's, when it was shown that gel monoliths could be transformed with retained shape into oxide [2-4] and that the use of alkoxide precursors allow for low sintering temperatures [5, 6]. Since then, although monoliths have turned out the least important of the many possibilities of sol–gel synthesis, other aspects have attracted a continuously growing interest. Now sol–gel processing is a well established method used in laboratories and industries all over the world, and a large number of review articles and books have been published on the topic [7-12], as well as an excellent web-site [13]. Sol-gel process is a versatile solution process for making the ceramic materials. In general, the sol-gel involves the transition of a system from a liquid sol (mostly colloidal) into a solid gel phase. Applying the sol-gel process, it is possible to fabricate ceramic materials in a wide variety of forms, ultra fine powders, thin film coatings, microporous inorganic membranes and extremely porous aerogel materials. The starting material used in the preparation of the sol is usually inorganic metal salts or metal organic compounds. In the typical sol-gel process, the precursors are subjected to a series of hydrolysis and polymerization reactions to form a colloidal suspension or a sol. Further processing of the sol enables one to make ceramic materials in different forms. With further drying and heat treatment the gel is converted into dense particles. The sol gel process also has other potential advantages over other traditional processing techniques such as better homogeneities, low processing temperature and improved material properties [7]. The detail steps for the synthesis of the studied materials by sol-gel method are shown in the Fig. 2.3. The required amounts of high purity nitrates of

precursors were dissolved in the double distilled water to form an aqueous solution. An equal amount of ethylene glycol was added to this solution for polymerization with continuous stirring. This solution was then heated on a hot plate at temperature of ~80 ^{0}C till a dry thick sol was formed.

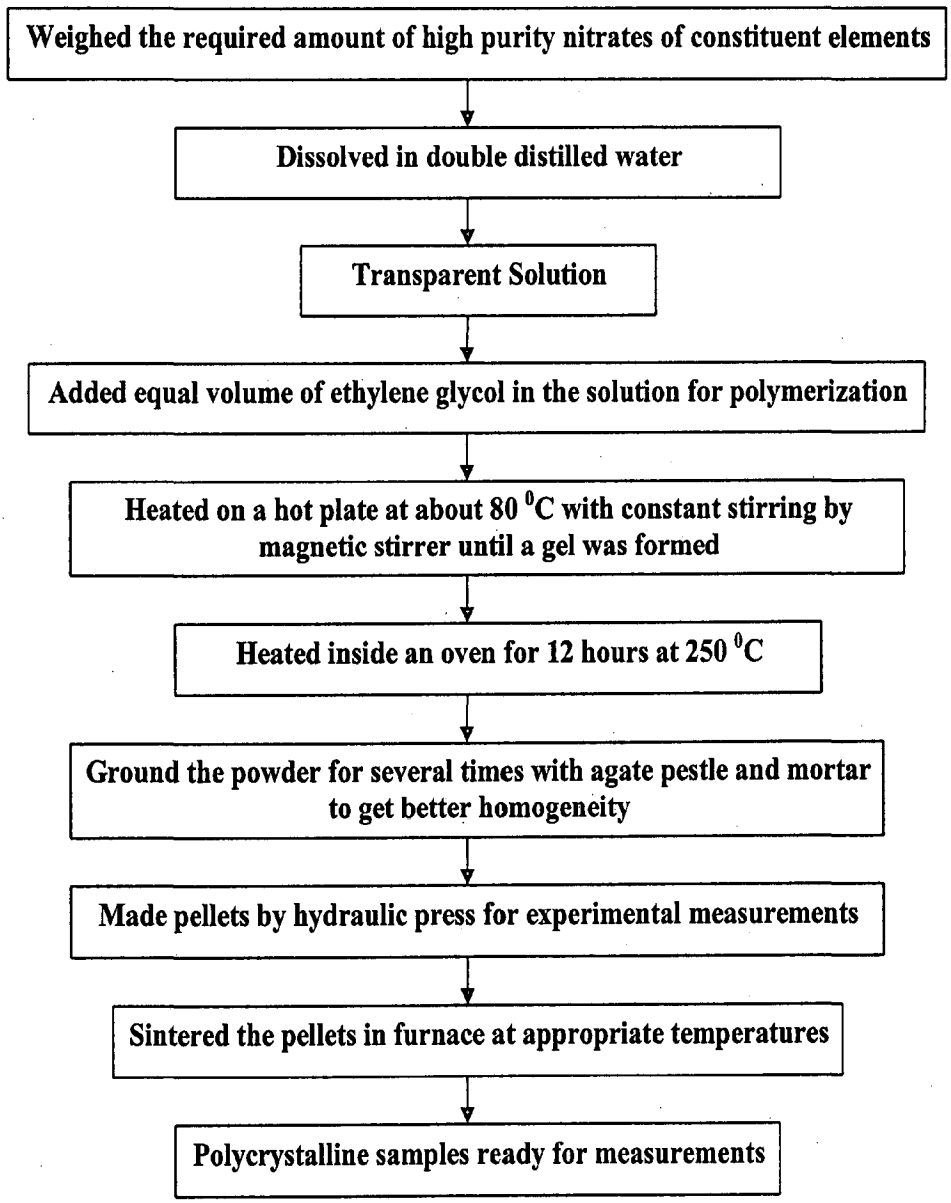

Figure 2.3: The detail steps for the synthesis of the studied materials by sol-gel method.

This was further decomposed in an oven at a temperature of 250 ^{0}C to get the dry fluffy material. The polymeric precursor thus obtained was calcined at 350 ^{0}C for 12 h. The resulting powder was pressed in the form of pellets and sintered at desired temperatures. Now the sample is ready for further characterizations. There are several reports [14-18] on the synthesis of manganites by sol-gel based methods.

2.3 X-RAY DIFFRACTION

X-rays are the electromagnetic radiation whose frequencies lie in general intermediate between the UV and gamma radiation. X-rays are produced from the inner (core) level electronic transitions in an atom, which are termed as characteristic radiation. The production of X-rays is known since long (1895, Wilhelm Conrad Rontgen in Germany discovered the X-rays). The exact nature of X-rays was established in 1912 when phenomenon of x-rays diffraction was discovered. This effect was first demonstrated by Max Von Laue, after seventeen years of its discovery and provided a new method for investigating the fine structure of matter. Since crystal lattice consists of parallel rows of atoms equivalent to the parallel lines of the diffraction grating, the interplaner spacing could be successfully determined by using X-ray diffractometer. Thus the phenomenon of diffraction can reveal the details of internal structure of the order of angstrom. X-ray being electromagnetic wave, interact with the electron cloud of the atom and can be absorbed by the matter in two distinct ways, by scattering and by true absorption. The scattering of X-rays by atoms is similar in many ways to the scattering of the visible light by dust particles in air. True absorption is caused by electronic transition within the atom and best considered from the viewpoint of the quantum theory of radiation. The phenomenon of diffraction could be explained by considering the scattering of X-rays by atomic electron cloud. When X-rays are subjected to

fall upon a matter, the electrons of the atoms constituting the matter vibrate due to the interaction of the fluctuating electric field of X-rays with the same frequency as that of X-rays. In turn, they act as a source of radiation and thereby emit radiation of the same frequency as of the radiation, which made them to vibrate. Thus the incident radiation appears to be scattered by the atoms and this scattering is possible in all the directions. The scattered ray will be completely in phase in some direction and completely out of phase in other directions. Thus a diffracted ray may be defined as a beam composed of a large number of rays, which are completely in phase and mutually reinforce (constructive interference) one another to form a diffracted beam in a particular direction, which satisfies the Bragg's law. In all the other directions of space, the scattered beams are out of phase and cancel one another (destructive interference). The Bragg's law for diffraction relates the possibility of constructive interference to the inter-planer spacing of the crystals as follows [19]

$$2d \sin\theta = n\lambda \tag{2.1}$$

where λ is the wavelength of the X-rays, d is the spacing between planes, and θ is the angle of incidence (Bragg's angle) that the X-ray beam makes with the plane of atoms (hkl) and n is the order of diffraction. Schematic diagram for illustrating Bragg's law for X-ray diffraction is shown in Fig. 2.4.

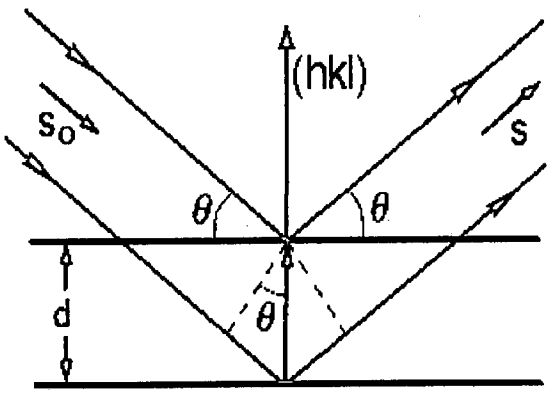

Figure 2.4: Schematic diagram for illustrating Bragg's law for X-ray diffraction.

2.3.1 X-ray powder diffractometer

X-ray powder diffraction is a non-destructive technique widely applied for the characterization of crystalline materials. This method has been traditionally used for phase identification, quantitative analysis and the determination of structure imperfections [20]. Important advances in structural studies of manganites and double perovskites research have relied heavily on the powder diffraction technique. In the present investigations, this powder diffraction technique is employed for the phase identification and structural characterization of bulk manganites and double perovskites. The **Bruker AXS D8 Advance** powder diffractometer, with CuK_α radiation (λ=1.5406 Å), operating at 40 kV & 30 mA, has been used in the present work.

Some solids can be prepared only as micro-crystalline powders and hence their structure cannot be determined using single crystal diffraction techniques. Also the structures of some materials which are in the form of hydrocarbons and resins cannot be determined by single crystal diffraction methods. In such cases we can determine the structure of the material using powder diffraction data. The ability to determine crystal structures using powder diffraction promises to open up many avenues in structural sciences. Powder diffractometer projects the three-dimensional lattice into a one-dimensional lattice. We can determine the orientation, unit cell dimensions, stress/strain, crystal structure, etc from the information obtained in the powder diffraction pattern.

The modern X-ray technique, which is used in powder diffractometer, gives a series of peaks instead of diffraction rings. In this technique, a detector is used instead of the film. A monochromatic incident ray is used to give a good peak resolution. The powder is filled in the hole of a sample holder. The set up requires that if reflection is obtained when the beam is

incident at an angle θ with the lattice plane, the reflected beam is recorded at an angle of 2θ, which is referred to as θ-2θ scan. This is shown in Fig. 2.5.

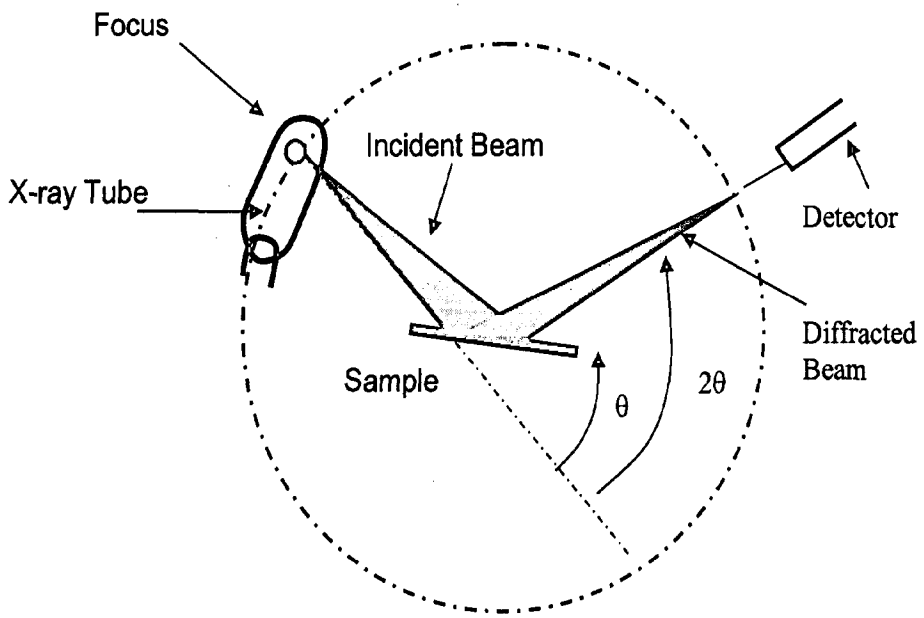

Figure 2.5: Schematic diagram of X-ray diffractometer.

The peak positions and the intensities are readily obtained from the chart. The powder diffractometer uses an x-ray detector like a proportional or scintillation counter to measure the positions of the diffracted beams. Diffractometer is a widely used method because it measures the intensities directly.

2.3.2 Indexing of X-ray diffraction patterns

When a powdered sample of crystalline material is placed in a diffractometer and bathed in X-rays then a characteristic pattern can be recorded, known as the diffraction pattern. The diffraction pattern is unique for each crystalline material. The positions of the peaks give us information that can be used to determine the cell parameters, and the

intensities of the peaks give us information about the crystallinity of the materials. Each peak present in the pattern has its own set of indices. More than one diffraction peak can be located exactly at the same position. The process of determining the (hkl) associated with an individual peak is known as indexing the pattern. The position of diffraction peaks and the d spacing that they represent, provide information about the location of the planes in the crystal structure. Each peak measures a d-spacing that represents a family of lattice planes. Each peak also has an intensity which differs from others in the pattern and reflects the relative strength of the diffraction. The accurate determination of the interplaner spacing, lattice parameter etc. provides an important basis in understanding various properties of the material. The d-spacing for a most general crystal system (Triclinic) can be calculated using the formula [19]

$$\frac{1}{d^2} = \frac{1}{V^2}\left[\begin{array}{l} h^2b^2c^2\sin^2\alpha + k^2c^2a^2\sin^2\beta + l^2a^2b^2\sin^2\gamma + \\ 2abc\left\{\begin{array}{l} kla(\cos\beta\cos\gamma - \cos\alpha) + \\ hlb(\cos\alpha\cos\gamma - \cos\beta) + hkc(\cos\alpha\cos\beta - \cos\gamma) \end{array}\right\} \end{array}\right] \qquad (2.2)$$

where V = volume of the unit cell = abc $(1- \cos^2\alpha - \cos^2\beta - \cos^2\gamma + \cos\alpha\cos\beta\cos\gamma)^{1/2}$ and a, b, c, α, β, γ are the lattice parameters and h, k, l are the miller indices.

Each reflection assigned by some hkl values, equates the inter-planar spacing with unit cell parameters. The typical assignments of hkl values to the reflections are called indexing. In most of trial method, the system is assumed cubic initially and thus by reducing above equation to simpler forms. The trials for indexing of all the observed reflections are made with lowering the lattice symmetry to tetragonal, orthorhombic and so on. There are various computer programs, namely TREOR, VISOR, ITO, CELL, UNITCELL, POWDER, INDEXING etc. also available for automatic determination of the unit cell parameters from

the observed d values. The observed unit cell parameters are refined using their calculated indices and observed d-values. The unit cell parameters are feed to adjust in the best way to fit the observed experimental data. It needs to be mentioned here; the solutions obtained are trivial and can not be free from mistakes. It is always user's decision for judging the accuracy of unit cell parameters.

2.3.3 Crystallite size determination

When the size of the individual crystals is less than about 0.1 μm (1000 Å), the term "particle size" is usually used, but the term "crystallite" size is more precise. The X-ray diffraction technique can be successfully used to determine the crystallite size of the materials. This is based on line broadening phenomenon during X-ray diffraction. For large crystallites, the diffraction peaks occur only at precise Bragg angle locations. This is because of the canceling of the diffractions by incoherent scattering at other angles by lattice planes within the large crystal structure. If the particle size is smaller such that there are insufficient lattice planes to effectively cancel all incoherent scattering at angle close to the Bragg's angle and net result will be a broadening of the diffraction peak around the Bragg's angle. This phenomenon of widening of diffraction peak is related to incomplete cancellation of small deviations from the Bragg's angle in small crystallite and is known as particle size broadening. Particle size broadening is differentiated from the normal width of diffraction peaks related to instrumental effects. In most cases, the particle size broadening will not be observed with crystallite size larger than 1μm. Although a considerable amount of theoretical and experimental work have been done on powder profiles to determine the crystallite size and lattice strain. Wilson [20, 21], Warren-Averbach [22] and Scherrer's [19] theories are considered as the most promising among all for the purpose. When the breadth $\beta_{1/2}$ (full width at half maximum) of the pure diffraction profile is ascribed to small crystallite size, the

broadening caused by small crystallite size can be related to the size of grain by Scherrer's formula given below which has been used to estimate the crystallite size (P) of very small crystals from the measured width of their diffraction curves [23].

$$P = \frac{K\lambda}{\beta_{1/2}\cos\theta_B} \tag{2.3}$$

where P is the crystallite size, λ is the wavelength, K is the shape factor typically has a value around 0.9 and $\beta_{1/2}$ is the full width at half maximum (FWHM). Here, $\beta_{1/2}$ is given by (B-b), where B is the breadth of the observed diffraction line at the half intensity maximum and b is the instrumental broadening.

2.4 SCANNING ELECTRON MICROSCOPE (SEM)

The scanning electron microscope (SEM) is a powerful tool which is capable of producing high-resolution images of a sample surface and used to measure many characteristics of the sample such as composition, surface topography, crystallography etc [24-27]. In the present study **LEO-435VP** scanning electron microscope has been used. The SEM uses electrons instead of light to form an image. A beam of electrons is produced at the top of the microscope by heating of a metallic filament. The electron beam follows a vertical path through the column of the microscope. It makes its way through electromagnetic lenses, which focus and direct the beam down towards the sample. The types of signals produced, when the focused electron beam impinges on the specimen surface, including secondary electrons, back scattered electrons, characteristics X-rays, Auger electrons and photons of various energies. They are obtained from the specific volumes within the sample and used to measure many characteristics of the sample.

In SEM, the primary signal of interest is the variation in secondary electron emission that takes place as the electron beam is swept in raster across the surface of a specimen due to differences in surface topography. The secondary electrons are confined near the beam impact area, which permit images to be obtained at relatively high resolution (~10 nm). SEM images have a characteristic three-dimensional appearance due to large depth of focus of the scanning electron beam and are useful for judging the surface structure of the sample.

2.4.1 Principles of scanning electron microscopy

There are several different modes of operation of the SEM, each corresponding to the collection of different types of signals arising from the incident primary electron beam. A schematic diagram of electron interaction with specimen is shown in Fig. 2.6.

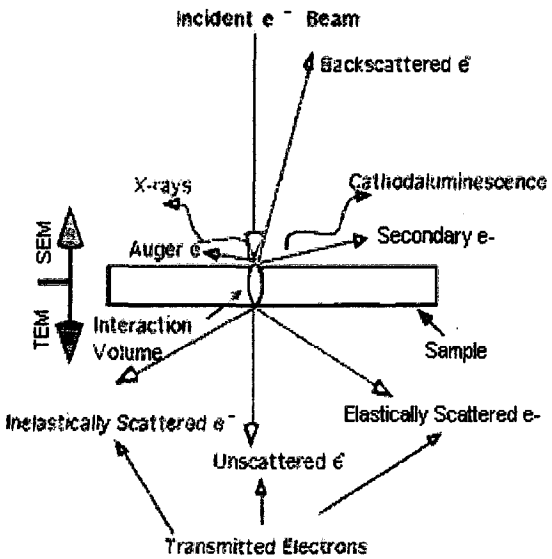

Figure 2.6: A schematic diagram of electron interaction with a thin specimen.

The five main modes are as follows:

(1) **Emission mode**: The secondary electrons emitted from the specimen are collected by detector. These electrons may have energies less than 50 eV and comes from the

material within approximately 5 nm of the specimen surface. This is the most common mode of operating the SEM. It is suitable for obtaining information concerning the surface of the specimen.

(2) **Reflective mode:** The primary electrons back scattered from the specimen are collected by detector. These electrons have an energy range close to the energy of incident primary electron beam and they come from the material within a few microns of the specimen surface. This mode provides information which is more characteristics of the bulk materials.

(3) **Absorptive mode**: In this mode, an electrical lead is attached to the specimen and the current which flows through the lead to earth is used as signal. Any local increases in the number of secondary emitted electrons or primary reflected electrons causes a corresponding local decrease in the absorbed current. Consequently, absorptive mode images are complementary in contrast to emissive and reflective mode images.

(4) **Transmission mode**: For this mode, those electrons that completely penetrate thin specimens are collected. These electrons have a wide energy range, depending on the nature and thickness of specimen. This mode often enables thicker specimen to be examined and high contrasts to be obtained.

(5) **X-ray mode**: For the X-ray mode, the emitted x-rays are collected and used as the signal. Either the X-rays are used as they arise (non-dispersive), or particular wavelengths are selected (dispersive) with the aid of a crystal spectrometer or pulse-height analyzer. This mode is the basis of X-ray probe micro-analyzer.

2.4.2 Working of SEM in emissive mode

In the present investigations, we have used the SEM in its most common mode e.g. emission mode by collecting the secondary electrons. The block diagram of SEM is shown in

Fig. 2.7. The electrons from a heated filament are accelerated by a voltage commonly in the range 10 to 30 kV and directed down the centre of an electron optical column usually consisting of different magnetic lenses.

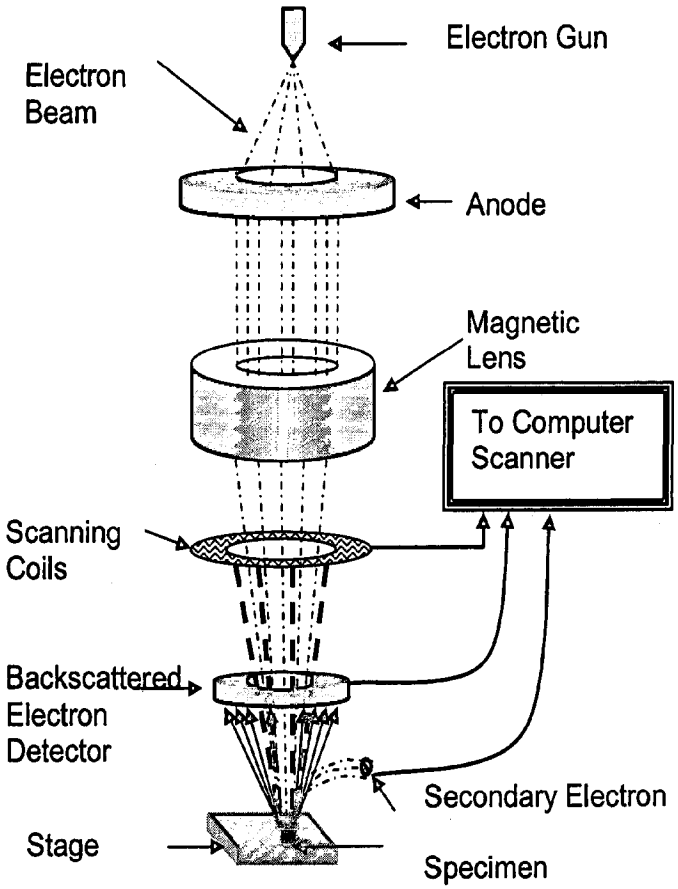

Figure 2.7: Schematic diagram of scanning electron microscope.

These lenses cause the electrons to be formed into a fine electron beam that fall onto the surface of a solid specimen and made to scan on a raster on the surface by a deflection system. The electron beam incident on the specimen surface results in the emission of secondary electrons in this emissive mode. Detectors collect the secondary or backscattered electrons, and convert them to a signal that is sent to a viewing screen similar to the one in an ordinary television, producing an image. The times associated

with the emission and collection of secondary electrons is negligibly small compared with the times associated with the scanning of incident electron beam across specimen surface. Hence, there is one-to-one correspondence between the number of secondary electrons collected from any particular point on the specimen surface and image formation.

There are basically two types of scanning electron microscopes. First one is regular SEM, which requires a conductive sample and another one is environmental SEM, which are used to examine a non-conductive sample without coating it with a conductive material. The SEM, which is used in the present investigations, is the first one and the following requirements are needed for preparing samples:

(1) Removal of the water, solvents, or other materials that could vaporize while in the vacuum.

(2) Firmly mounting of the samples.

(3) Coating of gold on non-metallic samples, such as ceramics, bugs, plants etc., to make them electrically conductive. Metallic samples are placed directly into the SEM.

2.5 ENERGY DISPERSIVE X-RAY SPECTROSCOPY (EDXS)

Energy dispersive X-ray spectroscopy is an analytical tool predominantly used for chemical characterization. Being a type of spectroscopy, it relies on the investigation of a sample through interactions between light and matter, analyzing X-rays in its particular case. The emitted characteristic X-rays may be analyzed for their energy and intensity, the energy being the signature of the element emitting them and the intensity as to how much of it is present. Detection of X-ray by energy dispersive spectrometer is accomplished by employing a detector which is a negatively biased Si chip into which lithium has been diffused and onto

which a thin contact Au layer has been evaporated. The X-ray from the specimen enters a wafer of pure silicon, carefully treated with lithium so that there are no impurities or irregularities in the structure that can trap electrons. As the X-rays enter the silicon, each one gives its energy by creating photoelectrons by ionization of silicon atoms. Since each ionization takes 3.9 eV of energy, the final result is a number of ionized silicon atoms (and an equivalent number of electrons) equal to the X-ray energy divided by 3.8 (and thus linearly proportional to the energy of X-rays). The electrons are collected in less than a microsecond (before the next X-ray photon enters into the detector) by an applied bias voltage and integrated by a field-effect-transistor preamplifier. The output of this preamplifier is a series of steps, with the height of each step proportional to the energy of the corresponding X-ray. Both the silicon wafer and the field effect transistor are cooled to liquid nitrogen temperature to reduce the electronic noise in the output signal. This signal is further amplified and differentiated in low noise amplifier to produce a string of pulses, each one corresponding to an X-ray photon and with a height proportional to its energy. The pulses are measured and counted by multichannel analyser which functions by allowing each pulse to charge up a small capacitor and measuring the time required to discharge it again with a constant current. The resulting time is used as an address to store a count in spectrum in the memory of the devices. Since the time is proportional to pulse height and thus to X-ray energy, the result is the build-up of a spectrum of counts versus X-ray energy. This spectrum is then presented for viewing by the operator using a display. The energies at which peaks occur in the spectrum are readily identified with the element that produces the X-rays, thus giving elemental analysis of the specimen. The size of the peaks can thus be accounted in determining the amount of various elements present quantitatively.

The active area of the detector is usually between 10 to 30 mm^2 and its collection angle is a function of both this value and the distance from the detector to the specimen. Typical collection angles are in the range of 0.05-0.1 steradian (ster), which is only a small fraction of the total characteristics X-ray signal which is generated uniformly over 45 ster. The collection angle could obviously be improved by either expanding the active area or moving the detector closer to the specimen. Both options are limited by the space available in the microscope near the specimen. Also, it is customary to shield the Si chip from the presence of hydrocarbon contaminants in the vicinity of the specimen by use of a thin (±0.1μm) Be window. It should be kept in consideration that the ultralight elements are difficult to detect because of the high absorption of the low energy X-ray in the specimen itself and the less fluorescence yield coming out of the light elements. An important aspect in the EDAX analysis is the resolution which is defined as the width of the peaks in the spectrum and is usually specified as the full width at half maximum (FWHM) of a 5.9 keV manganese K_α peak from a radioactive F source. The importance of resolution is that it describes the interferences between peaks that are near each other in energy, very wide peaks overlap more than narrow peaks and make the analysis difficult for the same elements.

2.6 ELECTRICAL RESISTIVITY MEASUREMENT

Measurement of resistivity is very important for the magnetoresistive materials because the magnetoresistance (MR) ratio is calculated from resistivity measurements in different magnetic fields. In the present work, we have measured the variation of resistivity with temperature (ρ-T) in varying magnetic fields (0-12 kOe) over a temperature range of 80–350 K by using the "four probe" technique.

2.6.1 Four-probe method

Many conventional methods for measuring the resistivity are unsatisfactory because of including the contact resistance. Also there is generally minority carrier injection by one of the current carrying contacts. An excess concentration of minority carriers will affects the potential of other contacts and modulate the resistance of the materials. The four probes method overcomes the difficulties mentioned above and also offers several other advantages. It permits measurements of resistivity in samples having a wide variety of shapes, including the resistivity of small volumes within bigger pieces of samples. By this way the resistivity on both sides of a p-n junction can be determined with good accuracy.

The basic model of the four probe method is shown in Fig. 2.8. Four sharp probes are placed on a flat surface of the material to be measured, current is passed through the two outer probes and the floating voltage is measured across the inner pair of probes. In the present work, the bulk samples were prepared in the form of rectangular pellets of dimension 10 x 2 x 1 mm^3. The four evenly-spaced contact points were made by painting silver paste on the sample, which was heated up to 100 ^{0}C in air for half an hour to minimize the contact resistance. The operational procedure consist of passing a small DC current through the sample, which is placed in an inner cavity where the temperature is decreased by dipping the sample in liquid nitrogen or increased by a heater and measure the voltage drop between the two voltage wires after a fixed temperature interval. The temperature in an inner cavity is monitored through thermocouple. The signals from the voltage wires and from a thermocouple are collected, measured by a nano-voltmeter and multimeter, and recorded as resistance (Ω) and temperature (K).

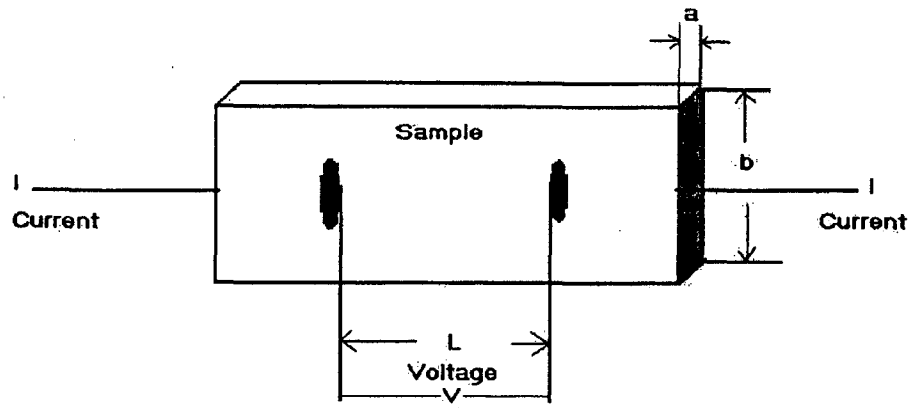

Figure 2.8: Block diagram of four probe arrangement.

The sample resistivity is calculated by using the formula:

$$\rho = \frac{V}{I} . \frac{ab}{L} (\Omega - cm) \tag{2.4}$$

where V is the voltage measured across two inner probes, I is the current passed through the sample, L (cm) is the length in voltage contact and a, b, are cross sectional sides. For this purpose **Keithley's 2182A-Nanovoltmeter, 2400-Constant Source Meter** and **2000-Multimeter** have been used. For magnetoresistance measurements, the probe with mounted sample has been placed between the poles of an electromagnet, which is capable to produce the magnetic field in the range of -12 to +12 kOe. The magnetoresistance (MR) ratio is calculated by measuring the resistivity over a temperature range of 80–350 K without and with magnetic field (0-12 kOe).

The MR ratio is calculated by using the formula:

$$MR(\%) = \frac{[\rho(0,T) - \rho(H,T)]}{\rho(H,T)} \times 100\% \qquad (2.5)$$

where ρ(0,T) and ρ(H,T) are the resistivity values for zero and applied fields, respectively.

2.7 VIBRATING SAMPLE MAGNETOMETER (VSM)

The most commonly used method for the characterization of magnetic materials is the vibrating sample magnetometer (VSM). Vibrating sample magnetometer (VSM) operates on Faraday's law of induction, which tells us that a changing magnetic field will produce an induced current. This induced current can be measured and can tell us information about the changing magnetic field. VSM is used to measure the magnetic behavior of magnetic materials. VSM operates by first placing the sample to be studied in a constant magnetic field. If the sample is magnetic, this constant magnetic field will magnetize the sample by aligning the magnetic domains, or the individual magnetic spins, with the field. The stronger the constant field, the larger the magnetization will be. The magnetic dipole moment of the sample will create a magnetic field around the sample, sometimes called the magnetic stray field. As the sample is moved up and down, this magnetic stray field is changing as a function of time and can be sensed by a set of pick-up coils. The alternating magnetic field will cause an induced current in the pick-up coils according to Faraday's law of induction. This current will be proportional to the magnetization of the sample. The greater magnetization results the greater induced current. The induction current is amplified by a trans-impedance amplifier and lock-in amplifier. The various components are hooked up to a computer interface. Using controlling and monitoring software, the system tells, how much the sample

is magnetized and how its magnetization depends on the strength of the constant magnetic field.

Generally, there are two types of magnetometers: DC magnetometer and AC magnetometer. In the present investigations, we have used the **Princeton Applied Research (Model 155)** DC magnetometer that based on an induction technique using pick-up coils. The block diagram of vibrating sample magnetometer is shown in Fig. 2.9. The electromagnet used in this VSM produces the magnetic field in the range of -10 to +10 kOe. The magnetization is measured at particular constant magnetic field. The sample is mounted at the end of a rigid rod attached to a mechanical resonator, which oscillates the sample, usually in a vertical direction, at a fixed frequency (ω). In our magnetometer, the frequency, ω is 80 Hz. There is a set of pick-up coils nearby the sample. The sample frequency is synchronized with the lock-in amplifier. As the sample moves, its magnetic field, which is proportional to its magnetic moment (M), alters the magnetic flux (dM/dt) through the coils. This induces a current directly proportional to dM/dt, which can be amplified and detected using lock-in amplifier. The external magnetizing field is provided by a horizontal electromagnet.

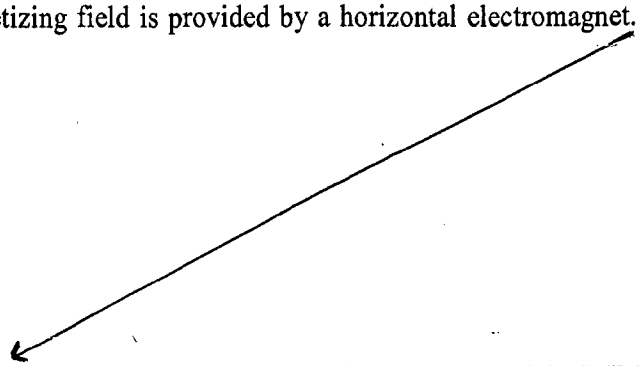

It is of the great importance that the design of the VSM ensures that the vibration of the sample produces no vibration of the pick-up coils, relative to the magnet. If that would be the case, it would result in large spurious signals. This problem is reduced if the magnetic

field is very homogeneous and thus we use large electromagnet with large pole piece diameter in our magnetometer.

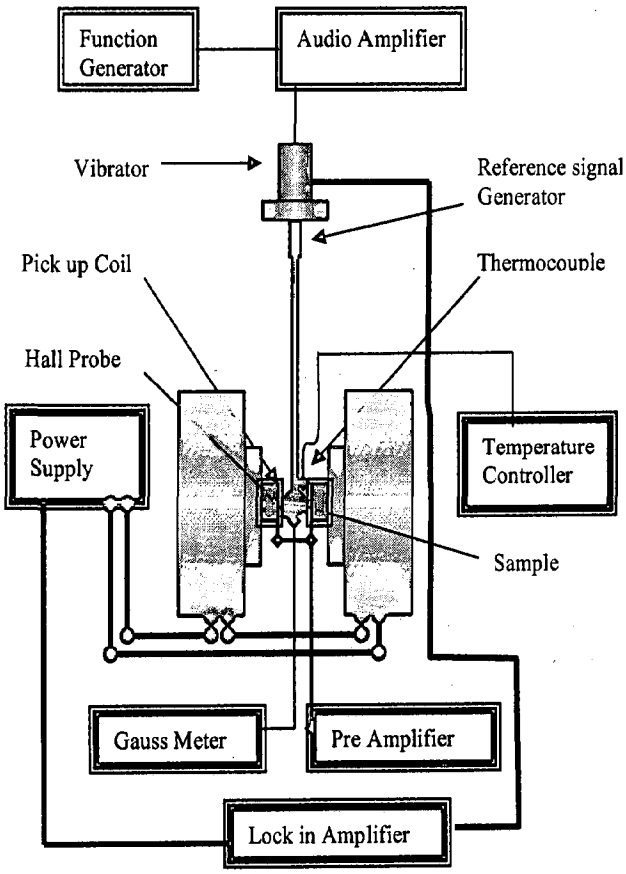

Figure 2.9: The block diagram of vibrating sample magnetometer.

2.8 SPECIFICATIONS OF THE INSTRUMENTS USED

(a) X-ray Diffractometer

Model: Bruker AXS D-8 Advance

Target: Cu (Ni filtered Cu-Kα X-rays of wavelength 1.5406 Å)

Working Voltage: 10 to 140 kV

Tube current: 4.4 to 40 mA

(b) Scanning Electron Microscope (SEM)

Model: LEO 435-VP

Operating Voltage: 15 to 30 kV

Resolution: 6 nm

(c) Energy Dispersive X-ray Analysis (EDAX)

Model: EDAX' TSL, AMETEK

Operating Voltage: 15 to 30 kV

Element range: all above Be

(d) Nanovoltmeter

Model: Keithley 2182A

Voltage range: 10 mV to 100 V

Resolution: 1 nV

(e) Constant Source Meter

Model: Keithley 2400

Current range: ± 50 pA to ± 1 A

Voltage range: ± 1 μV to ± 200 V

Resolution: 50 pA and 1 μV

(f) Multimeter

Model: Keithley 2000

Thermocouple used: K type Alumel/Chromel

Temperature range: -200 to 1372 ^{0}C

Resolution: 0.001 ^{0}C

Accuracy relative to reference junction: ± 0.5 ^{0}C

(g) Electromagnet

Model: Control Systems and Devices

Pole diameter: 150 mm

Pole gap: 40 mm (fixed)

Magnetic field range: -12 to +12 kOe

Field sensitivity: ± 0.25 %

(h) Vibrating Sample Magnetometer (VSM)

Model: 155, Princeton Applied Research

Range: 0.00001 to 100 emu

Temperature range: 77 to 1060 K

Sample weight: 20 mg (in powder form)

Sample size: Diameter 2.5 mm, Length 1-2.5 mm

Magnetic field range: -10 to +10 kOe

REFERENCES

1. Greskovich S C, "Milling treatise on materials science and technology", Ceramic fabrication processes, (Edited by Wang F F Y, academic Press, New York) Vol. **9**, (1976).
2. Yoldas B E, "Alumina gels that form porous transparent Al_2O_3", J. Mater. Sci., **10**, 1856 (1975).
3. Yoldas B E, "Preparation of glasses and ceramics from metal-organic compounds", J. Mater. Sci., **12**, 1203 (1977).
4. Yamane M, Shinji A & Sakaino T, "Preparation of a gel from metal alkoxide and its properties as a precursor of oxide glass", J. Mater. Sci., **13**, 865 (1978).
5. Mazdiyasni K S, Dolloff R T & Smith II J S, "Preparation of high-purity submicron barium titanate powders", J. Am. Ceram. Soc., **52**, 523 (1969).
6. Smith II J S, Dolloff R T & Mazdiyasni K S, "Preparation and characterization of alkoxy-derived $SrZrO_3$ and $SrTiO_3$", J. Am. Ceram. Soc., **53**, 91 (1970).
7. Brinker C J & Scherer G W, Sol–Gel science, (Academic, New York, 1990).
8. Livage J, "The gel route to transition metal oxides", J. Solid State Chem., **64,** 322 (1986).
9. Chandler C D, Roger C & Hampden-Smith M J, "Chemical aspects of solution routes to perovskite-phase mixed-metal oxides from metal-organic precursors", Chem. Rev., **93**, 1205 (1993).
10. Zelinski B J J & Uhlmann D R, "Gel technology in ceramics", J. Phys. Chem. Solids, **45**, 1069 (1984).
11. Pierre A C, "Sol-gel processing of ceramic powders", Ceramic Bulletin, **70**, 1281 (1991).

12. Westin G, "A study of sol-gel preparation of Mn-Sb oxides via bimetallic alkoxides or mixed acetate-alkoxide routes", Chem. Commun. (Stockholm University) **4,** 1 (1994).

13. The Sol-gel gateway: www.solgel.com.

14. Lisboa-Filho P N, Mombru A W, Pardo H, Ortiz W A & Leite E R, "Influence of processing conditions on the crystal structure and magnetic behavior of $La_{0.7}Ca_{0.3}MnO_{3\pm\delta}$ samples", J. Phys. Chem. Solids, **64,** 583 (2003).

15. Vertruyen B, Rulmont A, Cloots R, Ausloos M, Dorbolo S & Vanderbemden P, "Synthesis of CMR manganate compounds: the consequences of the choice of a precursor method", Mater. Lett, **57,** 598 (2002).

16. Mahesh R, Mahendiran R, Raychoudhary A K & Rao C N R, "Effect of particle size on the giant magnetoresistance of $La_{0.7}Ca_{0.3}MnO_3$", Appl. Phys. Lett., **68,** 2291 (1996).

17. Shankar K S, Kar S, Subbanna G N & Raychaudhuri A K, "Enhanced ferromagnetic transition temperature in nanocrystalline lanthanum calcium manganese oxide ($La_{0.67}Ca_{0.33}MnO_3$)", Solid State Commun., **129,** 479 (2004).

18. Li R W, Xiong H, Sun J R, Li Q A, Wang J H, Zhang J & Shen B G, "Super paramagnetism and transport properties of ultrafine $La_{2/3}Ca_{1/3}MnO_3$ powders", J. Phys.: Condens. Matter, **13,** 141 (2001).

19. Cullity B D & Stock S R, "Elements of X-ray diffraction", (Prentice Hall Publishing Comp., New Jersy) (2001).

20. Wilson A J C, "Variance as a measure of line broadening", Nature, **193,** 568 (1962).

21. Wilson A J C, "On Variance as a measure of line broadening in diffractometry, general theory and small particle size", Proc. Phys. Soc. (London), **80,** 286 (1962).

22. Warren B E & Averbach B L, "The effect of cold-work distortion on X-ray patterns", J. Appl. Phys., **21,** 595 (1950).

23. De Keiyser Th H, Langford J I, Mittemeijer & Vogels A B P, "Use of the Voigt function in a single-line method for the analysis of X-ray diffraction line broadening", J. Appl. Cryst., **15**, 308 (1982).

24. Brooker G R, "Modern diffraction and imaging techniques in material science", (eds. Amelincks S, Geveres, Rement G, Van Landuyt J), (North-Holland publishing co. Amsterdam) 533 (1970).

25. Goldstein J I, Yakowitz H (ed.), "Practical scanning electron microscope", (Plenum Press, New York) (1975).

26. Heal J W, Sparrow J T & Cross P M, "Use of the scanning electron microscope", (Pergamon Press, Oxford) (1972).

27. Grundy P J & Jones G A, "Electron microscopy in the study of materials", (Edward Arnold, London) pp. 175 (1976).

Chapter - 3

SINTERING TEMPERATURE EFFECT ON MAGNETOTRANSPORT PROPERTIES OF NANOPHASIC $La_{0.7}Sr_{0.3}MnO_3$ AND $La_{0.67}Ca_{0.33}MnO_3$ MANGANITES

3.1 INTRODUCTION

The observation of colossal magnetoresistance in a narrow temperature range around the ferromagnetic transition temperature (Tc) in single crystals and epitaxial films of doped manganites generally requires the large applied magnetic fields (> 1 Tesla), which severely restricts their potential applications [1-3]. So, to observe the large MR over a wide temperature range and in relatively smaller external applied magnetic fields (~mT) is the goal of many research groups working in this field world wide. Significant differences in the magnetoresistance (MR) properties of polycrystalline and single crystal material have been reported since the initial discovery of CMR in the manganites. Initial work on bulk polycrystalline samples has shown a substantial MR at temperatures much below T_C whereas the MR magnitude below T_C is usually very small in single crystals or epitaxial films of the same composition [4, 5]. A number of subsequent studies, both on bulk and thin film samples, have confirmed the important role of grain boundaries (GB's) on the MR behaviour of manganites because of enhanced MR at low field of the order of few oersted [4-26].

One of the first reports regarding the effect of particle size on the transport and magnetic properties of polycrystalline $La_{0.7}Ca_{0.3}MnO_3$ has come from Mahesh et al. [6]. They prepared samples with different particle sizes (0.025-3.5 μm) by citrate-gel route followed by

heat treatment at different temperatures in an appropriate atmosphere. For a direct comparison of the properties of the samples as a function of grain size, it is important to ensure that the Mn^{4+} concentration remains same in different samples, since it is crucial factor in controlling the transport and magnetic properties. They found that the resistivity (ρ) of the LCMO samples increases substantially as particle size decreases. Moreover, the ratio of the resistivity (ρ) at 4.2 K and at the peak close to Tc, decreases with increasing the particle size. Tc is also observed to be broadened with decreasing the particle size. Moreover, the samples with particle size ~0.25 μm even do not exhibit a well defined transition temperature. They also noted that despite of these changes, the MR near the peak did not show any significant changes with the particle size. However, the MR at 4.2 K has low-field and high-field component and the low-field component increases with decrease in particle size. So by this study, they concluded that the substantial part of the MR at low temperatures arises from the grain boundaries.

Another study by Hwang et al. [5] further elaborated the role of GB's in manganites by direct comparison of the MR and field-dependent magnetization at low temperatures for single crystal and bulk polycrystalline samples of $La_{0.67}Sr_{0.33}MnO_3$ (LSMO). Single crystal of LSMO was grown by floating zone method, whereas polycrystalline LSMO samples were prepared through conventional solid-state reaction method by sintering the samples in air at 1300 °C and 1700 °C. Both the single crystal and polycrystalline samples show a sharp drop in ρ at Tc. However, at low temperatures, ρ of the polycrystalline samples is found to be significantly higher than that for the single crystal. Hwang et al. also showed that ρ at 5 K is 35 μΩ-cm for single crystal LSMO, while the ρ of the 1700 °C polycrystalline sample is about an order of magnitude higher due to additional scattering introduced by the GB's. Furthermore, the ρ of the 1300 °C sample is almost an order of magnitude larger than the

1700 °C sample due to the smaller grain size. Despite the differences in ρ, the temperature dependence of magnetization at 0.5 T is quite similar for these three samples. MR studies show that for the single crystal there is negligible MR at low temperatures, and with increasing temperature, there is increase in negative MR. Correspondingly, the magnetization shows a rapid rise because of magnetic domain rotation at low applied fields, followed by a slow approach toward saturation at higher fields. The variation in the magnetization at various temperatures for the single crystal closely tracks the MR, strongly suggesting that the suppression of magnetic fluctuations is the origin of the negative MR in the single crystal sample. Further, it is also observed that unlike the single crystal, both polycrystalline samples (sintered at 1300 °C and 1700 °C) exhibit a sharp drop in the resistance at low fields followed by a slower background negative MR at higher fields. The sharp drop is greatest at the lowest temperatures and decreases with increasing temperature. In contrast to the resistivity variations, the magnetization data are very similar to that for the single crystal. This suggests that the MR in the polycrystalline samples is dominated by intergrain effects and sharp drop in resistance by applying the magnetic field is associated with magnetic domain rotation. In order to analyze the temperature (T) dependence of the low field MR component, Hwang et al. have back-extrapolated the high field $\rho(H)/\rho(0)$ to find the zero-field intercept and calculated the magnitude of the MR associated with magnetic domain rotation. Their result clearly showed that MR increases with decreasing temperature. Another important observation was that the MR in the polycrystalline samples above 0.5 T appears to have exactly the same magnetic field (H) dependence for the entire temperature range (5–280 K). It appears that the MR has weak H^2 dependence in addition to the visually obvious dominant H linear term. They concluded that LFMR observed in polycrystalline LSMO is due to spin polarized tunneling between misaligned grains. It was further shown by Wang et al. [7] that,

phenomenologically, one has to distinguish weak and strong links between the grains. Only weakly linked grain boundaries give considerable low field magnetoresistance. Gupta et al. [8] have systematically explored the properties of epitaxial and polycrystalline films of $La_{0.67}Ca_{0.33}MnO_3$ (LCMO), $La_{0.67}Sr_{0.33}MnO_3$ (LSMO), and $La_{0.75}MnO_3$ and found that, unlike the epitaxial films, the polycrystalline films show substantial MR over a wide temperature range in all three systems. They used a wide-angle Kerr microscope to image the domains in the polycrystalline manganite films of LSMO. Because these domains have different coercivities, they are weakly coupled and orient successively in an increasing field. This work clearly brings out the difference between magnetization in polycrystalline and epitaxial LSMO films at microscopic level, which gives a qualitative idea about the LFMR in polycrystalline samples. Additional information regarding the behaviour of polycrystalline films has come from Shreekala et al. [27], who have studied the effect of crystallinity on the MR in $La_{0.67}Ba_{0.33}MnO_3$ (LBMO) and LCMO films. They have grown epitaxial films on $LaAlO_3$ and $Bi_4Ti_3O_{12}$ buffered yttria-stablized zirconia (YSZ) substrates. Polycrystalline films show the mixture of orientations when deposited on polycrystalline YSZ substrates, whereas oriented polycrystalline films are formed on YSZ buffered Si substrate. The MR in the epitaxial films is maximum close to Tc while polycrystalline films show a monotonic increase in MR with decreasing temperature, which is the behaviour of low field magnetoresistance. The above discussion makes it evident that in the polycrystalline samples (both bulk and thin films) colossal magnetoresistance (CMR) can be observed at relatively low magnetic fields (~mT). This is important for the application point of view of CMR because the applications are feasible only at low magnetic fields (~mT).

During the last decade, nanocrystalline form of various materials has also drawn considerable attention because they typically exhibit physical and chemical properties that

are distinct from their bulk counterparts. The physical properties of manganites are also expected to depend on particle size due to both the nanoscale phase inhomogeneities inherent to these materials and additional surface effects. Hwang et al. [5] pointed out that the large low field magnetoresistance (LFMR) of the polycrystalline samples is dominated by spin polarized tunneling between neighbouring grains. This is quite different from their single crystals and epitaxial films counterparts where the double exchange mechanism is prominent. The bulk samples of manganites were usually synthesized by the conventional ceramic methods that need higher sintering temperature and long annealing time to obtain homogenous composition and desired structure. These methods are not appropriate for many advanced applications, due to formation of large particles, agglomerates, poor homogeneity, undesirable phases, abnormal grain growth and an imprecise stoichiometric control of cations. However, the sol gel process has potential advantage over the other methods not only for achieving homogenous mixing of the components on the atomic scale, but also for the possibility of forming desired shapes which are of technological importance. Other advantages of the sol-gel route are lower processing temperatures, short annealing times, high purity of materials, good control of size and shape of the particles and particle size well below 100 nm at the lower processing temperature. There are several reports on the synthesis of nanophasic manganites by sol-gel based synthesis methods [6, 28-36] but none of them seems to have carried out extensive studies on the effect of sintering temperature on sol-gel synthesized manganites in relation to low field magnetotransport properties. In this chapter, we have described and discussed the synthesis of $La_{0.7}Sr_{0.3}MnO_3$ and $La_{0.67}Ca_{0.33}MnO_3$ perovskite manganites by low temperature sol-gel route and studied the effect of sintering temperature on low field magnetotransport properties.

3.2 EXPERIMENTAL

The nanophasic samples of $La_{0.7}Sr_{0.3}MnO_3$ (LSMO) and $La_{0.67}Ca_{0.33}MnO_3$ (LCMO) were synthesized via sol-gel method. The required amounts of high purity nitrates of La $LaN_3O_9.6H_2O$, Sr ($Sr\{NO_3\}_2.4H_2O$) or Ca ($Ca\{NO_3\}_2.4H_2O$) and acetate of Mn ($\{CH_3COO\}_2Mn.4H_2O$) were dissolved in the double distilled water to form an aqueous solution. An equal amount of ethylene glycol was added to this solution with continuous stirring. This solution was then heated on a hot plate at temperature of ~80-100 °C till a dry thick brown sol was formed. This was further decomposed in an oven at a temperature of 250 °C to get the dry fluffy material. The polymeric precursor thus obtained was calcined at 350 °C for 12 h. The resulting powder was separated into parts and pressed in the form of pellets and sintered at 600, 700, 800, 900 and 1000 °C for 12 h. Both kind of the samples $La_{0.7}Sr_{0.3}MnO_3$ and $La_{0.67}Ca_{0.33}MnO_3$ were synthesized by the same process as mentioned above. The $La_{0.7}Sr_{0.3}MnO_3$ samples sintered at 600, 700, 800, 900 and 1000 °C are referred to as **T6, T7, T8, T9,** and **T10,** respectively while the $La_{0.67}Ca_{0.33}MnO_3$ samples sintered at 600, 700, 800, 900 and 1000 °C are referred to as **P6, P7, P8, P9,** and **P10**, respectively.

The structural characterization was done by using X-ray diffraction (Bruker AXS D-8 Advance, CuK_α radiation) technique at room temperature and surface morphology was investigated by using a scanning electron microscope (SEM Model LEO 435-VP operating at 15 kV). The temperature dependence of the resistivity of samples was measured by a standard four-probe method using Keithley instruments with and without magnetic fields (0-12 kOe). The DC magnetization measurements were done by using vibrating sample magnetometer (VSM Model 155, Princeton Applied Research).

3.3 RESULTS AND DISCUSSION OF $La_{0.7}Sr_{0.3}MnO_3$

3.3.1 X-ray diffraction studies

X-ray diffraction patterns, recorded at room temperature, of the $La_{0.7}Sr_{0.3}MnO_3$ (LSMO) samples are shown in Fig. 3.1. The X-ray diffraction results indicate that all the samples T6, T7, T8, T9 and T10 sintered at 600, 700, 800, 900 and 1000 °C, respectively correspond to pure LSMO phase with no detectable secondary phases within the accuracy of measurement.

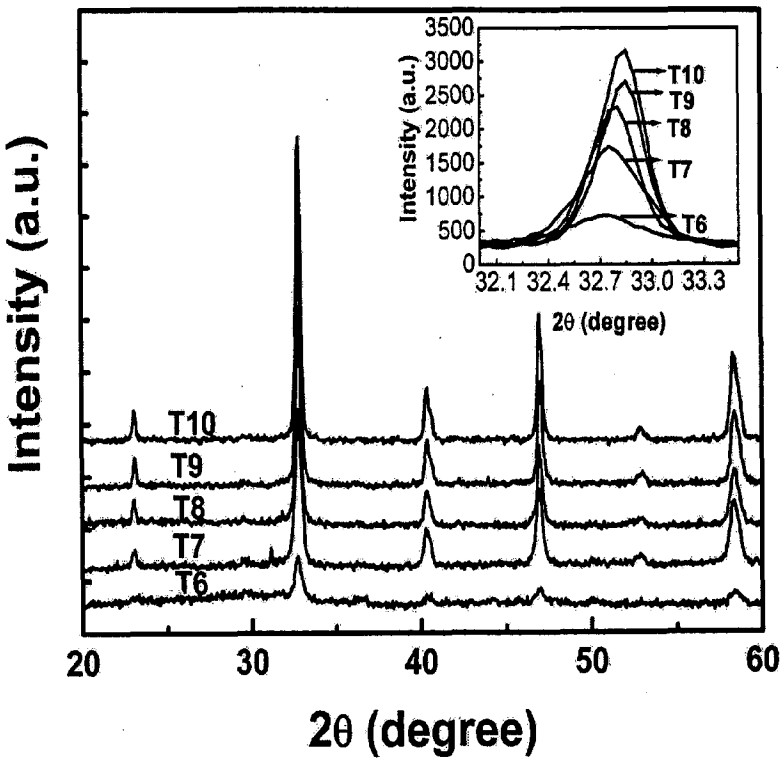

Figure 3.1: X-ray diffraction patterns of $La_{0.7}Sr_{0.3}MnO_3$ samples sintered at 600 °C (T6), 700 °C (T7), 800 °C (T8), 900 °C (T9) and 1000 °C (T10). Inset shows the variation in intensity with 2θ of most intense (121) peak (near 2θ = 33°).

The pure LSMO phase has been obtained at the sintering temperature as low as 600 °C. The intensity of diffraction peaks for LSMO perovskite phase increases as the sintering

temperature increases from 600 to 1000 °C indicating that the crystallinity of LSMO phase becomes better and particle size increases as sintering temperature increases. Inset of Fig. 3.1 shows the most intense (121) reflection (near $2\theta = 33°$) of T6, T7, T8, T9, and T10 samples. It is clear from the inset that as sintering temperature increases, the intensity of the (121) reflection increases and there is a decrease in full width at half maximum (FWHM), hence the particle size increases. The shifting of (121) peak towards higher value of Bragg angle indicates that the lattice parameter decreases with increasing the sintering temperature. The calculated lattice parameters (orthorhombic unit cell parameters a, b, c,) and cell volume of unit cell (V = abc) are shown in Table 3.1.

Table 3.1: Unit-cell parameters, cell volume, particle size and grain size of $La_{0.7}Sr_{0.3}MnO_3$ samples sintered at different temperatures.

Sintering temp.	Unit-cell parameters			Unit cell	Particle size	Grain size
T_S (^{0}C)	a(Å)	b (Å)	c(Å)	vol. (Å)^3	from XRD (nm)	from SEM(nm)
600	5.486	7.732	5.451	231.2192	31	37
700	5.454	7.709	5.481	230.4480	39	48
800	5.467	7.691	5.465	229.7852	51	66
900	5.426	7.679	5.485	228.5394	56	115
1000	5.417	7.664	5.473	227.2165	60	163

It is observed that the cell volume of the unit cell decreases as sintering temperature increases. The average particle sizes of the samples are determined from X-ray data using Scherrer's formula ($PS \sim K\lambda / \beta\cos\theta$, where K~0.89 is the shape factor, λ is wavelength of x-rays, β is the FWHM and θ is Bragg angle) [37]. The calculated average particle sizes are ~31, ~39, ~51, ~56 and ~60 nm for the samples sintered at 600, 700, 800, 900 and 1000 °C, respectively.

3.3.2 Microstructural analysis

The representative SEM images of the samples T7, T8, T9, and T10 are shown in Fig. 3.2 (a)-(d), respectively. It can be seen from Fig. 3.2 that the grain boundaries in sample (T7) are not clear and there is a long neck between two grains. With the increase of sintering temperature from sample (T7) to sample (T10), the size of grain becomes larger, the grain boundaries become clear, and the necks among grains disappear.

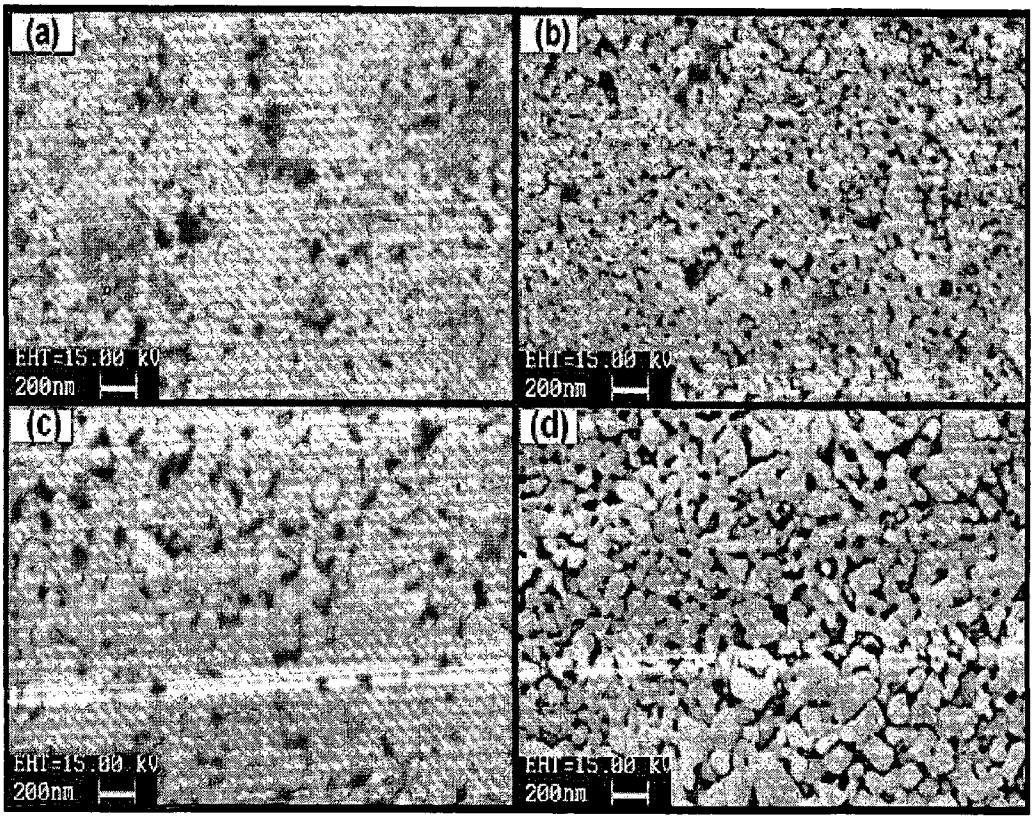

Figure 3.2: Scanning electron micrographs of $La_{0.7}Sr_{0.3}MnO_3$ samples sintered at different temperatures: (a) 700 °C (T7), (b) 800 °C (T8), (c) 900 °C (T9) and (d) 1000 °C (T10).

When the size of grain becomes larger, the grain boundary effects should also decrease from sample (T7) to sample (T10) because of the decrease of number of grain boundaries. The average grain sizes measured from SEM micrographs are ~37, ~48, ~66, ~115 and ~163 nm for the samples T6, T7, T8, T9, and T10, respectively.

3.3.3 Magnetic properties

The magnetization curves of all the samples measured under 5 kOe field in the temperature range (80-450 K) are shown in Fig. 3.3. All the samples show the paramagnetic (PM) - ferromagnetic (FM) transition at a particular temperature (Tc). We observed a slight variation in Tc for the samples sintered at different temperatures. The transition temperatures determined from the peak in (dM/dT)-T curves are found to be ~311, ~321, ~324, ~326 and ~330 K for the samples T6, T7, T8, T9, and T10, respectively.

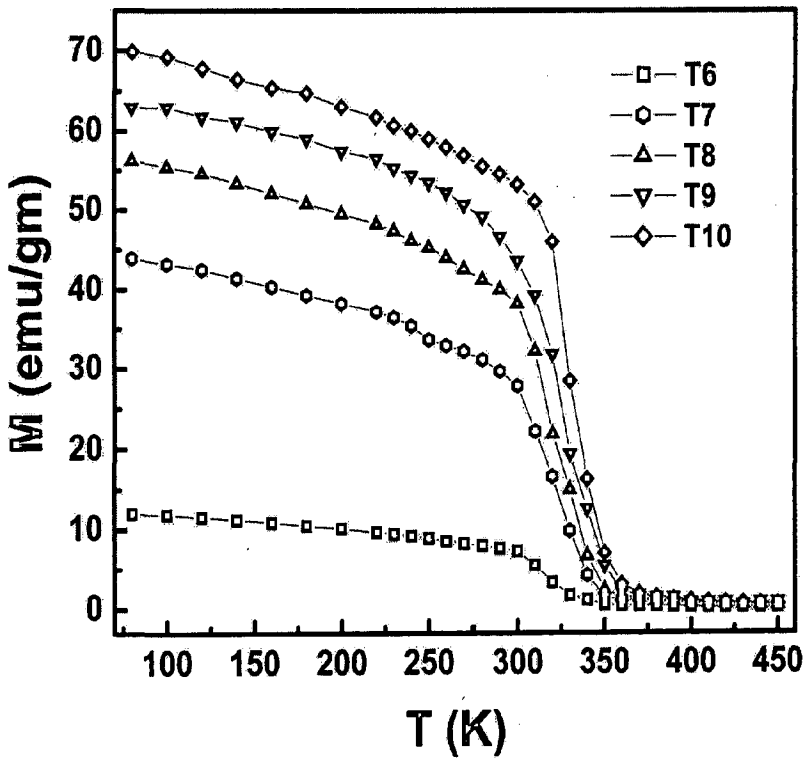

Figure 3.3: Temperature dependence magnetization at 5 kOe of $La_{0.7}Sr_{0.3}MnO_3$ samples sintered at different temperatures.

Moreover, the magnetization also decreases as sintering temperature decreases. The value of magnetization (M) at 80 K for the samples T6, T7, T8, T9 and T10 are 11.96, 43.88, 56.28, 62.95 and 69.88 emu/gm, respectively. It may be because of formation of extra grain boundaries as sintering

temperature decreases and leading to enhanced broken Mn-O-Mn bonds at the surface, which causes decrease in the magnetization values. This is the most general observation in case of nanoparticles of the manganite system [30, 38]. However, a report by Fu [22] on the $La_{0.8}Ca_{0.2}MnO_3$ nanoparticle system, shows results contradicting the above facts on reduced particle size. He reported that the magnetization increases as particle size decreases due to strain at the grain boundaries. Zhang et al. also analyzed in detail the effect of the annealing on the magnetization for various x values in $La_{1-x}Sr_xMnO_3$ system [39]. They found that at low doping ($x < 0.25$), the magnetization decreases with an increase in sintering temperature and for higher doping ($x > 0.25$), the magnetization increases with an increase in sintering temperature. So our results supports the Zhang et al. [39], i.e. for $x > 0.25$ the magnetization decreases with decreasing the sintering temperature and grain boundaries play the important role in reduction of magnetization. The magnetization versus field (M-H) curves at 300 K for the studied samples are displayed in Fig. 3.4.

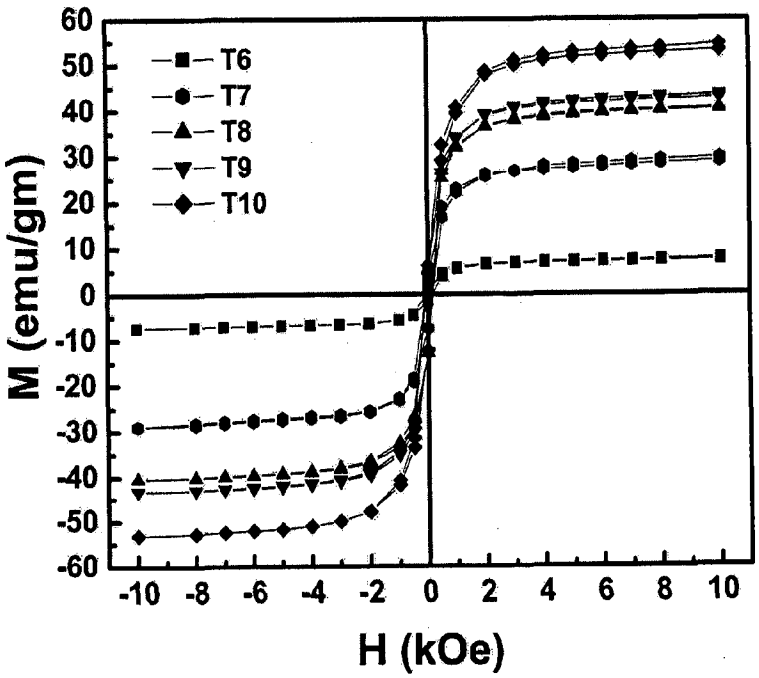

Figure 3.4: Field dependence magnetization (M-H) curves at room temperature of $La_{0.7}Sr_{0.3}MnO_3$ samples sintered at different temperatures.

M-H curves also show that the magnetization of the samples decreases with decreasing the sintering temperature. This demonstrates that ferromagnetic order is weakened and magnetic disorder increases on reducing the sintering temperature.

3.3.4 Electrical resistivity measurements

The temperature dependence resistivity at zero field measured in temperature range (80-325 K) for the studied samples is shown in Fig. 3.5. The resistivity of the samples increases as the sintering temperature or particle size decreases. The values of resistivity are 59.19, 1.59, 0.76, 0.39 and 0.14 Ω-cm at room temperature (300 K) for the samples T6, T7, T8, T9 and T10, respectively. Thus, the resistivity of sample T6 increases by more than one order of magnitude as compared to sample T10. This increase in resistivity is caused due to enhanced scattering of the charge carriers by increasing the grain boundaries as sintering temperature decreases. On increasing the sintering temperature, the particle size increases leading to a decrease in grain boundaries and magnetic disorder. This causes decrease in scattering of the carriers and hence decrease in the resistivity. All the studied samples show an insulator ($d\rho/dT<0$) to metal ($d\rho/dT>0$) transition at a particular temperature (T_{IM}) on lowering the temperature. The value of insulator to metal transition temperatures are ~175, ~228, ~245, ~273 and ~303 K for the samples T6, T7, T8, T9 and T10, respectively. Thus the value of transition temperature decreases from 303 to 175 K as the sintering temperature decreases from 1000 to 600 °C. The T_{IM} is an extrinsic property and strongly depends on the synthesis condition and microstructure (e.g. grain boundaries). The strong suppression in the value of T_{IM} with decreasing the sintering temperature is due to suppression of double exchange (DE) mechanism because of increase in non magnetic phase fraction, which is due to enhanced grain boundaries as a consequence of lower sintering temperature.

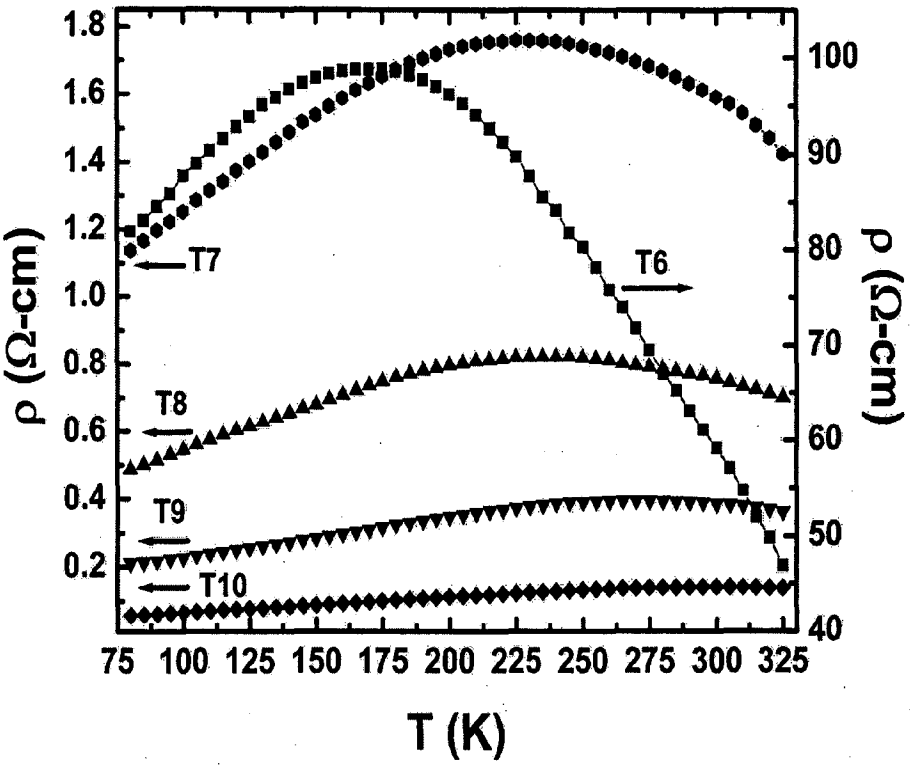

Figure 3.5: Temperature dependence resistivity at zero field of $La_{0.7}Sr_{0.3}MnO_3$ samples sintered at different temperatures.

Thus lowering the sintering temperature reduces the metallic transition temperature and increases the resistivity. It is also noted that there is a large difference between the value of T_{IM} and Tc for the samples sintered at lower temperatures. The variation of T_{IM} and Tc with sintering temperature is shown in Fig. 3.6. From the Fig. 3.6 it is clear that there is substantial decrease in T_{IM} (303-175 K) when sintering temperature decreases from 1000-600 °C, whereas Tc decreases only marginally (330-311 K). This difference is due to the fact that Tc is an intrinsic property and does not show much dependence on sintering temperature while T_{IM} is an extrinsic property that strongly depends upon the grain boundaries and hence the sintering temperature [40].

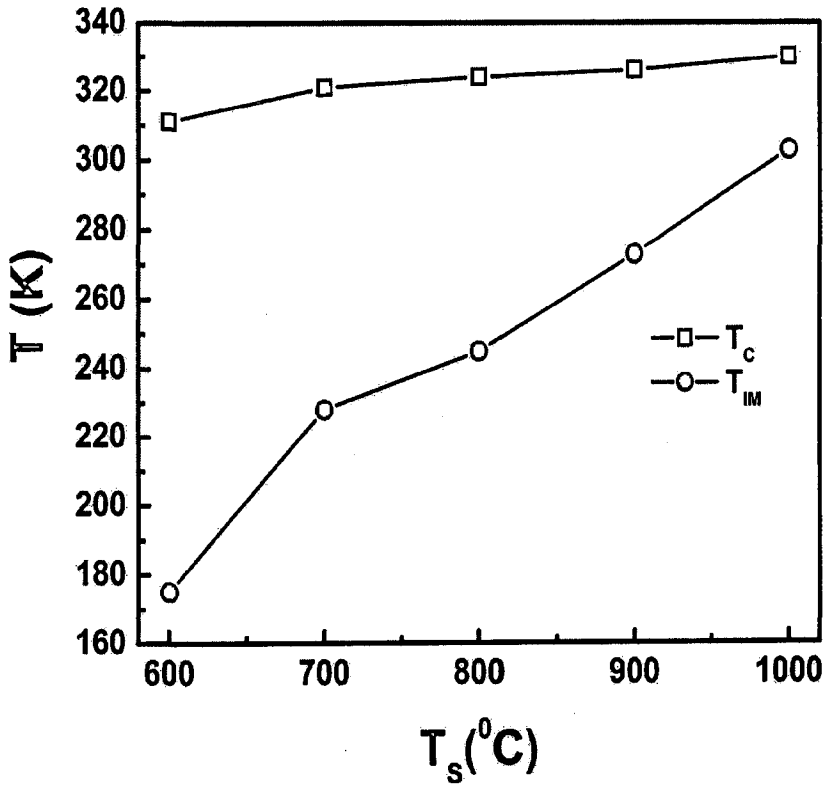

Figure 3.6: Variation of insulator-metal transition temperature (T_{IM}) and PM-FM transition temperature (Tc) with sintering temperatures.

3.3.5 Magnetoresistance studies

The temperature dependence of magnetoresistance (MR) for the studied samples measured in the range 80-300 K at the field of 1 kOe and 10 kOe are shown in Fig. 3.7. The MR ratio is defined as MR (%) =[ρ(0,T) – ρ(H,T)] / ρ(H,T) × 100 %, where ρ(0,T) and ρ(H,T) are the resistivity values for zero and applied fields, respectively. The MR of all the samples measured at 1 and 10 kOe, increases on lowering the sintering temperature. The MR values at 80 K are 15.3, 12.9, 10.8, 9.4 & 7.9 % at 1 kOe and 28.9, 26.5, 24.1, 22.5 & 21.1 % at 10 kOe for the samples T6, T7, T8, T9 and T10, respectively (as shown in Table 3.2). The measurements of MR at both fields reveal that the maximum MR is observed for the sample T6 sintered at lowest temperature (600 °C).

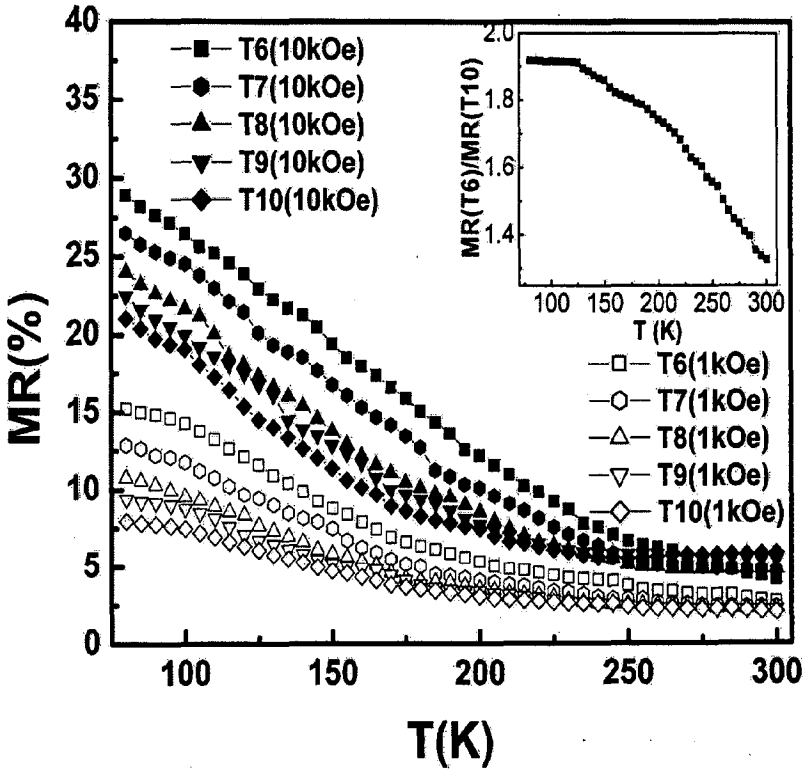

Figure 3.7: Temperature dependence magnetoresistance (MR) in a field of 1kOe and 10 kOe of $La_{0.7}Sr_{0.3}MnO_3$ samples sintered at different temperatures. Inset shows the MR (T6) / MR (T10) ratio with temperature at 1 kOe.

This enhancement in MR basically arises due to the intergrain spin polarized tunneling across the grain boundaries at T<Tc as proposed by Hwang et al. [5]. The existence of the grain boundaries is a key ingredient in the mechanism of electric transport, since it constitutes the barriers through which carriers should cross or tunnel [5]. The grain boundary contribution usually increases on decreasing the sintering temperature. So, in our samples low field magnetoresistance (LFMR) increases with decreasing the sintering temperature because of enhanced spin polarized tunneling through increased grain boundaries as sintering temperature decreases. So, in the present case, LFMR increases with decreasing sintering

temperature because we are increasing the disordered surface by decreasing the sintering temperature or particle size [38, 41].

Table 3.2: Insulator-metal transition temperature (T_{IM}), paramagnetic-ferromagnetic transition temperature (Tc) and magnetoresistance (MR) of $La_{0.7}Sr_{0.3}MnO_3$ samples sintered at different temperatures.

T_S (^{0}C)	T_{IM} (K)	Tc (K)	MR (%) at 80 K	
			1 kOe	10 kOe
600	175	311	15.3	28.9
700	228	321	12.9	26.5
800	245	324	10.8	24.1
900	273	326	9.4	22.5
1000	303	330	7.9	21.1

The reduction in magnetization with decreasing the sintering temperature (Fig. 3.3) also supports the magnetic spin disorder induced by grain boundaries in samples sintered at lower temperatures and this spin disorder is suppressed by applying the magnetic field, resulting the enhancement in MR.* The variation of the ratio of MR of sample T6 and T10, measured at 1 kOe, with temperature is shown in the inset of Fig. 3.7. It shows that the ratio of MR increases with decreasing the temperature and the MR of sample T6 at 80 K is almost two times of the MR of sample T10 at 1 kOe while it is ~1.4 times at 10 kOe. Moreover, as we go from sample T10 to T6, the value of MR at 80 K increases from 7.9 to 15.3 % at 1 kOe while 21.1 to 28.9 % at 10 kOe (see Table 3.2). So, the percentage change in MR at 80 K for sample T6 with respect to sample T10 is ~94 % at 1 kOe and ~37 % at 10 kOe. This shows that the percentage change in MR for sample T6 with respect to sample T10 is more at low field (1 kOe) as compared to higher field (10 kOe). Continuous enhancement in MR with decreasing the temperature (300 to 80 K) also supports its low field magnetoresistance behaviour. As Hwang et al. [5] demonstrated that the MR in the polycrystalline samples

* The enhancement in resistivity at low temperature (80 K) from 0.06 to 81.84 Ω-cm on reducing the sintering temperature from 1000 to 600 °C (see Fig. 3.5) supports the enhanced

exhibits two distinct regions: large MR at low fields dominated by spin-polarised tunneling between grains and high field MR which is remarkably temperature independent from 5 to 280 K. They also showed that the low field MR caused through spin-polarised tunneling increases with decreasing the temperature and high field MR above 0.5 T remains temperature independent over a wide range from 5 to 280 K. In our case, the MR is not constant with temperature and it increases with decreasing the temperature for both (1 and 10 kOe) field scales, which demonstrates that this enhanced MR is first one, i.e., low field MR dominated by spin-polarised tunneling through increased grain boundaries as sintering temperature decreases. In the present case, this low field MR behaviour is up to 10 kOe which is possibly due to our low sintering temperature as compared to 1300 and 1700 °C sintering temperature of Hwang et al. [5]. So in our case the spin-polarised tunneling phenomenon is more effective due to enhanced grain boundaries as sintering temperature is low. Therefore, the more enhancements in MR at low fied (1 kOe) is caused by enhanced spin polarized tunneling through increased grain boundaries as sintering temperature decreases.

The magnetic field dependence of MR for all the studied samples measured in magnetic field range of 0-12 kOe at 80 K is shown in Fig. 3.8. Analysis of Fig. 3.8 shows that with increase in the magnetic field from 0 to 12 kOe, the MR of all the samples increases with increasing the magnetic field and the large MR value is found in the samples sintered at lower temperature. The maximum MR is observed in sample T6 sintered at the lowest temperature (600 °C). The value of MR at 80 K for the sample T6 is 30.3 % while it is 22.1 % for the samples T10 at 12 kOe. It should also be noted that the variation of MR does not show any saturation in MR even up to 12 kOe but the percentage change in MR for sample T6 with respect to sample T10 is more at low field (1 kOe) as compared to higher field (10

kOe). This enhancement in MR as sintering temperature decreases again caused through spin polarized tunneling at the grain boundaries.

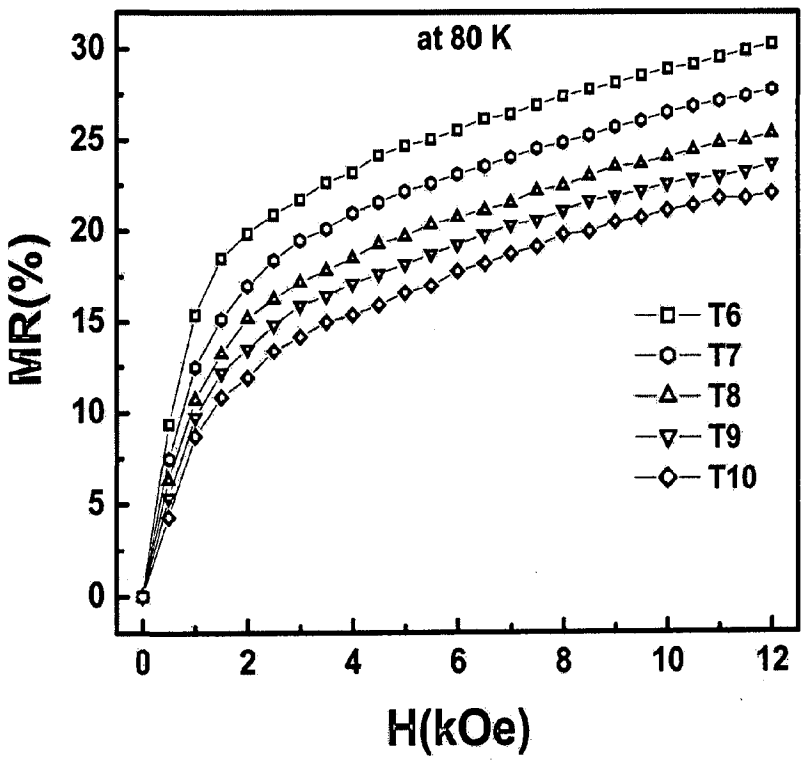

Figure 3.8: Field dependence magnetoresistance (MR) in the range (0-12 kOe) at 80 K of $La_{0.7}Sr_{0.3}MnO_3$ samples sintered at different temperatures.

3.4 RESULTS AND DISCUSSION OF $La_{0.67}Ca_{0.33}MnO_3$

3.4.1 X-ray diffraction studies

The room temperature X-ray diffraction patterns of the $La_{0.67}Ca_{0.33}MnO_3$ samples are shown in Fig. 3.9. The XRD results indicate that all the samples P6, P7, P8, P9 and P10 sintered at temperature of 600, 700, 800, 900 and 1000 ^{0}C, respectively are in pure single LCMO phase with no detectable secondary phases within the accuracy of measurement. Like LSMO, here also complete pure LCMO phase has been obtained at the temperature as low as 600 °C. The intensity of diffraction peaks for LCMO perovskite phase increases as the

sintering temperature increases from 600 to 1000 °C indicating that the crystallinity of LCMO becomes better and particle size increases as sintering temperature increases.

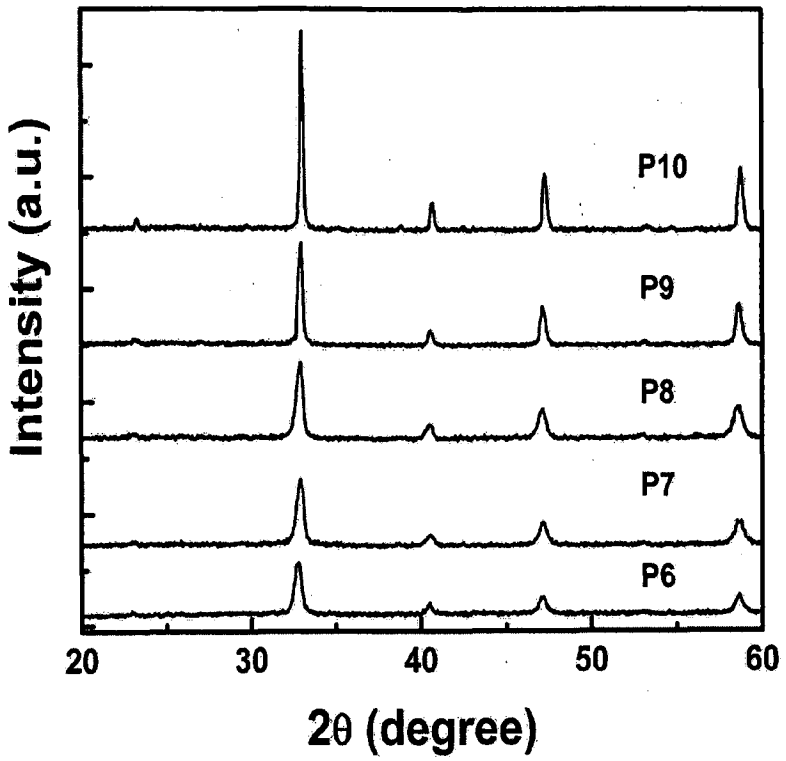

Figure 3.9: X-ray diffraction patterns of the $La_{0.67}Ca_{0.33}MnO_3$ samples sintered at 600 °C (P6), 700 °C (P7), 800 °C (P8), 900 °C (P9) and 1000 °C (P10).

Figure 3.10 shows the (121) reflection (near $2\theta = 33°$) of P6, P7, P8, P9, and P10 samples. It is clear from the Fig. 3.10 that as sintering temperature increases, the intensity of the (121) reflection increases and there is a decrease in full width at half maximum (FWHM), hence the particle size increases. The shifting of (121) peak towards higher value of Bragg angle indicates that the lattice parameters decrease as the sintering temperature increases. The calculated lattice parameters (orthorhombic unit cell parameters a, b, c,) and cell volume of unit cell (V = abc) are shown in Table 3.3.

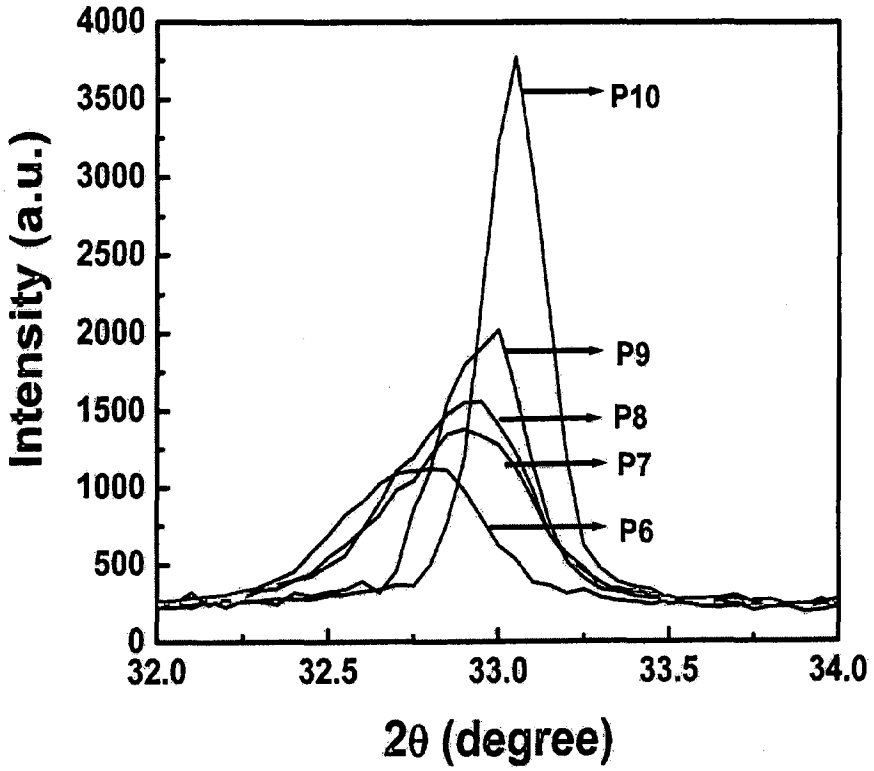

Figure 3.10: The comparison of intensity with 2θ of most intense (121) peak for the $La_{0.67}Ca_{0.33}MnO_3$ samples sintered at different temperatures.

Table 3.3: Variation of lattice parameters, cell volumes, particle size and grain size of $La_{0.67}Ca_{0.33}MnO_3$ samples with sintering temperature.

Sintering temp. (^{0}C)	Lattice parameters a (Å)	b (Å)	c (Å)	Cell volume (Å)^3	Particle size (nm) (by XRD)	Grain size (nm) (by SEM)
600	5.455	7.708	5.459	229.5353	~23	~32
700	5.435	7.678	5.469	228.2209	~25	~54
800	5.417	7.645	5.479	226.9016	~28	~72
900	5.430	7.646	5.458	226.6040	~44	~145
1000	5.416	7.626	5.464	225.6764	~67	~254

It is observed that the cell volume of the unit cell decreases as particle size increases. The same trend was observed in $La_{0.7}Sr_{0.3}MnO_3$ system. The average particle sizes of the samples

are again estimated from X-ray data using Scherrer's formula (as estimated in case of $La_{0.7}Sr_{0.3}MnO_3$). The calculated average particle sizes are ~23, ~25, ~28, ~44 and ~67 nm for the samples sintered at 600, 700, 800, 900 and 1000 °C, respectively.

3.4.2 Microstructural analysis

The representative SEM images of the samples P7, P8, P9, and P10 are shown in Fig. 3.11 (a)-(d), respectively. SEM pictures reveal that grain size increases and porosity decreases as sintering temperature increases. It can also be seen from SEM pictures that the grain boundaries in sample (P7) are not clear and there is a long neck between two grains.

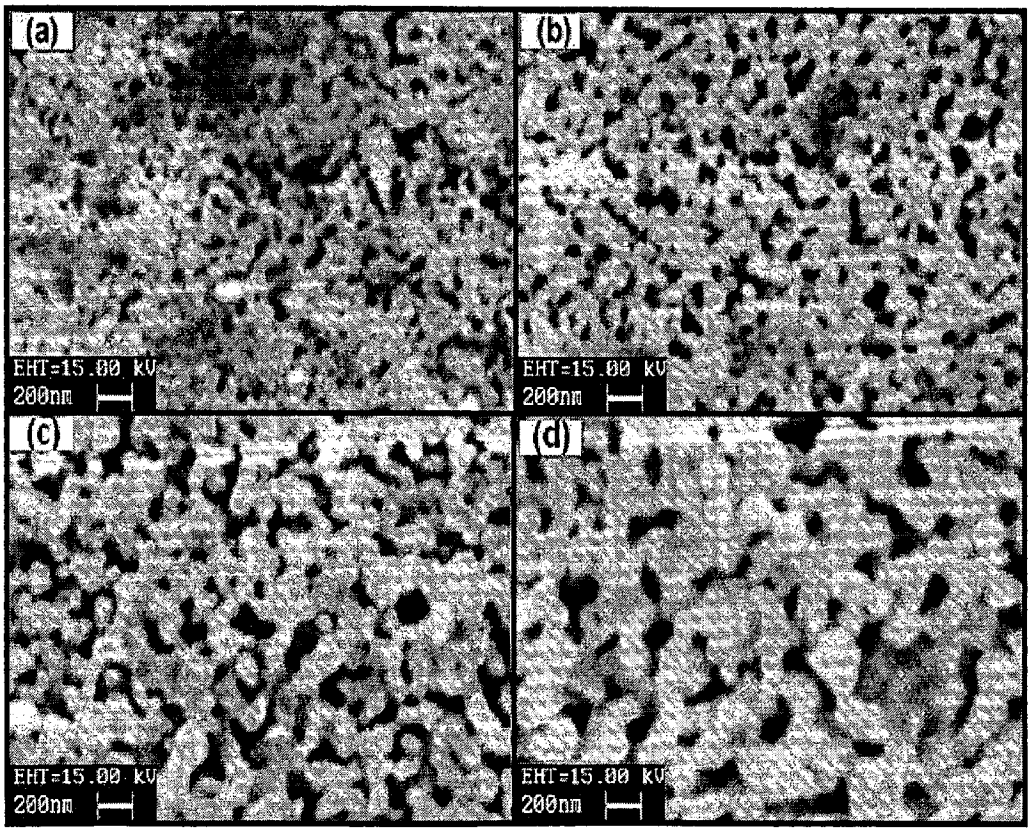

Figure 3.11: Scanning electron micrographs of $La_{0.67}Ca_{0.33}MnO_3$ samples sintered at different temperatures (a) 700 °C (P7), (b) 800 °C (P8), (c) 900 °C (P9) and (d) 1000 °C (P10).

With the increase of sintering temperature from sample (P7) to sample (P10), the size of grain becomes larger, the grain boundaries become obvious, grain connectivity improves and the necks among grains disappear. The average grain sizes measured from SEM micrographs are ~32, ~54, ~72, ~145 and ~254 nm for the samples P6, P7, P8, P9, and P10, respectively. The variations of particle sizes (obtained from the width of XRD peaks) and the grain sizes (obtained from SEM) are shown in Table 3.3. Both particle size and grain size increase as the sintering temperature increases. However, it has been observed that there is a difference between particle size and grain size at all sintering temperature and is more pronounced at high sintering temperatures. This difference is due to the fact that grains are composed of several particles, which may introduce the internal stress or defects in the structure.

3.4.3 Magnetic properties

The magnetization curves of all the samples measured under 5 kOe field in the temperature range (80-350 K) are shown in Fig. 3.12. All the samples show the PM-FM transition at a particular temperature (Tc). We observed a slight variation in Tc for the samples sintered at different temperatures. The transition temperatures determined from the peak in (dM/dT)-T curves are found to be ~258, ~262, ~269, ~280 and ~288 K for samples P6, P7, P8, P9, and P10, respectively. Moreover, the value of magnetization decreases as the sintering temperature decreases. The value of magnetization (M) at 80 K for the samples P6, P7, P8, P9 and P10 are 32.16, 60.30, 66.41, 72.17 and 78.01 emu/gm, respectively. The reduction in magnetization with decreasing the sintering temperature is the same trend as we observed in case of $La_{0.7}Sr_{0.3}MnO_3$. This reduction may be again because of change in the lattice geometry as lattice parameters and cell volume change and the formation of extra

grain boundaries with reduction in particle size, leading to enhanced broken Mn-O-Mn bonds at the surface that hamper exchange interactions and hence decrease in magnetization.

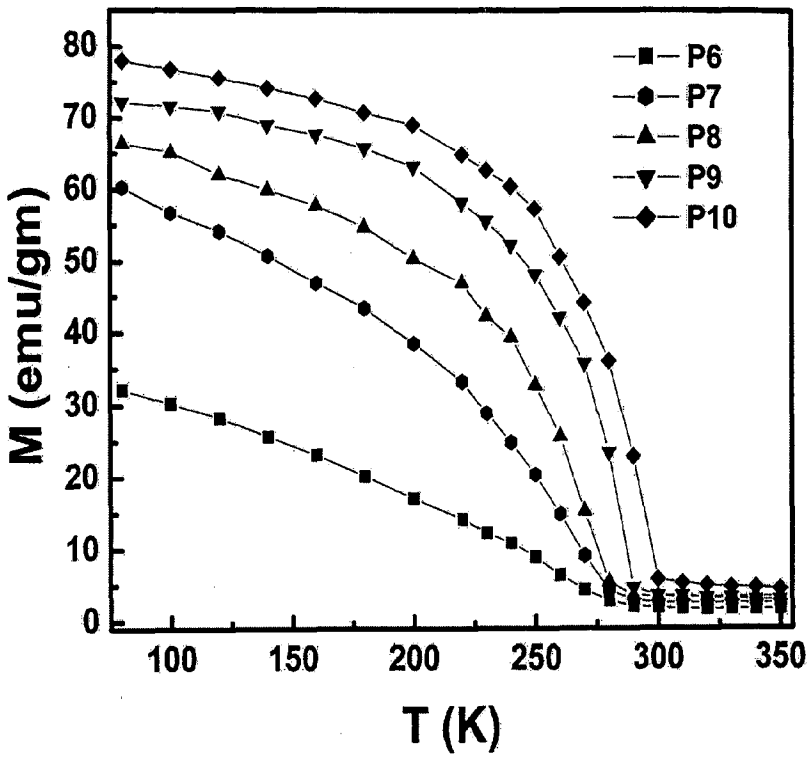

Figure 3.12: Magnetization as a function of temperature measured at 5 kOe of $La_{0.67}Ca_{0.33}MnO_3$ samples.

So our results again support the Zhang et al. [39] results, i.e. for x > 0.25, magnetization decreases with decreasing the sintering temperature and grain boundaries play the role in reduction of magnetization. It has also been observed that as the sintering temperature decreases the width of transition broadens, which suggests that at low sintering temperature grains are loosely connected, which are visible in the scanning electron micrographs shown in Fig. 3.11. The magnetization versus field (M-H) curve at 80 K for the studied samples is displayed in Fig. 3.13. M-H curves also show that the magnetization of the samples decreases

with decreasing the sintering temperature. This demonstrates that ferromagnetic order is weakened and magnetic disorder increases on reducing the sintering temperature.
In the present case, the values of saturation magnetization for the sample P10, P9, P8 and P7 are almost consistent with the literature values reported by Hueso et al [19]. However, the reduction in saturation magnetization for the sample P6 (sintered at 600 °C) is much more.

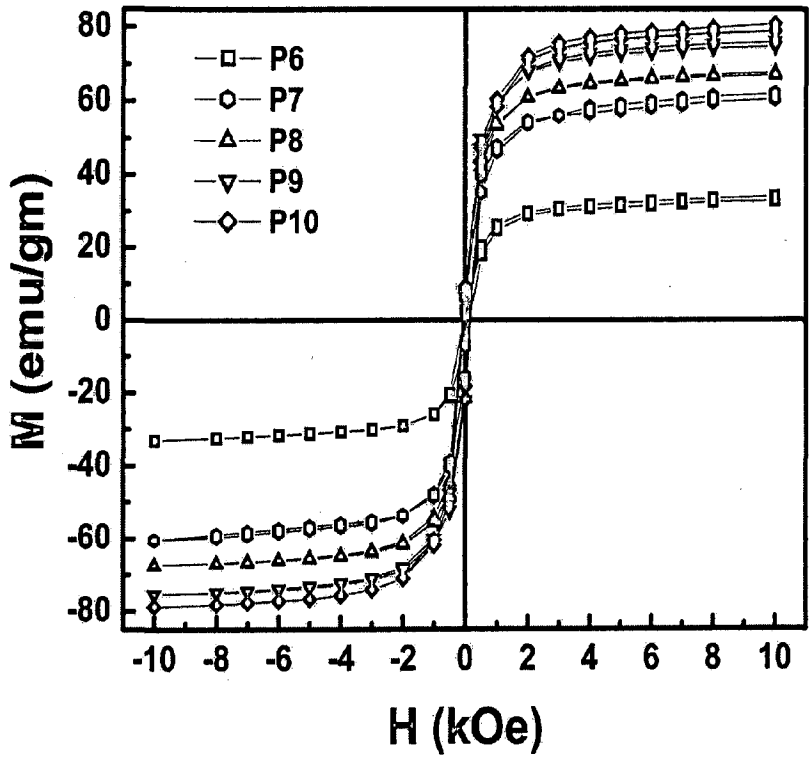

Figure 3.13: Magnetization versus field (M-H) curves at 80 K of $La_{0.67}Ca_{0.33}MnO_3$ samples.

3.4.4 Electrical resistivity measurements

The temperature dependence of resistivity measured in temperature range (80-300 K) at zero field for the studied samples is shown in Fig. 3.14. The resistivity of the samples increases as the sintering temperature decreases. The values of resistivity are 18.53, 1.43, 0.46, 0.31 and 0.084 Ω-cm at 80 K while 7.84, 1.23, 0.99, 0.46 and 0.17 Ω-cm at room temperature (300 K) for the samples P6, P7, P8, P9 and P10, respectively. Thus, the resistivity of sample P6 increases by more than two orders of magnitude as compared to sample P10 at low temperature (80 K). This increase in resistivity is caused due to enhanced

scattering of the charge carriers by increasing the grain boundaries as particle size decreases by lowering the sintering temperature and due to presence of disorderness.

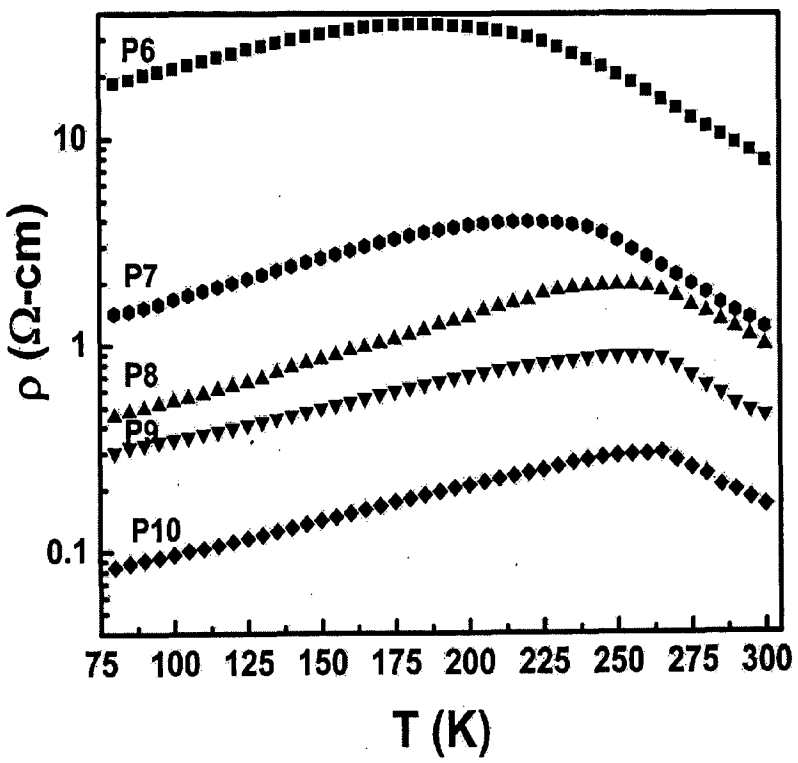

Figure 3.14: Resistivity as a function of temperature at zero field of $La_{0.67}Ca_{0.33}MnO_3$ samples.

On increasing the sintering temperature, the particle size increases leading to a decrease in grain boundaries and the associated disorder. This results the decrease in scattering of the carriers and hence decrease in the resistivity. All the studied samples show an insulator ($d\rho/dT<0$) to metal ($d\rho/dT>0$) transition at a particular temperature (T_{IM}) on lowering the temperature. The value of metal to insulator transition temperatures are ~186, ~225, ~257, ~261 and ~272 K for the samples P6, P7, P8, P9 and P10, respectively. Thus the value of transition temperature decreases (272-186 K) as the sintering temperature decreases from 1000 to 600 °C. The T_{IM} is an extrinsic property and strongly depends on the synthesis

condition and microstructure (e.g. grain boundaries). The strong suppression in the value of T_{IM} with decreasing the sintering temperature is due to suppression of DE mechanism because of increase in non magnetic phase fraction, which is due to enhanced grain boundaries as a consequence of low sintering temperature. Thus lowering the sintering temperature reduces the metallic transition temperature and increases the resistivity. It is again noted that there is a large difference between the value of T_{IM} and Tc for smaller size particles sintered at lower temperatures. The variation of T_{IM} and Tc with sintering temperatures is shown in Fig. 3.15.

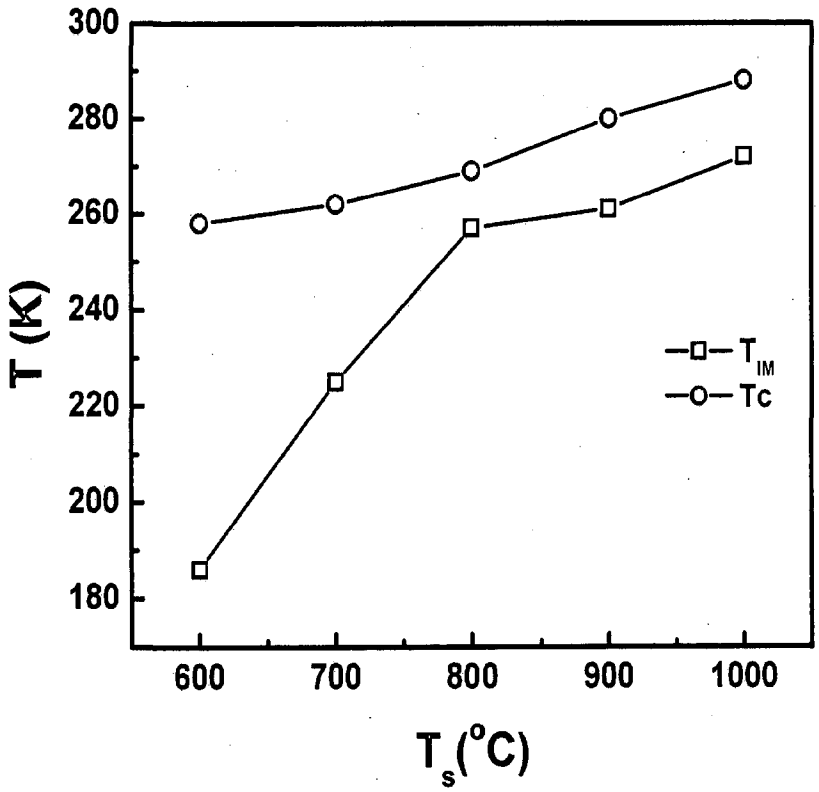

Figure 3.15: Variation of insulator-metal transition temperature (T_{IM}) and PM-FM transition temperature (Tc) with sintering temperatures.

This difference is due to the fact that Tc is an intrinsic property and does not show the large change as a function of sintering temperature while T_{IM} is an extrinsic property that strongly depends upon the grain boundaries [40].

3.4.5 Magnetoresistance studies

The magnetoresistance is the key property of these perovskite manganites. The temperature dependence of magnetoresistance (MR) in a field of 10 kOe for all the studied samples is shown in Fig. 3.16. All samples show the increase in MR at low temperature (T<Tc) as the sintering temperature decreases. The MR values at 80 K are 32.6, 28.9, 26.1, 23.2 and 20.6 % for the samples P6, P7, P8, P9 and P10, respectively at 10 kOe.

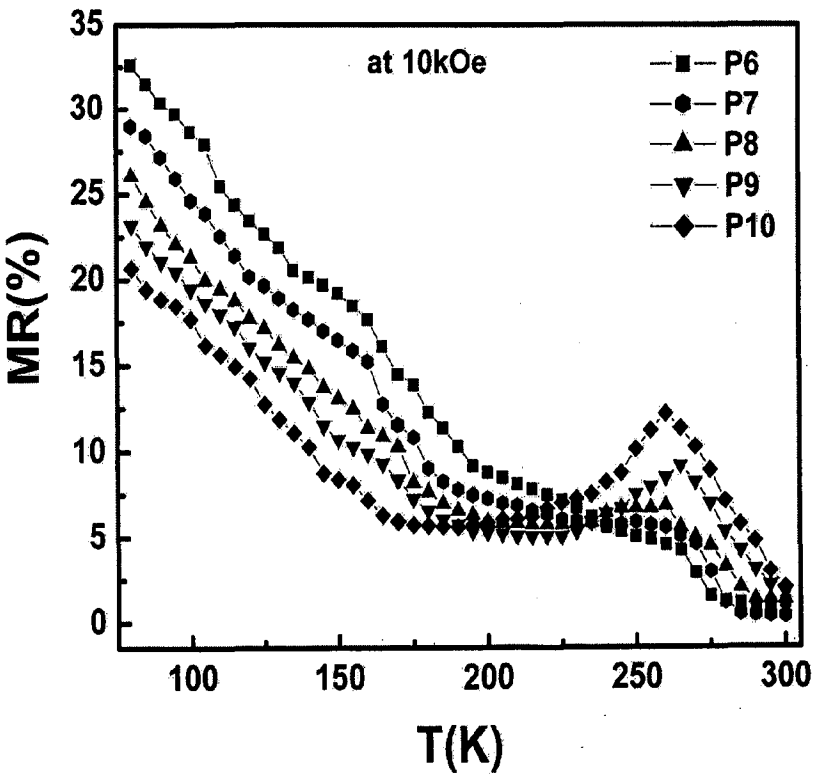

Figure 3.16: Magnetoresistance (MR) as a function of temperature in a field of 10 kOe of $La_{0.67}Ca_{0.33}MnO_3$ samples.

The maximum MR at 80 K is observed for the sample P6 sintered at 600 °C, i.e. the lowest sintering temperature. The appearance of peak in MR-T curve around Tc indicates the contribution of intrinsic component of MR, which arises due to DE mechanism around Tc. The peak MR values at 265 K are 4.2, 5.1, 5.6, 9.1 and 11.3 % for the samples P6, P7, P8, P9 and P10, respectively. However, this peak around Tc is higher in the P10 sample sintered at 1000 °C in comparison to other samples. The magnitude of MR peak around Tc decreases as we reduce the sintering temperature. Thus, lowering the sintering temperature leads to enhancement in MR in low temperature region (T<Tc) and reduction in MR in the high temperature region (around Tc) (see Table 3.4).

Table 3.4: Insulator-metal transition temperature (T_{IM}), paramagnetic-ferromagnetic transition temperature (Tc) and magnetoresistance (MR) of the $La_{0.67}Ca_{0.33}MnO_3$ samples sintered at different temperatures.

Sintering temperature (^{0}C)	T_{IM} (K)	Tc (K)	MR (%) at 10 kOe	
			80 K	265 K
600	186	258	32.6	4.2
700	225	262	28.9	5.1
800	257	269	26.1	5.6
900	261	280	23.2	9.1
1000	272	288	20.6	11.3

In the manganites, two distinct contributions of MR have been pointed out so far. One is the intrinsic MR which arises due to suppression of spin fluctuations when the spins are all aligned in the sample on application of magnetic field. This MR has the highest value near the ferromagnetic transition temperature and decreases as the temperature decreases. This is generally observed in the case of single crystal samples and single crystal thin films. In the polycrystalline samples, there is an additional MR, which is extrinsic in nature, arising due to

the intergrain spin polarized tunneling across the grain boundaries present in the sample. This contribution usually increases as the temperature decreases. Until recently, it was believed that the former mechanism is responsible for the MR at high fields and the latter at low fields. But recent experiments have shown that the high-field response is also due to the existence of the grain boundary and the nature of grain boundary is a key ingredient in the mechanism of electric transport, since it constitutes the barriers through which carriers should cross or tunnel [5]. In our samples low field magnetoresistance (LFMR) at T<Tc increases while high field magnetoresistance (HFMR) (around Tc) decreases with decreasing the sintering temperature. So, in the present case, LFMR at T<Tc increases with decreasing the sintering temperature because we are increasing the disordered surface by decreasing the sintering temperature or particle size [38, 41]. The reduction in magnetization as the sintering temperature decreases (Fig. 3.12) also supports the magnetic spin disorder induced by grain boundaries in the smaller particle samples and this spin disorder is suppressed when magnetic field is applied, resulting the enhancement in MR. The disappearance of HFMR (around Tc) in the smaller particle size samples can be explained by weakening of DE mechanism as sintering temperature is lowered. HFMR, which arises due to DE mechanism around Tc, is mostly found in single crystal samples, so as we reduce the sintering temperature the DE mechanism is suppressed and HFMR decreases with decreasing the sintering temperature.

The magnetic field dependence of MR of all the studied samples measured in magnetic field range of 0-12 kOe at 80 K is shown in Fig. 3.17. Analysis of Fig. 3.17 shows that with increase in the magnetic field from 0 to12 kOe, the MR of all the samples increases with increasing the magnetic field. The maximum MR is observed in sample P6 sintered at the lowest temperature (600 °C). As the sintering temperature decreases, the MR increases.

The value of MR at 80 K for the sample P6 sintered at 600 °C is ~15.1 % at 1 kOe and ~32.6 % at 10 kOe while it is ~9.6 % at 1 kOe and ~20.7 % at 10 kOe for the sample P10 sintered at 1000 °C. So, the percentage change in MR at 80 K for sample P6 with respect to sample P10 is ~57 % at 1 kOe and ~58 % at 10 kOe. This shows that the percentage change in MR is almost same at both fields (1 and 10 kOe) and the variation of MR does not show any saturation even up to 12 kOe. This enhancement in MR as the sintering temperature decreases is again caused through spin polarized tunneling at the grain boundaries.

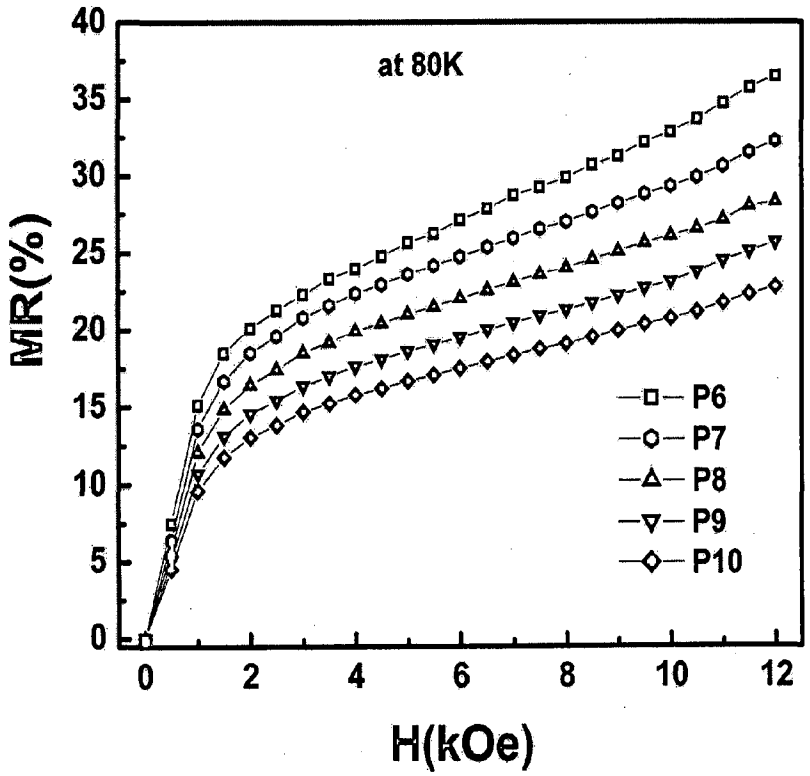

Figure 3.17: Magnetoresistance (MR) as a function of magnetic field in the range (0-12 kOe) at 80 K of $La_{0.67}Ca_{0.33}MnO_3$ samples.

3.5 CONCLUSIONS

In summary, we have successfully prepared the $La_{0.7}Sr_{0.3}MnO_3$ and $La_{0.67}Ca_{0.33}MnO_3$ samples by sol-gel process and studied the sintering temperature effect on magnetotransport and magnetic properties. The main highlights of the work are given below:

1. XRD results reveal that all the samples, synthesized at different sintering temperatures, have pure LSMO and LCMO perovskite phase with orthorhombic unit cells. It is observed that the lattice parameters and cell volume of the unit cell decrease as sintering temperature increases.
2. The crystallinity of LSMO and LCMO becomes better and particle size increases as sintering temperature increases. The calculated average particle sizes using Scherrer's formula are ~31, ~39, ~51, ~56 and ~60 nm for the LSMO samples and ~23, ~25, ~28, ~44 and ~67 nm for the LCMO samples sintered at 600, 700, 800, 900 and 1000 °C, respectively.
3. The average grain sizes measured from SEM micrographs are found to be ~37, ~48, ~66, ~115 and ~163 nm for the LSMO samples and ~32, ~54, ~72, ~145 and ~254 nm for the LCMO samples sintered at 600, 700, 800, 900 and 1000 °C, respectively.
4. The magnetic measurements show only slight variation of Tc with the sintering temperatures. The transition temperatures determined from the peak in (dM/dT)-T curves are found to be ~311, ~321, ~324, ~326 and ~330 K for the LSMO samples and ~258, ~262, ~269, ~280 and ~288 K for LCMO samples sintered at 600, 700, 800, 900 and 1000 °C, respectively.
5. The resistivity increases and the value of insulator ($d\rho/dT<0$) to metal ($d\rho/dT>0$) transition temperature decreases from 303 to 175 K for LSMO samples and 272 to 186 K for LCMO samples as sintering temperature decreases from 1000 to 600 °C.

6. It has been observed that low field magnetoresistance at T<Tc increases as the sintering temperature decreases. The measurements of variation of MR with field and temperature reveal that in both of the cases, the maximum MR is observed in samples sintered at the lowest temperature (600 °C). In case of LSMO, the value of MR at 80 K for the sample T6 sintered at 600 °C is ~15.3 % at 1 kOe and ~28.9 % at 10 kOe while it is ~7.9 % at 1 kOe and ~21.1 % at 10 kOe for the sample T10 sintered at 1000 °C. So, the percentage change in MR at 80 K for sample T6 with respect to sample T10 is ~94 % at 1 kOe and ~37 % at 10 kOe. This shows that the percentage change in MR is more at low field (1 kOe) as compared to higher field (10 kOe).
7. In case of LCMO, along with the increment in MR below Tc, there is a peak in MR-T curve around Tc indicating the contribution of intrinsic component of MR, which arises due to DE mechanism around Tc and this peak around Tc is higher in the P10 sample sintered at 1000 °C in comparison to other samples. The magnitude of MR peak around Tc decreases as we reduce the sintering temperature. Thus, lowering the sintering temperature leads to enhancement in MR in low temperature region (T<Tc) and reduction in MR in the high temperature region (around Tc). This high temperature (around Tc) MR peak could not be observed in LSMO case because the Tc of LSMO is ~330 K and we did the MR measurement only up to 300 K. In case of LCMO, the value of MR at 80 K for the sample P6 sintered at 600 °C is ~15.1 % at 1 kOe and ~32.6 % at 10 kOe while it is ~9.6 % at 1 kOe and ~20.6 % at 10 kOe for the sample P10 sintered at 1000 °C. So, the percentage change in MR at 80 K for sample P6 with respect to sample P10 is ~57 % at 1 kOe and ~58 % at 10 kOe. This shows that the percentage change in MR is almost same at both fields (1 and 10 kOe).

8. It is suggested that this enhancement in LFMR for the samples sintered at lower temperature is due to enhanced spin polarized tunneling by increasing the grain boundary contribution as sintering temperature decreases.

Both of these studies clearly indicate that the maximum MR is observed in sample sintered at the lowest temperature (600 °C), which has smallest particle size. This observed magnetoresistance increases with decreasing the temperature. Moreover, it is also observed that percentage change in MR is more at low field (~1 kOe) in comparison to high field (~10 kOe) for LSMO samples while it is almost same in case of LCMO. It has been concluded that the grain boundaries play the key role in the enhancement of LFMR and this enhanced MR, observed in smaller (nano) particles, is useful in the development of nano-size based magnetoresistive devices.

REFERENCES

1. Jin S, Tiefel T H, McCormack M, Fastnacht R A, Ramesh R & Chen L H, "Thousandfold change in resistivity in magnetoresistive La-Ca-Mn-O films", Science, **264**, 413 (1994).
2. Haghiri-Gosnet A M & Renard J P, "CMR manganites: physics, thin films and devices", J. Phys. D: Appl. Phys., **36**, R127, (2003).
3. Preliier W, Mercey B & Haghiri-Gosnet A M, "Encyclopedia of nanoscience and nanotechnology" edited by Nalwa H S, vol **X**, pp 1-18 (2003).
4. Schiffer P, Ramirez A P, Bao W & Cheong S W, "Low temperature magnetoresistance and the magnetic phase diagram of $La_{1-x}Ca_xMnO_3$", Phys. Rev. Lett., **75**, 3336 (1995).
5. Hwang H Y, Cheong S W, Ong N P & Batlogg B, "Spin-polarized intergrain tunneling in $La_{2/3}Sr_{1/3}MnO_3$", Phys. Rev. Lett., **77**, 2041 (1996).
6. Mahesh R, Mahendiran R, Raychaudhuri A K & Rao C N R, "Effect of particle size on the giant magnetoresistance of $La_{0.7}Ca_{0.3}MnO_3$", Appl. Phys. Lett., **68**, 2291 (1996).
7. Wang X L, Dou S X, Liu H K, Ionescu M & Zeimetz B, "Large low-field magnetoresistance over a wide temperature range induced by weak-link grain boundaries in $La_{0.7}Ca_{0.3}MnO_3$", Appl. Phys. Lett., **73**, 396 (1998).
8. Gupta A, Gong G Q, Xiao G, Dumcombe P R, Lecoeur P, Trouilloud P, Wang Y Y, Dravid V P & Sun J Z, "Grain-boundary effects on the magnetoresistance properties of perovskite manganite films", Phys. Rev. B, **54**, R15629 (1996).
9. Ju H L, Gopalkrishnan J, Peng J L, Li Q, Xiong G C, Venkatesan T & Greene R L, "Dependence of giant magnetoresistance on oxygen stoichiometry and magnetization in polycrystalline $La_{0.67}Ba_{0.33}MnO_z$", Phys. Rev. B, **51**, 6143 (1995).

10. Li X W, Gupta A, Xiao G & Gong G Q, "Low-field magnetoresistive properties of polycrystalline and epitaxial perovskite manganite films", Appl. Phys. Lett., **71**, 1124 (1997).

11. Raju A R, Aiyer H N, Venkatanagarajuna B, Mahendiren R, Raychaudhariand A K and Rao C N R, "Epitaxial films of $La_{1-x}MnO_3$ exhibiting CMR prepared using nebulized spray pyrolysis", J. Phys. D: Appl. Phys., **30**, L71 (1997).

12. Mathur N D, Burnell G, Issac S P, Jackson T J, Teo B S, MacManus Driscoll J L, Cohen L F, Evetts J E & Blamire M G, "Large low-field magnetoresistance in $La_{0.7}Ca_{0.3}MnO_3$ induced by artificial grain boundaries", Nautre, **387**, 266 (1997).

13. Steenbeck K, Eick T, Kirsch K, O'Donnel K & Steinbeiss E, "Influence of a 36.8° grain boundary on the magnetoresistance of $La_{0.8}Sr_{0.2}MnO_{3-\delta}$ single crystal films", Appl. Phys. Lett., **71**, 968 (1997).

14. Steenbeck K, Eick T, Kirsch K, Schmidt H G & Steinbeiss E, "Tunneling-like magnetoresistance in bicrystal $La_{0.8}Sr_{0.2}MnO_{3-\delta}$ thin films", Appl. Phys. Lett., **73**, 2506 (1998).

15. Pignard S, Vincent H, Senateur J.P, Frohlich K & Souc J, "Effect of crystallinity on the magnetoresistive properties of $La_{0.8}MnO_{3-\delta}$ thin films grown by chemical vapor deposition", Appl. Phys. Lett., **73**, 999 (1998).

16. Westerburg W, Martin F, Friedrich S, Maier M & Jakob G, "Current dependence of grain boundary magnetoresistance in $La_{0.67}Ca_{0.33}MnO_3$ films", J. Appl. Phys., **86**, 2173 (1999).

17. Ziese M, Heydon G, Hohne R, Esquinazi P & Dienelt J, "Step-edge magnetoresistance in $La_{0.7}Ca_{0.3}MnO_3$ films", Appl. Phys. Lett., **74**, 1481 (1999).

18. de Andres A, Garcia-Hernandez M, Martinez J L & Prieto C, "Low-temperature magnetoresistance in polycrystalline manganites: connectivity versus grain size", Appl. Phys. Lett., **74,** 3884 (1999).

19. Hueso L E, Rivas J, Rivadulla F & Lopez-Quintela M A, "Tuning of colossal magnetoresistance via grain size change in $La_{0.67}Ca_{0.33}MnO_3$", J. Appl. Phys., **86,** 3881 (1999).

20. Todd N K, Mathur N D, Issac S P, Evetts J E & Blamire M G, "Current–voltage characteristics and electrical transport properties of grain boundaries in $La_{1-x}(Sr/Ca)_xMnO_3$", J. Appl. Phys., **85,** 7263 (1999).

21. Sun J Z, Abraham D W, Rao R A & Eom C B, "Thickness-dependent magnetotransport in ultra thin manganite films", Appl. Phys. Lett., **74,** 3017 (1999).

22. Fu Y, "Grain-boundary effects on the electrical resistivity and the ferromagnetic transition temperature of $La_{0.8}Ca_{0.2}MnO_3$", Appl. Phys. Lett., **77,** 118 (2000).

23. Vertruyen B, Cloots R, Rulmont A, Dhalenne G, Ausloos M & Vanderbemden Ph, "Magnetotransport properties of a single grain boundary in a bulk La–Ca–Mn–O material", J. Appl. Phys., **90,** 5692 (2001).

24. Lopez-Quintela M A, Huesco L E, Rivas J & Rivadulla F, "Intergranular magnetoresistance in nanomanganites", Nanotechnology, **14,** 212 (2004).

25. Patil S I, Ogale A S, Shinde S R, Kundaliya D C, Ogale S B & Bhagat S M, "Grain-boundary control and low-field magnetoresistance in $La_{0.7}Sr_{0.3}MnO_3$", J. Appl. Phys., **97,** 10H707 (2005).

26. Dey P & Nath T K, "Enhanced grain surface effect on the temperature dependent behaviour of spin polarized tunneling magnetoresistance of nanometric manganites", Appl. Phys. Lett., **87,** 162501 (2005).

27. Shreekala R, Rajeshwari M, Ghosh K, Goyal A, Gu J Y, Kwon C, Trajanovic Z, Boettcher T, Greene R L, Ramesh R & Venkatesan T, "Effect of crystallinity on the magnetoresistance in perovskite manganese oxide thin films", Appl. Phys. Lett., **71**, 282 (1997).

28. Sanchez R D, Rivas J, Vazquez-Vazquez C, Lopez-Quintela M A, Causa M T, Tovar M & Oseroff S B, "Giant magnetoresistance in fine particle of $La_{0.67}Ca_{0.33}MnO_3$ synthesized at low temperatures", Appl. Phys. Lett., **68**, 134 (1996).

29. Vazquez-vazquez C, Blanco M C, Lopez-quintela M A, Sanchez R D, Rivas J & Oseroff S B, "Characterization of $La_{0.67}Ca_{0.33}MnO_{3\pm\delta}$ particles prepared by the sol–gel route", J. Mater. Chem., **8**, 991 (1998).

30. Rivas J, Hueso L E, Fondado A, Rivadullo F & Lopez-Quintela M A, "Low field magnetoresistance effects in fine particles of $La_{0.67}Ca_{0.33}MnO_3$ perovskites", J. Magn. Magn. Mater., **221**, 57 (2000).

31. Pandya D K, Kashyap S C & Pattanaik G R, "Magnetoresistive behaviour of $La_{0.67}(Ca_{0.33-x}Pb_x)MnO_3$ nano powders prepared at lower temperature", J. Alloys Compd., **326**, 255 (2001).

32. Vertruyen B, Rulmont A, Cloots R, Ausloos M, Dorbolo S & Vanderbemden P, "Synthesis of CMR manganate compounds: the consequences of the choice of a precursor method", Mater. Lett., **57**, 598 (2002).

33. Dutta A, Gayathri N & Ranganathan R, "Effect of particle size on the magnetic and transport properties of $La_{0.875}Sr_{0.125}MnO_3$", Phys. Rev. B, **68**, 054432 (2003).

34. Lisboa-Filho P N, Mombru A W, Pardo H, Ortiz W A & Leite E R, "Influence of processing conditions on the crystal structure and magnetic behavior of $La_{0.7}Ca_{0.3}MnO_{3\pm\delta}$ samples", J. Phys. Chem. Solids., **64**, 583 (2003).

35. Lisboa-Filho P N, Mombru A W, Pardo H, Leite E R & Ortiz W A, "Extrinsic properties of colossal magnetoresistive samples", Solid State Commun., **130,** 31 (2004).

36. Shankar K S, Kar S, Subbanna G N & Raychaudhuri A K, "Enhanced ferromagnetic transition temperature in nanocrystalline lanthanum calcium manganese oxide ($La_{0.67}Ca_{0.33}MnO_3$)", Solid State Commun., **129,** 479 (2004).

37. De Keiyser Th H, Langford J I, Mittemeijer & Vogels A B P, "Use of the Voigt function in a single-line method for the analysis of X-ray diffraction line broadening", J. Appl. Cryst., **15,** 308 (1982).

38. Balcells L I, Fontcuberta J, Martinez B & Obradors X, "High-field magnetoresistance at interfaces in manganese perovskites", Phys. Rev. B, **58,** R14697 (1998).

39. Zhang N, Yang W, Ding W, Xing D & Du Y, "Grain size-dependent magnetism in fine particle of perovskite $La_{1-x}Sr_xMnO_z$", Solid State Commun., **109,** 537 (1999).

40. de Andres A, Garcia-Hernandez M & Martinez J L, "Conduction channels and magnetoresistance in polycrystalline manganites", Phys. Rev. B, **60,** 7328 (1999).

41. Zhu T, Shen B G, Sun J R, Zhao H W & Zhan W S, "Surface spin-glass behavior in $La_{2/3}Sr_{1/3}MnO_3$ nanoparticles", Appl. Phys. Lett., **78,** 3863 (2001).

Chapter - 4

ENHANCED LOW FIELD MAGNETORESISTANCE IN $(La_{0.7}Sr_{0.3}MnO_3)_{1-x}/(NiO)_x$ AND $(La_{0.7}Sr_{0.3}MnO_3)_{1-x}/(TiO_2)_x$ COMPOSITES

4.1 INTRODUCTION

As discussed in the section 3.1 of chapter 3 that the intrinsic CMR observed near Tc is found in a magnetic field scale of several tesla and in a narrow temperature range, which is not very appealing for applications. On the other hand, extrinsic effects like grain boundary magnetoresistance (GBMR) observed at low fields and over a wide temperature range, seem to be more appropriate for device applications. Achieving a large magnetoresistance at low fields and at/around room temperature which is necessary for consideration of practical applications is still a challenge. It was found that polycrystalline manganites exhibit a wide temperature range MR whose origin lies in the existence of interfaces and grain boundaries [1–3]. This extrinsic low field magnetoresistance (LFMR) effect observed in polycrystalline materials is caused due to spin polarised tunneling [1, 4] and spin dependent scattering [5] as the conduction electrons travel across the grain boundaries. The tunneling process takes place across the interfaces or grains separated by an energy barrier related to the magnetic disorder. Hence dilution with an insulating material in the manganites adjusts the barrier layer and thus influences the tunneling process. Since these extraneous effects act as pinning centers in remagnetization by domain wall displacement, a small field will align the neighbouring FM grains and hence an enhanced MR response is achieved at low fields and low temperatures. Therefore, a spin misorientation at the magnetically virgin state is crucial to obtain an

enhanced MR. This extrinsic effect is observed in a wide temperature range, at low field (<1 kOe) and makes it more useful from the application point of view. Extrinsic MR in ferromagnetic oxides usually falls into three broad classes, namely grain boundary MR, spin-polarized transport in ferromagnetic tunneling junctions MR and domain-wall MR [6]. Gupta et al. [2] investigated the effects of magnetic domain boundary pinning by polycrystalline grain boundaries and an enhanced MR was observed in a low temperature region. Very recently, it was reported that introduction of a second phase, usually a nonmagnetic or an antiferromagnetic inorganic insulator, into the ferromagnetic manganites matrix would lead to an improved MR [5, 7–9]. As it is known that composite materials represent new material variant synthesized from two (or more) materials so that the individuality of the components is maintained in the composite. However, the properties of the composite materials are better (improved) than the properties of any of the individual components. In the case of magnetoresistance materials, the central aim is to synthesize a material which shows large magnetoresistance at low fields and near room temperature. Any single CMR material does not meet all the requirements. However, one or two of the above criterions are satisfied by a single colossal magnetoresistance material. Therefore, some attempts have been made to synthesize the composites of these manganites with inorganic insulators [5-17], which may show large magnetoresistance at low fields and at near room temperatures.

The initial work in the area of CMR composites was reported by Balcells et al. [5] and Petrov et al. [7]. Balcells et al. [5] have studied the magnetoresistance of $(La_{2/3}Sr_{1/3}MnO_3)_x/(CeO_2)_{1-x}$ composite (x = 100, 80, 60, 40, 30, 25, 20 vol.%) as a function of composition x, temperature and magnetic field and have found a dramatic enhancement of LFMR for samples close to the metallic percolation threshold. The improved field sensitivity is found to be fairly large even at room temperature. They observed two peaks in the

resistivity curve and the resistivity rises by 6–7 orders of magnitude at the percolation threshold, x_p = 20 % and a LFMR increases about 1.5 % at H = 100 Oe and 300 K. A broad peak in the resistivity curve at around 250 K has been attributed to the poor inter-grain contacts. But the LFMR response, due to intergrain coupling, at $x = x_p$ is very weak. The high field response has been attributed mainly to the magnetic and electrical characteristics of the grains. Petrov et al. [7] have studied the electrical and magnetic transport properties of $(La_{0.67}Ca_{0.33}MnO_3)_x/(SrTiO_3)_{1-x}$ (x = 10–100 vol.%) composites. A high field MR as well as low field MR close to percolation threshold, x_p = 60 % is attributed due to increased disorder at the grain boundaries and is about an order of magnitude higher than the corresponding pure LCMO value. The resistivity goes up by 6 orders of magnitude above x_p. MR also increases with x and becomes maximum at $x = x_p$ and then goes down. Magnetization versus temperature curve shows an upturn below 50 K and does not saturate up to 50 kOe, which has been ascribed to the highly disordered nonmagnetic interfacial region. Composites with other insulating materials like yttria stabilised zirconia (YSZ) [18], silica (SiO_2) [19], alumina (Al_2O_3) [20, 21] are also reported. $(LSMO)_{1-x}/(YSZ)_x$ composites with varying x (0 to 5 %) have been investigated by Xia and his co-workers [18]. Broadening of T_C and shifting of T_{IM} to lower temperatures are observed. But T_{IM}, interestingly decreases up to $x \leq$ 2 % and then start to increase. Room temperature MR of the composites is higher as compared to pure LSMO at 3 T field. They did not find any percolation threshold in the system. The transport and magnetic properties have been explained on the basis of the reaction products between LSMO and YSZ. They have proposed a two-channel conduction model for the composites. $(LSMO)_{1-x}/(SiO_2)_x$ for x = 0.0–1.0 mol.% composites show resistivity rise with increasing x and shifting of T_{IM} towards lower temperatures as observed by Huang et al. [19]. In this case the MR behaviour of the composite is superior at T > 150 K

but inferior for T < 150 K. MR at 300 K is 21.4 % for x = 0.20 but 17.7 % for x = 0.0 at 50 kOe field. Spin-polarised tunnelling through the LSMO grains in the presence of the insulating SiO_2 at the grain boundaries is ascribed for the observed effect. Another insulating inert material Al_2O_3, used for the junction MR devices, has been used by Hueso et al. [20] to form the composite $(LCMO)_{1-x}/(Al_2O_3)_x$ (x = 0.0–25 vol. %). They have seen a threshold percolation at x = 10 vol. %. Resistivity rises by 3 orders of magnitude with increasing Al_2O_3 content (x) at 100 K and transition temperature shifts towards lower temperature like other CMR composites. But no metal–insulator transition is observed for $x \geq 8$ %. The resistivity behaviour throughout the whole temperature range is fitted based on a two-channel conduction model. They have observed the maximum MR at the conduction threshold (x = 10 %) at 77 K and 7.5 kOe. $(LSMO)_{1-x}/(MgO)_x$ (x = 0.0–0.5) composites exhibit a pronounced LFMR compared to pure LSMO which is < 1 % at $H \leq 1$ kOe and low temperatures. For x = 0.05, MR is 25 % at T = 4.2 K and 50 kOe field. Even a small amount of MgO ($x \leq 0.05$) changes the intrinsic metallic bulk electron transport into a grain boundary controlled extrinsic behaviour [22]. HFMR is also increased up to 50–60 % in the range 4.2–200 K at 50 kOe. In case of $(LSMO)_x/(SrMeO_3)_{1-x}$ composite [23, 24] (Me = Ti, Zr, x = 20–70 mol.%), the MR enhancement point is dependent on the annealing temperature. For $LSMO/SrTiO_3$, the MR is 1.5 % at H = 100 Oe and T = 298 K, and it is 2.5 % at the same field and temperature for $LSMO/SrZrO_3$. Yan et al. [25] have investigated the LFMR of the $LSMO/CoFe_2O_4$ composite for a single composition of 20 wt% $CoFe_2O_4$. The resistivity of the composite is about an order of magnitude larger than that of the same grain-sized pure LSMO. A large LFMR has been obtained in this composite compared to pure LSMO. At 5 kOe, the MR of 20 wt% composite is 10 % at 280 K and 5 % at 290 K whereas these values for pure LSMO are 2 and 1 %, respectively. The high resistivity of the composite is attributed

to the random scattering of the spin electrons at the surfaces of the magnetic $CoFe_2O_4$ grains. Since the spin-dependent scattering of the conduction electrons at the grain boundaries is highly field sensitive, the magnetic scattering of the polarised charge carriers may be responsible for the LFMR. Another interesting system with a hard ferromagnetic insulator (HFMI) as the second phase of the composite is reported by Huang et al. [26]. They have studied $(L_{0.67}Sr_{0.33}MnO_3)_{1-x}/(BaFe_{11.3}(ZnSn)_{0.7}O_{19})_x$ (BAM) composites as a function of vol.% (0.0–1.0) of the insulating phase. A resistivity rise with increasing x, indicates a percolative system. Gupta et al. [8] have reported the magnetotransport studies of LSMO–glass composites. They have reported an enhanced LFMR of about 1.8 % at 200 Oe and room temperature for 25 wt% of glass, the percolation threshold composition for the system. They have further argued that the glass layer, as an amorphous insulator, sits within the grain boundaries of the LSMO and acts as a barrier for spin-polarised tunnelling thereby enhancing the LFMR. They have also found the sudden resistivity jumps around the percolation threshold. The broad peak in the resistivity curve is understood on the basis of a parallel resistor model where the sample is considered to be made of a parallel network of conducting and insulating channels.

The magnetoresistance of $(La_{0.7}Ca_{0.3}MnO_3)_{0.5}/(La_{0.7}Sr_{0.3}MnO_3)_{0.5}$ composite [27] has been investigated as a function of sintering temperature. Raising the sintering temperature triggers the interfacial reaction between LCMO and LSMO which dictates the MR property over a wide temperature range across the room temperature. The resistivity of the composite goes on decreasing with sintering temperature. This has been attributed to the presence of the new reaction product, $La_{0.7}Ca_{0.15}Sr_{0.15}MnO_3$, which is a low resistivity component compared to pure LCMO. MR width of about 60 K around T_{IM} rises to about 120 K for the sample sintered at 1300 °C. The coexistence of multiphase in the interface associated with the

chemical and magnetic inhomogeneity is the probable cause of the broad MR response across the room temperature as suggested by the authors. Another such composite study is $(LSMO)_{1-x}/(Sm_{0.7}Sr_{0.3}MnO_3)_x$ (SSMO) [28] with x = 0.0–1.0. Since the transition temperature for SSMO is 63 K, it behaves as a paramagnetic insulator at high temperature and the combination effectively acts as a FM-insulator composite. The resistivity increases by two orders of magnitude with increasing SSMO content, shifting T_{MI} towards lower temperatures for the composites. Maximum MR of 28.3 % is obtained at 293 K for x = 0.6 (percolation threshold) which rises to 46.4 % at 200 K for x = 0.7 and at 50 kOe. Observed LFMR is attributed due to spin-polarised tunnelling through the LSMO grains but the HTMR enhancement is because of enhanced magnetic disorder due to the presence of PM SSMO in LSMO grain boundaries which leads to the blocking of spin coupling between the neighbouring LSMO grains and hence improved HTMR. Composites such as $(LSMO)_{1-x}/(Pr_{0.5}Sr_{0.5}MnO_3)_x$ (PSMO) with x = 0.0–1.0 have been studied by Liu et al. [14] and Yuan et al. [29]. Resistivity increases and T_{IM} shifts to lower temperatures with increasing x and has been explained in terms of spin-coupling layer inside LSMO grains. A ferromagnetic/metal type composite (LCMO/Ag) has been investigated by Huang et al. [30] and a large enhancement in MR near room temperature and a dramatic decrease in resistivity for the composite has been reported.

Moreover the composite between a CMR and a superconducting component e.g. $(LSMO)_{1-x}/(La_{1.85}Sr_{0.15}CuO_4)_x$ (LSCO) (x = wt. fraction, 0.0–0.9) [31] has also been studied and a tuning between positive and negative MR is observed. Above the superconducting transition of LSCO all samples show negative MR up to room temperature for $x < 0.5$. But as the applied field increases, a positive MR comes into picture for samples with $x > 0.5$ because of the magnetic breakdown of the superconducting coupling within LSCO grains.

This magnetic field and composition sensitive competition between the positive and negative MR reveals the coexistence of a ferromagnetic and superconductive ordering in the system that favours the materials to be used as a magnetic field sensitive device like vortex detector. But it limits its applicability only in the low temperature because for the superconductive ordering the material must have to be subjected below the superconducting transition temperature of LSCO.

In the present investigations, we have synthesized the $(La_{0.7}Sr_{0.3}MnO_3)_{1-x}/(NiO)_x$ and $(La_{0.7}Sr_{0.3}MnO_3)_{1-x}/(TiO_2)_x$ composites with x = 0.0–0.20 and studied their magnetic and low field magnetotransport properties. Here, $La_{0.7}Sr_{0.3}MnO_3$ (LSMO) is parent perovskite manganite in which insulating NiO and TiO_2 are added as second phase material in order to modify the grain boundary properties, which influence the LFMR.

4.2 EXPERIMENTAL

The $La_{0.7}Sr_{0.3}MnO_3$ (LSMO) samples were prepared via solid state reaction method by using La_2O_3, $SrCO_3$ and MnO_2 powders. These powders were mixed in the requisite ratio, ground and then calcined at 900 °C for 12 h. The calcined mixture was reground and mixed properly and pressed in the form of pellets and sintered at 1300 °C for 20 h with intermediate grindings to obtain LSMO sample with single phase perovskite structure. The sintered pellets were reground and the resulting LSMO powder was mixed with commercial NiO and TiO_2 powder according to the nominal ratio of $(LSMO)_{1-x}/(NiO)_x$ and $(LSMO)_{1-x}/(TiO_2)_x$ with x = 0, 0.05, 0.10, 0.15 and 0.20. After thoroughly grinding the resulting $(LSMO)_{1-x}/(NiO)_x$ and $(LSMO)_{1-x}/(TiO_2)_x$ powders were pelletized at a pressure 5 MPa/cm^2 and then sintered at 1000 °C for 2 h. The low sintering temperature for small duration was chosen to avoid inter-diffusion between LSMO and second phase material (NiO and TiO_2). By this procedure, the

NiO and TiO_2 introduced as second phase of the composites mainly segregated at the grain boundaries and on the surfaces of the LSMO grains. The structural characterization was done by using X-ray diffraction at room temperature and surface morphology was investigated by scanning electron microscopy. Resistivity as a function of temperature was measured by a standard four-probe method equipped with Keithley instruments without and with magnetic fields (0-12 kOe). The DC magnetization measurements were done by using vibrating sample magnetometer.

4.3 RESULTS AND DISCUSSION OF $(La_{0.7}Sr_{0.3}MnO_3)_{1-x}/(NiO)_x$ COMPOSITE

4.3.1 X-ray diffraction studies

The X-ray diffraction (XRD) patterns of the composite $(LSMO)_{1-x}/(NiO)_x$ samples, recorded at room temperature, are shown in Fig. 4.1.

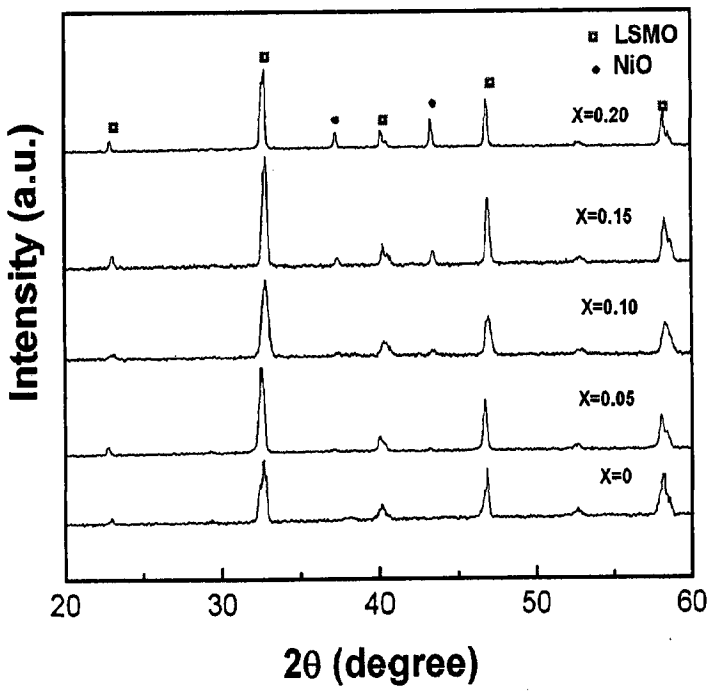

Figure 4.1: X-ray diffraction patterns of the $(LSMO)_{1-x}/(NiO)_x$ composites.

The patterns show two different sets of peaks: one for perovskite LSMO phase and another for cubic NiO. No other phases were detected in the samples by XRD. The Bragg peaks of LSMO and NiO phases do not shift, indicating that cell parameter of LSMO and NiO do not change after sintering. This also indicates that there is no reaction between LSMO and NiO and it is expected that NiO introduced as second phase of the composite mainly segregates at the grain boundaries and on the surfaces of the LSMO grains.

4.3.2 Microstructural analysis

The SEM micrographs of $(LSMO)_{1-x}/(NiO)_x$ composites for x = 0 and x = 0.10 are shown in Fig. 4.2 (a) and (b), respectively. A clear grain boundary is observed in pure LSMO as shown in Fig. 4.2 (a). However, by addition of NiO the grain boundaries of $(LSMO)_{1-x}/(NiO)_x$ composite become ambiguous as shown in Fig. 4.2 (b). From the SEM image (Fig. 4.2 (b)), it is also clear that the smaller particles of doped NiO segregated mainly at the grain boundaries and on the surfaces of larger size LSMO grains. These results also demonstrate that $(LSMO)_{1-x}/(NiO)_x$ composites are the mixture of two phases. In Fig. 4.2 (b), LSMO and NiO grains are indicated by white and black arrows, respectively to distinguish them.

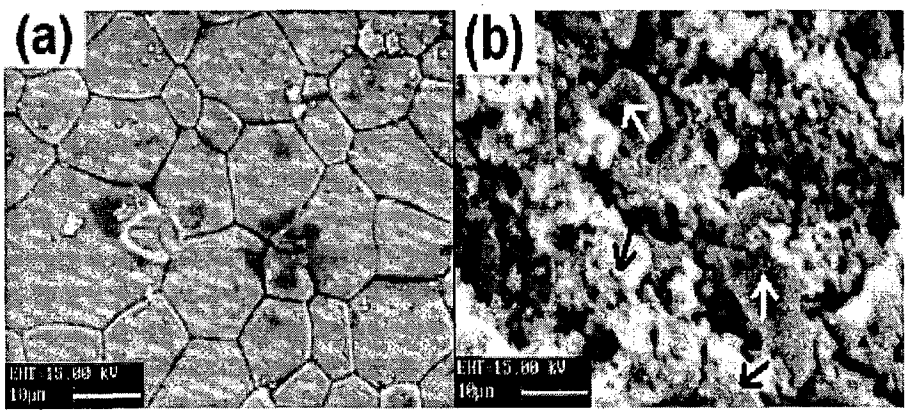

Figure 4.2: Scanning electron micrographs of $(LSMO)_{1-x}/(NiO)_x$: (a) x = 0 and (b) x = 0.10.

4.3.3 Magnetic properties

The temperature dependence of magnetization has been measured at 5 kOe and is shown in Fig. 4.3. The value of magnetization (M) at 80 K are 81.38, 80.10, 77.70, 73.66 and 68.70 emu/gm for x = 0.0, 0.05, 0.10, 0.15 and 0.20, respectively. This successive decrease in M with increasing NiO concentration is expected and is due to decrease in the volume fraction of ferromagnetic LSMO phase and increase in the antiferromagnetic NiO phase in the composites.

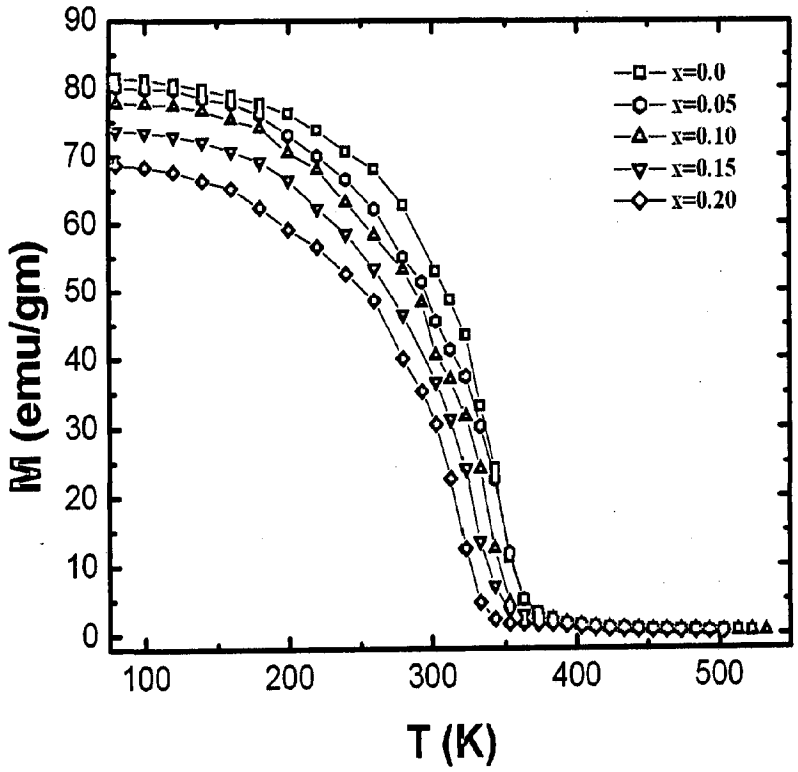

Figure 4.3: Temperature dependence of magnetization at 5 kOe of the $(LSMO)_{1-x}/(NiO)_x$ composites.

All the composites have almost similar behaviour of magnetization as a function of temperature and there is a shift in paramagnetic (PM) to ferromagnetic (FM) phase transition temperature (Tc), which moves towards lower value with increase in the NiO content. The

transition temperatures determined from the peak in (dM/dT)-T curve are found to be ~343, 342, 338, 325 and 318 K for samples x = 0.0, 0.05, 0.10, 0.15 and 0.20, respectively. As observed by SEM, NiO segregates into the grain boundaries/interfacial regions and this interfacial/grain boundary segregation of NiO affects the double exchange (DE) mechanism and this is more pronounced in the FM domain walls. This consequently leads to the suppression of PM-FM transition temperature towards the lower value with increase in NiO concentration. In fact, the reduction in the magnetization also suggests the suppression of DE mechanism resulting suppression of the ferromagnetic alignment of Mn ions. This indicates the magnetic spin disorder induced by the grain boundaries in the composites. The magnetic hysteresis loops measured at room temperature for the $(LSMO)_{1-x}/(NiO)_x$ samples with x = 0.0, 0.05, 0.10, 0.15 and 0.20 are displayed in Fig. 4.4.

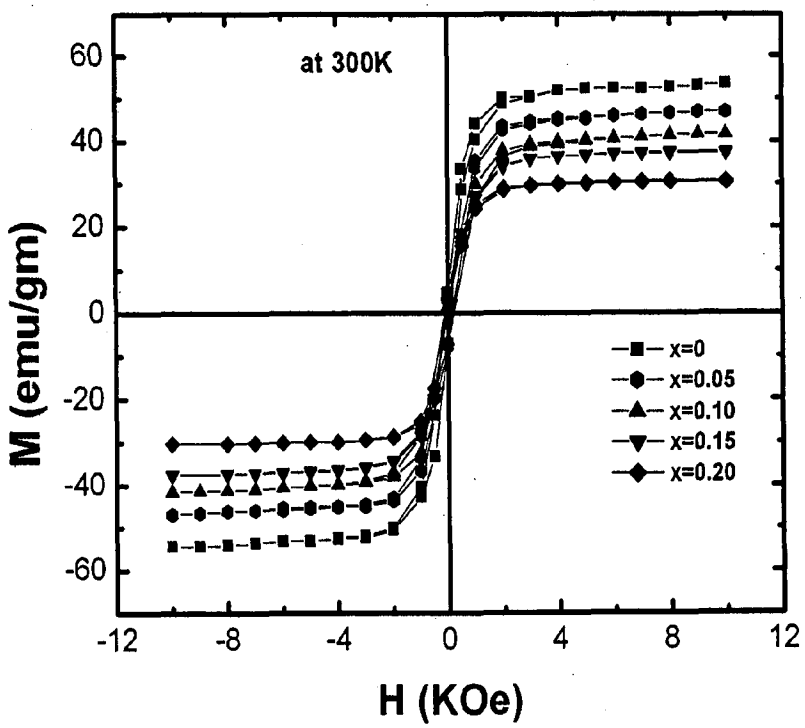

Figure 4.4: Magnetic hysteresis loops at room temperature of the $(LSMO)_{1-x}/(NiO)_x$ composites.

M-H curve indicates that the magnetization of the samples increases rapidly at low fields and then tends to saturate at higher field. The value of magnetization of composites decreases with x. This demonstrates that the ferromagnetic order is weakened and magnetic disorder is increased with NiO content. Thus inclusion of antiferromagnetic NiO dilutes the magnetization of composite samples even at room temperature.

If we calculate the value of saturation magnetization (M_s) (from Fig. 4.4) according to the magnetization of parent LSMO and its weight fraction in the composites, then the value of M_s of the composites with x = 0.05, 0.10, 0.15 and 0.20 are 50.94, 48.26, 45.58 and 42.9 emu/gm which are greater than the observed experimental values 46.86, 41.64, 37.30 and 30.81 emu/gm, respectively.

4.3.4 Electrical resistivity measurements

The temperature dependence resistivity of all the samples measured by four probe technique at zero field is shown in Fig. 4.5. As expected, the metal like conductivity is found in pure LSMO with a metallic transition at T_{IM} ~315 K. With increasing NiO concentration, x, the zero field resistivity of $(LSMO)_{1-x}/(NiO)_x$ composites increases and the metal-insulator transition shifts successively towards lower temperatures. The metal-insulator transition points (T_{IM}) are measured to ~227, 212, 198 and 156 K for x = 0.05, 0.10, 0.15 and 0.20, respectively and these values are much lower than the value of T_{IM} ~315 K observed in pure LSMO. The different electrical transport behaviour and high resistivity of the composites could be related to the effect of dopant NiO on electrical transport channel in the composites. In pure LSMO, the electrical transport is achieved through a direct contact between LSMO grains. However, in doped composites, there are two kinds of conduction channels parallel connected to each other [32, 33]. One is related to LSMO grains, which determines the transport properties of the system through direct contact between LSMO grains and other is related to dopant NiO. Since the dopant is mainly segregated at the grain boundaries and on the surfaces of LSMO grains producing energy barriers to electrical transport process and due to this higher resistivity is observed for the doped composites.

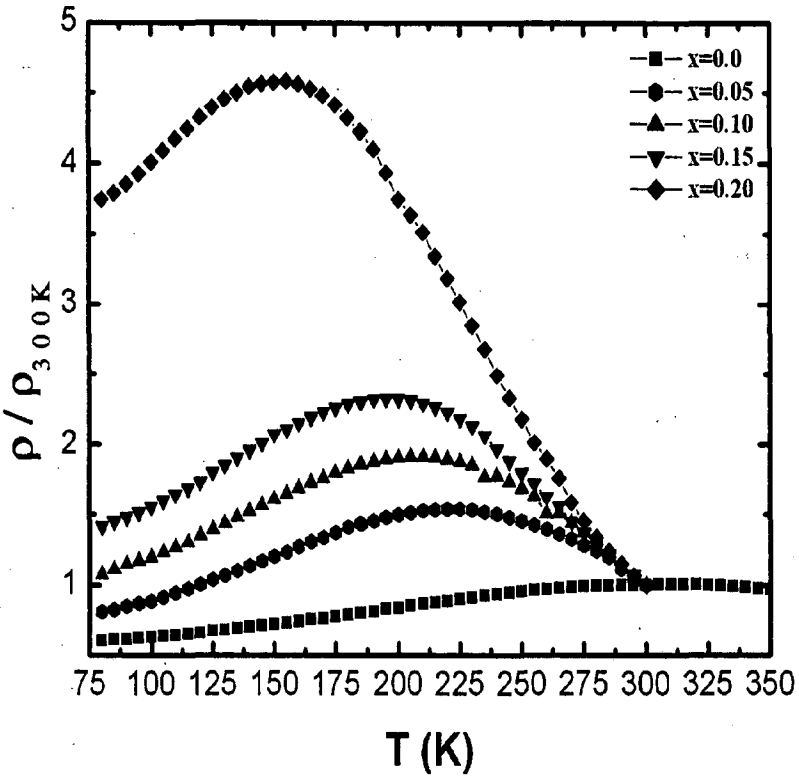

Figure 4.5: Temperature dependence of normalized resistivity at zero field of the $(LSMO)_{1-x}/(NiO)_x$ composites.

4.3.5 Magnetoresistance studies

The magnetic field dependence of MR of all the studied samples at a fixed temperature 80 K measured in magnetic field range of 0-12 kOe is shown in Fig. 4.6. Figure 4.6 indicates that the change in MR is more in the doped composites as compared to pure LSMO which indicates that the enhancement in MR basically comes through the formation of composites. It suggests that spin polarized tunneling across the FM grains may be the possible transport phenomena in the doped composite samples for enhancement in MR [1]. Moreover, the change in MR is more at low field (up to 3 kOe) for x = 0.05, 0.10 and 0.15 as compared to the virgin LSMO sample and the maximum MR change is obtained at H~3 kOe for the sample with x = 0.15. The values of MR at 80 K are ~14.34, ~15.68, ~16.94 & ~19.84

% at 3 kOe field while the same are ~17.58, ~19.05, ~20.39 & ~21.99 % at 12 kOe field for x = 0, 0.05, 0.10 and 0.15, respectively. Thus, the observed enhancement in MR at 80 K with respect to pure LSMO (x = 0) is ~9, ~18 & ~38 % at 3 kOe field while the same is ~8, ~16, & ~25 % at 12 kOe field for x = 0.05, 0.10 and 0.15, respectively. By the addition of insulating antiferromagnetic NiO, the spin disorder is produced through the tunneling process at the grain boundaries and when a magnetic field is applied, the spin disorder is suppressed, resulting the high MR, especially at low field ~3 kOe. On the other hand, extra magnetic disorder at the interfaces also increases the magnetic domain scattering at the grain boundary regions [34, 35].

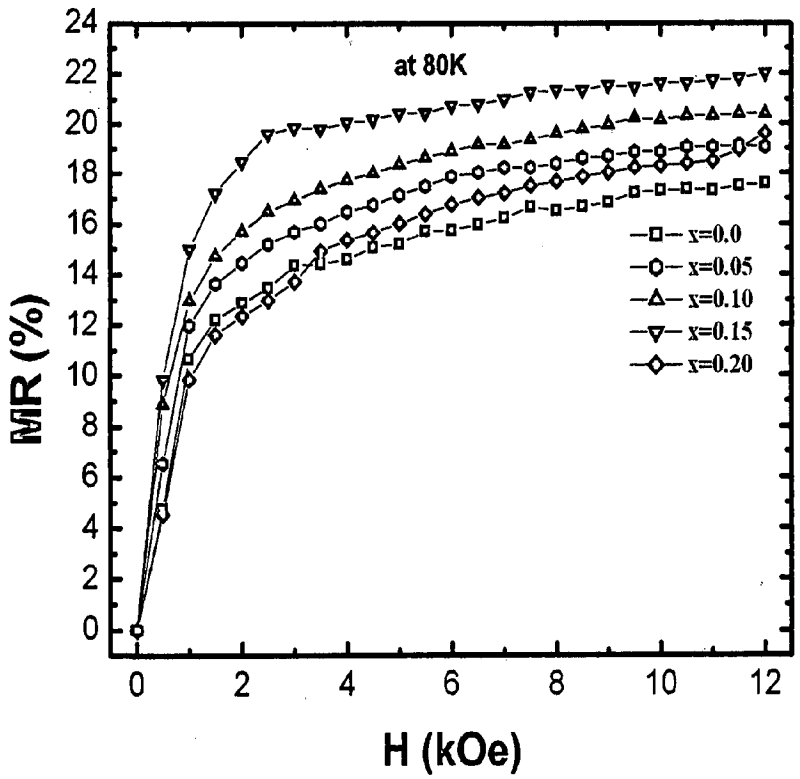

Figure 4.6: Magnetic field dependence of magnetoresistance (MR) in magnetic field (0-12 kOe) at 80 K of the $(LSMO)_{1-x}/(NiO)_x$ composites.

In the pure LSMO, the conduction electrons are almost polarized inside a magnetic domain and are easily transferred between pairs of Mn^{3+} and Mn^{4+} ions. However, when these electrons travel across grains, strong spin dependent scattering at the boundaries will lead to a high resistivity. Application of a moderately low field can align the domains into a parallel configuration causing the drop in the resistivity and enhancement in LFMR. Thus the overall change in LFMR at low temperature is due to enhanced spin disorder in the intergranular regions which leads to enhanced spin polarized tunneling. The spin polarized tunneling is controlled by the thickness of the insulating NiO layer. The reduction in MR for the composite with x = 0.20 at low field may be because of grain boundaries becoming too thick for electron tunneling. However, the magnetic field dependence of MR at room temperature is different from the same at 80 K as shown in Fig. 4.7.

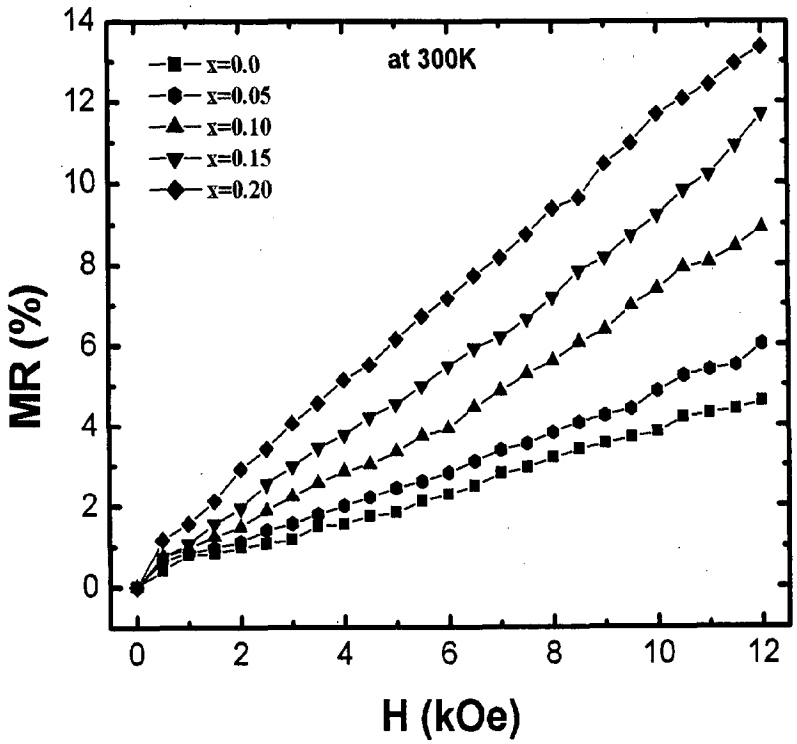

Figure 4.7: Magnetic field dependence of magnetoresistance (MR) in magnetic field (0-12 kOe) at 300 K of the $(LSMO)_{1-x}/(NiO)_x$ composites.

The magnetic field dependence MR curve at 80 K (as shown in Fig. 4.6) clearly indicates the sharp enhancement in MR at low fields and it saturates at the higher values of fields while at room temperature the MR increases with field almost linearly (as shown in Fig. 4.7) in whole field range (0-12 kOe), which is high field magnetoresistance (HFMR) behaviour. This HFMR originates from the ordering of grain boundary spins and provides the information about the magnetic behaviour of grain boundary region [36]. In our case, this HFMR increases with increasing the NiO concentration in the composite samples and is maximum for the composite with x = 0.20. The value of MR at 300 K is ~13.34 % for the composite with x = 0.20 while it is ~4.59 % for pure LSMO at 12 kOe field.

The temperature dependence of magnetoresistance (MR) in a field of 3 kOe for the composite samples is shown in Fig. 4.8. The values of MR are large for the composites with x = 0.05, 0.10 and 0.15 and less for x = 0.20 as compared to pure LSMO (x = 0) at the temperature below 120 K. The MR ratios at 80 K are ~15.87, 16.64, 20.14 and 12.19 % for the composites with x = 0.05, 0.10, 0.15 and 0.20, respectively while ~14.28 % for pure LSMO at 3 kOe field. This indicates that the MR ratio in the composites (up to x = 0.15) is larger than that in pure LSMO. This enhanced MR effect obviously comes through the formation of composites. The increase in MR at low temperature seems to be due to enhanced tunneling across LSMO grain boundaries and additional grain boundary effects introduced by NiO grains. Usually this low temperature MR results mainly from a grain boundary effect as proposed by Hwang et al. [1]. According to this, the spin polarized tunneling between neighbouring grains of manganites is responsible for the magnetoresistance effect in the polycrystalline samples. This tunneling takes place across the grain boundaries or interfaces especially at low temperatures (T<Tc). However, decrease in

MR, for x = 0.20 at low temperature region (below 120 K), may be because of the grain boundaries becoming too thick for the spin preserving electron tunneling.

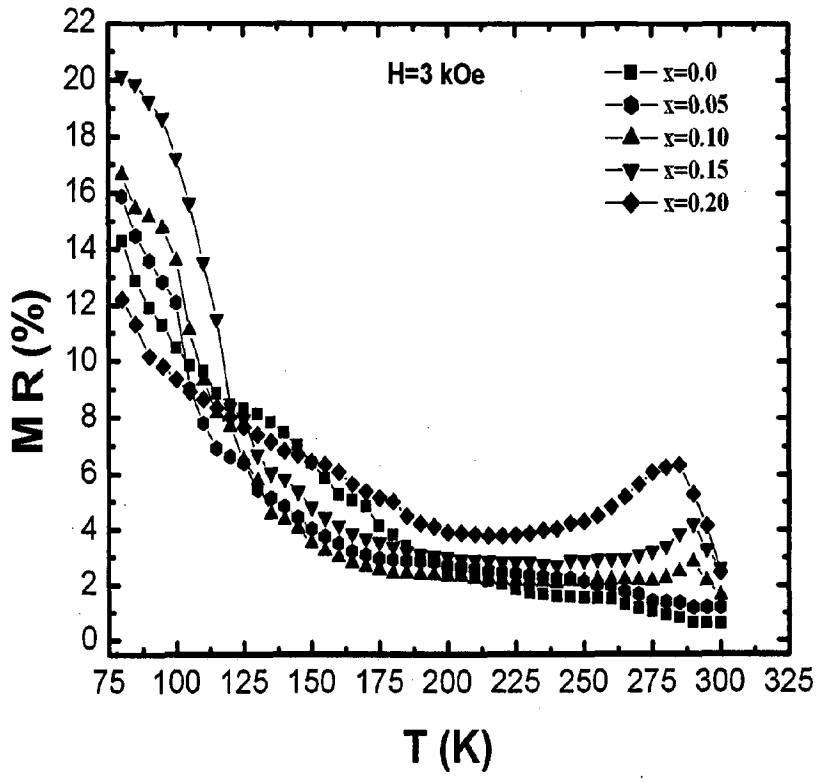

Figure 4.8: Temperature dependence of magnetoresistance (MR) in a field of 3 kOe of the $(LSMO)_{1-x}/(NiO)_x$ composites.

The enhancement in MR is also observed at high temperature (near room temperature) in all the composites. The value of this high temperature MR increases with NiO dopant. The maximum MR change is observed for the composites with x = 0.20. The value of MR at 285 K is ~6.34 % for the composite with x = 0.20 while ~0.80 % for pure LSMO at 3 kOe field. This large enhancement in MR at high temperature region is concerned to high field magnetoresistance phenomena. It is clear from the Fig. 4.7 that the field dependence MR at room temperature follows the HFMR behaviour and the value of MR increases almost linearly with field for all NiO concentrations. So, the enhancement in MR at/around room

temperature for all the composites is concerned to HFMR. This HFMR originates by the magnetic disorder produced by the antiferromagnetic coupling of the grain boundaries [36]. The room temperature M-H curve (Fig. 4.4) also shows that the magnetization of the composites decreases with NiO content which demonstrates that the ferromagnetic order of LSMO is weakened and magnetic disorder is produced which suppresses the ferromagnetic alignment of the Mn ions and this leads to enhanced MR around room temperature [28].

4.4 RESULTS AND DISCUSSION OF $(La_{0.7}Sr_{0.3}MnO_3)_{1-x}/(TiO_2)_x$ COMPOSITE

4.4.1 X-ray diffraction studies

Figure 4.9 shows the XRD patterns of $(LSMO)_{1-x}/(TiO_2)_x$ samples, where intensity has been plotted on the logarithmic scale.

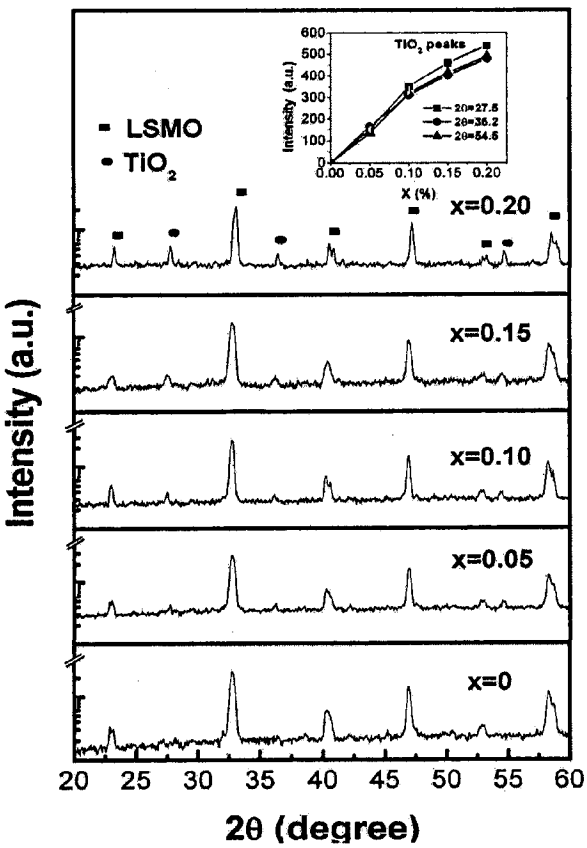

Figure 4.9: X-ray diffraction patterns of the $(LSMO)_{1-x}/(TiO_2)_x$ composites on logarithmic scale. Inset shows the intensity versus x curve of TiO_2 peaks.

The pattern of virgin (x = 0) sample shows a single perovskite structure. With TiO_2 addition, the TiO_2 phase, as evidenced by TiO_2 diffraction maxima, appears indicating that samples are composed of two phases: LSMO perovskite and TiO_2. With increasing TiO_2 concentrations, the TiO_2 peaks grow almost linearly in intensity as shown in the inset of Fig. 4.9. This indicates that there is very less possibility of reaction between LSMO and TiO_2 and all TiO_2 introduced as second phase of the composite mainly segregates at the grain boundaries and on the surfaces of the LSMO grains.

4.4.2 Microstructural analysis

The coexistence of two phases can also be seen from SEM micrographs which clearly indicate the two different types of crystallites. The SEM micrographs of $(LSMO)_{1-x}/(TiO_2)_x$ samples with x = 0, x = 0.10, x = 0.15 and x = 0.20 are shown in Fig. 4.10 (a)-(d), respectively.

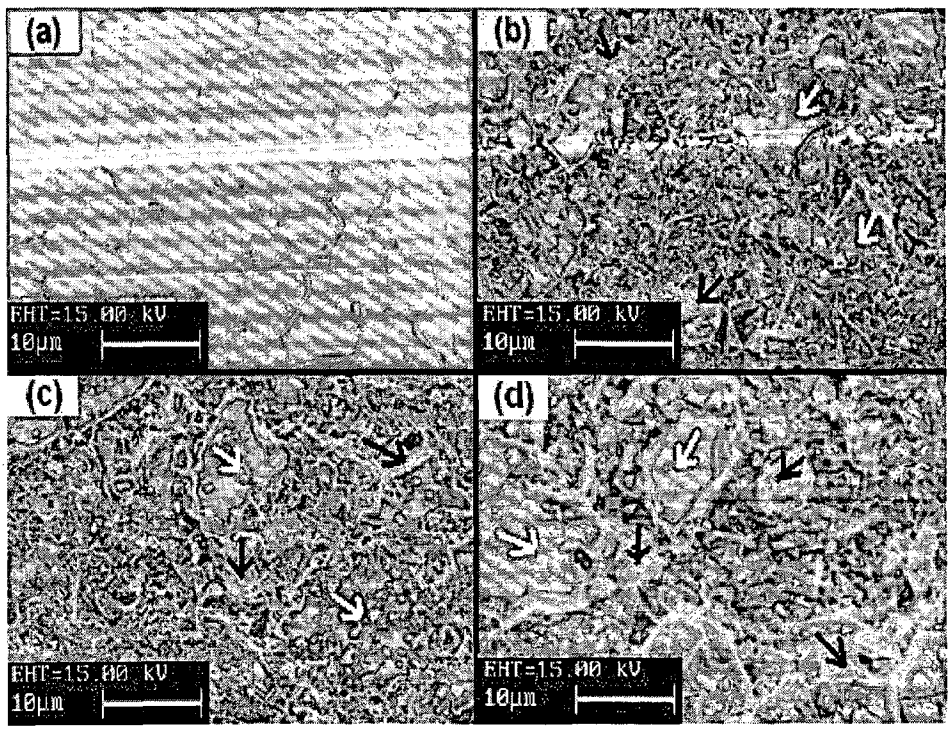

Figure 4.10: Scanning electron micrographs of $(LSMO)_{1-x}/(TiO_2)_x$ with (a) x = 0, (b) x = 0.10, (c) x = 0.15 and (d) x = 0.20.

A clear grain boundary is observed in pure LSMO as shown in Fig. 4.10 (a). However, the grain boundaries of $(LSMO)_{1-x}/(TiO_2)_x$ composites become ambiguous as shown in Fig. 4.10 (b)-(d). From the SEM image, it is also clear that the large LSMO grains are well distributed and surrounded by white color TiO_2 powder. In SEM micrographs, the LSMO and TiO_2 regions are indicated by white and black arrows, respectively, to distinguish them.

4.4.3 Magnetic properties

The temperature dependence of magnetization has been measured at 5 kOe and is shown in Fig. 4.11. The value of magnetization (M) at 80 K are 81.93, 78.50, 71.66, 67.74 and 60.66 emu/gm for x = 0.0, 0.05, 0.10, 0.15 and 0.20, respectively. This successive decrease in M with increasing TiO_2 concentrations is expected and is due to decrease in the volume fraction of ferromagnetic LSMO phase and increase of nonmagnetic TiO_2 phase in these composites. The magnetization decreases almost linearly with TiO_2 concentrations (x) as shown in the inset of Fig. 4.11. This supports the fact that successive decrease in M with increasing TiO_2 concentration is due to decrease in the volume fraction of LSMO phase. All the composites, studied in the present work, have almost similar behaviour of magnetization as a function of temperature. Moreover, the paramagnetic (PM) to ferromagnetic (FM) phase transition temperature (Tc) is almost independent of TiO_2 content (x) and is ~345 K for all the samples. This is due to the fact that the PM-FM phase transition is an intrinsic and intragrain property. The observed constancy of Tc also indicates that stoichiometry of LSMO phase within the grains remains essentially unchanged as TiO_2, which can not be accommodated within the perovskite structure, sits on the grain boundaries and on the surfaces of LSMO grains. Furthermore the reduction in magnetization suggests the suppression of DE mechanism resulting suppression of the ferromagnetic alignment of Mn

ions. This indicates the magnetic spin disorder induced by grain boundaries in the composites.

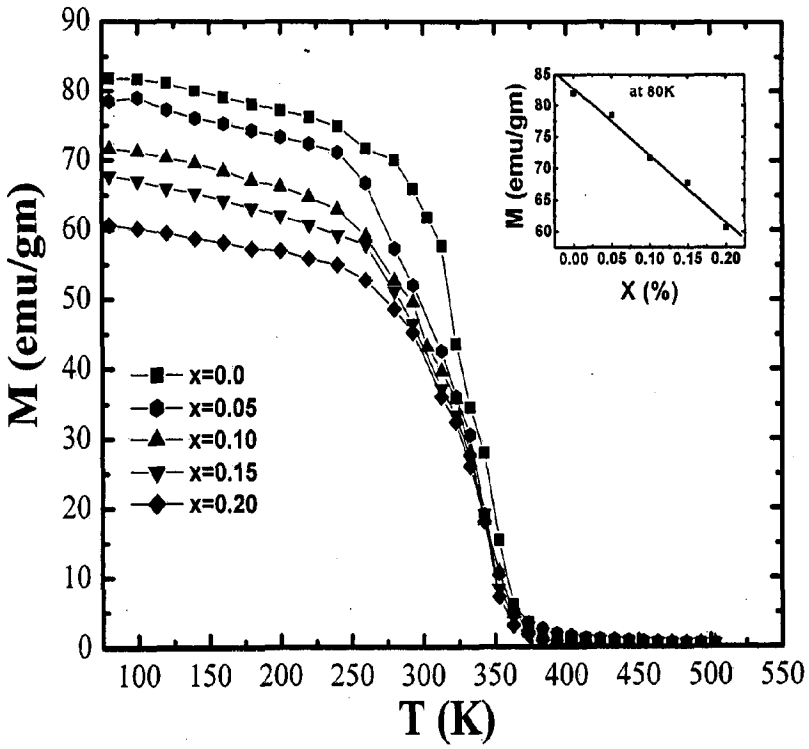

Figure 4.11: Temperature dependence of magnetization at 5 kOe of the $(LSMO)_{1-x}/(TiO_2)_x$ composites.

The magnetic hysteresis loops at room temperature for the $(LSMO)_{1-x}/(TiO_2)_x$ samples with x = 0.0, 0.05, 0.10, 0.15 and 0.20 are displayed in Fig. 4.12. M-H curves show that the magnetization of the samples increases rapidly at low fields and then tends to saturate at higher field. The value of magnetization of composites decreases with x because of decrease in the volume fraction of LSMO phase. This demonstrates that ferromagnetic order is weakened and magnetic disorder increases with TiO_2 content. Thus inclusion of TiO_2 dilutes the magnetization of the composite samples.

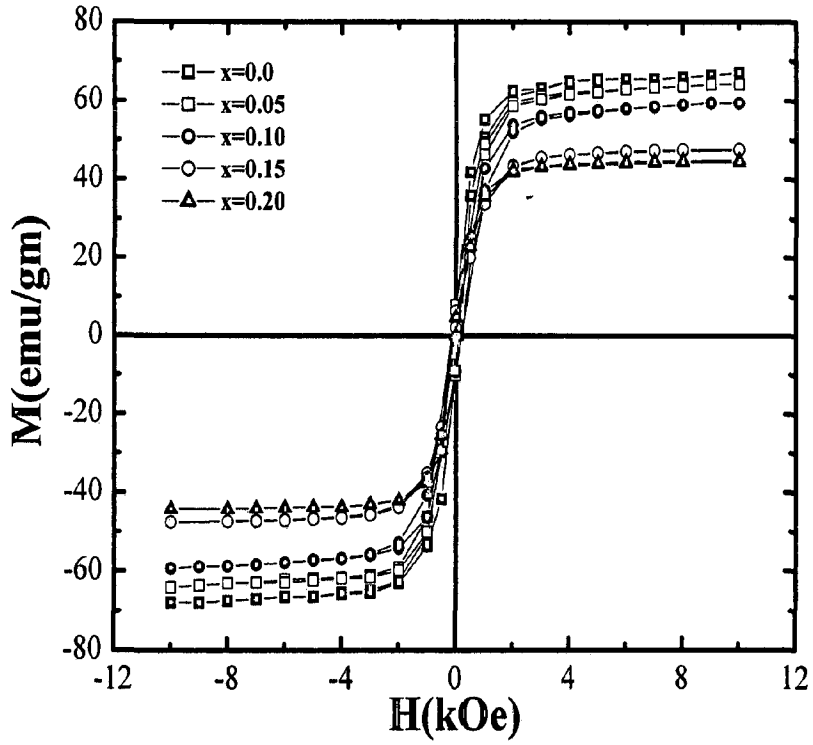

Figure 4.12: Magnetic hysteresis loops of the $(LSMO)_{1-x}/(TiO_2)_x$ composites.

4.4.4 Electrical resistivity measurements

The temperature dependence of resistivity for all the samples measured by four probe technique at zero field is shown in Fig. 4.13. As expected, the metal like conductivity is found in pure LSMO with a metallic transition at T_{IM} ~315 K. With increasing TiO_2 concentration, x, the zero field resistivity of $(LSMO)_{1-x}/(TiO_2)_x$ composites increases and the metal-insulator transition shifts successively towards lower temperatures. The metal-insulator transition points (T_{IM}) are measured to ~240, ~220, ~205 and ~185 K for x = 0.05, 0.10, 0.15 and 0.20, respectively and these values are much lower than the value of T_{IM} ~315 K, observed in pure LSMO (x = 0).

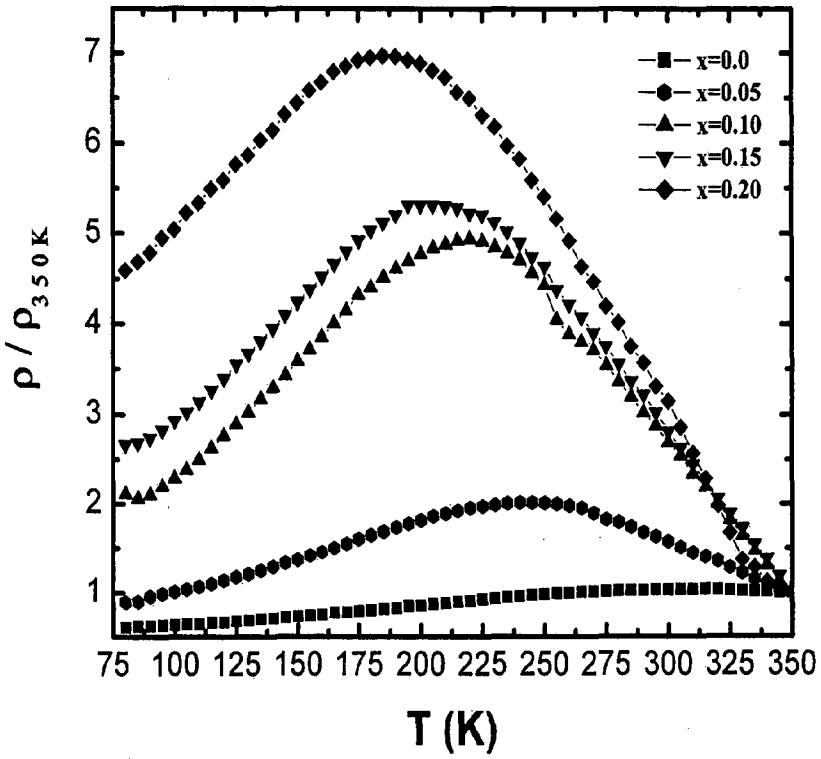

Figure 4.13: Resistivity versus temperature curves at zero field of the $(LSMO)_{1-x}/(TiO_2)_x$ composites.

As observed from SEM micrographs (Fig. 4.10 (b)-(d)), TiO_2 segregates at the grain boundaries and envelopes the LSMO grains and thus forming a layer. The thickness of this layer increases with increasing TiO_2 concentration. The strong suppression of the T_{IM} as compared to T_C is caused by the TiO_2 induced disorders and also by the increase in the nonmagnetic-insulating phase fraction in the composites. This causes the increase in the carrier scattering leading to a corresponding enhancement in the resistivity. Moreover, in pure LSMO, the electrical transport is achieved through a direct contact between LSMO grains. However, in doped composites, there are two kinds of conduction channels parallel connected to each other [32, 33]. One is related to LSMO grains, which determines the

transport properties of the system through direct contact between LSMO grains and other is related to dopant TiO_2.

4.4.5 Magnetoresistance studies

The temperature dependence of magnetoresistance (MR) in a field of 3 kOe for all the studied samples is shown in Fig. 4.14. It is clear from Fig. 4.14 that the temperature dependence of MR has two distinct regimes. The MR of pure LSMO, in the high temperature region (T>130 K), is larger than all composites for x = 0.05, 0.10, 0.15 and 0.20, while in low temperature region (T<130 K), the same is higher for the composites having low TiO_2 concentration, viz., x ~0.05 and 0.10.

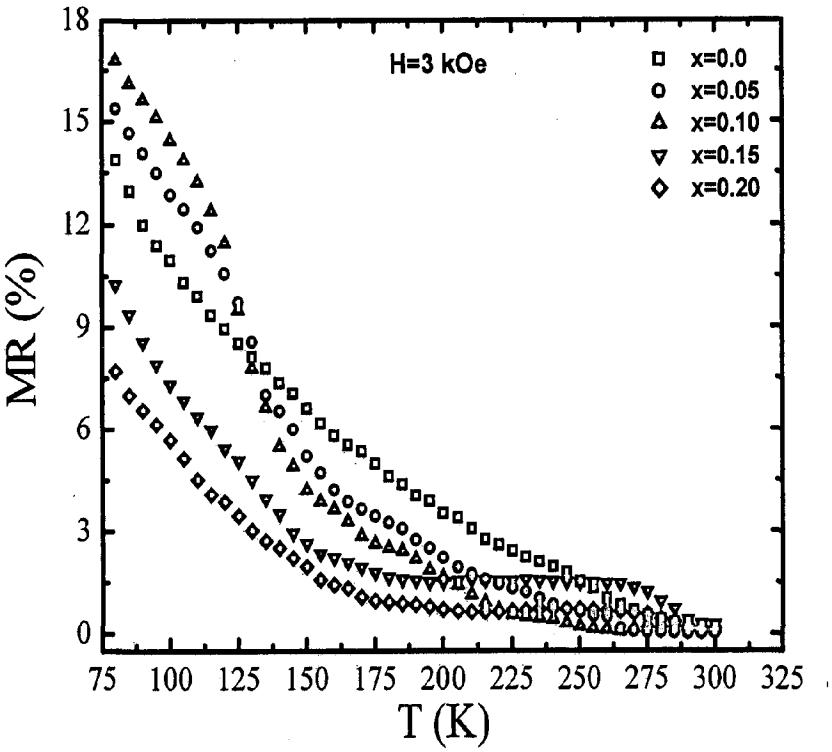

Figure 4.14: Temperature dependence of magnetoresistance (MR) in a field of 3 kOe of the $(LSMO)_{1-x}/(TiO_2)_x$ composites.

The observed MR ratio at 80 K is ~15.4 % and ~17.8 % for the composites with x = 0.05 and 0.10, respectively while ~13.9 % for pure LSMO at 3 kOe field. So, the observed enhancement in MR at 80 K with respect to pure LSMO (x = 0) is ~11 % & ~28 % for the composites with x = 0.05 and 0.10, respectively, at 3 kOe field. This increase in MR in low temperature region (below 130 K) seems to be due to enhanced tunneling across LSMO grain boundaries and additional grain boundary effects introduced by TiO_2 grains. As proposed by Hwang et al. [1], the spin polarized tunneling between neighbouring grains of manganites is responsible for the magnetoresistance effect in polycrystalline samples. This tunneling takes place across the grain boundaries or interfaces, which produce the spin disorder. The reduction in magnetization with TiO_2 concentration (Fig. 4.11) also supports the magnetic spin disorder induced by grain boundaries in the composites and this spin disorder is suppressed by applying the magnetic field, resulting the enhancement in MR. As Fig. 4.14 indicates, we get the enhancement in MR for the composites with x = 0.05 and 0.10 only at temperatures below 130 K which confirms that this enhanced MR basically comes from grain boundary effects in our samples because it is well known that LFMR is mainly attributed to a grain boundary effect especially at temperature T<Tc. However, with further increase in TiO_2 level from x = 0.10, the MR decreases even at low temperatures, which may result because the grain boundaries become too thick for spin preserving electron tunneling.

The magnetic field dependence of MR of all the samples measured in magnetic field range of 0-12 kOe at 80 K is shown in Fig. 4.15. Analysis of Fig. 4.15 shows that with increase in the magnetic field from 0 to 12 kOe, the value of MR for low TiO_2 doping (x = 0.05 and 0.10) is larger than pure LSMO (x = 0.0) and smaller than pure LSMO for x > 0.10. It suggests that magnetic field sensitive MR can be enhanced only at low concentrations of TiO_2 secondary phase (up to x = 0.10 in the present case).

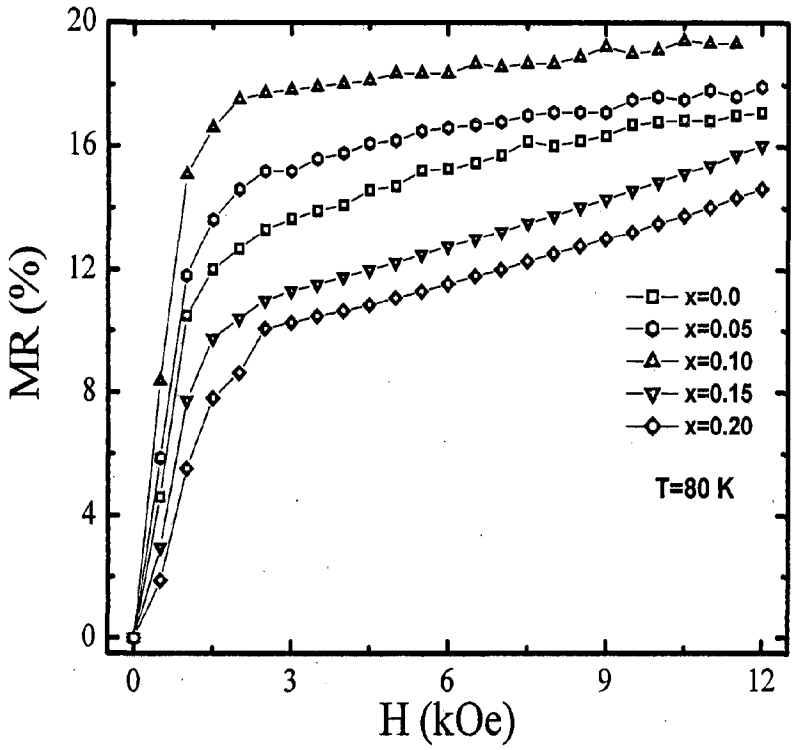

Figure 4.15: Magnetic field dependence of magnetoresistance (MR) in magnetic field (0-12 kOe) at 80 K of the $(LSMO)_{1-x}/(TiO_2)_x$ composites.

The MR increases sharply at low fields and saturate for the higher value of fields. The values of MR at 80 K are ~13.9, ~15.4 % and ~17.8 % at 3 kOe while the same are ~17.1, ~17.9 % and ~19.3 % at 12 kOe for the composite samples with x = 0, 0.05, and 0.10, respectively. This shows that the percent change in MR for the composites with x = 0.05 and 0.10 with respect to pure LSMO (x = 0) is more at low fields (up to 3 kOe). The percentage change in MR with respect to pure LSMO at 80 K is ~11 and ~28 % at 3 kOe field while the same is ~5 and ~13 % at 12 kOe field for the composites with x = 0.05 and 0.10, respectively. This indicates that large change in MR is produced at low fields and this LFMR is caused through spin disorder by the tunneling process at the grain boundaries and

when a magnetic field is applied, the spin disorder is suppressed, resulting the high MR, especially at low field (~3 kOe).

4.5 CONCLUSIONS

In this work, we have successfully prepared the composite of $La_{0.7}Sr_{0.3}MnO_3$ with NiO and TiO_2 as second phase material via solid-state reaction process and investigated their microstructural, magnetic and magnetotransport properties. The main highlights of the work are summarized below:

1. The X-ray diffraction patterns show a single perovskite structure for the virgin (x = 0) sample and two different sets of peaks for the composites: one for perovskite LSMO phase and another for NiO or TiO_2 phase depending on the composite $(LSMO)_{1-x}/(NiO)_x$ or $(LSMO)_{1-x}/(TiO_2)_x$.
2. The Bragg reflections of LSMO and second phase material (NiO and TiO_2) do not shift, indicating that cell parameter of LSMO and NiO or TiO_2 do not change after sintering. This also indicates that there is no reaction between LSMO and NiO or TiO_2 and it is expected that NiO and TiO_2 introduced as second phase of the composite mainly segregates at the grain boundaries and on the surfaces of the LSMO grains.
3. The value of magnetization and paramagnetic (PM) to ferromagnetic (FM) phase transition temperature (Tc) decreases with increasing the NiO concentration (x), in case of $(LSMO)_{1-x}/(NiO)_x$ composite. The transition temperatures determined from the peak in (dM/dT)-T curve for $(LSMO)_{1-x}/(NiO)_x$ composites are found to be ~343, 342, 338, 325 and 318 K for samples x = 0.0, 0.05, 0.10, 0.15 and 0.20,

respectively. However in case of $(LSMO)_{1-x}/(TiO_2)_x$, Tc is almost independent of TiO_2 content (x) and is ~345 K for all the samples.

4. The resistivity increases and the value of insulator ($d\rho/dT<0$) to metal ($d\rho/dT>0$) transition temperature shifts successively towards lower temperatures with x in both of composites. The metal-insulator transition points (T_{IM}) are measured to ~315, ~227, 212, 198 and 156 K for $(LSMO)_{1-x}/(NiO)_x$ and ~315, ~240, 220, 205 and 185 K for $(LSMO)_{1-x}/(TiO_2)_x$ for x = 0.0, 0.05, 0.10, 0.15 and 0.20, respectively.

5. MR measurements with temperature show that the MR ratio in the $(LSMO)_{1-x}/(NiO)_x$ composites is larger than pure LSMO (x = 0) up to x = 0.15 while the same is larger than pure LSMO only up to x = 0.10 in case of $(LSMO)_{1-x}/(TiO_2)_x$ in low temperature region (below 130 K).

6. Moreover in case of $(LSMO)_{1-x}/(NiO)_x$, the MR increases even at high temperature (near room temperature) for all the compositions (x) and the magnetic field dependence of MR at room temperature is different from the MR at 80 K and this room temperature MR increases with field almost linearly (as shown in Fig. 4.7) in whole field range (0-12 kOe), which is HFMR behaviour.

7. MR measurements with field show that the change in MR as compared to the virgin LSMO sample is more at low field (up to 3 kOe) for x = 0.05, 0.10 and 0.15 for $(LSMO)_{1-x}/(NiO)_x$ composites and x = 0.05 and 0.10 for $(LSMO)_{1-x}/(TiO_2)_x$ composites. The observed enhancement in MR for $(LSMO)_{1-x}/(NiO)_x$ composite at 80 K with respect to pure LSMO (x = 0) is ~9, ~18 & ~38 % at 3 kOe field while the same is ~8, ~16, & ~25 % at 12 kOe field for x = 0.05, 0.10 and 0.15, respectively. Similarly the percentage change in MR for $(LSMO)_{1-x}/(TiO_2)_x$

composite with respect to pure LSMO (x = 0) at 80 K is ~11 and ~28 % at 3 kOe field while the same is ~5 and ~13 % at 12 kOe field for the composites with x = 0.05 and 0.10, respectively. This shows that percentage change in MR of both composites with respect to pure LSMO is more at low field (~3 kOe) in comparison to high field (~12 kOe).

In both of the studies, an enhancement in magnetoresistance is observed up to a certain concentration (x) of second phase materials (NiO and TiO_2). The enhancement in MR is observed up to x = 0.15 in case of $(LSMO)_{1-x}/(NiO)_x$ while up to x = 0.10 in case of $(LSMO)_{1-x}/(TiO_2)_x$ below 120 K and 130 K, respectively. Moreover, in $(LSMO)_{1-x}/(NiO)_x$ system, the enhancement in MR is observed even at room temperature. Most important is that this enhancement in MR is more at low fields up to 3 kOe, which is useful for the potential applications.

REFERENCES

1. Hwang H Y, Cheong S W, Ong N P & Batlogg B, "Spin-polarized intergrain tunneling in $La_{2/3}Sr_{1/3}MnO_3$", Phys. Rev. Lett., **77**, 2041 (1996).
2. Gupta A, Gong G Q, Xiao G, Duncombe P R, Ttouilloud P, Lecoeur P, Wang Y Y, Dravid V P & Sun J Z, "Grain-boundary effects on the magnetoresistance properties of perovskite manganite films", Phys. Rev. B, **54**, R15629 (1996).
3. Wang X L, Dou S X, Liu H K, Ionescu M & Zeimetz B, "Large low-field magnetoresistance over a wide temperature range induced by weak-link grain boundaries in $La_{0.7}Ca_{0.3}MnO_3$", Appl. Phys. Lett., **73**, 396 (1998).
4. Gutpa A & Sun J Z, "Spin-polarized transport and magnetoresistance in magnetic oxides", J. Magn. Magn. Mater., **200**, 24 (1999).
5. Balcells L I, Carrillo A E, Martinez B & Fontcuberta J, "Enhanced field sensitivity close to percolation in magnetoresistive $La_{2/3}Sr_{1/3}MnO_3/CeO_2$ composites", Appl. Phys. Lett., **74**, 4014 (1999).
6. Ziese M, "Extrinsic magnetotransport phenomena in ferromagnetic oxides", Rep. Prog. Phys., **65**, 143 (2002).
7. Petrov D K, Krusin-Elbaum L, Sun J Z, Field C & Duncombe P R, "Enhanced magnetoresistance in sintered granular manganite/insulator systems", Appl. Phys. Lett., **75**, 995 (1999).
8. Gupta S, Ranjit R, Mitra C, Raychaudhuri P & Pinto R, "Enhanced room-temperature magnetoresistance in $La_{0.7}Sr_{0.3}MnO_3$-glass composites", Appl. Phys. Lett., **78**, 362 (2001).

9. Liu J M, Li J, Huang Q, You L P, Wang S J, Ong C K, Wu Z C, Liu Z G & Du Y W, "Partially crystallized $La_{0.5}Sr_{0.5}MnO_3$ thin films by laser ablation and their enhanced low-field magnetoresistance", Appl. Phys. Lett., **76**, 2286 (2000).

10. Das D, Chowdhury P, Das R N, Srivastava C M, Nigam A K & Bahadur D, "Solution sol–gel processing and investigation of percolation threshold in $La_{2/3}Ca_{1/3}MnO_3$: $xSiO_2$ nanocomposite", J. Magn. Magn. Mater., **238**, 178 (2002).

11. Sun J R, Shen B G, Yeung H W & Wong H K, "Formation of interfacial phase and its effects on the magnetic and transport properties of the $La_{0.82}Ca_{0.18}MnO_3$/ $La_{0.18}Ca_{0.82}MnO_3$ composite", J. Phys. D: Appl. Phys., **35**, 173 (2002).

12. Xia Z C, Yuan S L, Zhang G H, Zhang L J, Tang J, Feng W, Liu J, Peng G, Liu L, Li Z Y, Zheng Q H, Cheng L, Tang C Q, Liu S & Xiong C S, "Effect of low Fe_3O_4 doping in $La_{0.67}Ca_{0.33}MnO_3$", J. Phys. D: Appl. Phys., **36**, 217 (2003).

13. Xia Z C, Yuan S L, Tu F, Tang C Q, Peng G, Zhang G H, Liu L, Liu J, Li Z Y, Yang Y P, Xiong C S & Xiong Y H, "Grain boundaries and low-field transport properties in colossal magnetoresistance materials", J. Phys. D: Appl. Phys., **35**, 177 (2002).

14. Liu J M, Yuan G L, Sang H, Wu Z C, Chen X Y, Liu Z G, Du Y W, Huang Q & Ong C K, "Low-field magnetoresistance in nanosized $La_{0.7}Sr_{0.3}MnO_3$/ $Pr_{0.5}Sr_{0.5}MnO_3$ composites", Appl. Phys. Lett., **78**, 1110 (2001).

15. Bahadur D & Das D, "Properties of CMR composites", Proc. Indian Acad. Sci. (Chem. Sci.), **115**, 587 (2003).

16. Das D, Srivastava C M, Bahadur D, Nigam A K & Malik S K, "Magnetic and electrical transport properties of $La_{0.67}Ca_{0.33}MnO_3$ (LCMO): x ZnO composites", J. Phys.: Condens. Matter, **16**, 4089 (2004).

17. Awana V P S, Tripathi R, Balamurugan S, Kishan H & Takayama-Muromachi E, "Magneto-transport of high TCR (temperature coefficient of resistance) $La_{2/3}Ca_{1/3}MnO_3$:Ag polycrystalline composites", Solid State Commun., **140**, 410 (2006).

18. Xia Z C, Yuan S L, Zhang L J, Zhang G H, Feng W, Tang J, Liu L, Liu S, Liu J, Peng G, Li Z Y, Yang Y P, Tang C Q & Xiong C S, "Enhancement of magnetoresistances at room temperature in YSZ doping $La_{0.67}Sr_{0.33}MnO_3$ system", Solid State Commun., **125**, 571 (2003).

19. Huang Y H, Yan C H, Wang S, Luo F, Wang Z M, Liao C S & Xu G X, "Chemical synthesis of $La_{0.7}Sr_{0.3}MnO_3$/silica homogeneous nanocomposites", J. Mater. Chem., **11**, 3296 (2001).

20. Hueso L E, Rivas J, Rivadulla F & López-Quintela M A, "Magnetoresistance in manganite/alumina nanocrystalline composites", J. Appl. Phys., **89**, 1746 (2001).

21. Hueso L E, Rivas J, Rivadulla F & Lopez-Quintela M A, "Magnetic and intergranular transport properties in manganite/alumina composites", J. Non-Cryst. Solids, **287**, 324 (2001).

22. Koster S A, Moshnyaga V, Samwer K, Lebedev O I, Tendeloo G V, Shapoval O & Belenchuk A, "Doping of interfaces in $(La_{0.7}Sr_{0.3}MnO_3)_{1-x}$: $(MgO)_x$ composite films", Appl. Phys. Lett., **81**, 1648 (2002).

23. Shlyakhtin O A, Shin K H & Oh Y J, "Enhancement of low field magnetoresistance by chemical interaction in bulk composites $La_{0.7}Sr_{0.3}MnO_3/SrMeO_3$ (Me = Ti, Zr)", J. Appl. Phys., **91**, 7403 (2002).

24. Shlyakhtin O A, Oh Y J & Tretyakov Y D, "Enhanced low field magnetoresistance at room temperature in $La_{0.7}Sr_{0.3}MnO_3/SrTiO_3$ ($SrZrO_3$) composites", Solid State Commun., **117**, 261 (2001).

25. Yan C H, Xu Z G, Zhu T, Wang Z M, Cheng F X, Huang Y H & Liao C S, "A large low field colossal magnetoresistance in the $La_{0.7}Sr_{0.3}MnO_3$ and $CoFe_2O_4$ combined system", J. Appl. Phys., **87**, 5588 (2000).

26. Huang Q, Li J, Huang X J, Ong C K & Gao X, "Effect of magnetic coupling on the magnetoresistive properties in $La_{0.67}Sr_{0.33}MnO_3/BaFe_{11.3}(ZnSn)_{0.7}O_{19}$ composites", J. Appl. Phys., **90**, 2924 (2001).

27. Hong C S, Kim W S & Hur N H, "Wide colossal magnetoresistance around room temperature in $La_{0.7}Ca_{0.3}MnO_3/La_{0.7}Sr_{0.3}MnO_3$ composite", Solid State Commun., **121**, 657 (2002).

28. Yan C H, Luo F, Huang Y H, Li X H, Wang Z M, Liao C S, Zhao H W & Shen B G, "Enhanced room temperature magnetoresistance in $La_{0.7}Sr_{0.3}MnO_3/ Sm_{0.7}Sr_{0.3}MnO_3$ nanocomposites", J. Appl. Phys., **91**, 7406 (2002).

29. Yuan G L, Liu J M, Liu Z G, Du Y W, Chan H L W & Choy C L, "Preparation of nanosized $La_{0.7}Sr_{0.3}MnO_3/Pr_{0.5}Sr_{0.5}MnO_3$ composites with enhanced low-field magnetoresistance", Mater. Chem. Phys., **75**, 161 (2002).

30. Huang Y H, Yan C H, Luo F, Song W, Wang Z M & Liao C S, "Large enhancement in room-temperature magnetoresistance and dramatic decrease in resistivity in $La_{0.7}Ca_{0.3}MnO_3$–Ag composites", Appl. Phys. Lett., **81**, 76 (2002).

31. Li X H, Huang Y H, Wang Z M & Yan C H, "Tuning between negative and positive magnetoresistance in $(La_{0.7}Sr_{0.3}MnO_3)_{1-x}(La_{1.85}Sr_{0.15}CuO_4)_x$ composites", Appl. Phys. Lett., **81**, 307 (2002).

32. Mark Rubinstein J, "Two-component model of polaronic transport", J. Appl. Phys., **87**, 5019 (2000).

33. de Andres A, Garcia-Hemandez M, Martinez J L & Prieto C, "Low-temperature magnetoresistance in polycrystalline manganites: connectivity versus grain size", Appl. Phys. Lett., **74**, 3884 (1999).

34. Ju H L, Gopalkrishnan J, Peng J L, Li Q, Xiong G C, Venkatesan T & Greene R L, "Dependence of giant magnetoresistance on oxygen stoichiometry and magnetization in polycrystalline $La_{0.67}Ba_{0.33}MnO_z$", Phys. Rev. B, **51**, 6143 (1995).

35. Schiffer P, Ramirez A P, Bao W & Cheong S W, "Low temperature magnetoresistance and the magnetic phase diagram of $La_{1-x}Ca_xMnO_3$", Phys. Rev. Lett., **75**, 3336 (1995).

36. Gangineni R B, Dorr K, Kozlova N, Nenkov K, Muller K H, Schultz L & Seetha Lakshmi L, "Dependence of the high-field grain-boundary magnetoresistance of ferromagnetic manganites on Curie temperature", J. Appl. Phys., **99**, 053904 (2006).

LOW FIELD MAGNETOTRANSPORT IN $(La_{0.67}Ca_{0.33}MnO_3)_{1-x}/(Co_3O_4)_x$ AND $(La_{0.67}Ca_{0.33}MnO_3)_{1-x}/(PPS)_x$ COMPOSITES

5.1 INTRODUCTION

In the previous chapter, we discussed that the intrinsic CMR observed near Tc is found on a magnetic field scale of several tesla and in a narrow temperature range, which is not very appealing for applications. On the other hand, extrinsic effects like grain boundary magnetoresistance (GBMR) observed at low fields and over a wide temperature range, seem to be more appropriate for device applications. To achieve a large magnetoresistance at low fields and at/around room temperature, which is appealing for consideration of practical applications, is the aim of researchers in this field.

It was recently reported that introduction of a second phase, usually a nonmagnetic or an antiferromagnetic inorganic insulator, into the ferromagnetic manganites matrix would lead to an improved MR [1-5]. Various attempts have been made to enhance the low field MR through controlling the grain boundary effects by forming composites of the CMR oxides with secondary phases such as insulating oxides, magnetic materials or with other CMR oxides [1-11]. In addition to these, some studies have also been carried out on magnetic-polymer composites [12-16]. In the introduction part of chapter 4, we have described in detail many previous studies reported on the CMR composites with some inorganic insulator oxides. The studies reported on the CMR composites with organic insulators (polymers) are given below.

Huang and his group [12] have studied the $(LCMO)_{1-x}$/(polyparaphenylene, $PPP)_x$ (x = wt. fraction, 0.0–0.6) composites. They reported that the MR enhances significantly at lower temperatures for the composite, which is three times larger than pure LCMO at 5 K. T_{IM} for the composites with x = 0.1 shifts to 56 K from 172 K for pure LCMO which is much lower than the corresponding magnetic transition temperature (Tc) and has been attributed to the grain boundary dominated transport. Resistivity increases almost by five orders of magnitude at the percolation threshold composition. PPP is not able to form thin enough layers between the LCMO grains to act as tunneling barriers and hence could not change the tunneling conduction through the composite. But it possibly induces a spin disorder at the LCMO surface and certainly changes the magnetic ordering at the grain boundaries. Similar studies have been carried out by Yan et al. [13] for the $(LSMO)_{1-x}(PPP)_x$ composites (wt. fraction of PPP, x = 0.0, 0.2, 0.6, 1.0). They have found a remarkable LFMR especially at low temperature and at H < 5 kOe. Amongst the polymer most commonly used are polyparaphenylene (PPP) [12, 14] and polymethyl methaacrylate (PMMA) [16]. However, no study seems to be available in literature on manganites - polyphenylene sulfide (PPS) composite. PPS is a semicrystalline polymer with high temperature resistance, dimensional stability and average electrical characteristics. PPS also has excellent resistance to a broad variety of chemicals even at high temperature. Therefore, there is a less possibility of PPS to chemically react with manganites and it will serve only as the transport barrier in the manganites matrix to adjust the tunnel barriers and hence the magnetoresistance.

In this chapter, we have described and discussed the synthesis of $La_{0.67}Ca_{0.33}MnO_3$ composites with insulating oxide Co_3O_4 and polymer, polyphenylene sulfide (PPS) and studied their magnetic and low field magnetotransport properties.

5.2 EXPERIMENTAL

The $La_{0.67}Ca_{0.33}MnO_3$ (LCMO) samples were prepared via sol-gel method. The aqueous solution of high purity nitrates of La, Ca and Mn have been taken in the desired stoichiometric proportions. An equal amount of ethylene glycol has been added to this solution with continuous stirring. This solution is then heated on a hot plate at temperature of ~80-100 °C till a dry thick brown sol is formed. This has been further decomposed in an oven at a temperature of 250 °C to get the dry fluffy material. The resulting precursor powder is calcined at 600 °C for 12 h. The calcined mixture was reground and sintered at 1000 °C for 12 h. The prepared LCMO powders were mixed with Co_3O_4 and PPS to make the composites as follows:

(a) The obtained LCMO powder with single phase perovskite structure was completely mixed with a commercial Co_3O_4 powder according to the nominal ratio of $(LCMO)_{1-x}/(Co_3O_4)_x$ with x = 0.0, 0.05, 0.10, 0.15 and 0.20. The resulting $(LCMO)_{1-x}/(Co_3O_4)_x$ powder was pelletized at a pressure of 5 MPa/cm^2 and then sintered at 1000 °C for 2 h. By this procedure, the Co_3O_4 introduced as second phase of the combined system mainly segregated at the grain boundaries and on the surfaces of the LCMO grains.

(b) The obtained LCMO powder with single phase perovskite structure was thoroughly mixed with PPS according to the ratio of $(LCMO)_{1-x}$ $(PPS)_x$ with x = 0.0, 0.10, 0.20 and 0.30 and subsequently pressed into pellets at a pressure of 5 MPa/cm^2. After that, the pellets were sintered at 400 °C for 2 h in air in order to make the well connection between adjacent LCMO particles and polymer. The low sintering temperature for small duration was chosen to avoid inter-diffusion of LCMO and PPS.

The structural characterization was examined by employing X-ray diffraction (Bruker AXS D-8 Advance, CuK_α radiation) technique at room temperature and surface morphology

was investigated by field emission scanning electron microscope (FESEM, Model FEI Quanta 200F). Resistivity as a function of temperature was measured by a standard four-probe method using Keithley instruments without or with magnetic fields (0-12 kOe). The DC magnetization measurements were done by using vibrating sample magnetometer (VSM Model 155, Princeton Applied Research).

5.3 RESULTS AND DISCUSSION OF $(La_{0.67}Ca_{0.33}MnO_3)_{1-x}/(Co_3O_4)_x$ COMPOSITE

5.3.1 X-ray diffraction studies

Figure 5.1 shows the room temperature XRD patterns of $(LCMO)_{1-x}/(Co_3O_4)_x$ combined samples.

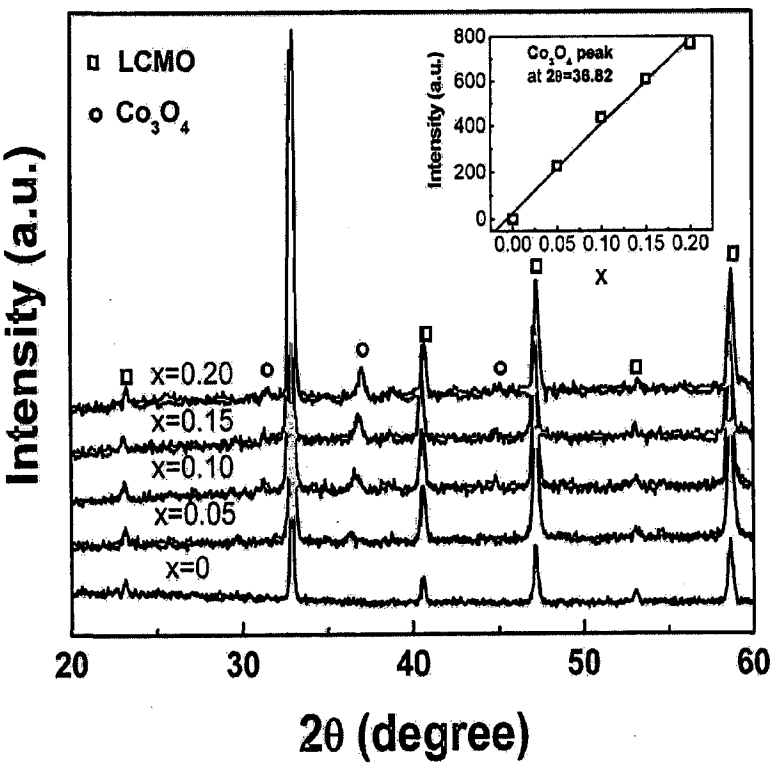

Figure 5.1: X-ray diffraction patterns of $(LCMO)_{1-x}/(Co_3O_4)_x$ combined samples. Inset shows the intensity versus x plot of most intense Co_3O_4 peak.

The XRD patterns of the combined samples show two different sets of XRD peaks, corresponding to pseudo cubic perovskite LCMO and cubic spinel Co_3O_4 structure. No extra phase is obtained indicating that the reactions between LCMO and Co_3O_4 are negligible. Moreover, with increasing Co_3O_4 concentrations, the intensity of the most intense Co_3O_4 peak ($2\theta=36.82^{o}$) increases almost linearly as shown in the inset of Fig. 5.1. This also supports the above fact that there is negligible reaction between LCMO and Co_3O_4 and almost all Co_3O_4 introduced as second phase of the composite mainly segregates at the grain boundaries and on the surfaces of the LCMO grains.

5.3.2 Microstructural analysis

The coexistence of two phases can also be seen from SEM micrographs which clearly indicate the presence of two different types of crystallites. The SEM micrographs of $(LCMO)_{1-x}/(Co_3O_4)_x$ combined samples with x = 0 and x = 0.10 are shown in Fig. 5.2 (a) & (b), respectively. A clear grain boundary is observed in pure LCMO as shown in Fig. 5.2 (a). However, the grain boundaries of $(LCMO)_{1-x}/(Co_3O_4)_x$ combined samples become ambiguous by the addition of Co_3O_4 as shown in Fig. 5.2 (b).

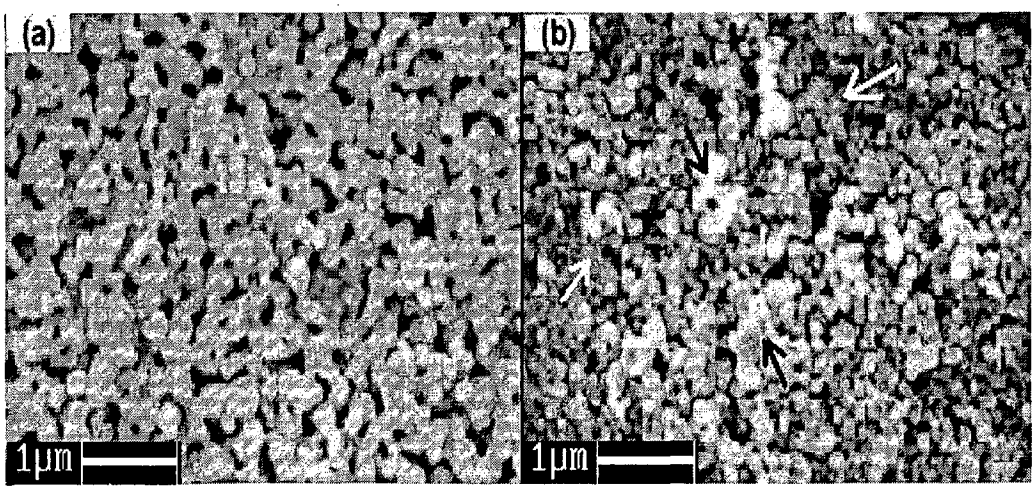

Figure 5.2: Scanning electron micrographs of $(LCMO)_{1-x}/(Co_3O_4)_x$ combined samples: (a) x = 0.0 and (b) x = 0.10.

From the SEM image (Fig. 5.2 (b)), it is also clear that the doped Co_3O_4 segregated mainly at the grain boundaries and on the surfaces of LCMO grains. In Fig. 5.2 (b), the LCMO and Co_3O_4 grains are indicated by white and black arrows, respectively, to distinguish them.

5.3.3 Magnetic properties

The temperature dependence of magnetization measured at 5 kOe is shown in Fig. 5.3. The value of magnetization (M) at 80 K are 78.3, 70.12, 65.3, 60.85 and 58.1 emu/gm for x = 0.0, 0.05, 0.10, 0.15 and 0.20, respectively. These successive decreases in M with increasing Co_3O_4 concentrations are due to decrease in the volume fraction of ferromagnetic LCMO phase and extra magnetic disorder caused by Co_3O_4 in these combined samples.

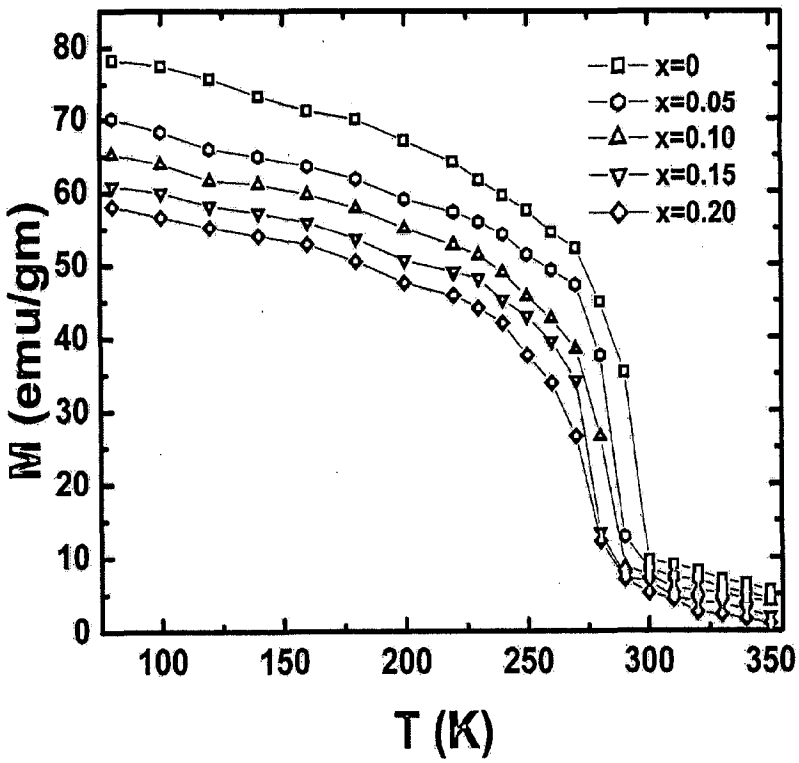

Figure 5.3: Temperature dependence of magnetization at 5 kOe of $(LCMO)_{1-x}/(Co_3O_4)_x$ combined samples.

The reduction in value of magnetization for the combined samples are more than the value calculated by taking into account the LCMO weight fraction in the composites, which suggests the extra magnetic disorder caused by Co_3O_4 in the combined samples. All the combined samples have almost similar behaviour of magnetization as a function of temperature and there is a small shift in paramagnetic (PM) to ferromagnetic (FM) phase transition temperature (Tc), which moves towards lower value as Co_3O_4 content increases. The transition temperatures determined from the peak in (dM/dT)-T curves are found to be ~289, 281, 279, 275 and 270 K for the samples with x = 0.0, 0.05, 0.10, 0.15 and 0.20, respectively. As observed by XRD and SEM, Co_3O_4 segregates into the grain boundaries and on the surfaces of LCMO grains and this grain boundary segregation of Co_3O_4 affect the double exchange (DE) mechanism and this is more pronounced in the FM domains walls [13]. This consequently leads to the suppression of PM-FM transition temperature towards the lower value with increase in Co_3O_4 concentration. The reduction in the magnetization also suggests the suppression of DE mechanism resulting suppression of the ferromagnetic alignment of Mn ions. This indicates the magnetic spin disorder induced by the grain boundaries in the combined system.

5.3.4 Electrical resistivity measurements

The temperature dependence of resistivity for the $(LCMO)_{1-x}/(Co_3O_4)_x$ combined samples measured by four probe technique at zero field is shown in Fig. 5.4. As expected, the metal like conductivity is found in pure LCMO while with increasing Co_3O_4 concentration, x, the zero field resistivity of $(LCMO)_{1-x}/(Co_3O_4)_x$ combined samples increases within one or two orders of magnitude, particularly at lower temperatures, when x varies from 0.0 to 0.20. It can be seen from Fig. 5.4 that the value of resistivity at 80 K increases from 0.03 to 853 Ω-

cm when x increases from x = 0.0 to x = 0.20. Meanwhile, the virgin LCMO (x = 0) shows the clear metal-insulator transition at a temperature (T_{IM}) ~260 K while the transition disappears in combined samples and they show insulating/semiconducting behaviour in the whole measured temperature range (80-300 K). The increase of resistivity and disappearance of I-M transition can qualitatively be explained by enhanced grain boundaries. Since Co_3O_4 behaves as a paramagnetic insulator above 40 K, therefore $(LCMO)_{1-x}/(Co_3O_4)_x$ combined samples are similar to the ferromagnet/insulator type composites. Large number of interfaces and boundaries between LCMO and Co_3O_4 grains may act as additional barriers. This causes the increase in the carrier scattering leading to enhancement in the resistivity.

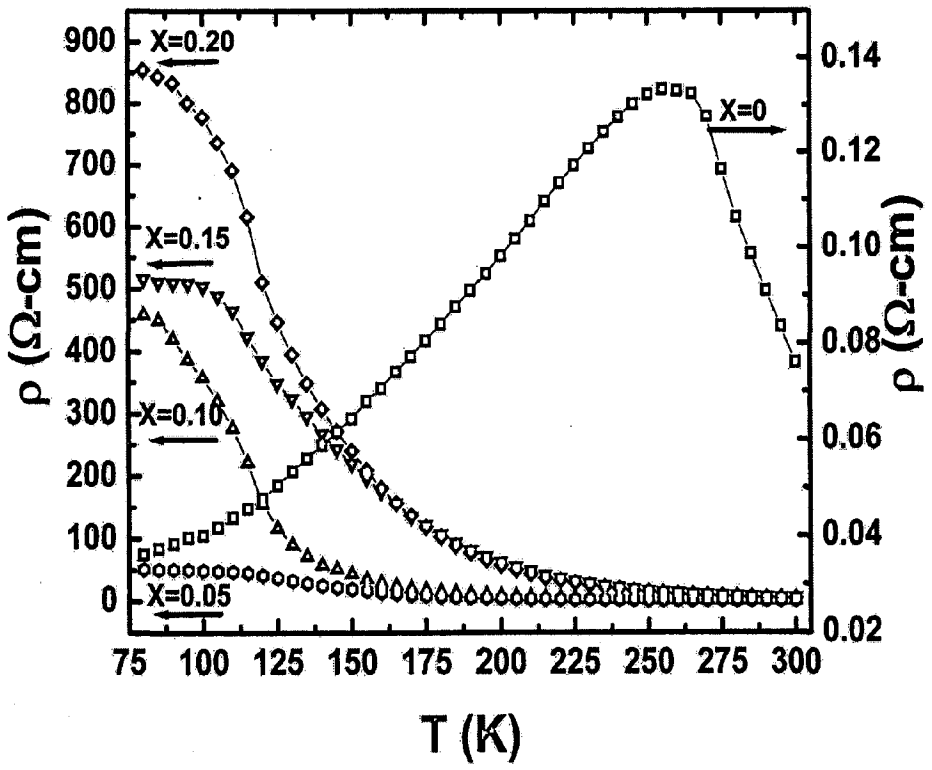

Figure 5.4: Temperature dependence of resistivity at zero field of $(LCMO)_{1-x}/(Co_3O_4)_x$ combined samples.

The metallic transition is suppressed because of Co_3O_4 induced disorders and also by the increase in the insulating Co_3O_4 phase fraction in the combined system. Moreover, in pure LCMO, the electrical transport is achieved through a direct contact between LCMO grains. However, in the combined samples, there are two kinds of conduction channels parallel connected to each other [17, 18]. One is related to LCMO grains, which determines the transport properties of the system through direct contact between LCMO grains and other is related to Co_3O_4. It is also noticeable that there is a large difference between the values of metal-insulator transition temperature (T_{IM}) and paramagnetic-ferromagnetic transition temperature (Tc) for the combined samples. The value of T_{IM} in the virgin sample (x = 0) is 260 K while it comes below 80 K in the combined samples and they show insulating/semiconducting behaviour (Fig. 5.4) in whole measured temperature range (80-300 K). On the other hand, Tc decreases only marginally (289-270 K) when x increases from 0.0 to 0.20 in the combined samples. This difference is due to the fact that Tc is an intrinsic property and does not show much dependence on grain boundaries while T_{IM} is an extrinsic property that strongly depends upon the grain boundaries [17].

5.3.5 Magnetoresistance studies

The temperature dependence of magnetoresistance (MR) in a field of 3 kOe for all the measured samples is shown in Fig. 5.5. We find that $(LCMO)_{1-x}/(Co_3O_4)_x$ combined samples having low Co_3O_4 concentration, i.e., x ~0.05 and 0.10 exhibit a distinct enhanced MR as compared to parent LCMO in low temperature region (T < 125 K). We plot the x dependence of MR in the inset of Fig. 5.5. The values of MR ratio at 80 K are ~20.77 and ~24.68 % for the combined samples with x = 0.05 and 0.10, respectively while ~18.36 % for pure LCMO at 3 kOe. So, the observed enhancement in MR at 80 K with respect to pure LCMO (x = 0) is

~13 & ~35 % for the composites with x = 0.05 and 0.10, respectively, at 3 kOe. This increase in MR at low temperature seems to be due to enhanced tunneling across LCMO grain boundaries and additional grain boundary effects introduced by Co_3O_4 grains. As proposed by Hwang et al. [19], the spin polarized tunneling between neighbouring grains of manganites is responsible for the magnetoresistance effect in polycrystalline samples. This tunneling takes place across the grain boundaries or interfaces.

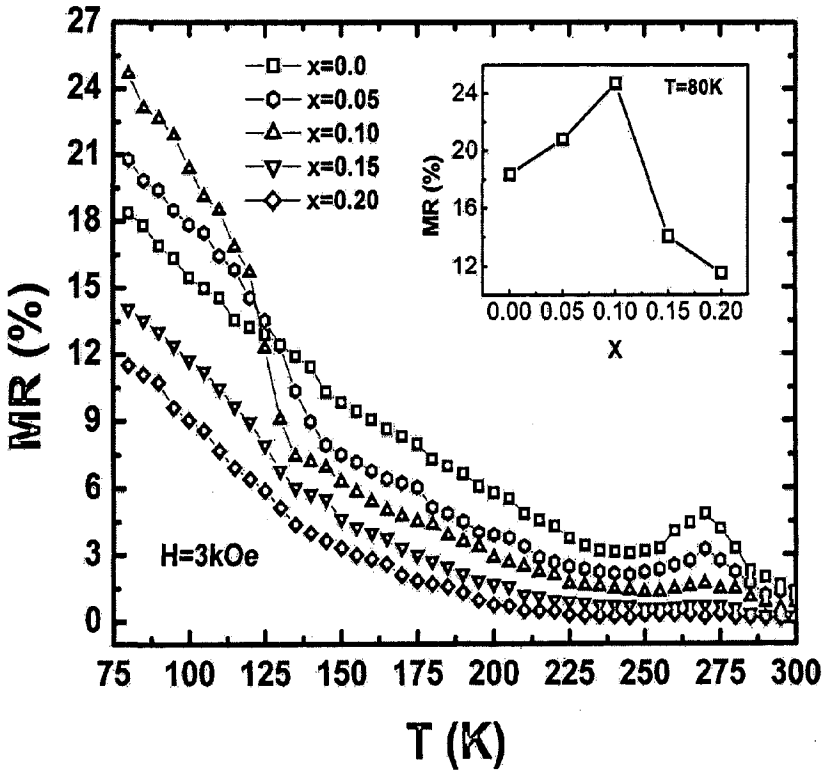

Figure 5.5: Temperature dependence of magnetoresistance (MR) in a field of 3 kOe of $(LCMO)_{1-x}/(Co_3O_4)_x$ combined samples. Inset shows the MR versus x curve.

As Fig. 5.5 indicates, we get the enhancement in MR of the combined samples with x = 0.05 and 0.10 only at temperatures below 125 K which suggests that this enhanced MR basically comes from grain boundary effects in our samples because it is well known that LFMR is mainly attributed to a grain boundary effect especially at temperature T<Tc [19]. However,

with further increase in Co_3O_4 level above x = 0.10, the MR decreases with respect to pure LCMO even at low temperature which may result because the grain boundaries become too thick for electron tunneling. Moreover, the MR near room temperature slightly decreases in all $(LCMO)_{1-x}/(Co_3O_4)_x$ combined samples. The value of room temperature (300 K) MR decreases from 1.36 to 0.10 % when x increases from 0.0 to 0.20. This slight decrease in high temperature (room temperature) MR is because of vanishing of the tunneling phenomena above Tc as Hwang [19] proposed that tunneling phenomena occurs only at T<Tc.

The magnetic field dependence of MR for all the samples measured in field (0-12 kOe) at 80 K is shown in Fig. 5.6. Generally, there are two aspects that influence the MR by applied field. One has to do with ferromagnetic domain wall movement of LCMO as in all ferromagnets, and other has to do with grain boundaries of LCMO, which contribute substantially to the LFMR in the temperature range below Tc. Analysis of Fig. 5.6 shows that with increase in the magnetic field from 0 to12 kOe, the value of MR for low Co_3O_4 doping (x = 0.05 and 0.10) is larger than pure LCMO (x = 0.0) and smaller for x > 0.10. It suggests that magnetic field sensitive MR can be enhanced with Co_3O_4 as a secondary phase impurity at low concentration only (up to x = 0.10 in the present case). The MR increases sharply at low fields and saturate for the higher values of the fields. The values of MR at 80 K are ~18.36, ~20.77 and ~24.68 % at 3 kOe while the same are ~28.27, ~30.05 % and ~31.73 % at 12 kOe for the composite samples with x = 0.0, 0.05 and 0.10, respectively. This shows that the percent change in MR for the composites with x = 0.05 and 0.10 with respect to pure LCMO is more at low fields (up to 3 kOe). The percentage change in MR with respect to pure LCMO (x = 0) at 80 K is ~13 and ~35 % at 3 kOe while that is ~6 and ~12 % at 12 kOe for the composites with x = 0.05 and 0.10, respectively. This indicates that large change in MR is produced at low fields (3 kOe) and this LFMR is caused through spin disorder (as

suggested by magnetization measurements) by the tunneling process at the grain boundaries and when a magnetic field is applied, the spin disorder is suppressed, resulting the high MR.

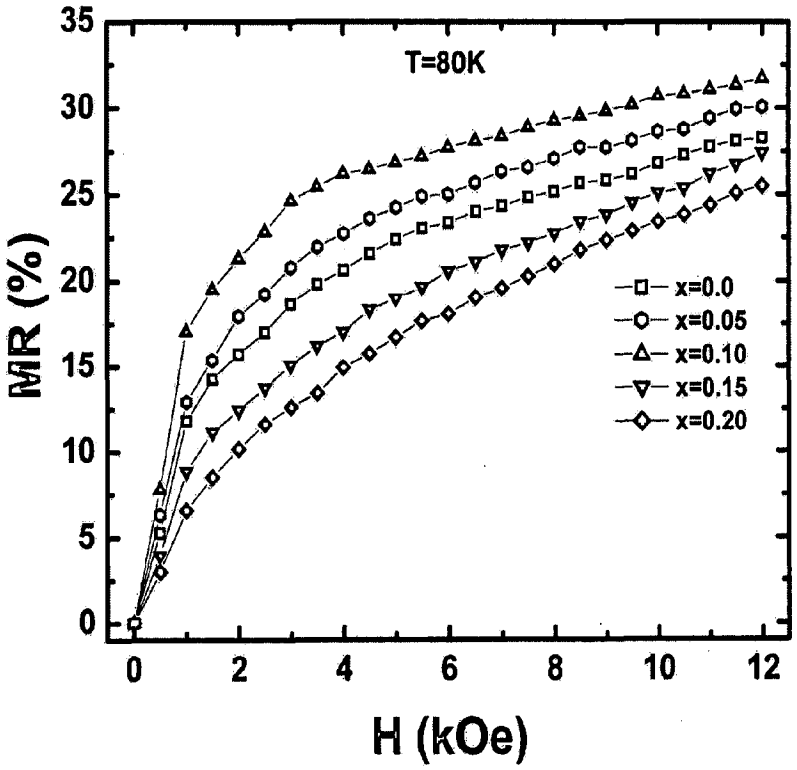

Figure 5.6: Magnetic field dependence of magnetoresistance (MR) in magnetic field (0-12 kOe) at 80 K of $(LCMO)_{1-x}/(Co_3O_4)_x$ combined samples.

5.4 RESULTS AND DISCUSSION OF $(La_{0.67}Ca_{0.33}MnO_3)_{1-x}/(PPS)_x$ COMPOSITE

5.4.1 Thermal gravimetric analysis (TGA)

Figure 5.7 shows the thermal gravimetric analysis (TGA) curves of $(LCMO)_{1-x}/(PPS)_x$ composite samples with (a) x = 1.0 and (b) 0.30. It is found that the decomposition of pure PPS (x = 1.0) and composite with x = 0.30 starts at about 465 °C and 450 °C, respectively. In both the cases, the dissociation temperatures are above the sintering temperature (400 °C) of the composite samples. This indicates that the final sintering of the composite pellets at ~400 °C does not lead to the decomposition of the polymer.

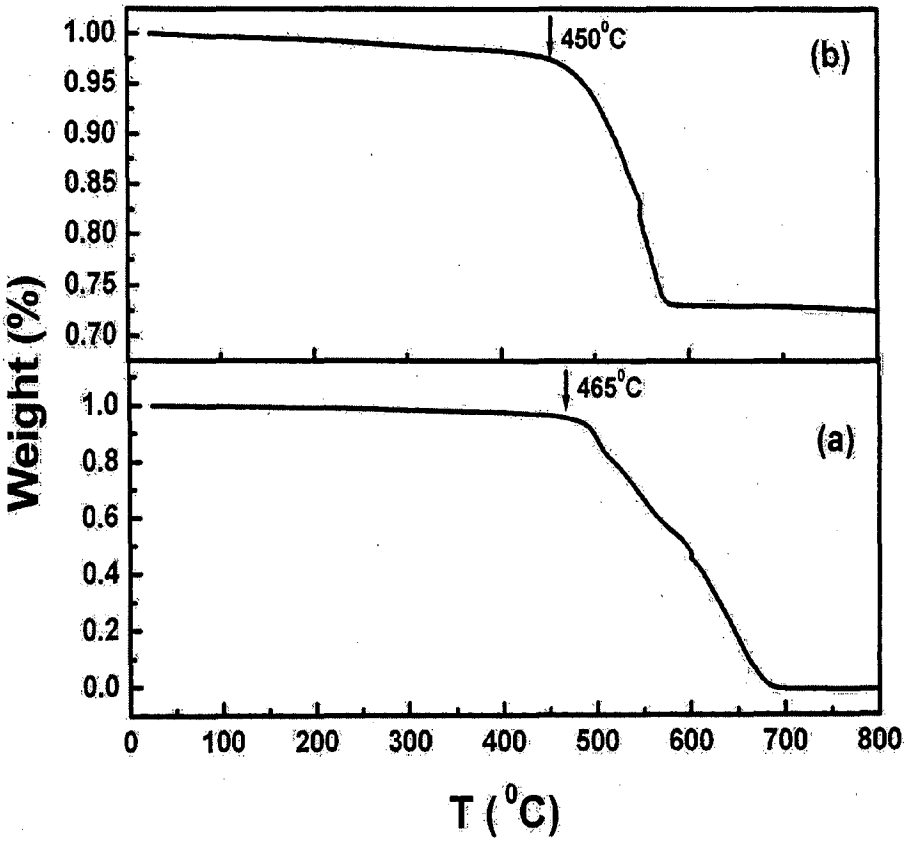

Figure 5.7: Thermal gravimetric analysis (TGA) curves of $(LCMO)_{1-x}/(PPS)_x$ composite samples: (a) x = 1.0 and (b) x = 0.30.

5.4.2 X-ray diffraction studies

The phases of the composite samples were characterized by x-ray diffraction (XRD) with CuK_α radiation. Fig. 5.8 shows the XRD patterns of $(LCMO)_{1-x}/(PPS)_x$ composite samples with x = 0.0, 0.10, 0.20, 0.30 and 1.0. The XRD pattern of the composites with x = 0.20 and 0.30 show two different set of diffraction peaks, corresponding to orthorhombic LCMO and PPS phases, which clearly indicates the coexistence of both LCMO and PPS phases. The pure LCMO sample has an orthorhombic unit cell with lattice parameters: a = 5.487 Å, b = 5.436 Å, c = 7.764 Å. The lattice parameters of LCMO in the $(LCMO)_{1-x}/(PPS)_x$ composite do not change within the accuracy of diffractometer. This shows that LCMO maintains its identity and there is no reaction between LCMO and PPS and PPS, introduced

as second phase of the composite, mainly segregates at the grain boundaries and on the surfaces of the LCMO grains.

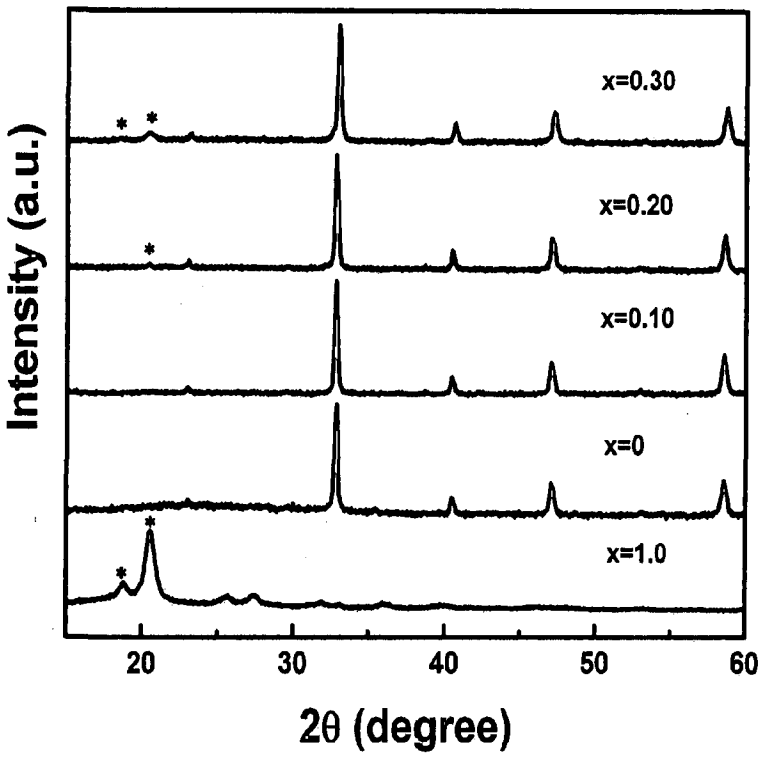

Figure 5.8: X-ray diffraction patterns of $(LCMO)_{1-x}/(PPS)_x$ composite samples with x = 1.0, 0.0, 0.10, 0.20 and 0.30. The asterisks represent the diffraction peaks arising from PPS.

5.4.3 Microstructural analysis

The coexistence of two phases also comes from SEM micrographs. The representative SEM micrographs of $(LCMO)_{1-x}/(PPS)_x$ composites with x = 0 and x = 0.20 are shown in Fig. 5.9 (a) and (b), respectively. The interfaces between PPS and LCMO can be distinguished clearly. The bright regions in Fig. 5.9 (b) are assigned to PPS and are indicated by black arrows. Moreover, the PPS is easily observable in the composites although its distribution within the LCMO matrix is not very uniform as shown in Fig 5.9 (b). Moreover, energy dispersive X-ray (EDAX) spectra of the doped composite sample for x =

0.20 (as shown in the inset of Fig. 5.9 (b)) shows the carbon peak along with La, Ca, Mn and O peaks, which also supports the presence of polymer in the doped composites. The Au peak in the EDAX spectra is due to coating of gold over surface of the sample to avoid charging.

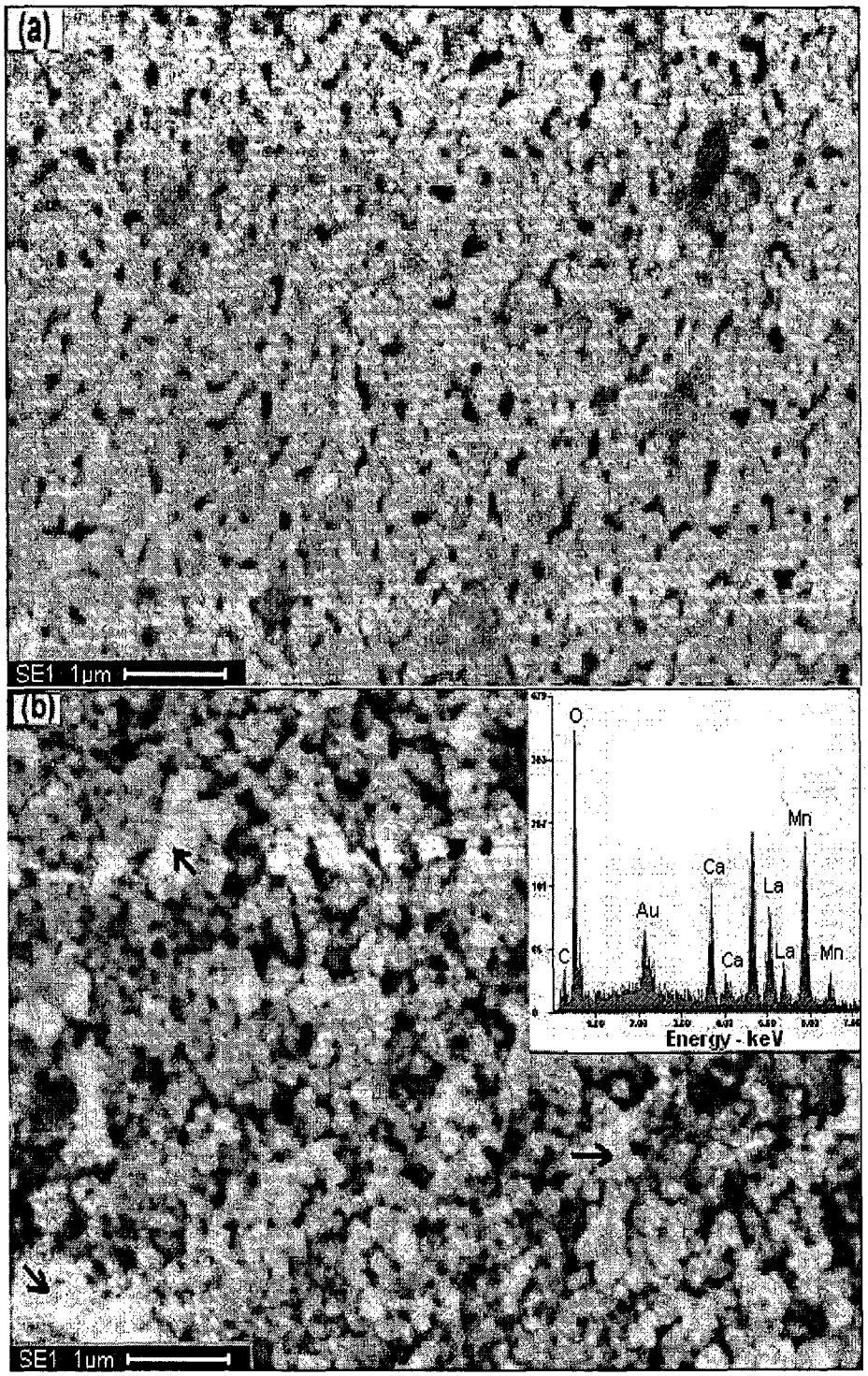

Figure 5.9: Scanning electron micrographs of $(LCMO)_{1-x}/(PPS)_x$ composite samples: (a) x = 0 and (b) x = 0.20. Inset shows the EDAX spectra of sample (b).

5.4.4 Magnetic properties

The temperature dependence of magnetization at 5 kOe for $(LCMO)_{1-x}/(PPS)_x$ with x = 0, 0.10, 0.20 and 0.30 is shown in Fig. 5.10. The value of magnetization (M) at 80 K are 79.82, 68.75, 60.00, and 51.67 emu/gm for x = 0.0, 0.10, 0.20 and 0.30, respectively. This successive decrease in M with increasing PPS concentration is due to decrease in the volume fraction of ferromagnetic LCMO phase and extra magnetic disorder caused by PPS in these composite samples.

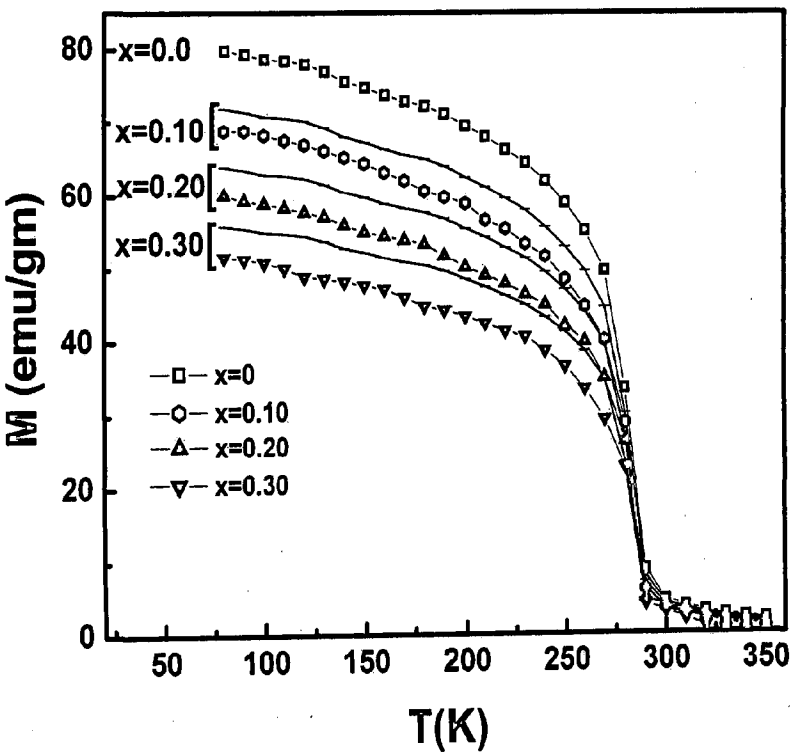

Figure 5.10: Temperature dependence of magnetization at 5 kOe of $(LCMO)_{1-x}/(PPS)_x$ composite samples. The solid lines represent the estimated M according to the M and weight fraction of LCMO for x = 0.10, 0.20 and 0.30.

Magnetic measurement shows that PPS is nonmagnetic in the whole measured temperature range. This suggests that the magnetization of the composites comes up only from LCMO.

According to the magnetization of parent LCMO and its weight fraction in the composites, the magnitude of magnetization (M) of composites with x = 0.10, 0.20 and 0.30 are estimated and their variations with temperature are shown by the solid lines in Fig. 5.10. The experimental curves are obviously lower than the as-estimated ones. This discrepancy in M leads us to take into account of the extra magnetic disorder caused by PPS in the composites. This extra magnetic spin disorder is induced by grain boundaries in the composites and suggests the suppression of DE mechanism resulting suppression of the ferromagnetic alignment of Mn ions. Since the PPS is not incorporated into the LCMO lattice and it segregates into the grain boundaries or interfacial regions, which blocks the Mn spins at grain boundaries and increases the anisotropy in the interfacial regions and misalignment of the magnetic moments of the neighbouring FM domains [17]. Therefore, despite the nonmagnetic character of PPS, it is expected to increase the magnetic disorder by disrupting the Mn-O-Mn bonds in the interfacial regions and hence suppression of the long range FM order. All the compositions of $(LCMO)_{1-x}/(PPS)_x$ composite have almost similar behaviour of magnetization as a function of temperature. Moreover, the paramagnetic (PM) to ferromagnetic (FM) phase transition temperature (Tc) determined from the peak in (dM/dT)-T curves is almost independent of PPS content (x) and is ~279 K for all the samples. This is due to the fact that the PM-FM phase transition is an intrinsic and intragrain property. The observed constancy of Tc also indicates that stoichiometry of LCMO phase within the grains remains essentially unchanged as PPS is not accommodated within the perovskite structure and it sits only at the grain boundaries and on the surfaces of LCMO grains. The magnetic hysteresis loops for the $(LCMO)_{1-x}/(PPS)_x$ samples with x = 0.0, 0.10, 0.20 and 0.30 are displayed in Fig. 5.11. M-H curves show that the magnetization of the samples increases rapidly at low fields and then tends to saturate at higher field. The value of magnetization of

composites again decreases with x because of reducing the volume fraction of LCMO phase and extra magnetic disorder due to PPS content. This demonstrates that ferromagnetic order is weakened and magnetic disorder increases with PPS content.

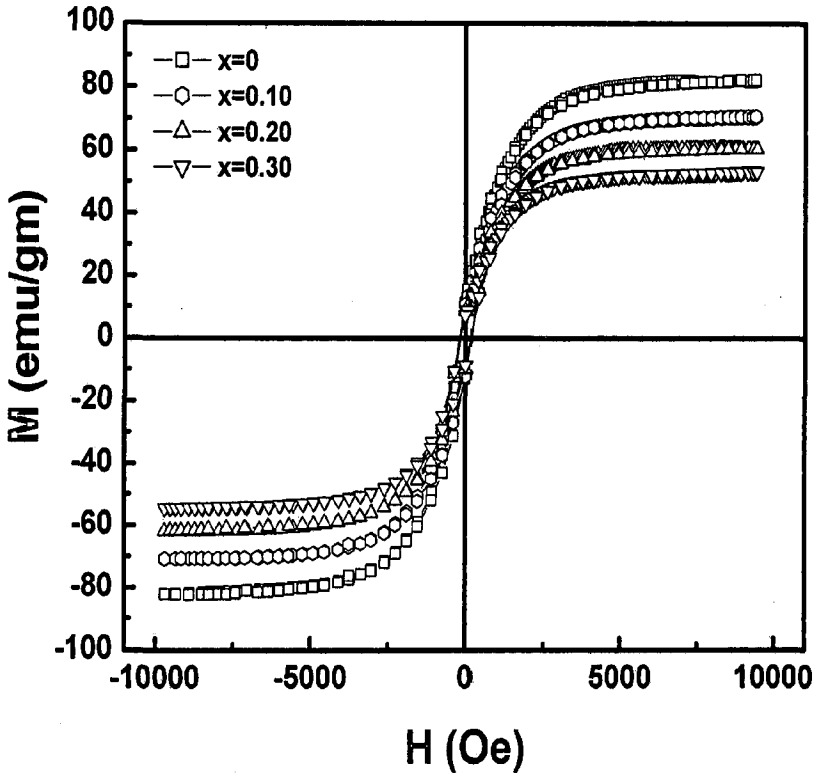

Figure 5.11: Field dependence magnetization (M-H) curves at 80 K of $(LCMO)_{1-x}/(PPS)_x$ composite samples.

5.4.5 Electrical resistivity measurements

The temperature dependence of resistivity without and with an applied field H = ~3 kOe, for the $(LCMO)_{1-x}/(PPS)_x$ with x = 0, 0.10, 0.20 and 0.30 is shown in Fig. 5.12. The metal like conductivity is found in pure LCMO while with increasing PPS concentration x, the zero field resistivity of $(LCMO)_{1-x}/(PPS)_x$ composite samples increases within two or three orders of magnitude even at room temperature, when x varies from 0 to 0.30. It can be seen from Fig. 5.12 that the value of resistivity at room temperature (300 K) increases from

1.24 to 617.4 Ω-cm when x increases from x = 0 to x = 0.30. At the same time, it is also observed that the resistivity has a reduction under the applied field especially at lower values of temperatures. Meanwhile, the virgin LCMO (x = 0) shows the clear insulator ($d\rho/dT<0$) to metal ($d\rho/dT>0$) transition at a temperature (T_{IM}) ~265 K while the value of transition decreases from 265 to 105 K when x increases from x = 0 to x = 0.30. The values of transition temperature (T_{IM}) are ~265, ~134, ~121 and ~105 K for the samples with x = 0, 0.10, 0.20 and 0.30, respectively.

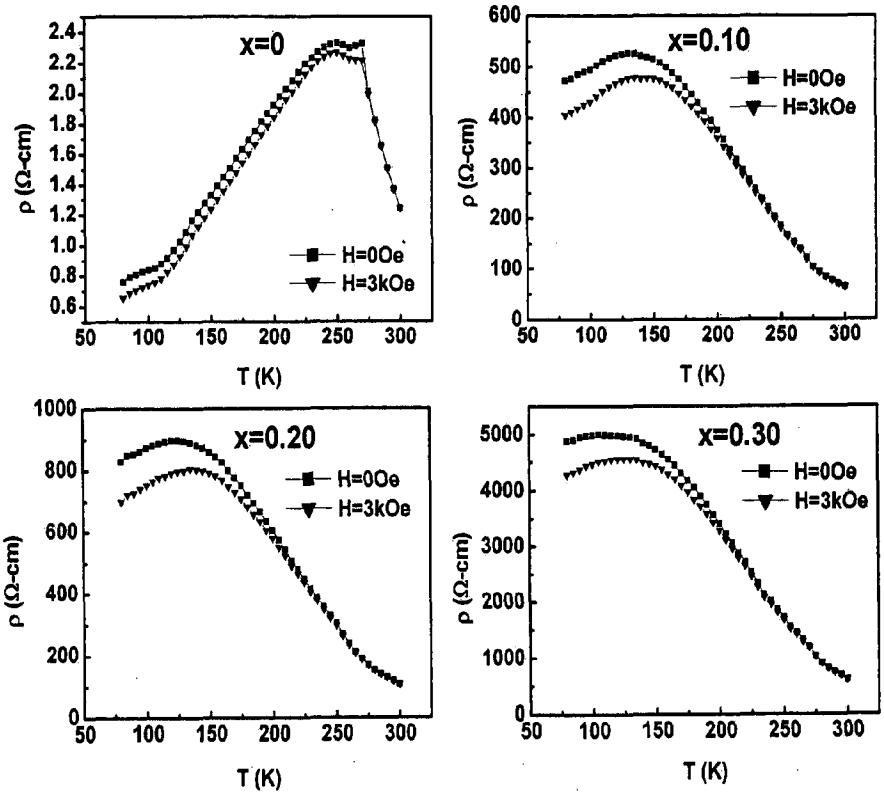

Figure 5.12: Temperature dependence of resistivity at zero and an applied field (H = 3 kOe) of $(LCMO)_{1-x}/(PPS)_x$ composite samples.

The strong suppression of the T_{IM} is caused by the PPS induced disorders and also by the increase in the non-magnetic-insulating PPS phase fraction in the composites. This causes the increase in the carrier scattering leading to a corresponding enhancement in the resistivity.

Moreover, in pure LCMO, the electrical transport is achieved through a direct contact between LCMO grains. However, in doped composites, there are two kinds of conduction channels parallel connected to each other [17, 18]. One is related to LCMO grains, which determines the transport properties of the system through direct contact between LCMO grains and other is related to embedded PPS. Since the PPS is mainly distributed at the grain boundaries and on the surfaces of LCMO grains and produces energy barriers to electrical transport process. Therefore, higher resistivity is observed for the doped composites as compared to the parent LCMO phase.

5.4.6 Magnetoresistance studies

The temperature dependence of magnetoresistance (MR) in a field of 3 kOe for the $(LCMO)_{1-x}/(PPS)_x$ composite samples is shown in Fig. 5.13. We find that $(LCMO)_{1-x}$ $(PPS)_x$ composite samples having low PPS concentration, viz., x ~0.10 and 0.20 exhibit an enhanced MR compared with the parent LCMO (x = 0) in low temperature region (T < 175 K). We plot the x dependence of MR in the inset of Fig. 5.13. The values of MR ratio at 80 K are ~16.73 and ~18.45 % for the composite samples with x = 0.10 and 0.20, respectively while ~15.73 % for pure LCMO at 3 kOe. So, the observed enhancement in MR at 80 K with respect to pure LCMO (x = 0) is ~7 & ~17 % for the composites with x = 0.10 and 0.20, respectively, at 3 kOe. This enhancement in MR at low temperature is commonly interpreted within the frame work of spin polarized tunneling across LCMO grain boundaries and additional grain boundary effects introduced by PPS. As proposed by Hwang et al. [19], the spin polarized tunneling between neighbouring grains of manganites is responsible for the low field magnetoresistance effect in polycrystalline samples. This tunneling takes place across the grain boundaries or interfaces, which produce the spin disorder. The magnetic measurements

(Fig. 5.10) also indicate the extra magnetic disorder induced by PPS content at the grain boundaries in the composites and this spin disorder is suppressed by applying the magnetic field, resulting the enhancement in MR.

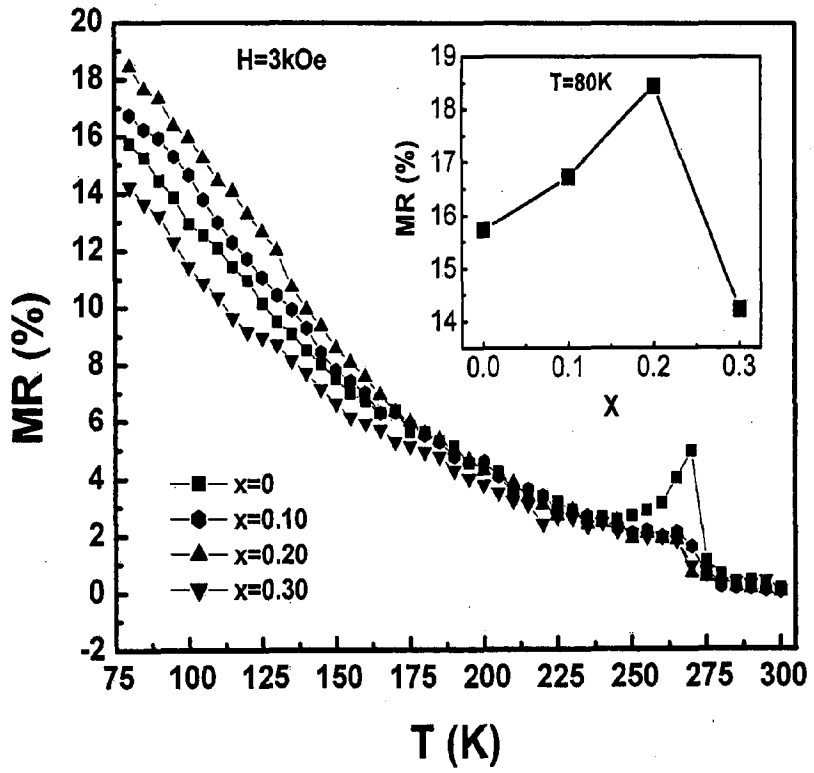

Figure 5.13: Temperature dependence of magnetoresistance (MR) in a field of 3 kOe of $(LCMO)_{1-x}/(PPS)_x$ composite samples. Inset shows the MR versus x curve.

As Fig. 5.13 indicates, we get the enhancement in MR for the composites with x = 0.10 and 0.20 at temperatures below 175 K which suggests that this enhanced MR basically comes from grain boundary effects in our samples because it is well known that LFMR is mainly attributed to a grain boundary effect especially at temperature T<Tc [19]. However, with further increase in PPS content from x = 0.20, the MR decreases with respect to pure LCMO even at low temperature which may result because the grain boundaries become too thick for electron tunneling.

The magnetic field dependence of MR for the $(LCMO)_{1-x}/(PPS)_x$ composite samples measured in magnetic field range of 0-12 kOe at 80 K is shown in Fig. 5.14. Analysis of Fig. 5.14 shows that with increase in the magnetic field from 0 to12 kOe, the value of MR for low PPS doping (x = 0.10 and 0.20) is larger than pure LCMO (x = 0.0) and smaller for x > 0.20. It suggests that magnetic field sensitive MR can be enhanced with PPS as a secondary phase impurity at low concentration only (up to x = 0.20 in the present case).

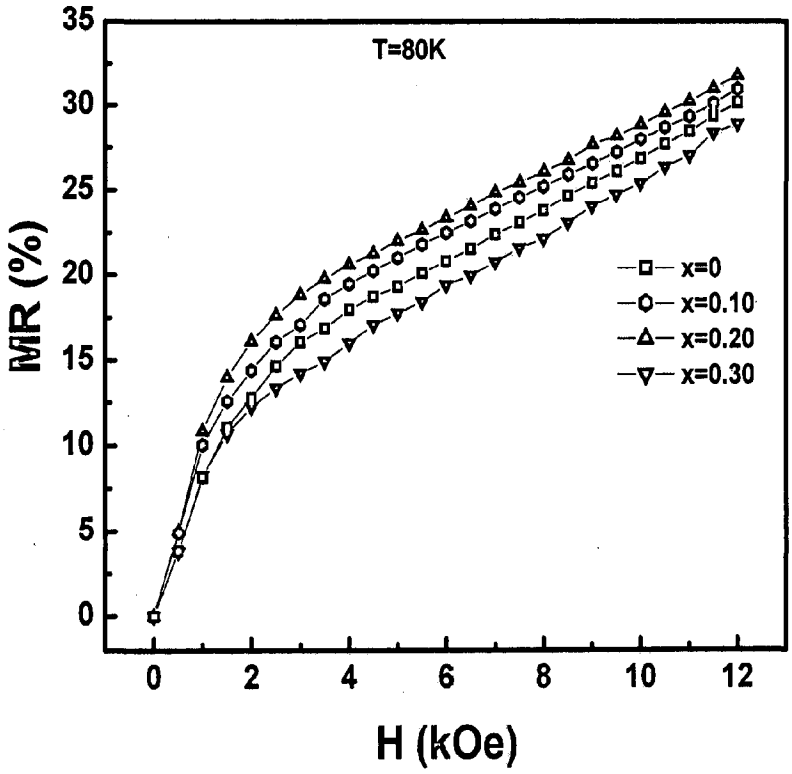

Figure 5.14: Magnetic field dependence of magnetoresistance (MR) in magnetic field (0-12 kOe) at 80 K of $(LCMO)_{1-x}/(PPS)_x$ composite samples.

The values of MR at 80 K are ~15.73, ~16.73 and ~18.45 % at 3 kOe while the same are ~30.15, ~30.93 % and ~31.75 % at 12 kOe for the composite samples with x = 0, 0.10 and 0.20, respectively. This shows that the percent change in MR for the composites with x = 0.10 and 0.20 with respect to pure LCMO (x = 0) is more at low fields (up to 3 kOe). The

percentage change in MR with respect to pure LCMO at 80 K is ~7 and ~17 % at 3 kOe field while the same is ~3 and ~6 % at 12 kOe field for the composites with x = 0.10 and 0.20, respectively. This indicates that large change in MR is produced at low fields and this LFMR is caused through spin disorder by the tunneling process at the grain boundaries and when an external magnetic field is applied, the spin disorder is suppressed and Mn spins within the disordered region realign along the field direction, as a consequence, MR improvement is obtained.

5.5 CONCLUSIONS

In this chapter work, we have successfully prepared the composite of $La_{0.67}Ca_{0.33}MnO_3$ with insulating oxide Co_3O_4 and polymer PPS as second phase material and investigated their microstructural, magnetic and magnetotransport properties. The main highlights of the work are given below:

1. The X-ray diffraction patterns show a single perovskite structure for the virgin (x = 0) sample and two different sets of peaks: one for perovskite LCMO phase and another for Co_3O_4 or PPS phase depending on the composite samples $(LCMO)_{1-x}/(Co_3O_4)_x$ or $(LCMO)_{1-x}/(PPS)_x$.
2. The most intense peak of second phase material (Co_3O_4 and PPS) increases almost linearly in intensity with increasing their concentrations. This supports the fact that there is negligible reaction between LCMO and second phase material (Co_3O_4 and PPS) and almost all second phase material (Co_3O_4 and PPS) mainly segregates at the grain boundaries and on the surfaces of the LCMO grains.
3. The value of magnetization decreases and paramagnetic (PM) to ferromagnetic (FM) phase transition temperature (Tc) shifts towards lower value as the Co_3O_4

content increases in the $(LCMO)_{1-x}/(Co_3O_4)_x$ composite. The transition temperatures determined from the peak in (dM/dT)-T curves for $(LCMO)_{1-x}/(Co_3O_4)_x$ composites are found to be ~289, 281, 279, 275 and 270 K for the samples with x = 0.0, 0.05, 0.10, 0.15 and 0.20, respectively. However, the value of Tc for $(LCMO)_{1-x}/(PPS)_x$ composites is almost independent of PPS content (x) and is ~279 K for all compositions.

4. The zero field resistivity of both the composites increases within one or two orders of magnitude, particularly at lower temperatures with increasing the concentration of Co_3O_4 and PPS. For $(LCMO)_{1-x}/(Co_3O_4)_x$ composite, the virgin LCMO (x = 0) shows the clear metal-insulator transition at a temperature (T_{IM}) ~260 K while the transition disappears in the combined samples and they show insulating/semiconducting behaviour in the whole measured temperature range (80-300 K). However for $(LCMO)_{1-x}/(PPS)_x$ composites, the virgin LCMO (x = 0) shows the clear insulator ($d\rho/dT<0$) to metal ($d\rho/dT>0$) transition at a temperature 265 K while the value of transition decreases from 265 to 105 K when x increases from x = 0 to x = 0.30.

5. The enhancement in MR with respect to parent LCMO is observed up to x = 0.10 for the $(LCMO)_{1-x}/(Co_3O_4)_x$ composites and up to x = 0.20 for $(LCMO)_{1-x}/(PPS)_x$ composites below the temperature 125 K and 175 K, respectively. The observed enhancement in MR at 80 K with respect to pure LCMO (x = 0) is ~13 & ~35 % for the $(LCMO)_{1-x}/(Co_3O_4)_x$ composites with x = 0.05 and 0.10, respectively, while the same is ~7 & ~17 % for the $(LCMO)_{1-x}/(PPS)_x$ composites with x = 0.10 and 0.20, respectively, at 3 kOe.

6. Moreover, the percent change in MR with respect to pure LCMO for both the composites is more at low field (~ 3 kOe) in comparison to high field (~12 kOe). The percentage change in MR with respect to pure LCMO (x = 0) at 80 K is ~13 & ~35 % at 3 kOe and ~6 & ~12 % at 12 kOe for the $(LCMO)_{1-x}/(Co_3O_4)_x$ composites with x = 0.05 and 0.10, respectively while the same is ~7 & ~17 % at 3 kOe and ~3 & ~6 % at 12 kOe for the composites $(LCMO)_{1-x}/(PPS)_x$ with x = 0.10 and 0.20, respectively.

Both of the studies show that the magnetoresistance enhances up to a certain doping concentration. The enhancement in MR is observed up to x = 0.10 in case of $(LCMO)_{1-x}/(Co_3O_4)_x$ while up to x = 0.20 in case of $(LCMO)_{1-x}/(PPS)_x$ below the temperature 125 K and 175 K, respectively. It has been suggested that this large change in MR, produced at low fields (~3 kOe), is related to enhance spin-polarised tunneling, which is manipulated by the spin disorder at the LCMO surfaces caused by Co_3O_4 and PPS.

REFERENCES

1. Balcells L I, Carrillo A E, Martinez B & Fontcuberta J, "Enhanced field sensitivity close to percolation in magnetoresistive $La_{2/3}Sr_{1/3}MnO_3/CeO_2$ composites", Appl. Phys. Lett., **74**, 4014 (1999).
2. Petrov D K, Krusin-Elbaum L, Sun J Z, Field C & Duncombe P R, "Enhanced magnetoresistance in sintered granular manganite/insulator systems", Appl. Phys. Lett., **75**, 995 (1999).
3. Gupta S, Ranjit R, Mitra C, Raychaudhuri P & Pinto R, "Enhanced room-temperature magnetoresistance in $La_{0.7}Sr_{0.3}MnO_3$-glass composites", Appl. Phys. Lett., **78**, 362 (2001).
4. Liu J M, Li J, Huang Q, You L P, Wang S J, Ong C K, Wu Z C, Liu Z G & Du Y W, "Partially crystallized $La_{0.5}Sr_{0.5}MnO_3$ thin films by laser ablation and their enhanced low-field magnetoresistance", Appl. Phys. Lett.,**74**, 2286 (2000).
5. Das D, Chowdhury P, Das R N, Srivastava C M, Nigam A K & Bahadur D, "Solution sol–gel processing and investigation of percolation threshold in $La_{2/3}Ca_{1/3}MnO_3$: x SiO_2 nanocomposite", J. Magn. Magn. Mater., **238**, 178 (2002).
6. Sun J R, Shen B G, Yeung H W & Wong H K, "Formation of interfacial phase and its effects on the magnetic and transport properties of the $La_{0.82}Ca_{0.18}MnO_3$ /$La_{0.18}Ca_{0.82}MnO_3$ composite", J. Phys. D: Appl. Phys., **35**, 173 (2002).
7. Xia Z C, Yuan S L, Zhang G H, Zhang L J, Tang J, Feng W, Liu J, Peng G, Liu L, Li Z Y, Zheng Q H, Cheng L, Tang C Q, Liu S & Xiong C S, "Effect of low Fe_3O_4 doping in $La_{0.67}Ca_{0.33}MnO_3$", J. Phys. D: Appl. Phys., **36**, 217 (2003).

8. Xia Z C, Yuan S L, Tu F, Tang C Q, Peng G, Zhang G H, Liu L, Liu J, Li Z Y, Yang Y P, Xiong C S & Xiong Y H, "Grain boundaries and low-field transport properties in colossal magnetoresistance materials", J. Phys. D: Appl. Phys., **35**, 177 (2002).

9. Yan C H, Luo F, Huang Y H, Li X H, Wang Z M, Liao C S, Zhao H W & Shen B G, "Enhanced room temperature magnetoresistance in $La_{0.7}Sr_{0.3}MnO_3/Sm_{0.7}Sr_{0.3}MnO_3$ nanocomposites", J. Appl. Phys., **91**, 7406 (2002).

10. Gaur A, Varma G D & Singh H K, "Enhanced low field magnetoresistance in $La_{0.7}Sr_{0.3}MnO_3/TiO_2$ composite", J. Phy. D: Appl. Phys., **39**, 3531 (2006).

11. Gaur A & Varma G D, "Magnetoresistance behaviour of $La_{0.7}Sr_{0.3}MnO_3$/NiO composites", Solid State Commun., **139**, 310 (2006).

12. Huang Y H, Chen X, Wang Z M, Liao C S, Yan C H, Zhao H W & Shen B G, "Enhanced magnetoresistance in granular $La_{2/3}Ca_{1/3}MnO_3$/polymer composites", J. Appl. Phys., **91**, 7733 (2002).

13. Yan C H, Huang Y H, Chen X, Liao C S & Wang Z M, "Improvement of magnetoresistance over a wide temperature range in $La_{2/3}Sr_{1/3}MnO_3$/polymer composites", J. Phys.: Condens. Matter, **14**, 9607 (2002).

14. Luo F, Wei S, Wang Z M & Yan C H, "Tuning negative and positive magnetoresistances by variation of spin-polarized electron transfer into π-conjugated polymers", Appl. Phys. Lett., **84**, 1719 (2004).

15. Dezanneau G, Sin A, Roussel H, Vincent H & Audier M, "Synthesis and characterisation of $La_{1-x}MnO_{3\pm\delta}$ nanopowders prepared by acrylamide polymerisation", Solid State Commun., **121**, 133 (2002).

16. Kumar J, Siwach P K, Singh R K, Singh H K, Singh R & Srivastava O N, "Low field magneto-transport in LBSMO–PMMA composite", J. Magn. Magn. Mater., **299**, 155 (2006).

17. de Andres A, Garcia-Hemandez M, Martinez J L & Prieto C, "Low-temperature magnetoresistance in polycrystalline manganites: connectivity versus grain size", Appl. Phys. Lett., **74**, 3884 (1999).

18. Mark Rubinstein J, "Two-component model of polaronic transport", J. Appl. Phys., **87**, 5019 (2000).

19. Hwang H Y, Cheong S W, Ong N P & Batlogg B, "Spin-polarized intergrain tunneling in $La_{2/3}Sr_{1/3}MnO_3$", Phys. Rev. Lett., **77**, 2041 (1996).

MAGNETORESISTANCE BEHAVIOUR OF Sr_2FeMoO_6 (WITH DIFFERENT PHASE PURITY) AND Ni DOPED $Sr_2(Fe_{1-x}Ni_x)MoO_6$ ($0 \leq x \leq 0.15$) DOUBLE PEROVSKITE

6.1 INTRODUCTION

Another promising candidate of the magnetoresistance family is the double perovskite Sr_2FeMoO_6 (SFMO). A publication by Kobayashi et al. in 1998 [1] triggered research interest in Sr_2FeMoO_6 due to their half metallic character, predicted by band structure calculations, and high Curie temperature (400-430 K). In these conditions, charge transport is realized by only one type of spin carrier, and consequently, a large magnetoresistance at room temperature is expected. Initial work shows that the single crystals [2] do not show significant MR but a substantial low field magnetoresistance (~5 % at 300 K and ~20 % at 5 K for H~1 T) [3, 4] often appears in polycrystalline samples that are likely to be of extrinsic origin from grain boundary or cation-disorder scattering similar to that of grain boundary MR observed in manganites [5]. A large number of studies has been done to understand the behaviour of MR and to observe the large MR at room temperature and relatively smaller external magnetic fields.

Kobayashi et al. [1] first reported that Sr_2FeMoO_6, an oxide material of $A_2BB'O_6$ type double perovskite structure, show high T_C and spin polarization. Fe-based double perovskite oxides A_2FeMoO_6 (A = Sr, Ba and Ca) have been examined for their remarkable tunnelling-type magnetoresistance (TMR) effect observed at low applied magnetic fields and room

temperature [2, 6–10]. Among the A_2FeMoO_6 materials, Sr_2FeMoO_6 shows the highest T_C (400–430 K) [1, 11–14] and other compounds Ca_2FeMoO_6 and Ba_2FeMoO_6 have Tc in the range 345–380 K [15–17], and 308–367 K [16, 18, 19], respectively. In these compounds, the B positions of the perovskite structure are occupied alternately by Fe and Mo atom, in such a way that each FeO_6 octahedron is corner-linked to six MoO_6 octahedra and vice versa. Each Fe cation that is misplaced in a Mo position is called an antisite (AS) defect. The magnetic structure of the material has been described as an ordered arrangement of parallel Fe^{3+} ($3d^5$, S = 5/2) magnetic moments antiferromagnetically coupled with Mo^{5+} ($4d^1$, S = 1/2) spins. The observed magnetoresistance (MR) has been associated with electron tunnelling through the insulator barriers formed at the grain boundaries (GB's). It is believed that the structure and microstructure of A_2FeMoO_6 are critical factors for the realization of large TMR values. The material properties are very sensitive to synthesis methods as well as processing conditions, such as sintering temperature, time, and atmosphere during heat treatment. The technologically interesting low-field TMR (at H < 1 T) is strongly dependent on the concentration of AS defects as well as on the grain size and nature of grain boundaries. Since the ionic sizes of Fe^{3+} and Mo^{5+} are similar, the concentration of AS defects in A_2FeMoO_6 is finite and Fe and Mo ions are positioned in a random fashion. The relation between the saturation magnetization (M_S) and the concentration of AS defects has been widely investigated [20–22]. Ogale et al. [20] performed Monte Carlo simulation to examine the effects of octahedral mis-site disorder (without and with the concomittant presence of oxygen vacancies) on the magnetization behavior of the Sr_2FeMoO_6 double perovskite. It is seen that magnetization decreases at about 0.065 μ_B/x and T_C at about -3 K/x with the mis-site defect concentration (x). The concomittant presence of oxygen vacancies enhances the rate of decrease of the saturation magnetization. L I Balcells et al. [21] showed that suitable

synthesis conditions allow the formation of Sr_2FeMoO_6 samples with a variable degree of Fe/Mo cationic ordering among the B and B' sublattices. This ordering translates into the saturation magnetization and thus to the effective spin polarization of the oxide which can be controlled and optimized. It is thought that the optimal polarization (100 %) is required to take full advantage of the intrinsic half-metallic nature of these oxides for tunnel magnetoresistance based devices. They have also provided strong evidence of the contribution of Fe-3d electrons to the conduction itinerant band. The influence of AS defects on the Curie temperature of double perovskites has also been studied [12, 23]. Navarro et al. [12] examined the effects of antisite defects and electron doping (La substitution) on the ferromagnetic-paramagnetic transition of Sr_2FeMoO_6 double perovskite. It has been found that antisites and resulting mixing of magnetic interactions promote a broadening of the PM-FM transition. The Curie temperature, as determined by Arrott plots or the inflection point criteria, inevitably reduces when increasing the AS concentration. Based on the results of ab initio calculations, Saha-Dasgupta and Sarma [24] showed that the presence of AS defects would result in a reduction of M_S and electron spin polarization at the Fermi level. Sanchez et al. [25] and Navarro et al. [26] identified the existence of AS defects within the grains as a cause of MR and M_S reduction. They also observed that the sample which have antisite defect up to 9 % has more MR. This observation indicates that the ideal Sr_2FeMoO_6 samples having fully ordered Fe/Mo sublattices may not be a pre-requisite for the materials suitable for spin devices. This shows that the TMR value can be influenced by the nature of GB's. Niebieskikwiat et al. [27] reported that when a material is weak in GB insulating barriers, the disorder of AS defects would results in TMR response deterioration. In contrast, for high resistivity values, the effect of AS defects is entirely masked by the effect of GB barriers, and the TMR is mainly determined by the strength of the GB barriers. Therefore in order to

improve the magnetotransport properties of this material, the most important factor is not to obtain an extremely high Fe/Mo ordering, but an enhancement of the GB insulating barriers is a required condition. They showed that in a sample with a saturation magnetization as low as 1.6 μ_B, the TMR is multiplied by a factor of ~3 due to GB effects. They took a parameter $s\Delta^{1/2}$, as a quantitative measure of the strength of the GB barriers, where Δ and s are the energy and width of the GB barriers, respectively. The microscopic physical properties of the GB's such as connectivity, defects structure, and local density of states are included in s and Δ, and the strength of GB barriers ($s\,\Delta^{1/2}$) can be directly measured by the value of resistivity [27]. It has also been observed that in polycrystalline samples of Sr_2FeMoO_6, the TMR can be readily improved through an oxygen-induced enhancement of GB barriers [28]. Niebieskikwiat et al. [28] studied the magnetic and electric properties of the $Sr_2FeMoO_{6+\delta}$ compound, for δ=0 and 0.04. They found that the oxidation process to obtain the δ=0.04 sample just induces the formation of a nonmagnetic $SrMoO_4$ impurity phase in the grain boundary regions. This impurity increases the resistivity more than two order of magnitude and leads to ~40 % enhancement in low field magnetoresistance for the sample δ = 0.04. Zhong et al. [29] synthesized the Sr_2FeMoO_6 samples by a wet chemistry method under controlled reduction conditions and they manipulated the properties of grain boundary barriers and managed to enhance the magnetoresistance up to 35 %. Moreover, it was also demonstrated by Yuan et al. [30, 31] that tunneling magnetoresistance can be observed in polycrystalline Sr_2FeMoO_6 via increasing the number of grain boundaries. Huang et al. [32, 33] also reported the large low field magnetoresistance in polycrystalline samples of SFMO. Consequently, the MR of polycrystalline Sr_2FeMoO_6 may be improved further by modifying the nature of the GB's.

In addition, LFMR has been found to be enhanced by doping at the Fe site [34]. Several investigations on cationic doping at both Sr and Mo sites have been done in order to explore and tailor LFMR in SFMO [35-37]. Zhou et al. [38] studied the influence of isovalent and aliovalent substitutions for Sr^{2+} on the room temperature MR. For the polycrystalline samples, $Sr_{1.9}A_{0.1}FeMoO_6$ (A=Ca, Ba, La or Pr), the best result was obtained with the Ba (0.1) sample, which showed a factor of 2 enhancement of the MR over that previously reported for Sr_2FeMoO_6. Doping of various elements (such as Co, Cu, Mn etc.) at Fe site in SFMO has been reported [39-46] but the correlation between such doping and the transport properties are not very well understood. It is well known that the magnetic structure, especially the anti-site defects, can be modified notably by doping at Fe sites. Consequently, the substitution of Fe ion should be more helpful in understanding the correlation between magnetic structure and magnetotransport in SFMO. Therefore, in order to understand the correlation between magnetic structure and MR in this compound, further investigations regarding the doping at Fe site in SFMO seem necessary.

In the present chapter, we studied the magnetic and transport properties of the Sr_2FeMoO_6 (with different phase purity) and Ni doped $Sr_2(Fe_{1-x}Ni_x)MoO_6$ ($0 \leq x \leq 0.15$) double perovskite prepared by solid state reaction method. We introduced the tunneling barriers by generating the small amount of insulating $SrMoO_4$ impurity phase at the grain boundaries of Sr_2FeMoO_6 grains during synthesis and a significant enhancement in LFMR is observed. We also studied the effect of Ni doping on the structural, magnetic and magnetotransport properties of $Sr_2Fe_{1-x}Ni_xMoO_6$ double perovskite.

6.2 EXPERIMENTAL

(a) The polycrystalline Sr_2FeMoO_6 samples with different phase purity were prepared by solid-state reaction process. The following three processes have been used in order to produce the samples of different purity:

1. For the first one, the appropriate proportions of $SrCO_3$, Fe_2O_3 and MoO_3 were mixed, ground and calcined at 900 ^{0}C for 12 h in air with intermediate grindings. The calcined mixture was reground, pelletized and sintered at 1200 ^{0}C in air. Unfortunately, pure Sr_2FeMoO_6 phase was not obtained and we got thermodynamically favoured $SrMoO_4$ phase and Sr_2FeMoO_6 phase equally. The sample synthesized by this procedure is referred to as sample A.
2. To avoid the formation of $SrMoO_4$, we synthesized the material in the reducing atmosphere, created by a gas mixture of 10%H_2+90%Ar so that some oxygen could be removed and it would help Mo to remain in 5^+ in place of 6^+ oxidation state and to dissolve in Sr_2FeMoO_6. The appropriate proportions of $SrCO_3$, Fe_2O_3 and MoO_3 were mixed, ground and calcined at 900 ^{0}C under flowing atmosphere of 10%H_2+90%Ar for 12 h with intermediate grinding. Afterwards, the calcined mixture was reground, pelletized and sintered at 1000 ^{0}C under flowing atmosphere of 10%H_2+90%Ar for 6 h. By this method we obtained the single Sr_2FeMoO_6 phase. The sample synthesized by this procedure is referred to as sample B.
3. To produce a small amount of $SrMoO_4$ impurity phase, the sample B was again heated at 1100 ^{0}C for 6 h in an evacuated (~10^{-3} torr) sealed quartz tube. By this way we obtained the Sr_2FeMoO_6 phase with small amount of $SrMoO_4$ impurity phase. It was found that this insulating $SrMoO_4$ goes at the grain

boundaries of Sr_2FeMoO_6 grains and produces the thin grain boundary tunneling barriers in the Sr_2FeMoO_6 matrix and will have a sensitive consequence on the magnetotransport properties as will be confirmed later. The sample synthesized by this procedure is referred to as sample C.

(b) The polycrystalline $Sr_2(Fe_{1-x}Ni_x)MoO_6$ ($0 \leq x \leq 0.15$) samples were also prepared by solid-state reaction process. Stoichiometric amounts of high purity $SrCO_3$, Fe_2O_3, NiO and MoO_3 were mixed and ground. The resulting mixture was calcined at 900 ^{0}C for 12 h in air with several intermediate grindings. The resulting powders were finely pulverized and pressed into pellets followed by sintering at 1000 ^{0}C under flowing atmosphere of argon-hydrogen mixture (90%Ar+10%H_2) for 6 h.

The structural characterization was done at room temperature by using X-ray diffraction (Bruker AXS D8 advance, CuK_α radiation) technique. The microstructure of the samples was examined with field emission scanning electron microscope (FESEM) (Model: FEI, Quanta 200 F, Netherlands). The elemental analysis of the sintered samples was carried out using energy dispersive X-ray analyzer (EDAX' TSL, AMETEK). The temperature dependence resistivity of the samples was measured by a standard four-probe method using Keithley instruments without and with magnetic fields (0-12 kOe). The DC magnetization measurements were done by using vibrating sample magnetometer (VSM Model 155, Princeton Applied Research).

6.3 RESULTS AND DISCUSSION OF Sr_2FeMoO_6 (WITH DIFFERENT PHASE PURITY)

6.3.1 X-ray diffraction studies

The phase purity and crystallographic structure of the samples have been investigated by X-ray diffraction technique. Figure 6.1 shows the room temperature X-ray diffraction patterns using CuK_α radiation. It is clearly observed that the sample A, sintered in air, has Bragg peaks of impurity $SrMoO_4$ phase and main Sr_2FeMoO_6 phase equally. The X-ray diffraction pattern of sample B, obtained by second process, shows Bragg peaks corresponding to only Sr_2FeMoO_6 phase. The XRD pattern of sample C, obtained by third process, shows that in addition to Bragg peaks of the main Sr_2FeMoO_6 phase, there are some Bragg peaks corresponding to the $SrMoO_4$ secondary phase. This $SrMoO_4$ phase is generated in the sample C possibly because of changing of the valence of some of Mo ions from Mo^{5+} to Mo^{6+} during its synthesis by heating in the evacuated sealed quartz tube.

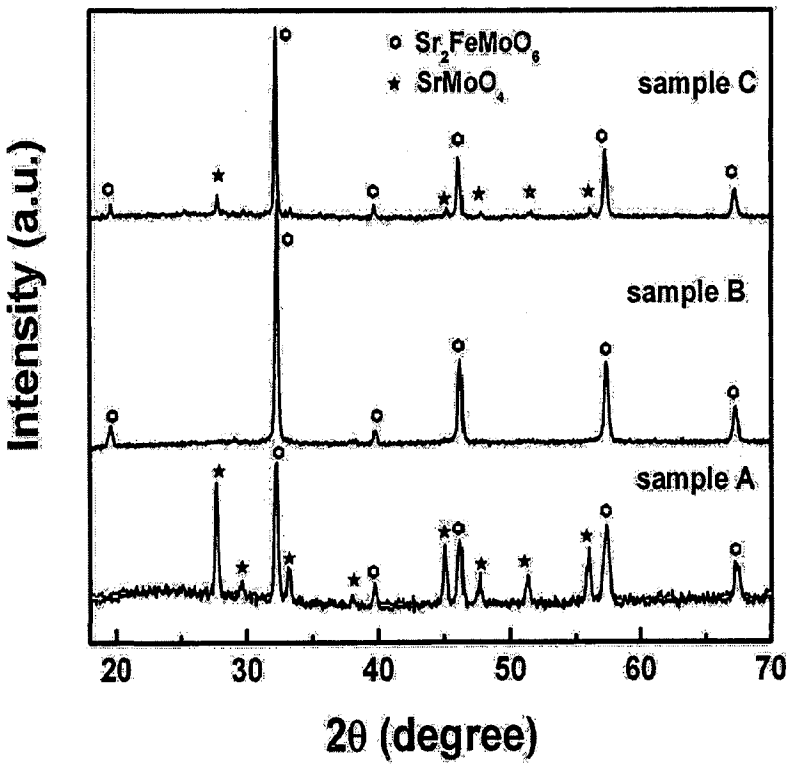

Figure 6.1: X-ray diffraction patterns of the samples A, B and C recorded at room temperature using CuK_α radiation.

Moreover, the XRD patterns also indicates that the intensity of superstructure peak (near 2θ = 19.6°) arising from the ordered arrangement of the Fe and Mo atoms in the double perovskite structure, decreases in the sample C as compared to the sample B. This indicates that Fe/Mo ordering is reduced and antisite defect increases in the sample C as compared to the sample B. The degree of Fe/Mo ordering, calculated on the basis of the relative intensity ratio of the superstructure peak (2θ = 19.6°) with the most intense peak of Sr_2FeMoO_6 (2θ = 32.2°) [47], is found to be 0.08 and 0.06, respectively, for the sample B and sample C. This reduction in Fe/Mo ordering may be because of generation of $SrMoO_4$ phase, which produces the excess of Fe in Sr_2FeMoO_6 matrix (as confirmed by EDAX results) and produces the antisite defects. A quantitative analysis of all the observed Bragg peaks of the sample C shows that the amount of $SrMoO_4$ impurity phase is ~10 %. The quantity of the phases has been estimated by comparing the intensity of the peaks corresponding to Sr_2FeMoO_6 and $SrMoO_4$ phase.

6.3.2 Microstructural and EDX analysis

The FESEM micrographs together with energy dispersive X-ray (EDX) spectra of the sample A, B and C are shown in the Fig. 6.2 (a), (b) and (c), respectively. The FESEM micrograph of the sample A (Fig. 6.2 (a)) shows that some material is distributed at the grain boundaries and forms thick uniform layers. The distribution of phases is analyzed with EDX analysis and it has been found that the material within the grains (for example point A) has the Fe rich Sr_2FeMoO_6 phase and at the grain boundaries (for example point B) $SrMoO_4$ phase. It means for the sample A, the $SrMoO_4$ phase is distributed at the grain boundaries of Sr_2FeMoO_6 grains and makes the thick layer at the grain boundaries. The average thickness of $SrMoO_4$ grain boundaries is ~1 μm, which is too thick for the electron tunneling.

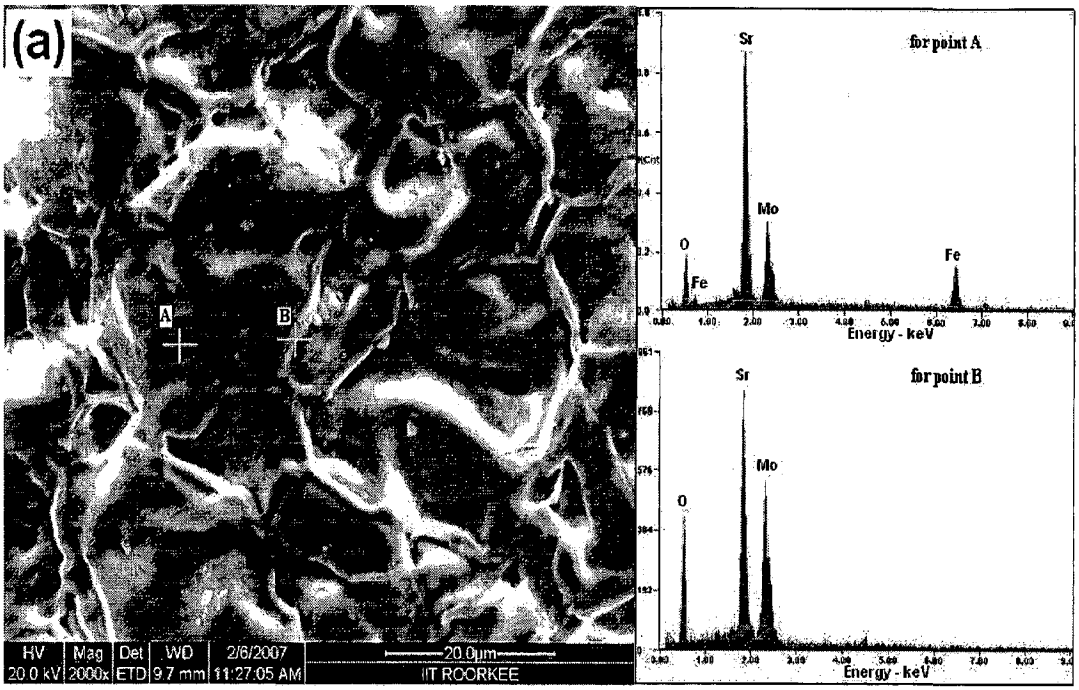

Figure 6.2: (a) FESEM micrograph with EDX spectra of the sample A.

However the sample B has single Sr_2FeMoO_6 phase at grains (point A) and grain boundaries (point B) (see Fig. 6.2 (b)) throughout the sample and chemical composition at every point corresponds to the proper 2 : 1 : 1 : 6 ratio of Sr : Fe : Mo : O. Moreover, the grain boundaries are not well defined in the sample B. Furthermore, in the sample C, $SrMoO_4$ phase again generates and segregates at the grain boundaries of Sr_2FeMoO_6 grains (see Fig. 6.2 (c)). It is also found through EDX analysis of the sample C that the Sr : Fe : Mo : O ratio at point A (at the grain) is approximately 2 : 1.1 : 1 : 6 which does not correspond to the proper ratio 2 : 1 : 1 : 6 of Sr_2FeMoO_6 phase. This excess amount of Fe is because of generation of $SrMoO_4$ phase and these extra Fe ions lead to antiferromagnetic Fe-O-Fe interactions and produce the antisite defects, which is also supported by XRD results. However, the Sr : Mo : O ratio at point B (at the grain boundaries) for sample C is approximately corresponds to $SrMoO_4$ phase. This shows that the grains of sample C are of Fe rich Sr_2FeMoO_6 phase and the material at the grain boundary is $SrMoO_4$.

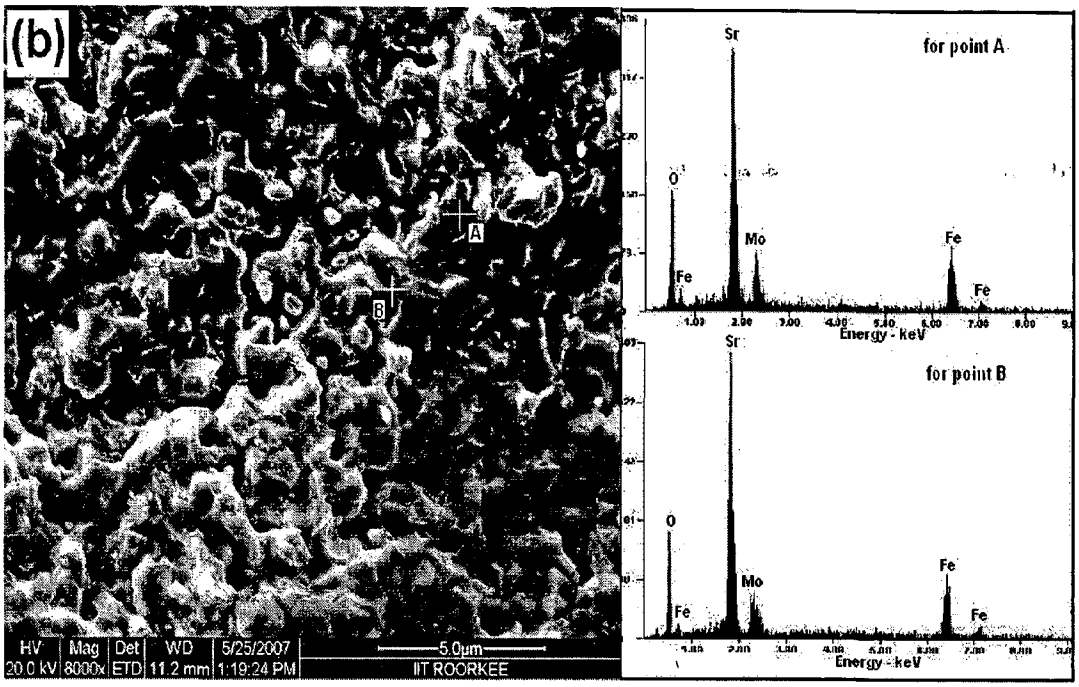

Figure 6.2: (b) FESEM micrograph with EDX spectra of the sample B.

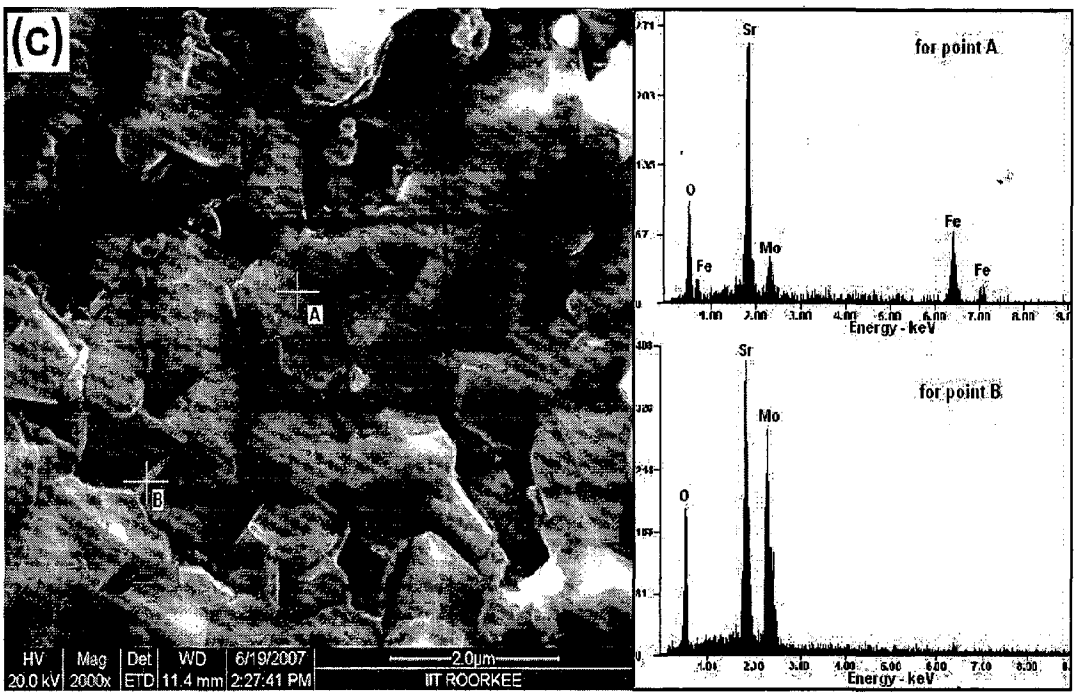

Figure 6.2: (c) FESEM micrograph with EDX spectra of the sample C.

Furthermore, in the sample C, the average thickness of $SrMoO_4$ grain boundary barriers is less as compared to sample A. Therefore, sample C has the possibility of tunneling the electrons through $SrMoO_4$ grain boundary barriers. On the basis of EDAX and FESEM, we can say that in the sample C, $SrMoO_4$ is mainly segregated at the grain boundaries of Sr_2FeMoO_6 grains and forms the thin grain boundary tunneling barriers for the conduction of charge carriers between Sr_2FeMoO_6 grains.

6.3.3 Magnetic properties

Figure 6.3 shows the hystresis loops of the samples B and C recorded at 80 K. These have typical ferromagnetic characteristic with small remanence (M_r ~2.05 emu/gm) and coercivity (H_c ~150 Oe). We also note that the magnetization value is maximum for sample B which has single Sr_2FeMoO_6 phase and decreases for the sample C which has 10 % insulating nonmagnetic $SrMoO_4$ impurity phase. The value of saturation magnetization (M_S) at 80 K is 19.41 and 16.42 emu/gm for the sample B and C, respectively. The decrease in magnetization (M) for the sample C is due to decrease in the volume fraction of ferromagnetic Sr_2FeMoO_6 phase, antisite defects and extra magnetic disorder caused by insulating $SrMoO_4$ phase. As $SrMoO_4$ is nonmagnetic, the phase fraction of magnetic Sr_2FeMoO_6 in sample C reduces, which results the reduction in magnetization of the sample C as compared to the sample B. This reduction in magnetization is more than the value calculated on the basis of the phase fraction of Sr_2FeMoO_6 phase in the sample C. This extra reduction in magnetization may be because of antisite defects as it is widely recognized that the anti-site defects diminish magnetization because the Fe spins in the Mo site antiferromagnetically coupled with the regular Fe spins. It has been reported by Ogale et al.

[20] that the antiferromagnetic Fe-O-Fe interactions grow with concentration of antisite defects, and accordingly, the domain Fe contribution to the magnetization decreases.

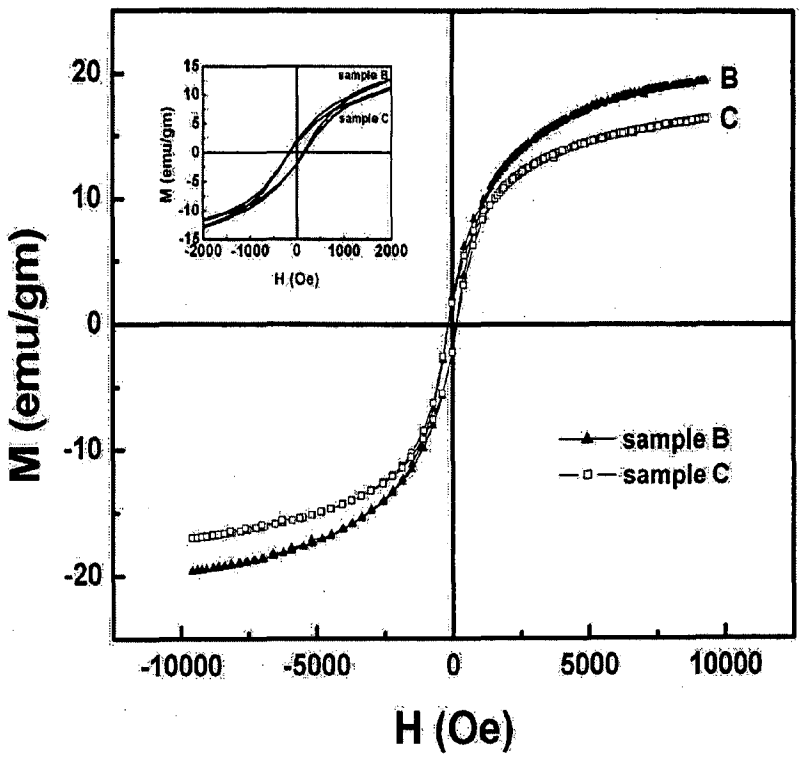

Figure 6.3: Field dependence magnetization (M-H) curves of the samples B and C at 80 K. Inset shows the magnified view of M-H curve up to 2 kOe field.

Furthermore, other possibility of extra reduction in magnetization may be due to spin disorder induced by $SrMoO_4$ grain boundary tunneling barriers in the sample C. Since the $SrMoO_4$ is not incorporated into the Sr_2FeMoO_6 lattice and it segregates into the grain boundaries or interfacial regions, which blocks the spins at grain boundaries and increases the anisotropy in the interfacial regions and misalignment of the magnetic moments of the neighbouring FM domains as explained for manganites [48].

6.3.4 Electrical resistivity measurements

The temperature dependence of resistivity without field for the sample B and C is shown in Fig. 6.4. Both of the samples exhibit semiconducting behaviour, i.e., their resistivity decreases with temperature over the entire measured temperature range (80-300 K). It is also observed that the resistivity of sample C is more as compared to sample B (as shown in Fig. 6.4). This is because the nonmagnetic $SrMoO_4$ impurity is induced to appear at the grain boundaries and the transport properties of the sample C is determined by the electron tunneling through $SrMoO_4$ induced grain boundaries. An enhancement of $SrMoO_4$ impurity level in the sample enhances the grain boundary effect on its resistivity.

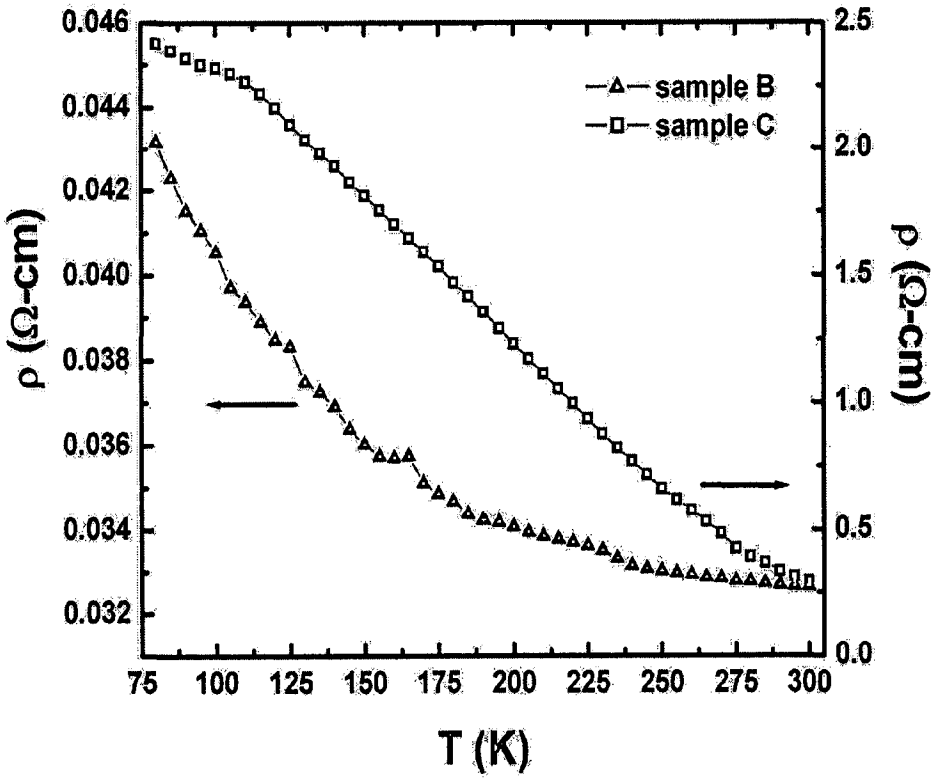

Figure 6.4: Temperature dependence of resistivity of the samples B and C at zero field.

Due to this the sample A, which has almost equal amount of $SrMoO_4$ phase, shows very high value of resistivity and it is not measurable within the range of our instruments and due to this, we could characterize only the samples B and C. The other reason of resistivity enhancement may be because of antisite defect that increases the disorderness leading to enhanced scattering of the charge carriers, which leads to carrier localization and raises the resistivity of the sample C in comparison to the sample B.

6.3.5 Magnetoresistance studies

The temperature dependence of magnetoresistance (MR) in a field of 3 kOe for the samples B and C is shown in Fig. 6.5. The MR ratio is defined as MR (%) =[ρ(0,T) – ρ(H,T)] / ρ(H,T) × 100%, where ρ(0,T) and ρ(H,T) are the resistivity values for zero and applied fields, respectively. It has been found that the sample C yields a significantly larger magnetoresistance than sample B. The values of MR at 80 K for the sample B and C are ~6.6 and ~9.1 %, respectively at 3 kOe. So, the observed enhancement in MR at 80 K for sample C with respect to Sample B is ~38 % at 3 kOe. This enhanced MR at low temperature shows typical behaviour of tunneling type magnetoresistance, which is commonly interpreted within the frame work of spin polarized tunneling across grain boundaries (introduced by impurity $SrMoO_4$ phase in the present case). The tunneling magnetoresistance dominates in the polycrystalline samples as Tomioka et al. [2] reported that no MR effect was found in the single crystal of ordered double perovskite Sr_2FeMoO_6. Hwang et al. [49] also proposed that the spin polarized tunneling between neighbouring grains of manganites is responsible for the low field magnetoresistance effect in polycrystalline samples. This tunneling takes place across the grain boundaries or interfaces, which produce the spin disorder. The reduction in

magnetization (Fig. 6.3) also indicates the magnetic disorder in the sample C and this spin disorder is suppressed by applying the magnetic field, resulting the enhancement in MR.

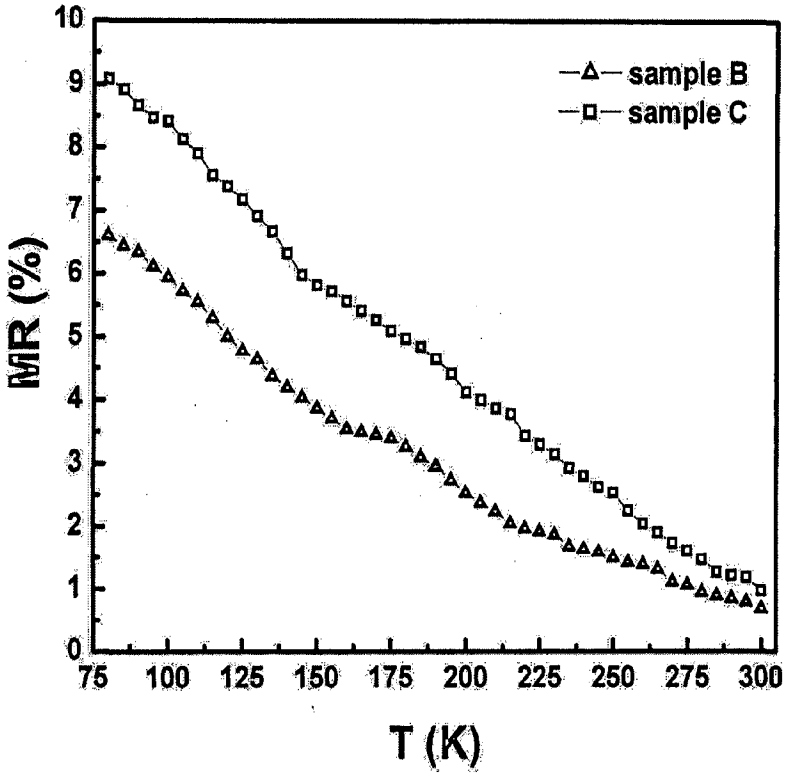

Figure 6.5: Temperature dependence of magnetoresistance (MR) of the samples B and C in a field of 3 kOe.

It is also noticeable from Fig. 6.5 that the value of MR at room temperature (300 K) is also higher for the sample C as compared to sample B. The values of MR at room temperature are 0.69 % and 0.96 % for the samples B and C, respectively at 3 kOe. This enhanced MR even at room temperature in Sr_2FeMoO_6 due to tunneling barriers is quite different from the manganites, in which the tunneling MR is observed only at low temperature range (<130 K) [50, 51]. It may be due to high Curie temperature (Tc ~410 K) of Sr_2FeMoO_6 because it is well known that the tunneling magnetoresistance, which mainly attributed to a grain boundary effect, start to increase with decreasing the temperature below Tc [49]. Moreover,

the antisite defects present in the sample C also help to improve the magnetoresistance because the antisite defects produce the magnetic disorder (as reduction in magnetization indicates), which is suppressed by applying the magnetic field, resulting the enhancement in MR.

The magnetic field dependence of MR for the samples B and C measured in magnetic field range of 0-12 kOe at 80 K is shown in Fig. 6.6. Analysis of Fig. 6.6 shows that with increase in the magnetic field from 0 to12 kOe, the value of MR for the sample C is larger than the sample B. It suggests that magnetic field sensitive MR can be enhanced by impurity $SrMoO_4$ phase through tunneling phenomena at grain boundaries and antisite defects as discussed above.

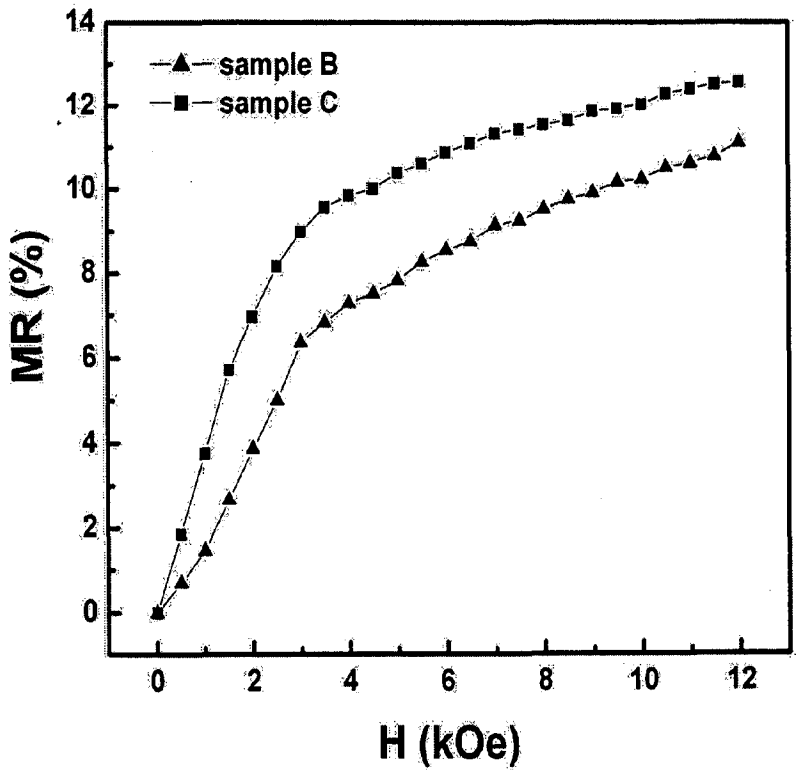

Figure 6.6: Magnetic field dependence of magnetoresistance (MR) at 80 K of the samples B and C in the magnetic field (0-12 kOe).

The values of MR at 80 K for the sample B and C are ~6.6 and ~9.1 % at 3 kOe while the same are ~11.1 and ~12.5 % at 12 kOe, respectively. So, the percent change in MR for the sample C with respect to sample B is more at low fields (up to 3 kOe). The percentage change in MR for the sample C with respect to sample B at 80 K is ~38 % at 3 kOe field while the same is ~13 % at 12 kOe field. This indicates that the large change in MR is produced at low fields (~3 kOe) and this LFMR is caused through spin disorder by the tunneling process at the grain boundaries and antisite defects.

6.4 RESULTS AND DISCUSSION OF Ni DOPED $Sr_2(Fe_{1-x}Ni_x)MoO_6$ ($0 \leq x \leq 0.15$)

6.4.1 X-ray diffraction studies

Figure 6.7 shows the X-ray diffraction patterns of the samples with composition $Sr_2(Fe_{1-x}Ni_x)MoO_6$, where x = 0, 0.05, 0.10 and 0.15. The XRD patterns reveal that most of the dominant diffraction peaks are of the perovskite structure of Sr_2FeMoO_6 and only two weak peaks correspond to $SrMoO_4$ phase. This minority $SrMoO_4$ phase is because of presence of some Mo ions in 6^+ states. The amount of $SrMoO_4$ impurity phase is ~6, ~7, ~9 and ~8 % for the samples with x = 0, 0.05, 0.10 and 0.15, respectively. The quantity of the $SrMoO_4$ phase has been estimated by comparing the intensity of the Bragg peaks corresponding to $SrMoO_4$ and Sr_2FeMoO_6 phase. All the diffraction peaks corresponding to $Sr_2(Fe_{1-x}Ni_x)MoO_6$ perovskite phase have been marked by corresponding (h,k,l) values in Fig. 6.7. All the samples exhibit a superstructure peak (101) arising from the ordered arrangement of the Fe and Mo atoms in the double perovskite structure. It is widely known that such atomic order is apt to be disturbed. Namely, Fe ions occupy the Mo site and vice versa. This is the so-called anti-site (AS) defect and is sensitive to synthesis conditions. The intensity of the

superstructure reflection (101) peak obviously decreases with increasing Ni content, indicating an increase of the anti-site defects.

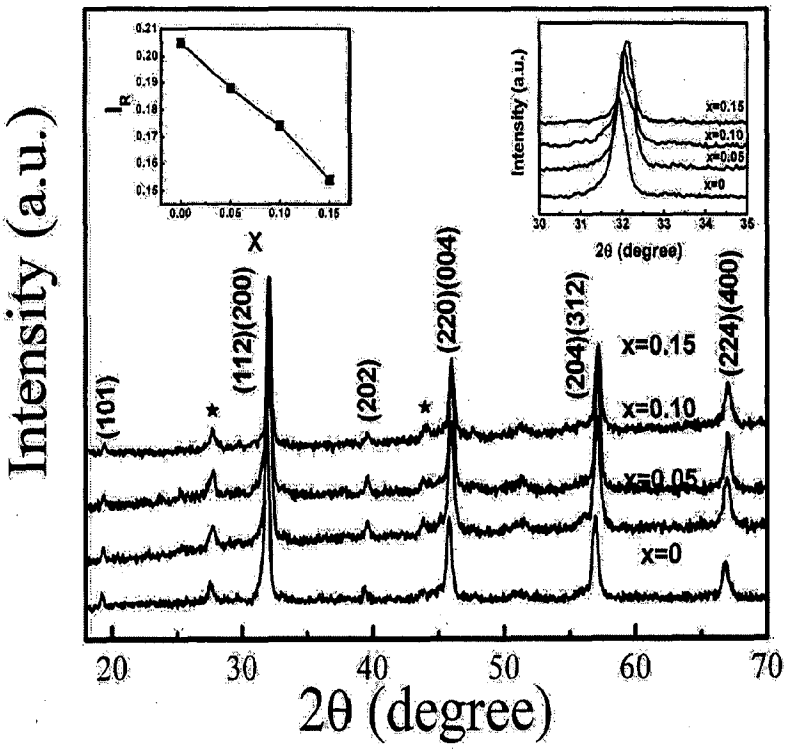

Figure 6.7: X-ray diffraction patterns of samples $Sr_2(Fe_{1-x}Ni_x)MoO_6$ recorded at room temperature using CuK_α radiation. The (hkl) indexing of the peaks is shown for SFMO structure. The peaks belonging to the minority $SrMoO_4$ phase are marked by * sign. Right side inset shows the shift in (112) reflection and left side inset shows the variation of the relative intensity ratio $I_{(101)}/[I_{(112)}+I_{(200)}]$ with Ni doping level x.

Left side inset of Fig. 6.7 shows that the relative intensity ratio $I_R = I_{(101)}/[I_{(112)}+I_{(200)}]$ decreases almost linearly as the Ni doping level x increases from 0 to 0.15. This indicates that Fe/Mo ordering is reduced and antisite defect increases with increasing the Ni concentration. Right side inset of Fig. 6.7 shows that the XRD peak [(112) (200)] shifts towards higher Bragg angle with increasing the Ni content which indicates that the lattice parameters decrease with increasing Ni content. Thus reduction in lattice dimensions induces

the larger disorder in the Fe/Mo sublattices and hence results the more anti-site defects with Ni concentration.

6.4.2 Magnetic properties

Magnetization versus applied field (M-H) curve for various x measured at 80 K is illustrated in Fig. 6.8. From this figure we can see that the saturation magnetic moment (M_S) decreases with increasing x (see inset of Fig. 6.8). The value of M_S reduces from 20.04 emu/gm for x = 0 to 14.71 emu/gm for x = 0.15. Such reduction in M_S is also reported in case of Cr and V substitution at Fe site [39, 41].

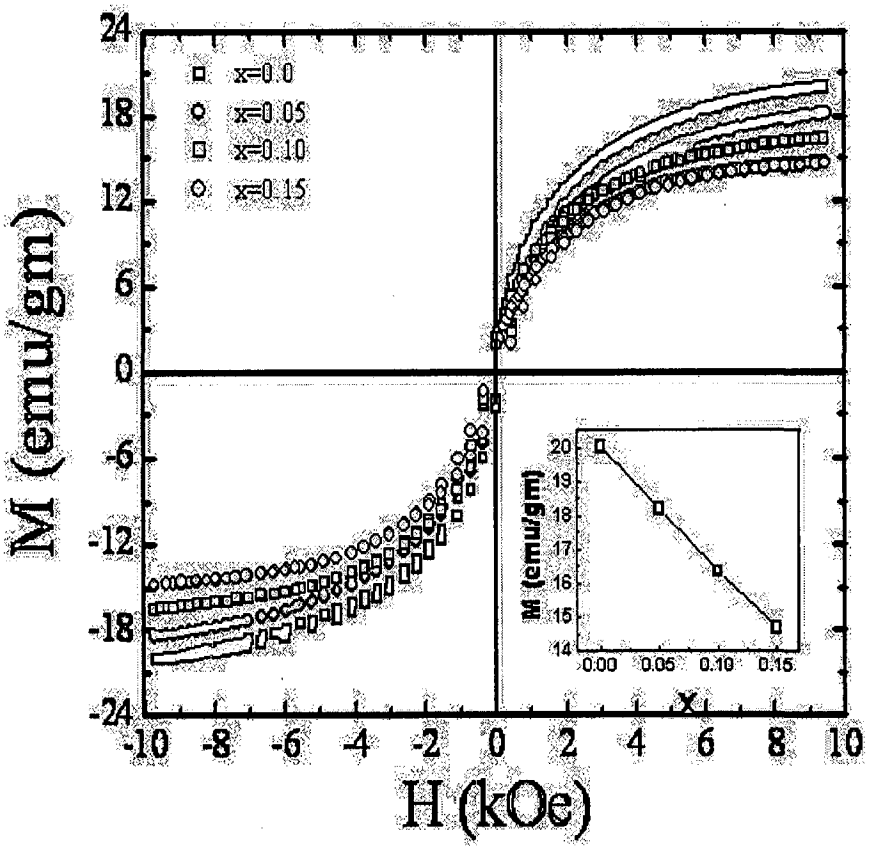

Figure 6.8: Field dependence magnetization (M-H) curves at 80 K of samples $Sr_2(Fe_{1-x}Ni_x)MoO_6$. Inset shows the dependence of magnetization on Ni doping level x.

It is widely recognized that the anti-site defects diminish M_S because the Fe spins in the Mo site antiferromagnetically coupled with the regular Fe spins. It has been reported by Ogale et al. [20] that the antiferromagnetic Fe-O-Fe interactions grow with the concentration of antisite defects, and accordingly, the domain Fe contribution to the magnetization decreases.

The temperature dependence of the magnetization for $Sr_2(Fe_{1-x}Ni_x)MoO_6$ with x = 0 to 0.15 measured at 5 kOe is shown in Fig. 6.9. The transition temperature T_C determined from the peak in (dM/dT)-T curves (data not plotted) are found to be ~408, ~410, ~417 and ~424 K for x = 0, 0.05, 0.10 and 0.15, respectively. It has been found that T_C is progressively raised from 408 K for x = 0 to 424 K for x = 0.15. The enhancement in Curie temperature is the key factor of this study. The inset shows the variation of the Curie temperature (Tc) with Ni concentration. The enhancement in Tc suggests the strengthening of ferromagnetic interactions despite of decrease in magnetization value. The basis behind the rising of Tc is that ferromagnetic alignment of next nearest neighboring Fe ions is favoured if the intermediate nonmagnetic Mo ion is substituted by a Fe ion. The magnetic moment of the Fe ions couple antiferromagnetically to nearest neighbours via a superexchange mechanism, resulting a ferrimagnetic like structure but with reduced magnetic moment. This strengthens the ferromagnetic coupling of the Fe with next nearest neighbours [12]. In fact the same idea has been pushed forward by Solovyev [52] who claimed that ferromagnetic order could not be established by purely electronic mechanism, but some amount of antisite disorder could do so. Moreover, the ferromagnetic character of dopent Ni may also play the role in the enhancement of Curie temperature along with increased antisite defects. In most of the previous studies, B site doping has been done by the non magnetic elements such as Cr [39], V [41] and Mn [53], which produce the antisite defects and reduces the Curie temperature with increasing the doping content.

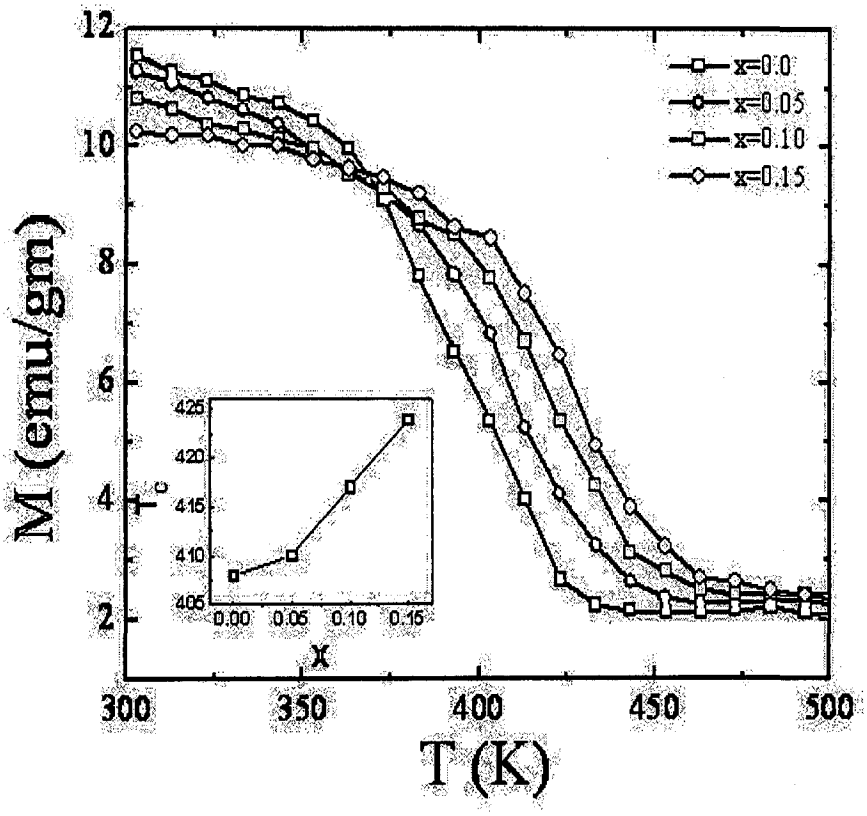

Figure 6.9: Temperature dependence of magnetization of $Sr_2(Fe_{1-x}Ni_x)MoO_6$ at 5 kOe. Inset shows the dependence of T_C on Ni doping level x.

But in our case dopent Ni is ferromagnetic and the net magnetic moment of Ni^{2+} ($3d^8$, S=1) is 2 μ_B, which may play the role of strengthening the magnetic interactions and hence leading to the enhancement in Curie temperature. Moreover, in Ni doped SFMO, Ni^{2+} cations not only affect the Fe/Mo ordering but also mediate the valence equilibrium between Fe^{3+}/Fe^{2+} and Mo^{5+}/Mo^{6+}. Consequently, the electronic itinerancy of the minority spin carriers from Mo cations is affected. Thus it is possible that Ni doping can reinforce the magnetic interactions in SFMO resulting in enhancement of Tc. However, in spite of these interactions the value of saturation magnetization decreases with increasing the Ni content. It is possibly because of

presence of large antiferromagnetically coupled Fe-O-Fe patches due to more antisite defects, which reduces the domain Fe contribution to the saturation magnetization.

6.4.3 Electrical resistivity measurements

The temperature dependence of resistivity without field for the sample $Sr_2(Fe_{1-x}Ni_x)MoO_6$ ($0 \leq x \leq 0.15$) is shown in Fig. 6.10. All the samples exhibit semiconducting behaviour, i.e., their resistivity decreases with temperature over the entire measured temperature range (80-300 K). The value of resistivity at room temperature increases from 0.029 to 0.50 Ω-cm with increasing the Ni concentration from x = 0 to x = 0.15. This is because of antisite defect that increases the disorderness leading to enhanced scattering of the charge carriers, which leads to carrier localization and raises the resistivity of the samples.

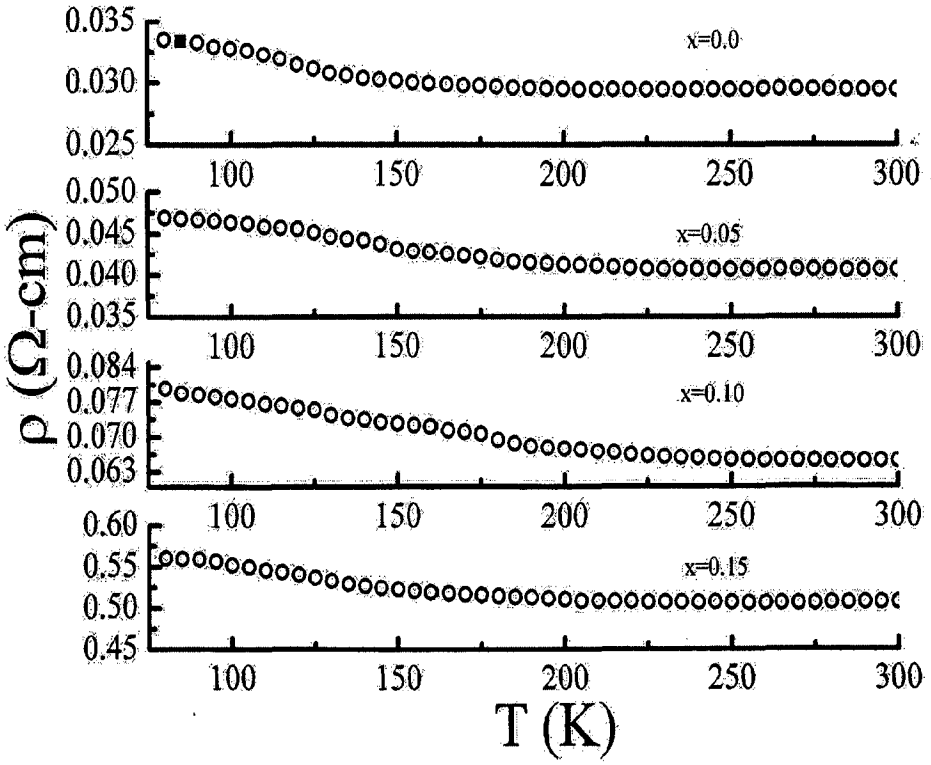

Figure 6.10: Temperature dependence of resistivity at zero field of $Sr_2(Fe_{1-x}Ni_x)MoO_6$.

6.4.4 Magnetoresistance studies

The temperature dependence of magnetoresistance (MR) in a field of 3 kOe for the samples $Sr_2(Fe_{1-x}Ni_x)MoO_6$ ($0 \leq x \leq 0.15$) is shown in Fig. 6.11. The value of MR at 80 K is ~8, ~7, ~5 and ~3 % for x = 0, 0.05, 0.10 and 0.15, respectively. An obvious decrease of the LFMR with x has been observed, which could be understood in term of the model proposed by Garcia-Hernandez et al. [5].

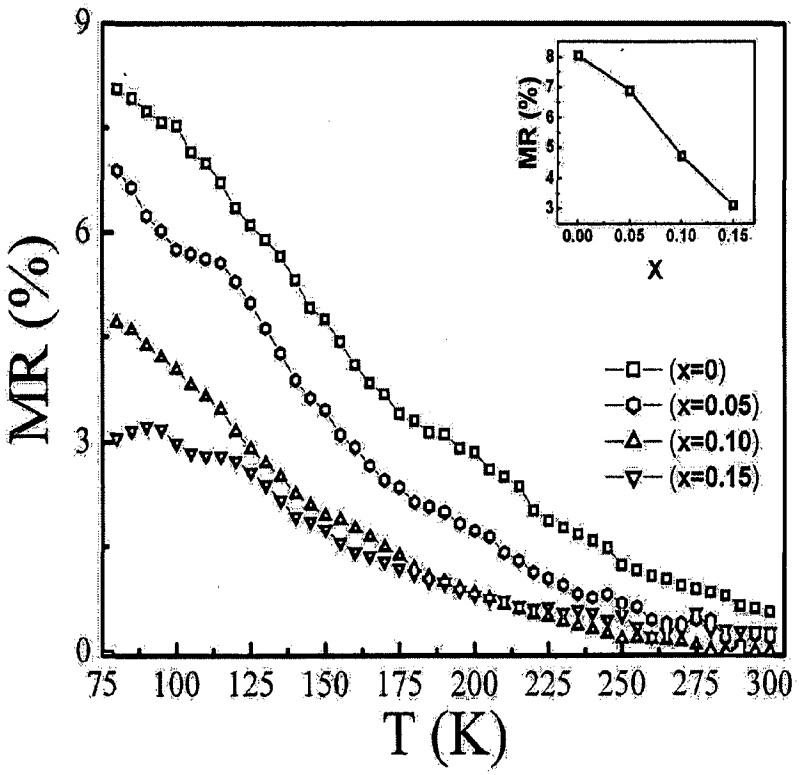

Figure 6.11: Temperature dependence of magnetoresistance (MR) of $Sr_2(Fe_{1-x}Ni_x)MoO_6$ in a field of 3 kOe. Inset shows the dependence of MR on Ni doping level x.

They related the observed linear dependence of LFMR on the saturation magnetization of $A_{2-x}A'_xFeMoO_6$ systems to the anti-site disorder at the Fe and Mo sites and argued that the observation resulted from a spin-dependent crossing of intra-granular barriers originated

from the presence of antiferromagnetic (AF) Fe-O-Fe patches that naturally develop when anti-site disorder occurs in the double perovskite and these Fe-O-Mo patches reduce the magnetization as well as MR. However, the exact reason of reduction in MR by Ni doping is not clear.

The magnetic field dependence of MR for all the studied samples measured in magnetic field range of 0-12 kOe at 80 K is shown in Fig. 6.12. Analysis of Fig. 6.12 shows that with increase in the magnetic field from 0 to12 kOe, the MR of all the samples increases with increasing the magnetic field but the MR value decreases with increasing the Ni concentration. The value of MR at 80 K for the sample with x = 0 is ~12 % while it is ~10 % for the samples with x = 0.15 in the field of 12 kOe.

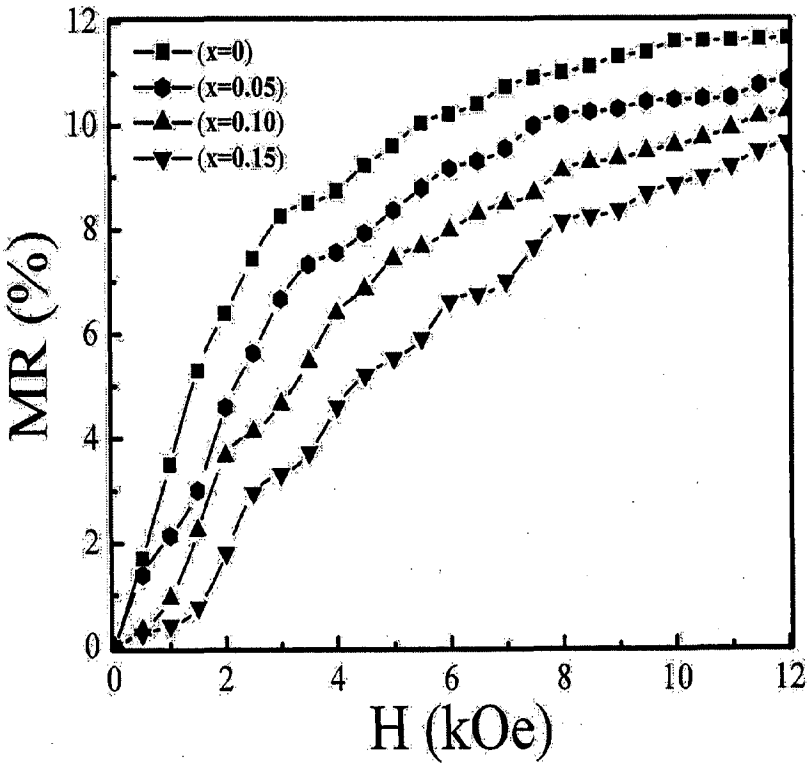

Figure 6.12: Magnetic field dependence of magnetoresistance (MR) at 80 K of $Sr_2(Fe_{1-x}Ni_x)MoO_6$ in the magnetic field (0-12 kOe).

6.5 CONCLUSIONS

In this chapter work, we have synthesized the Sr_2FeMoO_6 (with different phase purity) and Ni doped $Sr_2(Fe_{1-x}Ni_x)MoO_6$ ($0 \leq x \leq 0.15$) samples by solid state reaction method and investigated their microstructural, magnetic and magnetotransport properties. The Sr_2FeMoO_6 (with different phase purity) work has been discussed in section 6.3 and the salient features of the work are given below:

1. The X-ray diffraction patterns show that the sample A, sintered in air, has Bragg peaks of impurity $SrMoO_4$ phase along with main Sr_2FeMoO_6 phase equally while the sample B, sintered in the flowing atmosphere of $10\%H_2+90\%Ar$ gas, shows Bragg peaks corresponding to only pure Sr_2FeMoO_6 phase.
2. The XRD result also shows that in sample C, there is 10 % $SrMoO_4$ secondary phase along with main Sr_2FeMoO_6 phase.
3. The FESEM image and energy dispersive X-ray (EDX) spectra of the sample C show that in the sample C, $SrMoO_4$ is mainly segregated at the grain boundaries of Sr_2FeMoO_6 grains and forms the thin grain boundary tunneling barriers in the Sr_2FeMoO_6 matrix.
4. The magnetization value is maximum for the sample B which has single Sr_2FeMoO_6 phase and decreases for the sample C which has 10 % insulating nonmagnetic $SrMoO_4$ impurity phase.
5. Both of the samples B and C, exhibit semiconducting behaviour, i.e., their resistivity decreases with temperature over the entire measured temperature range (80-300 K) and the resistivity of sample C is more as compared to sample B.
6. The MR studies reveal that the sample C yields a significantly larger magnetoresistance than sample B. The values of MR at 80 K for the sample B

and C are ~6.6 and ~9.1 %, respectively at 3 kOe. So, the observed enhancement in MR at 80 K for sample C with respect to the sample B is ~38 % at 3 kOe.

7. It is also observed that the percent change in MR for the sample C with respect to sample B is more at low fields (up to 3 kOe). The percentage change in MR for the sample C with respect to sample B at 80 K is ~38 % at 3 kOe field while the same is ~13 % at 12 kOe field.
8. As compared to artificial fabrication of a multilayer structure, this is simple way to produce tunneling barriers to enhance the LFMR in double perovskites.

The $Sr_2(Fe_{1-x}Ni_x)MoO_6$ ($0 \leq x \leq 0.15$) work has been discussed in section 6.4 and the highlights of the work are listed below:

1. The XRD patterns reveal that most of the dominant diffraction peaks are of the perovskite structure of Sr_2FeMoO_6 and only two weak peaks correspond to $SrMoO_4$ phase. This minority $SrMoO_4$ phase is because of presence of some Mo ions in 6^+ states.
2. The intensity of the superstructure reflection (101) peak obviously decreases with increasing Ni content, indicating an increase of the anti-site defects. It is also shown that the XRD peak [(112) (200)] shifts towards higher Bragg angle with increasing the Ni content which indicates that the lattice parameters decrease with increasing Ni content.
3. The value of saturation magnetic moment (M_S) decreases with increasing x because of increasing the anti-site defects.
4. The temperature dependence of the magnetization results show that the Curie temperature significantly increases from ~408 to ~424 K when x varies from 0.0 to

0.15. The values of transition temperature (Tc) are found to be ~408, ~410, ~417 and ~424 K for x = 0.0, 0.05, 0.10 and 0.15, respectively.

5. All the samples exhibit semiconducting behaviour, i.e., their resistivity decreases with temperature over the entire measured temperature range (80-300 K) and the value of resistivity at room temperature increases from 0.029 to 0.50 Ω-cm with increasing the Ni concentration from x = 0.0 to x = 0.15.
6. The MR measurements with temperature and field clearly reveal that MR values decrease with increasing the Ni concentration from x = 0.0 to x = 0.15.

REFERENCES

1. Kobayashi K I, Kimura T, Sawada H, Terakura K & Tokura Y, "Room-temperature magnetoresistance in an oxide material with an ordered double-perovskite structure", Nature, **395**, 677 (1998).
2. Tomioka Y, Okuda T, Okimoto Y, Kumai R, Kobayashi K I & Tokura Y, "Magnetic and electronic properties of a single crystal of ordered double perovskite Sr_2FeMoO_6", Phys. Rev. B, **61**, 422 (2000).
3. Kim T H, Uehara M, Cheong S W & Lee S, "Large room-temperature intergrain magnetoresistance in double perovskite $SrFe_{1-x}(Mo \text{ or } Re)_xO_3$", Appl. Phys. Lett., **74**, 1737 (1999).
4. Shinde S R, Ogale S B, Greene R L, Venkatesan T, Tsoi K, Cheong S W & Millis A J, "Thin films of double perovskite Sr_2FeMoO_6: Growth, optimization, and study of the physical and magnetotransport properties of films grown on single-crystalline and polycrystalline $SrTiO_3$ substrates", J. Appl. Phys., **93**, 1605 (2003).
5. Garcia-Hernandez M, Martinez J L, Martinez-lope M J, Casais M T & Alonso J A, "Finding universal correlations between cationic disorder and low field magnetoresistance in FeMo double perovskite series", Phys. Rev. B, **86**, 2443 (2001).
6. Sharma A, Berenov A, Rager J, Branford W, Bugoslavsky Y, Cohen L F & MacManus-Driscoll J L, "Enhanced intergrain magnetoresistance in bulk Sr_2FeMoO_6 through controlled processing", Appl. Phys. Lett., **83**, 2384 (2003).
7. Sarma D D, Mahadevan P, Saha-Dasgupta T, Ray S & Kumar A, "Electronic Structure of Sr_2FeMoO_6", Phys. Rev. Lett., **85**, 2549 (2000).
8. Yanagihara H, Cheong W, Salamon M B, Xu S & Moritomo Y, "Critical behavior of single-crystal double perovskite Sr_2FeMoO_6", Phys. Rev. B, **65**, 092411 (2002).

9. Popov G, Greenblatt M & Croft M, "Large effects of A-site average cation size on the properties of the double perovskites $Ba_{2-x}Sr_xMnReO_6$: A d^5-d^1 system", Phys. Rev. B, **67**, 024406 (2003).

10. Phillips K, Chattopadhyay A & Millis A J, "Dynamical mean-field theory of double perovskite ferrimagnets", Phys. Rev. B, **67**, 125119 (2003).

11. Navarro J, Frontera C, Balcells L I, Martınez B & Fontcuberta J, "Raising the Curie temperature in Sr_2FeMoO_6 double perovskites by electron doping", Phys. Rev. B, **64**, 092411 (2001).

12. Navarro J, Nogues J, Munoz J S & Fontcuberta J, "Antisites and electron-doping effects on the magnetic transition of Sr_2FeMoO_6 double perovskite", Phys. Rev. B, **67**, 174416 (2003).

13. Frontera C, Rubi D, Navarro J, Garcıa-Munoz J L, Fontcuberta J & Ritter C, "Effect of band filling and structural distortions on the Curie temperature of Fe-Mo double perovskites", Phys. Rev. B, **68**, 012412 (2003).

14. Huang Y H, Linden J, Yamauchi H & Karppinen M, "Simple and efficient route to prepare homogeneous samples of Sr_2FeMoO_6 with a high degree of Fe/Mo order", Chem. Mater., **16**, 4337 (2004).

15. Rubi D, Frontera C, Fontcuberta J, Wojcik M, Jedryka E & Ritter C, "Ferromagnetic coupling in $Nd_xCa_{2-x}FeMoO_6$ double perovskites: Dominant band-filling effects", Phys. Rev. B, **70**, 094405 (2004).

16. Ritter C, Ibarra M R, Morellon L, Blasco J, Garcia J & De Teresa J M, "Structural and magnetic properties of double perovskites AA'$FeMoO_6$ (AA' = Ba_2, BaSr, Sr_2 and Ca_2)", J. Phys.: Condens. Matter, **12**, 8295 (2000).

17. Alonso J A, Casais M T, Martinez-Lope M J, Martinez J L, Velasco P, Munoz A & Fernandez-Diaz M T, "Preparation, crystal structure, and magnetic and magnetotransport properties of the double perovskite Ca_2FeMoO_6", Chem. Mater., **12**, 161 (2000).

18. Sriti F, Maignan A, Martin C & Raveau B, "Influence of Fe-site substitutions upon intragrain and intergrain magnetoresistance in the double-perovskite Ba_2FeMoO_6", Chem. Mater., **13**, 1746 (2001).

19. Zhong W, Wu X L, Tang N J, Liu W, Chen W, Au C T & Du Y W, "Magnetocaloric effect in ordered double-perovskite Ba_2FeMoO_6 synthesized using wet chemistry", Eur. Phys. J. B, **41**, 213 (2004).

20. Ogale A S, Ogale S B, Ramesh R & Venkatesan T, "Octahedral cation site disorder effects on magnetization in double-perovskite Sr_2FeMoO_6: Monte Carlo simulation study", Appl. Phys. Lett., **75**, 537 (1999).

21. Balcells L I, Navarro J, Bibes M, Roig A, Martınez B & Fontcuberta J, "Cationic ordering control of magnetization in Sr_2FeMoO_6 double perovskite", Appl. Phys. Lett., **78**, 781 (2001).

22. Sakuma H, Taniyama T, Kitamoto Y & Yamazaki Y, "Cation order and magnetic properties of double perovskite Sr_2FeMoO_6", J. Appl. Phys., **93**, 2816 (2003).

23. Alonso J L, Fernandez L A, Guinea F, Lesmes F & Martın-Mayor V, "Phase diagram and influence of defects in the double perovskites", Phys. Rev. B, **67**, 214423 (2003).

24. Saha-Dasgupta T & Sarma D D, "Ab initio study of disorder effects on the electronic and magnetic structure of Sr_2FeMoO_6", Phys. Rev. B, **64**, 064408 (2001).

25. Sanchez D, Alonso J A, Garcıa-Hernandez M, Martınez-Lope M J, Martınez J L & Mellergard A, "Origin of neutron magnetic scattering in antisite-disordered Sr_2FeMoO_6 double perovskites", Phys. Rev. B, **65**, 104426 (2002).

26. Navarro J, Balcells L I, Sandiumenge F, Bibes M, Roig A, Martınez B & Fontcuberta J, "Antisite defects and magnetoresistance in Sr_2FeMoO_6 double perovskite", J. Phys.: Condens. Matter, **13**, 8481 (2001).

27. Niebieskikwiat D, Prado F, Caneiro A & Sanchez R D, "Antisite defects versus grain boundary competition in the tunneling magnetoresistance of the Sr_2FeMoO_6 double perovskite", Phys. Rev. B, **70**, 132412 (2004).

28. Niebieskikwiat D, Caneiro A, Sanchez R D & Fontcuberta J, "Oxygen-induced grain boundary effects on magnetotransport properties of $Sr_2FeMoO_{6+\delta}$", Phys. Rev. B, **64**, 180406(R) (2001).

29. Zhong W, Liu W, Au C T & Du Y W, "Tunnelling magnetoresistance of double perovskite Sr_2FeMoO_6 enhanced by grain boundary adjustment", Nanotechnology, **17**, 250 (2006).

30. Yuan C L, Wang S G, Song W H, Yu T, Dai J M, Ye S L & Sun Y P, "Enhanced intergrain tunneling magnetoresistance in double perovskite Sr_2FeMoO_6 polycrystals with nanometer-scale particles", Appl. Phys. Lett., **75**, 3853 (1999).

31. Yuan C L, Zhu Y, Ong P P, Shen Z X & Ong C K, "Influence of preparation method on $SrMoO_4$ impurity content and magnetotransport properties of double perovskite Sr_2FeMoO_6 polycrystals", Solid State Commun., **129**, 551 (2004).

32. Huang Y H, Linden J, Yamauchi H & Karppinen M, "Large low-field magnetoresistance effect in Sr_2FeMoO_6 homocomposites", Appl. Phys. Lett., **86**, 072510 (2005).

33. Huang Y H, Yamauchi H & Karppinen M, "Competition between intragranular and intergranular tunneling magnetoresistance in polycrystalline Sr_2FeMoO_6", Phys. Rev. B, **74**, 174418 (2006).

34. Sui Y, Wang X J, Cheng J G, Liu Z G, Miao J P, Huang X Q, Lu Z, Qian Z N, Su W H, Tang J K & Ong C K, "Influence of nonmagnetic Al ions on magnetoresistance of double-perovskite $Sr_2Fe_{1-x}Al_xMoO_6$ ($0 \leq x \leq 0.30$)", J. Appl. Phys., **98**, 064505 (2005).

35. Yu R C, Zhao P, Li F Y, Liu Z X, Liu J & Jin C Q, "Effect of Ba content on initial magnetization of $Sr_{2-x}Ba_xFeMoO_6$ and the structural stability under high pressure", Phys. Rev. B, **69**, 214405 (2004).

36. Kobayashi K I, Okuda T, Tomioka Y, Kimura T & Tokura Y, "Possible percolation and magnetoresistance in ordered double perovskite alloys $Sr_2Fe(W_{1-x}Mo_x)O_6$", J. Magn. Magn. Mater., **218**, 17 (2000).

37. Rubi D, Frontera C, Nogues J & Fontcuberta J, "Enhanced ferromagnetic interactions in electron doped $Nd_xSr_{2-x}FeMoO_6$ double perovskites", J. Phys.: Condens. Matter, **16**, 3173 (2004).

38. Zhou J P, Dass R, Yin H Q, Zhou J S, Rabenberg L & Goodenough J B, "Enhancement of room temperature magnetoresistance in double perovskite ferrimagnets", J. Appl. Phys., **87**, 5037 (2000).

39. Feng X M, Rao G H, Liu G Y, Yang H R, Lin W F, Ouyang Z W & Liang J K, "Effects of Cr doping on the cationic ordering and magnetic properties of $Sr_2(Fe_{1-x}Cr_x)MoO_6$", Physica B, **344**, 21 (2004).

40. Kim J H, Ahn G Y, Park S I & Kim C S, "Effects of Cr doping on magnetic properties of ordered Sr_2FeMoO_6", J. Magn. Magn. Mater., **282**, 295 (2004).

41. Zhang Q, Rao G H, Feng X M, Liu G Y, Xiao Y G, Zhang Y & Liang J K, "Influence of V substitution for Fe on the transport and magnetic properties of Sr_2FeMoO_6", Solid State Commun., **133,** 223 (2005).

42. Chen L, Yuan C L, Xue J M & Wang J, "B-site ordering and magnetic behaviours in Ni-doped double perovskite Sr_2FeMoO_6", J. Phys. D: Appl. Phys., **38,** 4003 (2005).

43. Yuan C L, Zhu Y & Ong P P, "Effect of Cu doping on the magnetoresistive behavior of double perovskite Sr_2FeMoO_6 polycrystals", J. Appl. Phys., **91,** 4421 (2002).

44. Moritomo Y, Kusuya H, Akimoto T & Machida A, "Room-temperature magnetoresistance in Fe-site-substituted Sr_2FeMoO_6", Jpn. J. Appl. Phys., **39,** L360 (2000).

45. Sui Y, Wang X J, Qian Z N, Cheng J G, Liu Z G, Miao J P, Li Y, Su W H & Ong C K, "Enhancement of low-field magnetoresistance in polycrystalline Sr_2FeMoO_6 with Al doping", Appl. Phys. Lett., **85,** 269 (2004).

46. Pena A, Gutierrez-Martinez J, Barandiaran J M, Hernandez T & Rojo T, "Structure and magnetism in $Sr_2(Fe_{1-x}Al_x)MoO_6$ ($0 \leq x \leq 0.3$) double perovskite compounds", J. Phys.: Condens. Matter, **13,** 6535 (2001).

47. Li C, Cailei Y, Junmin X & Wang J, "Enhancement of magnetization and Curie temperature in Sr_2FeMoO_6 by Ni doping", J. Am. Ceram. Soc., **89,** 672 (2006).

48. de Andres A, Garcia-Hernandez M, Martinez J L & Prieto C, "Low-temperature magnetoresistance in polycrystalline manganites: connectivity versus grain size", Appl. Phys. Lett., **74,** 3884 (1999).

49. Hwang H Y, Cheong S W, Ong N P & Batlogg B, "Spin-polarized intergrain tunneling in $La_{2/3}Sr_{1/3}MnO_3$", Phys. Rev. Lett., **77,** 2041 (1996).

50. Gaur A, Varma G D & Singh H K, "Enhanced low field magnetoresistance in $La_{0.7}Sr_{0.3}MnO_3/TiO_2$ composite", J. Phy. D: Appl. Phys., **39**, 3531 (2006).

51. Kumar J, Singh R K, Siwach P K, Singh H K, Singh R & Srivastava O N, "Low field magneto-transport in LBSMO–PMMA composite", J. Magn. Magn. Mater., **299**, 155 (2006).

52. Solovyev I V, "Electronic structure and stability of the ferrimagnetic ordering in double perovskites", Phys. Rev. B, **65**, 144446 (2002).

53. Moritomo Y, Kusuya H, Machida A, Nishibori E, Takata M, Sakata M & Nakamura A, "Fe-site substitution effects on conductive ferromagnet Sr_2FeMoO_6", J. Phys. Soc. Jpn., **70**, 3182 (2001).

Chapter - 7

CONCLUSIONS AND RECOMMENDATIONS

In this chapter, we present a brief summary of the work contained in the thesis as presented in the chapters 3-6. The overall comments and conclusive remarks have also been added. This thesis describes and discusses the synthesis and characterization of half metallic compounds, $La_{0.7}Sr_{0.3}MnO_3$ (LSMO) and $La_{0.67}Ca_{0.33}MnO_3$ (LCMO) manganites and Sr_2FeMoO_6 double perovskite, which are technologically important in spintronics devices. The preliminary aim of this thesis work is to synthesize and characterize the LSMO and LCMO manganites and Sr_2FeMoO_6 double perovskite in order to improve their magnetotransport properties at low value of magnetic fields (<10 kOe). To improve the magnetotransport at low field, we applied the approach to disturb the high spin polarization of these half metallic compounds by modifying their grain boundaries so that when a small magnetic field is applied, the spins are aligned in magnetic field direction and hence an enhanced MR response is achieved at low fields. Therefore, a spin misorientation in the magnetically virgin state is crucial to obtain an enhanced MR. The enhanced MR observed in a wide temperature range and at low field (<10 kOe) is more useful from the application point of view. The spin polarization is disturbed through modifying the grain boundaries by various ways such as varying the particle size, making the composites of CMR perovskites (LSMO and LCMO) with some insulating inorganic oxides (NiO, TiO_2, Co_3O_4) and polymer (PPS). Moreover in Sr_2FeMoO_6 double perovskite, the tunneling barriers of insulating

$SrMoO_4$ phase have been generated at the grain boundaries of Sr_2FeMoO_6 grains to modify the grain boundaries by optimizing the synthesis conditions. The main conclusions drawn from the present investigations through the chapters 3-6 are as follows:

1. The nanophasic $La_{0.7}Sr_{0.3}MnO_3$ (LSMO) and $La_{0.67}Ca_{0.33}MnO_3$ (LCMO) samples have been prepared by sol-gel method (chapter 3). The particle sizes are varied to modify the number of grain boundaries by sintering the samples at different temperatures ranging from 600-1000 °C. Both T_{IM} and Tc shift towards lower temperature and magnetization decreases with decreasing the sintering temperature. In both the cases, all samples show the increase in MR at low temperature (T < Tc) as the sintering temperature decreases and it has been found that the maximum magnetoresistance is observed in the smallest particles sample, sintered at the lowest temperature (600 °C). Moreover, in case of LCMO, along with the increment in MR below Tc, there is a peak in MR-T curve around Tc indicating the contribution of intrinsic component of MR, which arises due to DE mechanism around Tc. The percentage change in MR at 80 K for the LSMO sample T6, sintered at 600 °C, with respect to the LSMO sample T10, sintered at 1000 °C, is ~94 % at 1 kOe and ~37 % at 10 kOe. This shows that the percentage change in MR is more at low field (1 kOe) as compared to higher field (10 kOe). However, this percentage change in MR for LCMO samples P6, sintered at 600 °C, with respect to LCMO sample P10, sintered at 1000 °C, is ~57 % and ~58 % at 1 and 10 kOe field, respectively (see Table 7.1). It has been argued that this enhancement in MR in the samples of smaller particles is because of enhanced spin polarized tunneling between the grains by assuming the increase of grain boundary contribution as the particle size of the sample decreases due to lowering of the sintering temperatures.

Table 7.1: Percentage change in MR of LSMO and LCMO samples sintered at 600 ^{0}C with respect to sample sintered at 1000 ^{0}C.

System	Sintering temperature for maximum MR (^{0}C)	Percentage change in MR at 80 K with respect to the sample sintered at 1000 ^{0}C	
		MR (%) at 1 kOe	MR (%) at 10 kOe
$La_{0.7}Sr_{0.3}MnO_3$	600	94	37
$La_{0.67}Ca_{0.33}MnO_3$	600	57	58

2. The composites of $La_{0.7}Sr_{0.3}MnO_3$ (LSMO) with insulating oxides NiO and TiO_2 {$(LSMO)_{1-x}/(NiO)_x$ and $(LSMO)_{1-x}/(TiO_2)_x$ with x = 0.0, 0.05, 0.10, 0.15 and 0.20} have been synthesized by solid state reaction method and study their magnetic and magnetotransport properties (chapter 4). The composites are synthesized in such a way so that second phase material (NiO and TiO_2) does not enter into the LSMO lattice and is found to remain at grain boundary regions and on the surfaces of LSMO grains without disturbing the stoichiometry of LSMO phase within the grain. It has been found that T_{IM} shifts towards lower temperature and magnetization decreases with increase of the NiO and TiO_2 content. The enhancement in MR is observed at low temperature below 120 K and 130 K, respectively for the composites $(LSMO)_{1-x}/(NiO)_x$ and $(LSMO)_{1-x}/(TiO_2)_x$ up to the doping density of x = 0.15 and x = 0.10, respectively at applied magnetic field H ~3 kOe. Moreover, the enhancement in MR is observed even at high temperature (near room temperature) for all the compositions of $(LSMO)_{1-x}/(NiO)_x$ composite. The maximum enhancement in MR at 80 K with respect to pure LSMO (x = 0) is ~38 % for the $(LSMO)_{1-x}/(NiO)_x$ composites with x = 0.15 and ~28 % for the $(LSMO)_{1-x}/(TiO_2)_x$ composites with x = 0.10 at 3 kOe field. It is also observed that the percent change in MR for the composites with respect to

pure LSMO is more at low fields (up to 3 kOe). The percentage change in MR with respect to pure LSMO (x = 0) at 80 K is ~38 % and ~28 % at 3 kOe field while the same is ~25 % and ~13 % at 12 kOe field for the composites $(LSMO)_{1-x}/(NiO)_x$ with x = 0.15 and $(LSMO)_{1-x}/(TiO_2)_x$ with x = 0.10, respectively (see Table 7.2). It is argued that this improved LFMR at low temperature (below 130 K) arises from the enhanced spin-polarized tunneling at the grain boundaries.

3. The composites of $La_{0.67}Ca_{0.33}MnO_3$ (LCMO) with inorganic oxide Co_3O_4 & organic polymer PPS {$(LCMO)_{1-x}/(Co_3O_4)_x$ and $(LCMO)_{1-x}/(PPS)_x$} have also been prepared to improve their magnetotransport behaviour at low value of applied magnetic fields (chapter 5). The composites are again synthesized in a manner so that second phase material (Co_3O_4 and PPS) does not enter into the LCMO lattice and is found to remain at grain boundary regions and on the surfaces of LCMO grains. Results show that the resistivity of the composite samples increases sharply especially in the low temperature range and magnetization decreases as a consequence of Co_3O_4 and PPS addition. An enhancement in low field magnetoresistance (LFMR) is observed for the composites up to the x = 0.10 for $(LCMO)_{1-x}/(Co_3O_4)_x$ and x = 0.20 for $(LCMO)_{1-x}/(PPS)_x$ composite below the temperature 125 K and 175 K, respectively. The maximum enhancement in MR at 80 K with respect to pure LCMO (x = 0) is ~35 % for the $(LCMO)_{1-x}/(Co_3O_4)_x$ composites with x = 0.10 and ~17 % for the $(LCMO)_{1-x}/(PPS)_x$ composites with x = 0.20 at 3 kOe field. It is also perceptible that the percent change in MR for the composites with respect to pure LCMO is more at low fields (up to 3 kOe). The percentage change in MR with respect to pure LCMO (x = 0) at 80 K is ~35 % and ~17 % at 3 kOe field while the same is ~12 % and ~6 % at 12 kOe field for the composites $(LCMO)_{1-x}/(Co_3O_4)_x$ with x = 0.10 and $(LCMO)_{1-x}/(PPS)_x$

with x = 0.20, respectively (see Table 7.2). This enhancement in LFMR is again related to enhanced spin-polarised tunneling, which is manipulated by the spin disorder at the LCMO surfaces caused by Co_3O_4 and PPS.

Table 7.2: Percentage change in MR of the different composites with respect to virgin sample (x = 0).

System	Composition (x), corresponding to maximum MR	Percentage change in MR at 80 K with respect to virgin sample (x = 0)	
		MR (%) at 3 kOe	MR (%) at 12 kOe
$(LSMO)_{1-x}/(NiO)_x$	0.15	38	25
$(LSMO)_{1-x}/(TiO_2)_x$	0.10	28	13
$(LCMO)_{1-x}/(Co_3O_4)_x$	0.10	35	12
$(LCMO)_{1-x}/(PPS)_x$	0.20	17	06

4. The single phase Sr_2FeMoO_6 (sample B) and Sr_2FeMoO_6 with 10 % $SrMoO_4$ impurity phase (sample C) have been synthesized by sintering the material in different environments and study their microstructural, magnetic and magnetotransport properties (section 6.3 of chapter 6). FESEM and EDAX results clearly indicate that in the sample C, the insulating $SrMoO_4$ phase is segregated at the grain boundaries of Sr_2FeMoO_6 grains and produces the thin tunneling barriers in the conduction of charge carriers between Sr_2FeMoO_6 grains. XRD results show that the generation of $SrMoO_4$ phase increases the antisite defect in the sample C. Both of the samples show semiconducting behaviour in the entire measured temperature range (80-300 K). The resistance of sample C is more as compared to sample B while the value of magnetization is less. The 38 % enhancement in magnetoresistance (MR) at 80 K is observed for the sample C (having 10 % insulating $SrMoO_4$ phase) as compared to

single phase sample B at 3 kOe. It is also observed that the percent change in MR for the sample C with respect to sample B is more at low fields (up to 3 kOe). The percentage change in MR for the sample C with respect to sample B at 80 K is ~38 % at 3 kOe field while the same is ~13 % at 12 kOe field (see Table 7.3). It is suggested that this enhancement in MR is due to intergrain tunneling through insulating nonmagnetic $SrMoO_4$ grain boundary barriers in the Sr_2FeMoO_6 matrix and subsequent antisite defects, leading to enhancement in low field magnetoresistance (LFMR). As compared to artificial fabrication of a multilayer structure, this is simple way to produce tunneling barriers by optimizing the synthesis conditions to enhance the LFMR in double perovskites.

Table 7.3: Percentage change in MR of sample C (Sr_2FeMoO_6 with 10 % impurity phase) with respect to the sample B (Pure Sr_2FeMoO_6).

Samples	MR ratio (%) at 80 K & 3 kOe	Percentage change in MR at 80 K with respect to the sample B	
		MR (%) at 3 kOe	MR (%) at 12 kOe
Sample B (Pure Sr_2FeMoO_6)	6.6	-	-
Sample C (Sr_2FeMoO_6 with 10 % impurity phase)	9.9	38	13

5. The effect of Ni doping at Fe site on magnetic and magnetotransport properties of $Sr_2(Fe_{1-x}Ni_x)MoO_6$ ($0 \leq x \leq 0.15$) double perovskite have also been studied (section 6.4 of chapter 6). X-ray diffraction results show that Ni doping reduces the Fe/Mo ordering and introduces more anti-site defects, which increase with Ni concentration. The Curie temperature (Tc) of $Sr_2(Fe_{1-x}Ni_x)MoO_6$ increases systematically from 408 K for x = 0 to 424 K for x = 0.15. However, magnetization decreases as Ni content

increases. Moreover, the low field magnetoresistance is observed to decrease with increasing the Ni concentration.

The results of the present thesis show that we successfully achieve the large magnetoresistance at low fields (~3 kOe) in both perovskites manganites and double perovskite by modifying their grain boundaries. So it can be concluded by these studies that MR can be made low field sensitive by disturbing the spin polarization of the half metallic compounds by modifying their grain boundaries. But this grain boundary modified low field magnetoresistance of large magnitude is observed only at low temperatures (<Tc) and this increases with decreasing the temperature. Thus, the value of low field magnetoresistance in the low temperature regime (<Tc) have definitely been improved. However, for technological applications, the large value of low field magnetoresistance is desired at room temperature. Therefore, intensive efforts are still required, by material science researchers, to achieve the significant low field magnetoresistance at room temperature.